博士論文

Search for solar axions with the Tokyo axion helioscope

(東京アクシオンヘリオスコープ装置による
太陽アクシオンの探索)

井上 慶純

Search for solar axions with the Tokyo axion helioscope

INOUE Yoshizumi

Department of Physics, School of Science, the University of Tokyo

October 2015

Abstract

The axion is a hypothetical particle which was introduced to solve the strong CP problem in the quantum chromodynamics (QCD). Solar axions are expected to be produced in the core of the sun, if it exists. We have searched for such axions using an axion helioscope which is equipped with a 2.3 m-long 4 T superconducting magnet, a container to hold dispersion-matching gas, a PIN-photodiode-array X-ray detector, and a telescope mount mechanism to track the sun. In the second phase of our long-term experiment, a mass region up to $m_a < 0.27\,\mathrm{eV}$ was newly explored by introducing helium-4 gas into the axion-to-photon conversion region. In the third phase, our apparatus was upgraded to search for heavier axions and a mass region around 1 eV was further explored.

As a result, we observed no significant excess of an axion signal for any scanned masses. From the absence of any evidence in both measurements, we set a new limit on the axion–photon coupling constant as $g_{a\gamma} < 6.5\text{–}10.4 \times 10^{-10}\,\mathrm{GeV}^{-1}$ for $0.06\,\mathrm{eV} < m_a < 0.27\,\mathrm{eV}$, and $g_{a\gamma} < 5.6\text{–}13.4 \times 10^{-10}\,\mathrm{GeV}^{-1}$ for $0.84\,\mathrm{eV} < m_a < 1.00\,\mathrm{eV}$ at 95% confidence level. Both limits are more stringent than the limit inferred from the solar-age consideration, and are excluding parameters beyond the helioseismological bound which involves more assumptions. The former is the first experimental search for solar axions which had the enough sensitivity to detect such axions that do not violate the solar model itself in this mass region. The latter is the first result to search for axions using a magnetic helioscope in the realistic $g_{a\gamma}$–m_a parameter region predicted by the axion models. At the time of publication of the above results, we successfully presented the highest sensitivities to the detection of solar axions.

In this thesis, we present the details of the experiment and the results as well as the technologies which were used to open up new parameter region.

Contents

Chapter 1

Introduction

It is widely believed that the SU(3) gauge theory, or the quantum chromodynamics (QCD), is the theory of the strong interactions. However, one open question referred to as "the strong CP problem" is left unresolved. It is a problem: why CP is conserved in the strong interaction experimentally although QCD gets CP violating effective interaction both from the QCD vacuum initial value and the quark mass matrix. The axion is the pseudo Nambu–Goldstone boson of a spontaneously broken symmetry $\mathrm{U}(1)_{\mathrm{PQ}}$ which was introduced to solve this problem by way of a dynamic mechanism [1, 2, 3].

A variety of laboratory axion searches has ruled out the original axion model in which the PQ-symmetry breaking occurred incidentally to the electroweak symmetry breaking. However, it is possible to construct variant models in which the PQ-symmetry breaking scale is much larger than the electroweak scale, $f_{\mathrm{PQ}} \gg f_W \approx 250\,\mathrm{GeV}$. Such axions are called "invisible axions" and are not completely ruled out yet.

The invisible axion was not merely a defensive modification to a theory. It motivated many astrophysical and cosmological interests. Figure 1.1 is a reproduction of a figure in Ref. [4] where astrophysical and cosmological bounds are summarized. One region at $10^{-6}\,\mathrm{eV} \lesssim m_a \lesssim 10^{-3}\,\mathrm{eV}$ is attractive from the cosmological aspects because the axion can be a good candidate of the cold dark matter. The other mass region at around one to a few eV is called the "hadronic axion window." In this region, such axions that couple to electrons at tree level are already ruled out by the cooling rate of the red giants since they would provide too-much efficient means to loose energy from stars. However, this mechanism do not exclude the KSVZ axions or the hadronic axions.

In the hadronic axion window, axions can be abundantly produced in the solar interior through the axion–photon coupling, yet moderately enough not to conflict with the apparent age of the sun. Sikivie [5] has suggested that such "solar axions" might be able to be detected by means of the so-called "axion helioscope experiment." Although the very place of the hadronic axion window and whether it is still open or not are controversial, direct observational search for solar axions should hold qualitative significance, since the sun is nevertheless the best known stellar object to us.

We have constructed an axion helioscope [6] with a dedicated superconducting magnet which can track the sun, and have carried out measurements to search for the solar axion. In this thesis, we will present the details on the

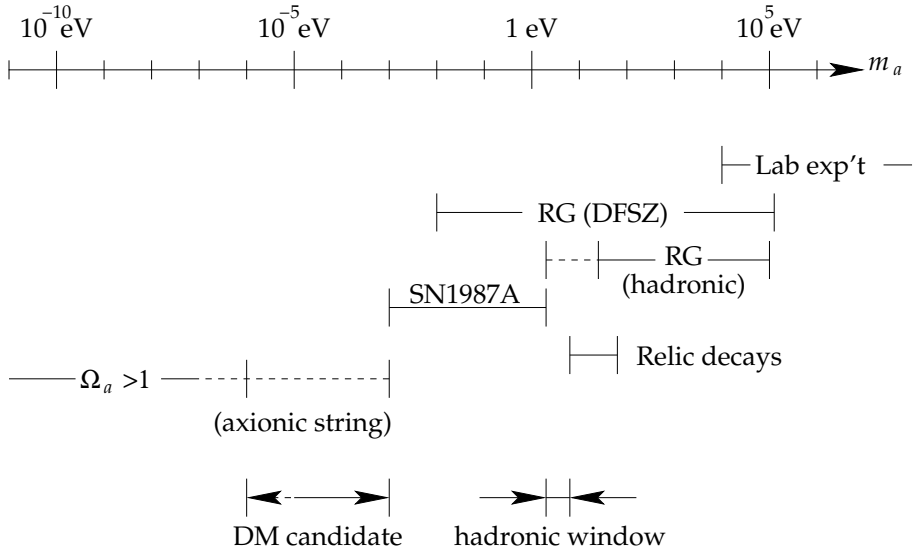

Figure 1.1: Summary of the laboratory, astrophysical, and cosmological constraints to the axion mass in Ref. [4]. This is a reproduction of a figure in it.

experiment and the result. In Chapter 2 we briefly review the axion physics. In Chapter 3, we will describe the detection principle of this experiment. There we will discuss the expected production rate of the solar axions, the limit on the axion models derived from the standard solar model, and the detection efficiency of the axion helioscope. Other solar axion searches including experiments using different detection principles are also touched on. In Chapter 4, we will describe the overview of our project including its aim, the basic design, and the past measurements. In Chapter 5, we will describe the detail of the apparatus. In Chapter 6, we describe the details of the Phase II measurement and its result. In Chapter 7, the Phase III measurement will be described including the upgraded apparatus, detail of the second series of the measurement, and the result. Finally, in Chapter 8, the summary of this thesis is described.

Chapter 2

Axion

In this chapter, we will shortly review the axion physics.

2.1 θ vacuum

In QCD, the vacuum must be a topologically non-trivial ground state [7]. It should be a pure gauge field which includes not only the trivial one $A_a^\mu = 0$ but also any gauge transformations of 0.

For simplicity, let us start with an SU(2) Yang–Mills theory and set the temporal gauge $A_a^0 = 0$ [8, 9]. Since QCD contains SU(2) as its subgroup, the following discussion also holds true for QCD. Under a gauge transformation Ω, the remaining spatial components of the gauge field transforms as follows:

$$A^i \equiv \frac{1}{2}\tau_a A_a^i \tag{2.1}$$

$$\to \Omega A^i \Omega^{-1} + \frac{i}{g}\Omega\nabla^i\Omega^{-1}. \tag{2.2}$$

Thus the pure gauge field is $A_a^i = 0$ or has the form

$$A^i = \frac{i}{g}\Omega\nabla^i\Omega^{-1}. \tag{2.3}$$

We demand further that the gauge fields should vanish at the spatial infinity by restricting the gauge transformations as

$$\Omega(\boldsymbol{x}) \to 1 \qquad \text{at } |\boldsymbol{x}| \to \infty. \tag{2.4}$$

Since Eq. (2.4) gives a mapping of three dimensional sphere S_3 of the three dimensional points at the spacial infinity into S_3 of the SU(2) group space, we can classify these gauge transformations into distinct topological classes (homotopy classes), $\Omega \in \{\Omega_n\}$, by the winding number n, where n is an integer. The winding number can be expressed in terms of an integral over the gauge fields as

$$n = \frac{ig^3}{24\pi^2}\int d^3x \ \mathrm{Tr}[\epsilon_{ijk}A_n^i A_n^j A_n^k], \tag{2.5}$$

where $A_n^i = \frac{i}{g}\Omega_n \nabla^i \Omega_n^{-1}$ is the pure gauge fields of winding number n. Hence the associated vacua $|n\rangle$ can also be classified likewise. For instance, the following gauge transformation has the winding number of $n = 1$ [10]:

$$\Omega_1(\boldsymbol{x}) = \frac{\boldsymbol{x}^2 - \lambda^2}{\boldsymbol{x}^2 + \lambda^2} + \frac{2i\lambda \boldsymbol{\sigma} \cdot \boldsymbol{x}}{\boldsymbol{x}^2 + \lambda^2} \tag{2.6}$$

which gives

$$\boldsymbol{A}_1(\boldsymbol{x}) = \frac{2\lambda}{g(\boldsymbol{x}^2 + \lambda^2)^2}[\boldsymbol{\sigma}(\boldsymbol{x}^2 - \lambda^2) - 2\boldsymbol{x}(\boldsymbol{\sigma} \cdot \boldsymbol{x}) - 2\lambda \boldsymbol{x} \times \boldsymbol{\sigma}] \tag{2.7}$$

and vanishing field strengths F_{ij}.

Existence of these non-trivial gauge configurations seems probable since it explains neatly why $\mathrm{U}(1)_A$ is not a symmetry of QCD. In the limit of vanishing quark masses of N flavors, QCD has a global vector- and axial symmetry: $\mathrm{U}(N)_V \times \mathrm{U}(N)_A$. As at least two of them we know is approximately massless, $m_u, m_d \simeq 0$, we would expect the strong interactions to be approximately $\mathrm{U}(2)_V \times \mathrm{U}(2)_A$ invariant.

Experimentally one finds that the vector symmetry $\mathrm{U}(N)_V$ is a good symmetry of nature corresponding to conservation of isospin times baryon number. The axial symmetry $\mathrm{U}(N)_A$, in contrast, is spontaneously broken by the quark condensation $\langle \bar{q}q \rangle \neq 0$. From the spontaneous symmetry breaking of $\mathrm{U}(2)_A$, one can expect four approximately massless Nambu–Goldstone bosons. Pions are light, $m_\pi \sim 135\,\mathrm{MeV}$, however, a light meson corresponding to $\mathrm{U}(1)_A$ is missing. This is dubbed the $\mathrm{U}(1)_A$ problem [11].

A solution to this was found by 't Hooft [7]. QCD is formally invariant under a $\mathrm{U}(1)_A$ transformation,

$$q_f \to e^{i\alpha\gamma_5/2} q_f. \tag{2.8}$$

Considering the current $J_5^\mu = \sum_f \bar{q}_f \gamma^\mu \gamma_5 q_f$, however, there are the chiral anomaly [12, 13, 14]

$$\partial_\mu J_5^\mu = \frac{g^2 N}{32\pi^2} F_a^{\mu\nu} \tilde{F}_{a\mu\nu}, \tag{2.9}$$

where $F_a^{\mu\nu}$ is the gluon field strength, $\tilde{F}_{a\mu\nu} = \frac{1}{2}\epsilon_{\mu\nu\alpha\beta} F_a^{\alpha\beta}$ its dual. It turned out that, with the existence of a non-trivial gauge configuration, the chiral anomaly leads to a violation of axial charge conservation, and $\mathrm{U}(1)_A$ is no longer a true symmetry of QCD.

However, the correct vacuum state of QCD can not be any one of these $|n\rangle$ vacua, since they are not invariant under gauge transformations:

$$\Omega_1 |n\rangle = |n+1\rangle. \tag{2.10}$$

The true QCD vacuum is a superposition of these and is called the θ-vacuum:

$$|\theta\rangle = \sum_n e^{-in\theta} |n\rangle, \tag{2.11}$$

which is obviously gauge invariant:

$$\Omega_1 |\theta\rangle = e^{i\theta} |\theta\rangle. \tag{2.12}$$

2.2 Strong CP problem

The vacuum angle θ is a constant of a vacuum and has observable physical effect [10, 15]. To see this, let us consider the vacuum-to-vacuum transition amplitude. The transition amplitude from $|\theta\rangle$ at $t = -\infty$ to $|\theta'\rangle$ at $t = +\infty$ is

$$\begin{aligned}\langle\theta'|\theta\rangle &= \sum_m \sum_n e^{im\theta' - in\theta}\langle m|n\rangle \\ &= \sum_n e^{in(\theta'-\theta)} \sum_\nu e^{i\nu\theta}\langle n+\nu|n\rangle. \end{aligned} \tag{2.13}$$

To find for the change in the winding number, $\nu = m - n$, in terms of the gauge field strengths, we utilize the fact that the chiral anomaly term $F\tilde{F}$ is expressed as a total divergence [16]

$$F_a^{\mu\nu}\tilde{F}_{a\mu\nu} = \partial_\mu K^\mu, \tag{2.14}$$

where

$$K^\mu = \epsilon^{\mu\alpha\beta\gamma} A_{a\alpha}\left(F_{a\beta\gamma} - \frac{g}{3} f_{abc} A_{b\beta} A_{c\gamma}\right), \tag{2.15}$$

and f_{abc} is the structure constants, so that the integral of $F\tilde{F}$ over all space time is expressed as a surface integral of K^μ:

$$\int d^4x\, F_a^{\mu\nu}\tilde{F}_{a\mu\nu} = \int d\sigma_\mu K^\mu. \tag{2.16}$$

For SU(2) pure gauge fields, and the temporal gauge, $K^i = 0$ and only K^0 is non vanishing:

$$K^0 = i\frac{4}{3} g \epsilon_{ijk}\,\mathrm{Tr}[A^i A^j A^k]. \tag{2.17}$$

Comparing Eqs. (2.5) and (2.17), we find

$$\nu = \left[\frac{g^2}{32\pi}\int d^3x\, K^0\right]_{t=-\infty}^{t=+\infty} = \frac{g^2}{32\pi}\int d^4x\, F_a^{\mu\nu}\tilde{F}_{a\mu\nu}. \tag{2.18}$$

Thus, we find for the path integral form of the vacuum-to-vacuum transition amplitude as

$$\langle\theta'|\theta\rangle = \delta(\theta'-\theta)\int [dA_\mu]\exp\left[i\int d^4x\, \mathscr{L}_{\mathrm{QCD}}^{\mathrm{eff}}\right], \tag{2.19}$$

where

$$\mathscr{L}_{\mathrm{QCD}}^{\mathrm{eff}} = \mathscr{L}_{\mathrm{QCD}} + \mathscr{L}_\theta, \tag{2.20}$$

and

$$\mathscr{L}_\theta = \theta\frac{g^2}{32\pi^2} F_a^{\mu\nu}\tilde{F}_{a\mu\nu}. \tag{2.21}$$

Equation (2.19) tells us that the vacuum angle θ does not change and hence any θ-vacuum can be a good vacuum. The added term to the effective QCD Lagrangian, $\mathscr{L}_\theta$, violates P, T, and CP reversal invariance.

If we include the weak interactions into the discussion, quarks acquire their masses via the breakdown of the electroweak group:

$$\mathscr{L}_{M_q} = -\bar{q}_{iR}(M_q)_{ij}q_{jL} - \bar{q}_{iL}(M_q^\dagger)_{ij}q_{jR}. \tag{2.22}$$

In general, the mass matrix M_q is complex. To go to a physical basis, one can make M_q real, positive, and diagonal by performing separate global unitary transformations on the left- and right quark fields, which involves a global chiral transformation. Because of the anomaly, chiral rotations change the θ-vacuum. Finally, the effective θ parameter should be modified as

$$\bar{\theta} = \theta + \arg\det M_q, \tag{2.23}$$

and the additional P, T, and CP violating term to the effective Lagrangian of the Standard model is

$$\mathscr{L}_{\bar{\theta}} = \bar{\theta}\frac{g^2}{32\pi^2}F_a^{\mu\nu}\tilde{F}_{a\mu\nu}. \tag{2.24}$$

This explicit CP violation should be seen as the electric dipolemoment of neutron as [17, 18]

$$d_n \simeq \frac{e\bar{\theta}m_q}{M_N^2}. \tag{2.25}$$

However, the present limit [19]

$$d_n < 2.9 \times 10^{-26}\, e\,\mathrm{cm} \tag{2.26}$$

suppresses $\bar{\theta}$ to be

$$|\bar{\theta}| < 10^{-10}. \tag{2.27}$$

This is the strong CP problem — why is $\bar{\theta}$ so small? In other words, it is a naturalness problem of a fine-tuning of two apparently independent parameters to cancel each other perfectly.

There are some possible solutions. If at least one of quarks were massless, e.g. $m_u = 0$, one can rotate the quark fields to vanish $\bar{\theta}$. Another approaches impose CP as the symmetry of nature, thus $\theta = 0$ is set at the Lagrangian level, and allow it to break spontaneously to realize the weak CP violation [20, 21]. However, these solutions seem less plausible after the success of the Kobayashi–Masukawa model. Today, the most accepted one is the axion model.

2.3 Axion model

In 1977, Peccei and Quinn showed that the CP-violating term vanished dynamically if a global chiral U(1) symmetry which is spontaneously broken is added to the Higgs sector of the Standard Model. This new symmetry $\mathrm{U}(1)_{\mathrm{PQ}}$ is called the Peccei–Quinn symmetry, or the PQ symmetry in short, and the resultant pseudo Nambu–Goldstone boson is called axion.

As the result of introduction of the broken $\mathrm{U}(1)_{\mathrm{PQ}}$, the Standard Model Lagrangian gets additional terms as:

$$\mathscr{L} = \mathscr{L}_{\mathrm{SM}} - \frac{1}{2}\partial_\mu a\partial^\mu a + \mathscr{L}_{\mathrm{int}}(\partial^\mu a, \psi) + N\frac{a}{f_{\mathrm{PQ}}}\frac{g^2}{32\pi^2}F_a^{\mu\nu}\tilde{F}_{a\mu\nu}, \tag{2.28}$$

where 'a' is the axion field which translates under a $\mathrm{U}(1)_{\mathrm{PQ}}$ transformation as

$$a(x) \to a(x) + \alpha f_{\mathrm{PQ}} \tag{2.29}$$

and f_{PQ} is the order parameter associated with the breaking of $\mathrm{U}(1)_{\mathrm{PQ}}$. The model-dependent axion–fermion interaction term $\mathscr{L}_{\mathrm{int}}(\partial^\mu a, \psi)$ arises from the need to make the Standard Model Lagrangian invariant under $\mathrm{U}(1)_{\mathrm{PQ}}$ transformation, and the last term

$$-V_{\mathrm{eff}} = N \frac{a}{f_{\mathrm{PQ}}} \frac{g^2}{32\pi^2} F_a^{\mu\nu} \tilde{F}_{a\mu\nu} \tag{2.30}$$

is the axion potential which arises from the chiral anomaly of the $\mathrm{U}(1)_{\mathrm{PQ}}$ current:

$$\partial_\mu J^\mu_{\mathrm{PQ}} = N \frac{g^2}{32\pi^2} F_a^{\mu\nu} \tilde{F}_{a\mu\nu}. \tag{2.31}$$

By means of Eq. (2.29), the origin of the axion field is selected as to vanish $\bar{\theta}$ so that what was the fixed vacuum angle $\bar{\theta}$ is now replaced with a dynamic field a. Hence the question of the strong CP problem is replaced with a new question where the stationary point of a is in the vacuum. Studies showed that V_{eff} is periodic in the effective vacuum angle $\bar{\theta} = N\frac{\langle a \rangle}{f_{\mathrm{PQ}}}$ in a form $\langle V_{\mathrm{eff}}[\bar{\theta}] \rangle \propto \cos\bar{\theta}$ [22], and that one of the minima is indeed at $\langle a \rangle = 0$ [23, 24]. Thus the strong CP problem is dynamically resolved.

In the original Peccei–Quinn–Weinberg–Wilczek axion model, or the "standard axion" model, the Higgs boson in the Standard Model was extended to carry PQ charge. Hence the PQ-symmetry breaking occurred incidentally to the electroweak symmetry breaking, $f_{\mathrm{PQ}} = f_W$. This model has been excluded by a variety of laboratory experiments. For example, the model predicts the branching ratio of $K^+ \to \pi^+ + a$ decay as

$$BR(K^+ \to \pi^+ + a) \geq 1.3 \times 10^{-5}, \tag{2.32}$$

which contradicts the experimental limit [25]

$$BR(K^{\to}\pi^+ + a) < 3.8 \times 10^{-8}. \tag{2.33}$$

However, f_{PQ} does not need to be equal to the electroweak scale. As we see in the subsequent section, larger f_{PQ} renders axions to have smaller mass, longer lifetime, and weaker couplings. Therefore, their experimental detection is more difficult in such "invisible axion" models with larger $f_{\mathrm{PQ}} \gg f_W$. In the Kim–Shifman–Vainshtein–Zakharov (KSVZ) model [26, 27], they introduced a complex scalar and an exotic heavy quark as the only fields that carry PQ charge. In the Dine–Fischler–Srednicki–Zhitnitskiĭ (DFSZ) model [28, 29], they added a scalar field to the original axion model and made the PQ-symmetry breaking to occur by the new scalar field.

2.4 Axion properties

The axion acquires a small mass as a result of the oscillating axion potential:

$$m_a = \frac{\sqrt{z}}{1+z} \frac{f_\pi m_\pi}{f_a} = 0.6\,\mathrm{eV} \left(\frac{10^7\,\mathrm{GeV}}{f_a} \right), \tag{2.34}$$

where $z = m_u/m_d \simeq 0.56$ the u- and d- quark mass ratio, $m_\pi = 135\,\mathrm{MeV}$ the pion mass, and $f_\pi = 93\,\mathrm{MeV}$ is the pion decay constant. As the PQ-symmetry breaking scale f_{PQ} always accompanies the coefficient of chiral anomaly N, we redefined it for convenience as

$$f_a \equiv \frac{f_{\mathrm{PQ}}}{N}. \tag{2.35}$$

At tree level, axion–fermion couplings arise from the need to make the Lagrangian invariant under $\mathrm{U}(1)_{\mathrm{PQ}}$ transformation. Generally, they are included in the interaction term $\mathscr{L}_{\mathrm{int}}$ in the pseudo-scalar form:

$$\mathscr{L}_{\mathrm{int}} \supset i g_{a\psi\psi} a \bar{\psi} \gamma_5 \psi, \tag{2.36}$$

where $g_{a\psi\psi} = Q^{\psi}_{\mathrm{PQ}} m_\psi / f_{\mathrm{PQ}} \propto m_a$ is the axion–fermion coupling constant, m_ψ is the fermion mass, and Q^{ψ}_{PQ} is the model-dependent PQ charge of the fermion which has an order of $\mathcal{O}(1)$. At low energies under Λ_{QCD}, axion–hadron couplings get contributed additionally from the mixing of physical axion with π^0. Although the KSVZ axions do not couple to electrons or ordinary quarks at tree-level, their couplings to nucleons are comparable to that of DFSZ axion as a result of this mixing. Because of this remarkable property, it is also called the hadronic axion.

What is omitted in Eq. (2.28) but is playing a key role for many searches is its coupling to two photons,

$$\mathscr{L}_{a\gamma\gamma} = -\frac{1}{4} g_{a\gamma} a F^{\mu\nu} \tilde{F}_{\mu\nu}, \tag{2.37}$$

where $F^{\mu\nu}$ is the electromagnetic field strength and $g_{a\gamma}$ is the axion–photon coupling constant. It arises as a result of the chiral anomaly of the $\mathrm{U}(1)_{\mathrm{PQ}}$ current in the triangle graph connected to two photons with fermions going around the loop as well as the mixing of physical axion with the π^0 and η. The coupling constant $g_{a\gamma}$ is given by

$$\begin{aligned} g_{a\gamma} &= \frac{\alpha}{2\pi f_a} \left[\frac{E}{N} - \frac{2(4+z)}{3(1+z)} \right] \\ &= 1.9 \times 10^{-10}\,\mathrm{GeV}^{-1} \left(\frac{m_a}{\mathrm{eV}} \right) (E/N - 1.92), \end{aligned} \tag{2.38}$$

where E/N depends on how PQ-charge is assigned to each fermion as

$$E/N = \frac{\sum_f (Q_{\mathrm{PQ}} Q_{em}^2)}{\sum_f (Q_{\mathrm{PQ}} Q_c^2)}. \tag{2.39}$$

For example, if the heavy quark in the KSVZ model does not carry any electromagnetic charge, $E/N = 0$, or if any axion model is embedded into an SU(5) grand unified theory (GUT), $E/N = 8/3$. While the above cases are often used as generic examples, many variant models with different E/N values can be constructed [30]. In general, a broad range of $g_{a\gamma}$ values is still possible for fixed m_a.

By this coupling, axions decay into two photons at a rate,

$$\begin{aligned} \Gamma_{a\to\gamma\gamma} &= \frac{g_{a\gamma}^2 m_a^3}{64\pi} \\ &= 1.1 \times 10^{-24}\,\mathrm{s} \left(\frac{m_a}{\mathrm{eV}} \right)^5 \qquad \text{for } E/N = 0. \end{aligned} \tag{2.40}$$

Hence, primordial axions with a mass less than $m_a \lesssim 20\,\mathrm{eV}$ can survive until now.

2.5 Constraints on axion models

2.5.1 Laboratory searches

Rare decays

As mentioned earlier, the axion has been constrained by laboratory experiments to search for rare decays including beam dump experiments ($p+\mathrm{Cu} \to X+a$ [31, 32, 33]), reactor experiments ($X^* \to X + a$ ($a + e \to e + \gamma$ or $a + Ze \to Ze + \gamma$) [34], $X^* \to X + a$ ($a \to \gamma + \gamma$): $X = {}^7\mathrm{Li}, {}^{97}\mathrm{Nb}$ [35]), rare nuclear transition searches (${}^{139}\mathrm{La}^* \to {}^{139}\mathrm{La} + a$ [36], ${}^{137}\mathrm{Ba}^* \to {}^{137}\mathrm{Ba} + a$ ($a \to \gamma + \gamma$) [37], ${}^{65}\mathrm{Cu}^* \to {}^{65}\mathrm{Cu} + a$ ($a \to \gamma + \gamma$, $a + e \to e + \gamma$ or $a + Ze \to Ze + \gamma$) [38, 39]) and heavy quarkonium rare decay searches ($J/\psi \to a + \gamma$ [40], $\Upsilon(1S) \to a + \gamma$ [41]).

Limits are given for various coupling constants or various combinations of coupling constants. In total, they correspond roughly to

$$f_a \gtrsim \mathcal{O}(10^{12}\,\mathrm{eV}) \qquad \text{or} \qquad m_a \lesssim \mathcal{O}(6 \times 10^3\,\mathrm{eV}). \tag{2.41}$$

Photon-regeneration experiment

The photon-regeneration experiment, often referred to as the light-shining-through-walls (LSW) experiment, exploits the axion–photon oscillation in the static magnetic field. In this method, two dipole magnets are aligned in line with an optical barrier inserted in between. The bore of the first magnet is irradiated with a photon beam, usually a strong laser beam, where a fraction of the photons propagating in the transverse magnetic field oscillates into axions. Photons are blocked by the wall, while axions can penetrate it, and a fraction of the axions then oscillates back into photons in the second dipole magnet.

Although there have been many experiments, and although their claimed target is not limited to axions, it is extremely challenging to search for invisible axions using this method. One of the most stringent limit is given by the ALPS (Any Light Particle Search) experiment [42] as

$$g_{a\gamma} \lesssim 7 \times 10^{-8}\,\mathrm{GeV}^{-1} \qquad \text{for } m_a \lesssim 5 \times 10^{-4}\,\mathrm{eV}, \tag{2.42}$$

which is orders of magnitude less restrictive than the solar axion searches and is far from realistic values expected from the axion models.

Vacuum dichroism and birefringence

The axion–photon interaction can be observed in the optical property of vacuum under a strong magnetic field, such as dichroism and birefringence [43]. The vacuum dichroism is a rotation of the photon polarization due to a depletion of its component parallel to the magnetic field. The vacuum birefringence can appear as a result of the mixing of axions into the parallel component of photons in the magnetic field. The mixing results a phase shift of the parallel component during its propagation, by which a linear polarized photon develops elliptical polarization.

Cameron *et al.* reported the following upper limit using this technique [44]:

$$g_{a\gamma} < 3.6 \times 10^{-7}\,\mathrm{GeV}^{-1} \qquad \text{for } m_a < 10^{-3}\,\mathrm{eV}. \tag{2.43}$$

Fifth-force experiment

A light pseudoscalar would mediate spin-dependent (semi-)long-range forces. A number of groups have attempted to search experimentally for such forces [45]. However, these constraints are still far from realistic values expected from the axion models.

2.5.2 Astrophysical searches

Search for solar axions

The sun can be a strong source of axions. Sikivie [5] suggested a novel experiment to detect such axions called "the axion helioscope." This method along with an alternative method to detect solar axions is reviewed in Chapter 3.

2.5.3 Cosmological searches

Microwave cavity axion search

In the masses $10^{-6}\,\mathrm{eV} < m_a < 10^{-3}\,\mathrm{eV}$, the axion is a good candidate for the cosmic cold dark matter (CDM) and could make a substantial contribution to the galactic halo mass density. Sikivie [5] suggested a technique to detect galactic halo axions by means of a resonant high-Q microwave cavity permeated by a strong magnetic field.

The ADMX experiment [46, 47] has achieved the sensitivity to reach KSVZ (hadronic) axions in the mass range

$$1.9\,\mu\mathrm{eV} < m_a < 3.53\,\mu\mathrm{eV} \tag{2.44}$$

using a cylindrical cavity of 50 cm diameter and 100 cm long surrounded by a 7.6-T superconducting solenoid.

Telescope search

For the eV mass range, the decays of relic axions into two photon can be observed as a narrow emission line from galaxies and galaxy clusters. By observing the intergalactic light in rich clusters, the following mass region was excluded [48, 49, 50],

$$3\,\mathrm{eV} < m_a < 8\,\mathrm{eV}. \tag{2.45}$$

2.5.4 Constraints from astrophysics

Axions can be produced in hot and dense astrophysical plasma, and thus can open an additional channel to transport energy out of stars. Modification to the existing astrophysical models leads to consequences which conflict with the observation. A recent review is given in Ref. [51].

The enhanced consumption of their nuclear fuel shortens the life-time of stars. Discussion on the solar life-time limit is given in Section 3.2.2.

The horizontal branch (HB) stars are considered to have reached to the helium-burning stage, while the red giant branch (RGB) stars are still having their degenerated helium cores. The Primakoff emission of axions ($\gamma + Ze \to Ze + a$) accelerate the helium consumption in HB stars, thereby shorten their life-time. Comparing the population of the HB- and RGB stars in the globular clusters, the following limit is given,

$$g_{a\gamma} < 10^{-10}\,\mathrm{GeV}^{-1}. \tag{2.46}$$

If axions couple to electrons, their emission by bremsstrahlung ($e + Ze \to Ze + e + a$) can enhance the cooling speed of white dwarfs. From the luminosity function of the pulsating white dwarf (ZZ Ceti star) G117-B15A, the following limit is given [52, 51]

$$g_{aee} < 1.3 \times 10^{-13}, \tag{2.47}$$

which corresponds to

$$m_a \lesssim \mathcal{O}(5 \times 10^{-3}\,\mathrm{eV}). \tag{2.48}$$

In the collapsing supernova cores, energy loss by axion emission through nucleon bremsstrahlung ($N + N \to N + N + a$) can result in a reduced neutrino burst duration. The observed duration of SN 1987A excludes roughly

$$\mathcal{O}(10^{-2}\,\mathrm{eV}) \lesssim m_a \lesssim \mathcal{O}(10\,\mathrm{eV}). \tag{2.49}$$

More strongly interacting axions are trapped in the core thus the signal duration is not affected. For even larger couplings, however, axions emitted from the axion sphere can cause too many events in the Kamiokande detector [53].

2.5.5 Constraints from cosmology

For large f_a values thus small m_a, the axion is attractive as a good candidate of the cold dark matter (CDM). It can be produced by the initial value misalignment [54, 55, 56] and by the decay of topological defects such as axionic strings and axionic domain walls [57, 58]. Before the axion field settle the vacuum angle $\bar{\theta}$ to the CP-conserving minimum, the universe starts with an arbitrary angle. After the breakdown of the $\mathrm{U}(1)_{\mathrm{PQ}}$, the axion field begin to oscillate around the potential minimum. This coherent oscillation represents a condensate of CDM. Furthermore, because of the periodic form of the axion potential, nearby vacua can drop to the different minima with vacuum angles differing by 2π. This forms topological defects at the borders and they eventually decay into axions adding to the CDM population. The expected cosmic axion density depends on the initial value as well as the exact scenario particularly whether inflation happens before or after the PQ phase transition. In order that the cosmic axion density does not exceed the observed CDM density, $\Omega_{\mathrm{CDM}}h^2 = 0.11$, the axion mass should be

$$m_a \gtrsim \mathcal{O}(10^{-5}\text{–}10^{-3}\,\mathrm{eV}). \tag{2.50}$$

For heavier axions, relic axions can be produced thermally from quarks and gluons, which would contribute to the hot dark matter density. Current constraint on a possible hot dark matter fraction provides a limit [59]

$$m_a \lesssim \mathcal{O}(1\,\mathrm{eV}). \tag{2.51}$$

Chapter 3

Solar axion and the detection technique

In this chapter, we will go into the principle of the axion helioscope which is the method used in our experiment. The expected production rate of the solar axions, the limit on the axion models derived from the standard solar model, and the detection efficiency of the axion helioscope are discussed. Finally, other solar axion searches including experiments using different detection principles are also touched on.

3.1 Concept of the detection

The basic idea of "the axion helioscope" experiment was suggested by Sikivie [5]. In order to detect axions, we exploit the two-photon coupling of the axions which is expressed by the following interaction term in the effective Lagrangian density,

$$\mathscr{L}_{a\gamma\gamma} = -\frac{g_{a\gamma}}{4} a F_{\mu\nu} \tilde{F}^{\mu\nu} = g_{a\gamma} a \boldsymbol{E} \cdot \boldsymbol{B}, \tag{3.1}$$

where a is the axion field, $F_{\mu\nu} = (\partial_\mu A_\nu - \partial_\nu A_\mu)$ the electromagnetic field strength tensor, $\tilde{F}^{\mu\nu} = (1/2)\epsilon^{\mu\nu\rho\sigma} F_{\rho\sigma}$ its dual, and $g_{a\gamma}$ the axion–photon coupling constant.

This axion–photon–photon vertex allows for an conversion of photons into axions in the presence of external electromagnetic fields as illustrated in Fig. 3.1.

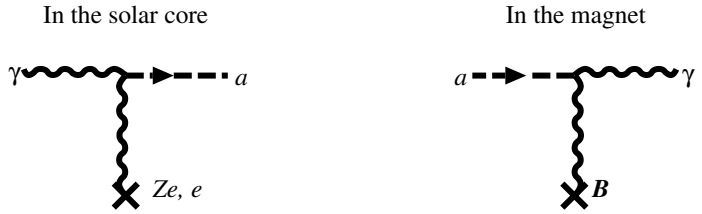

Figure 3.1: Primakoff process

This process is referred to as the Primakoff process. Thus axions may be produced in the solar interior where blackbody photons with energies of several keV would be converted in the fluctuating electromagnetic fields of the charged particles in the hot plasma. These keV axions from the sun are called "the solar axions."

The solar axions could then reconvert into keV X-rays by a strong magnetic field in the laboratory. The axion helioscope will consist of a large strong magnet and an X-ray detector which is positioned at the opposite side of the magnet from the sun as illustrated in Fig. 3.2. Since the magnetic field varies only over macroscopic scales, the axion-photon conversion is best visualized as a mixing phenomenon between two states in the presence of the external field: an initial axion state partly oscillates into a photon. This method presents an ideal opportunity to carry out a search for $\mathcal{O}(1\,\mathrm{eV})$ axions.

3.2 Solar axion

3.2.1 Solar axion production

The axion–photon interaction dominates the production of the solar axion through the Primakoff process. Such interaction remains even in hadronic axion models, where axions do not interact with electrons. Fukugita *et al.* [60] discussed the stellar energy loss due to axion emission with models with the tree-level axion–electron coupling. In general, such coupling opens another energy loss channel through, for example, the Compton-like process in addition to the Primakoff process. Due to different temperature dependencies of these two processes, the Primakoff process is relatively important as a mechanism of energy loss for main-sequence stars including the sun, on the other hand, the Compton-like process is likely to be dominant for red giants. Therefore, such models with the tree-level axion–electron coupling, like the DFSZ axions, tend to be strongly constrained by the excessive cooling of red giants, before solar axions bring a detectable phenomenon.

In the interior of the sun, blackbody photons can convert into axions in the fluctuating electric fields of the charged particles in the plasma. In calculating the emission rate for axions, however, we must consider the possible photon states in a plasma, where "free massless photons" do not exist. In an isotropic, nonmagnetized, nonrelativistic plasma there exist two types of excitation: transverse- and longitudinal plasmons. Transverse plasmons follow the

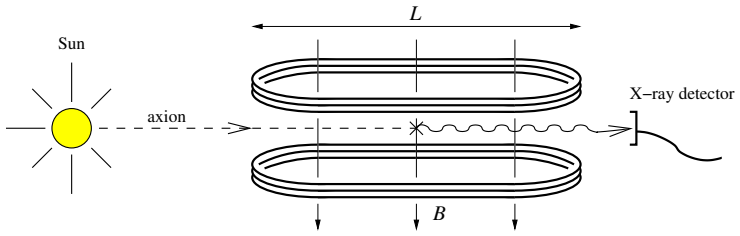

Figure 3.2: Conceptual rendering of the axion helioscope experiment.

dispersion relation [61]

$$\omega^2 = \omega_p^2 + \left[1 + \frac{T\omega_p^2}{m_e\omega^2}\right]\boldsymbol{k}^2, \tag{3.2}$$

while longitudinal plasmons follow the Bohm–Gross relation [61]

$$\omega^2 = \omega_p^2 + (3T/m_e)\boldsymbol{k}^2, \tag{3.3}$$

where ω is the frequency, $\boldsymbol{k}$ the wave number, m_e the electron mass, and T the temperature of the plasma. In both expressions, ω_p is the plasma frequency given as

$$\omega_p^2 = 4\pi\alpha N_e/m_e, \tag{3.4}$$

where N_e is the local electron density. Therefore, the conversion process is viewed as the plasmon decay process $\gamma_t \to \gamma_l + a$ or the plasmon coalescence process $\gamma_t + \gamma_l \to a$, where γ_t and γ_l are transverse and longitudinal plasmons, respectively. In a nonrelativistic plasma, $T \ll m_e$ so that Eq. (3.2) may be simplified as $\omega^2 = \omega_p^2 + \boldsymbol{k}^2$. Then one finds that a transverse plasmon γ_t behaves as a particle with effective mass of ω_p. Longitudinal plasmons γ_l, in contrast, oscillate with a fix frequency $\omega = \omega_p$. Thus, other processes, such as $\gamma_t \to \gamma_t + a$, are kinematically suppressed.

For larger wave numbers, longitudinal excitations are strongly damped for $|k_l| \gtrsim k_D$ by the Landau damping, where k_D is the Debye–Hückel wave number for the electrons given as

$$k_D^2 = 4\pi\alpha N_e/T. \tag{3.5}$$

If the momentum transfer in the transition $\gamma_t \to a$ exceeds k_D, the conversion process should be viewed as the Primakoff process by the individual charges $\gamma_t + Ze \to Ze + a$.

G. Raffelt [62] has discussed these processes in a unified picture by calculating the transition rate $\gamma_t \to a$ in the presence of the classical electric-field fluctuations of a plasma. The resulting transition rate of a transverse plasmon of energy ω into an axion is

$$R(\gamma_t \to a) = \frac{T\kappa^2}{(4\pi M)^2}\frac{\pi}{2}\left[\left[1 + \frac{\kappa^2}{4\omega^2}\right]\ln\left[1 + \frac{4\omega^2}{\kappa^2}\right] - 1\right], \tag{3.6}$$

where κ is the total inverse screening scale or the Debye–Hückel wave number for the all species of charged particles in the plasma. In general, it is given by

$$\kappa^2 = (4\pi\alpha/T)\sum_j Z_j^2 N_j, \tag{3.7}$$

where N_j is the number density of charged particles with charge $Z_j e$. In the solar center [63], $T = 1.3\,\mathrm{keV}$, $\omega_p = 0.3\,\mathrm{keV}$, and $\kappa = 9\,\mathrm{keV}$. The natural units where $\hbar = c = k_\mathrm{B} = 1$ is used in the above equations.

The frequency shift of the axion with respect to the incident transverse plasmon wave is on the order or smaller than the plasma frequency, $|\omega_a - \omega_t| \leq \mathcal{O}(\omega_p)$. Consequently, the energy of axion is close to the energy of the original photon, being smeared over a narrow interval of width about equal to ω_p.

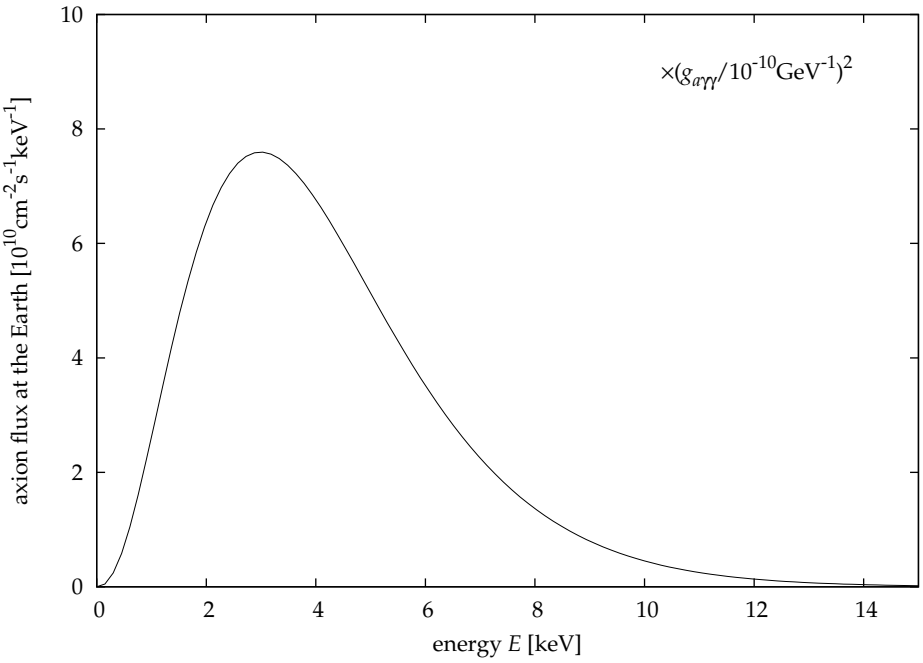

Figure 3.3: Differential solar axion flux at the Earth [51]. The analytic approximation as given in Eq. (3.8) is used.

The axion luminosity of the sun is then given by folding the photon–axion transition rate from Eq. (3.6) with the blackbody photon distribution, integrating over a standard solar model. An analytic approximation to the differential axion flux at the Earth is given as [51]

$$\frac{d\Phi_a}{dE} = 6.0 \times 10^{10}\,\mathrm{cm}^{-2}\,\mathrm{s}^{-1}\,\mathrm{keV}^{-1} \times \left(\frac{g_{a\gamma}}{10^{-10}\,\mathrm{GeV}^{-1}}\right)^2 \left(\frac{E}{\mathrm{keV}}\right)^{2.481} \exp\left[-\frac{E}{1.205\,\mathrm{keV}}\right]. \tag{3.8}$$

It is plotted in Fig. 3.3. The average energy of the solar axion is $\langle E\rangle = 4.2\,\mathrm{keV}$ and the total flux is

$$\Phi_a = 3.75 \times 10^{11}\,\mathrm{cm}^{-2}\mathrm{s}^{-1} \left(\frac{g_{a\gamma}}{10^{-10}\,\mathrm{GeV}^{-1}}\right)^2. \tag{3.9}$$

Reasonable changes in the solar model would not change the axion luminosity significantly. Most axions emerge from a region within $0.2R_\odot$, where $R_\odot$ denotes the solar radius. The angular radius of the axion source region as viewed from the Earth is $\delta_a \sim 0.9 \times 10^{-3}$ radian.

3.2.2 Limit from the standard solar model

Out of the various constraints on the axion models from astrophysical or cosmological considerations, we must respect the limit from the solar model itself

for this experiment to be self-consistent.

The apparent age of the sun gives the most obvious limit. Production of solar axions would give rise to an additional energy loss from the sun, which would shorten the life time of the sun. The condition that the sun has not burn out yet is

$$g_{a\gamma} < 2.3 \times 10^{-9}\,\mathrm{GeV}^{-1}. \tag{3.10}$$

This limit is relatively insensitive to details of the solar model.

A more stringent constraint has been given by Schlattl *et al.* [64]. They compared the helioseismological sound-speed profile data with a modified solar model based on the standard solar evolution with some anomalous solar energy losses by the Primakoff emission of axions. Then, they obtained an upper limit as

$$g_{a\gamma} < 1 \times 10^{-9}\,\mathrm{GeV}^{-1}. \tag{3.11}$$

3.3 Axion helioscope

3.3.1 Axion–photon mixing

The axion, having a two-photon vertex, can mix with photons in the presence of external electromagnetic fields via the Primakoff process where the virtual photon is provided by the external field. Furthermore, the axion is expected to be very light, leading to a near-degeneracy with the photon, where we can expect an axion–photon oscillation phenomenon, as is familiar from the neutrino oscillation.

In this section, we will shortly review this mixing phenomenon by partly following the formalism by Raffelt and Stodolsky [65] where a photon–axion mixed beam propagating through strong magnetic fields is discussed. They also take account of the magnetic vacuum birefringence arising from higher-order QED effects by using the Euler–Heisenberg effective Lagrangian. We will neglect it, however, since such effect is too small in our case.

The effective Lagrangian density for the axion–photon system is given as

$$\mathscr{L} = -\frac{1}{4}F_{\mu\nu}F^{\mu\nu} + \frac{1}{2}\partial_\mu a \partial^\mu a - \frac{1}{2}m_a^2 a^2 - \frac{g_{a\gamma}}{4} a F_{\mu\nu}\tilde{F}^{\mu\nu}. \tag{3.12}$$

The classical equations of motion derived from Eq. (3.12) are

$$(\Box + m_a^2)a = -\frac{g_{a\gamma}}{4}F_{\mu\nu}\tilde{F}^{\mu\nu}, \tag{3.13}$$

$$\partial_\mu F^{\mu\nu} = -g_{a\gamma}\partial_\mu a \tilde{F}^{\mu\nu}, \tag{3.14}$$

or

$$(\Box + m_a^2)a = g_{a\gamma}\boldsymbol{E}\cdot\boldsymbol{B}, \tag{3.15}$$

$$\nabla\cdot\boldsymbol{E} = -g_{a\gamma}\nabla a\cdot\boldsymbol{B}, \tag{3.16}$$

$$\nabla \times \boldsymbol{B} - \dot{\boldsymbol{E}} = g_{a\gamma}(\dot{a}\boldsymbol{B} + \nabla a \times \boldsymbol{E}). \tag{3.17}$$

While both electric and magnetic fields can cause Primakoff conversions, we will concentrate our attention on external *magnetic* fields, since we will deal with the axion–photon conversion in laboratory magnets. We may assume that the magnetic field is nearly homogeneous which varies over much larger scales than the photon or axion wavelength: typically the scales of magnets are $\mathcal{O}(1\,\mathrm{m})$ while keV photons or axions are $\lambda \sim \mathcal{O}(10^{-10}\,\mathrm{m})$.

Let us consider a photon–axion mixed beam with frequency ω propagating to the positive direction along z axis in the presence of an external magnetic field $\boldsymbol{B}_e$ and a refractive medium. The photon field A^μ is composed of $\boldsymbol{B}_e$, and two states of linear polarization parallel ($A_\parallel$) and perpendicular ($A_\perp$) with respect to the external field. By "parallel" component we mean the polarization state whose electric field vector lies in the plane of the wave vector $\boldsymbol{k}$ and the magnetic field $\boldsymbol{B}_e$. In general, the magnetic field is not necessarily transverse to the direction of propagation. Since the interaction is given in a form of $a\boldsymbol{E}\cdot\boldsymbol{B}$ (Eq. (3.1)), only the parallel photon component $A_\parallel$ mixes with axion, so that we may safely ignore the perpendicular component $A_\perp$ hereafter.

From Eqs. (3.13) and (3.14), we then obtain the following matrix form of the stationary wave equation for mixed $A_\parallel$ and a:

$$\left[\omega^2 + \partial_z^2 + \begin{pmatrix} Q & g_{a\gamma}B_t\omega \\ g_{a\gamma}B_t\omega & -m_a^a \end{pmatrix}\right]\begin{pmatrix} A_\parallel \\ a \end{pmatrix} = 0, \tag{3.18}$$

where B_t is the transverse component of $\boldsymbol{B}_e$, and the Lorentz gauge condition $\partial_\mu A^\mu = 0$ is used. We have chosen the phase of $A_\parallel$ such that the off-diagonal components become real. The effect of the refractive medium is incorporated in $Q = 2\omega^2(n_\gamma - 1)$, and the photon refractive index n_γ can be written, without loss of generality, $n_\gamma = 1 - m_\gamma^2/2\omega^2 - i\Gamma/2\omega$, where m_γ is the effective mass of the photon in the medium and Γ is the inverse absorption length for the photons. They are related to the atomic scattering factors f_1 and f_2. For X-rays, when the energy of the photon is sufficiently far above all resonances,

$$m_\gamma = \omega_p = \sqrt{\frac{4\pi\alpha N_e}{m_e}}, \tag{3.19}$$

is an exceedingly good approximation [66], where ω_p is the plasma frequency given in Eq. (3.4). This time, $N_e = \sum Z_i N_i$ is the electron density in the medium. In vacuum, Q vanishes, $Q = 0$.

3.3.2 Axion–photon conversion in a homogeneous magnetic field

When B_t is constant, Eq. (3.18) can be diagonalized by a rotation

$$\begin{pmatrix} A'_\parallel \\ a' \end{pmatrix} = \begin{pmatrix} \cos\vartheta & \sin\vartheta \\ -\sin\vartheta & \cos\vartheta \end{pmatrix}\begin{pmatrix} A_\parallel \\ a \end{pmatrix}, \tag{3.20}$$

where the mixing angle ϑ is given as

$$\frac{1}{2}\tan 2\vartheta = \frac{g_{a\gamma}B_t\omega}{Q + m_a^2}. \tag{3.21}$$

Then one finds that two eigenstates $A'_\parallel$, and a' develop as

$$A'_\parallel(z) = e^{-ik'_+ z} A'_\parallel(0), \tag{3.22}$$

$$a'(z) = e^{-ik'_- z} a'(0), \tag{3.23}$$

where

$$k'_\pm = \sqrt{\omega^2 + \frac{Q - m_a^2}{2} \pm \xi} \approx \omega - \frac{m_\gamma^2 + m_a^2}{4\omega} - i\Gamma/4 \pm \frac{\xi}{2\omega} \tag{3.24}$$

and

$$\xi = \frac{Q + m_a^2}{2\cos 2\vartheta} = \frac{g_{a\gamma} B_t \omega}{\sin 2\vartheta} = \omega\sqrt{(q - i\Gamma/2)^2 + (g_{a\gamma} B_t)^2}. \tag{3.25}$$

In the above expression,

$$q = k_\gamma - k_a \approx \frac{m_a^2 - m_\gamma^2}{2\omega} \tag{3.26}$$

is the momentum difference between photons and axions. From Eqs. (3.20), (3.22) and (3.23), we find for the transition amplitude as

$$\langle A(z)|a(0)\rangle = \frac{1}{2}(e^{-ik'_+ z} - e^{-ik'_- z}) \sin 2\vartheta, \tag{3.27}$$

thus the transition probability from axions to photons in a magnetic field of length L is given as

$$P_{a\to\gamma} = (g_{a\gamma} B_t \omega)^2 e^{-\Gamma L/2} \left| \frac{\sin \frac{\xi L}{2\omega}}{\xi} \right|^2, \tag{3.28}$$

where we used $\omega \gg |Q|^{1/2}$, $\omega \gg m_a$, and $\omega \gg g_{a\gamma} B_t$.

In the most idealized condition, where the medium is without absorption $\Gamma = 0$, and the effective mass of the photon in the medium is equal to the axion mass $m_\gamma = m_a$, the photon–axion system mixes maximally, i.e., $\vartheta = \pi/8$. Then Eq. (3.28) gives the maximum transition probability given as

$$\max P_{a\to\gamma} \approx (g_{a\gamma} BL/2)^2 \tag{3.29}$$

$$= 2.1 \times 10^{-19} \left(\frac{g_{a\gamma}}{10^{-10}\mathrm{GeV}^{-1}} \right)^2 \left(\frac{BL}{4\,\mathrm{T} \cdot 2.3\,\mathrm{m}} \right)^2. \tag{3.30}$$

When the absorption is absent $\Gamma = 0$, but the effective photon mass is at off-resonance $m_\gamma \neq m_a$, e.g. in vacuum, $\xi = \omega\sqrt{q^2 + (g_{a\gamma} B_t)^2} \approx \omega q$ is real, thus we find,

$$P_{a\to\gamma} = \frac{(g_{a\gamma} B_t)^2}{q^2} \sin^2 \frac{qL}{2}. \tag{3.31}$$

On the other hand, with a finite absorption, we can expanded ξ as

$$\xi \approx \omega(q - i\Gamma/2), \tag{3.32}$$

assuming $g_{a\gamma} B_t \ll \Gamma$. Thus we find from Eq. (3.28),

$$P_{a\to\gamma} = \frac{(g_{a\gamma} B_t)^2}{4(q^2 + \Gamma^2/4)} (1 + e^{-\Gamma L} - 2e^{-\Gamma L/2} \cos qL). \tag{3.33}$$

Equation (3.33) is identical to Eq. (3.31) in the limit $\Gamma \to 0$, and we recover Eq. (3.29) in the limit $q \to 0$.

3.3.3 Perturbative solution to the axion–photon conversion rate

In general, magnetic fields are not strictly homogeneous, so that we cannot solve Eq. (3.35) analytically. Here, we make use of the perturbed wave function approach outlined in Ref. [65], except that our "Hamiltonian" matrix is not Hermitian.

Since we have assumed that the variation of the magnetic field in space occurs enough slowly, and we may also assume that the refractive indices are very close to unity or $\omega \approx k$, we may use the following expansion,

$$\begin{aligned}\omega^2 + \partial_z^2 &= (\omega + i\partial_z)(\omega - i\partial_z) \\ &\approx (\omega + k)(\omega - i\partial_z) \\ &\approx 2\omega(\omega - i\partial_z).\end{aligned} \tag{3.34}$$

Then Eq. (3.18) is rewritten as a linearized form of the wave equation,

$$i\partial_z\psi = (\mathscr{H}_0 + \mathscr{H}_1)\psi \tag{3.35}$$

where $\psi = (A_x, A_y, a)$,

$$\mathscr{H}_0 = \omega + \begin{pmatrix} Q/2\omega & 0 & 0 \\ 0 & Q/2\omega & 0 \\ 0 & 0 & -m_a^2/2\omega \end{pmatrix}, \tag{3.36}$$

$$\mathscr{H}_1 = \frac{g_{a\gamma}}{2}\begin{pmatrix} 0 & 0 & B_x \\ 0 & 0 & B_y \\ B_x & B_y & 0 \end{pmatrix}, \tag{3.37}$$

B_x, B_y are the x, y components of the magnetic field, and A_x, A_y are the photon polarization states whose electric fields are parallel to the x- and y-axis, respectively.

Now this linearized form of wave equation is interpreted as a "Schrödinger equation" with the z coordinate playing the role of time. For $g_{a\gamma} \to 0$, the off-diagonal term $\mathscr{H}_1$ vanishes, and the equation is solved exactly,

$$\psi^{(0)}(z) = \mathcal{U}(z)\psi(0), \tag{3.38}$$

where

$$\mathcal{U}(z) = \exp\left[-i\int_0^z dz'\,\mathscr{H}_0(z')\right] \tag{3.39}$$

$$= e^{-i(\omega - m_a^2/2\omega)z}\begin{pmatrix} \zeta(z) & 0 & 0 \\ 0 & \zeta(z) & 0 \\ 0 & 0 & 1 \end{pmatrix}, \tag{3.40}$$

where

$$\zeta(z) = \exp\left[-\int_0^z dz'\,(iq(z') + \Gamma(z')/2)\right]. \tag{3.41}$$

Then we take $\mathscr{H}_1$ as a perturbation, and the first-order perturbative solution is given as,

$$\psi^{(1)}(z) = -i\,\mathcal{U}(z)\int_0^z dz'\,\mathcal{U}^{-1}(z')\mathscr{H}_1(z')\mathcal{U}(z')\psi(0). \tag{3.42}$$

Thus, we find for the transition probability,

$$\begin{aligned} P_{a\to\gamma} &= \sum_{i=x,y} |\langle A_i(L)|a(0)\rangle|^2 \\ &= \sum_{i=x,y} \frac{g_{a\gamma}^2}{4} \exp\left[-\int_0^L dz\,\Gamma(z)\right] \\ &\quad \times \left|\int_0^L dz\, B_i(z) \exp\left[\int_0^z dz'\,(iq(z') + \Gamma(z')/2)\right]\right|^2 . \end{aligned} \tag{3.43}$$

When B, Γ, and q are constant, we recover Eq. (3.33).

3.3.4 Expected detection power

From Eqs. (3.9) and (3.30), the photon flux at the X-ray detector is

$$\Phi_\gamma = 7.9 \times 10^{-8}\,\mathrm{cm}^{-2}\,\mathrm{s}^{-1} \left(\frac{g_{a\gamma}}{10^{-10}\,\mathrm{GeV}^{-1}}\right)^4 \left(\frac{BL}{4\,\mathrm{T}\cdot 2.3\,\mathrm{m}}\right)^2 . \tag{3.44}$$

Since the rate of the expected signal is extremely low, we should also measure the background rate using a half of the measurement time and should compare the signal rate with it. The reachable sensitivity of the helioscope is then expected to be

$$\begin{aligned} g_{a\gamma} \gtrsim\, & 5.4 \times 10^{-10}\,\mathrm{GeV}^{-1} \left(\frac{\Sigma}{3}\right)^{1/4} \left(\frac{BL}{4\,\mathrm{T}\cdot 2.3\,\mathrm{m}}\right)^{-1/2} \\ & \times \left(\frac{A_{\mathrm{eff}}}{10\,\mathrm{cm}^2}\right)^{-1/4} \left(\frac{R_{\mathrm{bg}}}{10^{-3}\,\mathrm{s}^{-1}}\right)^{1/8} \left(\frac{T}{\mathrm{day}}\right)^{-1/8} , \end{aligned} \tag{3.45}$$

where T is the time of measurement, A_{eff} is the effective area of the X-ray detector, R_{bg} is the background rate, and Σ is the significance of the signal as a ratio to the standard deviation error. Here,[1] all the detection efficiencies including trigger efficiency, loss by the window medium, geometrical shading, etc. are incorporated in A_{eff}. Among the parameters in Eq. (3.45), BL has the largest figure of merit and $g_{a\gamma}$ is scarcely sensitive to T or R_{bg}. If one need to accept larger background rate by $R_{\mathrm{bg}} \propto A_{\mathrm{eff}}$ to enlarge A_{eff}, it has little merit either.

3.4 Other solar axion searches

3.4.1 Helioscope searches

There have been a pioneer as well as a follower to ours and an on-going project which uses the axion helioscope method. Our experiment is described in the following chapters.

- BNL axion helioscope [67]

[1] The same symbol appearing in Section 6.8.2 includes only the loss by geometrical shading.

Lazarus *et al.* used a fixed conventional 2.2-T dipole magnet of 1.8-m long oriented toward the point of sunset and a proportional chamber X-ray detector. As the buffer gas, helium gas was introduced in the magnetic volume. Measurement with the conversion region evacuated and with two gas pressure settings yielded:

$$g_{a\gamma} < 3.6 \times 10^{-9}\,\mathrm{GeV}^{-1} \qquad \text{for } m_a < 0.03\,\mathrm{eV}, \tag{3.46}$$

$$g_{a\gamma} < 7.7 \times 10^{-9}\,\mathrm{GeV}^{-1} \qquad \text{for } 0.03\,\mathrm{eV} < m_a < 0.11\,\mathrm{eV}, \tag{3.47}$$

at 99.7% confidence level.

- CAST (CERN Axion Solar Telescope) [68]

  This is a recent axion helioscope experiment at CERN which was build after ours and resembles to ours except its scale of the apparatus as well as that of the collaboration. They used a decommissioned LHC superconducting dipole test magnet of 8.4 T and 10 m long. Hence its has two bores and they are at 1.8 K which is a lower temperature than ours. At both ends of the magnet, three different X-ray detectors were used: a conventional time projection chamber (TPC), a Micromegas gaseous detector, and a charge coupled device (CCD) with an X-ray focusing optics. It is mounted on a tracking mount capable of $\pm 5^\circ$ vertical and $\pm 40^\circ$ in the horizontal direction.

  With a vacuum conversion volume, they scanned up to $m_a < 0.02\,\mathrm{eV}$ [69, 70], and the mass range was extended to $m_a < 0.4\,\mathrm{eV}$ by filling the magnet bores with ^{4}He gas [71]. After our publication, they published a new result where the mass range was extended to $m_a < 1.17\,\mathrm{eV}$ using ^{3}He which has enough saturation vapor density at 1.8 K [72]. In summary, their most recent limits are,

$$g_{a\gamma} < 8.8 \times 10^{-11}\,\mathrm{GeV}^{-1} \qquad \text{for } m_a < 0.02\,\mathrm{eV}, \tag{3.48}$$

$$g_{a\gamma} < 2.2 \times 10^{-10}\,\mathrm{GeV}^{-1} \qquad \text{for } m_a < 0.4\,\mathrm{eV}, \tag{3.49}$$

$$g_{a\gamma} \lesssim 3.3 \times 10^{-10}\,\mathrm{GeV}^{-1} \qquad \text{for } m_a < 1.17\,\mathrm{eV}. \tag{3.50}$$

- IAXO (International Axion Observatory) [73]

  This is a proposed next generation axion helioscope aiming at a sensitivity of $g_{a\gamma} \sim \mathcal{O}(\text{a few } 10^{-12}\,\mathrm{GeV}^{-1})$.

3.4.2 Crystalline detectors

Another group of searches for solar axions have been carried out using crystalline detectors like germanium. This method [74] exploits the coherent Primakoff conversion of axions into photons when their angle of incidence satisfies a Bragg condition with a crystalline plane. Because of the short range of coherence, this method yields a constant sensitivity with regard to $g_{a\gamma}$ independent of m_a up to about 1 keV.

- SOLAX [75]

The experiment was carried out with the DEMOS detector in Sierra Grande, Argentina, which is a single crystal germanium detector of 1 kg. The analysis of 1.94 kg year of data yielded a bound,

$$g_{a\gamma} < 2.7 \times 10^{-9}\,\mathrm{GeV}^{-1}. \tag{3.51}$$

- DAMA [76]

  The DAMA collaboration used their 100 kg NaI(Tl) crystal scintillator in the Gran Sasso National Laboratory (LNGS for Laboratori Nazionali del Gran Sasso) of INFN, Italy, to search for the solar axions. With a statistics of 53437 kg day, they yielded a bound,

$$g_{a\gamma} < 1.7 \times 10^{-9}\,\mathrm{GeV}^{-1}. \qquad (90\%\ \mathrm{CL}) \tag{3.52}$$

- COSME [77]

  The COSME detector is a natural abundance germanium detector with a mass of 234 g operated in the Canfranc Underground Laboratory (LSC for Laboratorio Subterráneo de Canfranc), Spain. From an exposure of 72.7 kg day, they yielded a bound,

$$g_{a\gamma} < 2.78 \times 10^{-9}\,\mathrm{GeV}^{-1}. \tag{3.53}$$

- CDMS (Cryogenic Dark Matter Search) [78]

  The CDMS collaboration reported a upper limit,

$$g_{a\gamma} < 2.4 \times 10^{-9}\,\mathrm{GeV}^{-1}, \tag{3.54}$$

  by analyzing their 19 germanium detectors of about 250 g each in the Soudan Underground Laboratory, US.

Chapter 4

Tokyo Axion Helioscope

In this chapter, we will describe the overview of our project.

4.1 Detector design

Design of our axion helioscope, which was called *Sumico V* later, started in 1994. Some of the features of our detector follows:

- Aimed at solar axions with a mass, $m_a \leq$ (a few electronvolts), using the axion helioscope technique.
- Aim to achieve the enough sensitivity to $g_{a\gamma}$ which the axion models predict.
- Use cold dense gaseous helium as the buffer gas.
- Use PIN photodiodes as the X-ray detector.
- Use an X-ray window to separate buffer gas from the X-ray detector.
- Use superconducting magnet.
- Track the sun to realize longer measurement.

Our design target was to search for the solar axion in the hadronic axion window from about one elecronvolt to a few electronvolts.

As the most fundamental design basis, we decided to employ a superconducting magnet and to employ low temperature helium-4 gas at about the same temperature as the superconducting magnet as the dispersion matching medium.

Clearly from Eq. (3.33), medium with small absorption coefficient Γ such as hydrogen (H_2) or helium (He) is preferable. The values of hydrogen and helium of a density corresponding to $m_\gamma = 2\,\mathrm{eV}$ for X-ray photons of $E = 4\,\mathrm{keV}$ are $\Gamma_{H_2} = 0.2\,\mathrm{m}^{-1}$ and $\Gamma_{He} = 0.9\,\mathrm{m}^{-1}$, respectively [79]. K. van Bibber *et al.* [66] proposed an alternative scheme where a self-absorbing buffer gas is used as the X-ray detector. As the authors admit, however, this scheme is disadvantageous when background is taken into account.

In order to keep the gas pressure as low as possible, lower temperatures are preferred. Figure 4.1 shows the reachable masses with helium-4 gas plotted with

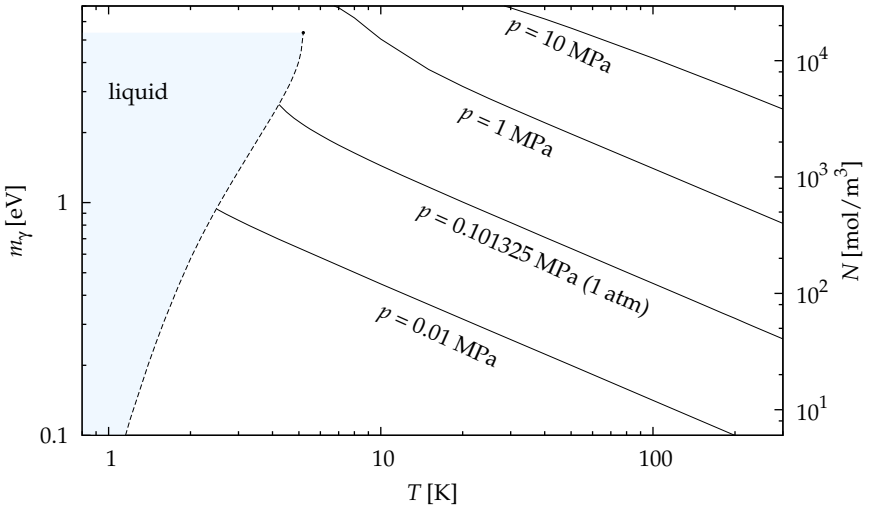

Figure 4.1: Reachable molar densities and the corresponding effective photon masses by helium-4 as a function of temperatures.

respect to the temperature. Solid curves show the equi-pressure contours for $p = 0.01\,\mathrm{MPa}$, 1 atmosphere (0.101325 MPa), 1 MPa, and 10 MPa. The dashed curve corresponds to the saturation line where liquid and vapor coexist, and, in the sky-blue area, helium-4 exists as liquid. The end point of the saturation line is the critical point, where $p_c = 0.227\,\mathrm{MPa}$ and $T_c = 5.1953\,\mathrm{K}$ [80].

For example, the density of 1 atmosphere of helium gas at its boiling point $4.222\,\mathrm{K}$ is $4.2 \times 10^3\,\mathrm{mol/m^3}$ [80]. It corresponds to the photon effective mass of $m_\gamma = 2.64\,\mathrm{eV}$, which coincides about the higher bound of the hadronic axion window. At room temperature, the pressure of the same density of helium gas would reach indeed 100 atmospheres.

If the temperature were too low, gaseous helium would condense and would separate into two phases. Thus one should keep its temperature higher than the saturation line.

This design also helps us to utilize the bore of the magnet as efficient as possible. Since the gas container and the magnet is about the same temperature, we can eliminate the needs of some thermal insulation layers between them.

Although hydrogen has smaller absorption coefficient than helium, use of hydrogen buffer was disfavored not only because it is dangerous to handle but also because it liquefies at a higher temperature than helium. Its critical point is $T_c = 33.24\,\mathrm{K}$ and $p_c = 1.30\,\mathrm{MPa}$. To obtain the same densities as helium, we need to keep it at higher temperatures and hence higher pressures.

Another important decision on the design of the helioscope was to put the X-ray detector outside the gas container by adopting an X-ray transparent window. In order to reduce background by external radiation, the X-ray detector should be surrounded by a thick and heavy radiation shielding. Bringing it inside the magnet seemed unrealistic as it would raise the building cost of the magnet by enlarging the total volume of the magnetic field. The alternative option was to extend the gas container or to adopt an X-ray window. The latter was chosen since it minimizes the heat injection to buffer gas.

We decided to adopt semiconductor detectors or, more specifically, the PIN photodiodes as the X-ray detector, since they are suited to the cryogenic detector design. A PIN photodiode itself produces little heat during its operation and we had confirmed experimentally that it performed as a good X-ray detector at cryogenic environment at least down to 13 K [81]. However, if we were to place the X-ray detector inside the gas container, the preamplifier circuits should be placed distant enough to make the heat injection from them negligibly small, since they should be operated at a higher temperature at 130 K and they emit considerable heat.

It seemed impossible to locate the preamplifiers distant from the PIN photodiodes while maintaining its performance as an X-ray detector. Furthermore, we realized later that the connection between the PIN photodiode and the cold ($\sim 130\,\mathrm{K}$) part of the preamplifier should be as short and rigid as possible to reduce microphonic noise as described in Section 5.4.1.

The length of the magnetic field L is restricted by various factors including the cost, the feasibility of tracking the sun, the space of the experimental site, the effect of gravity on the buffer gas, and the merit of enlarging L. Since we will gain nothing from its length for $\Gamma L \gg 1$, it was determined to be $L \simeq 2\,\mathrm{m}$.

4.2 Expected detection power

As a result of the adoption of the X-ray window, the gas pressure was limited by its maximum pressure, $p = 0.3\,\mathrm{MPa}$. The typical temperature of the magnet we built was 5–6 K. To be safe, we should lower the highest mass target at this slightly higher temperature. If we are to fill gaseous helium of $p \leq 1$ atmosphere at $T = 5.5\,\mathrm{K}$, we will be able to explore up to $m_a \leq 2.07\,\mathrm{eV}$. Even at the higher bound of the magnet temperature of 6 K, its pressure remains within a safety range as low as 1.2 atmospheres. In the following, we will use the helium density corresponding to

$$m_\gamma = 2\,\mathrm{eV} \text{ or } N = 2.41 \times 10^3\,\mathrm{mol/m^3} \tag{4.1}$$

as the benchmark for design although we did not reached that mass for various reasons. In terms of signal rate only, heavier masses are more facile to reach, since the coupling constant is proportional to the mass by Eq. (2.38). In terms of experimental difficulty, however, situations can be opposite.

Let us estimate the detection power of our helioscope for $m_a = 2\,\mathrm{eV}$ corresponding to the above benchmark density using the typical values of our detector: $BL = 4\,\mathrm{T} \times 2.3\,\mathrm{m}$, $A_{\mathrm{eff}} = 10\,\mathrm{cm^2}$, and $R_{\mathrm{bg}} = 10^{-3}\,\mathrm{s^{-1}}$. At this high density, Eq. (3.45) gets correction from the absorption by the buffer gas:

$$g_{a\gamma} \gtrsim 7.0 \times 10^{-10}\,\mathrm{GeV}^{-1} \left(\frac{\Sigma}{3}\right)^{1/4} \left(\frac{T}{\mathrm{day}}\right)^{-1/8}, \tag{4.2}$$

where the above typical values of the detector parameters are used. In hadronic axions (KSVZ axions) with $E = 0$, for example, the relation between $g_{a\gamma}$ and m_a is given as

$$g_{a\gamma} = 3.7 \times 10^{-10} \left(\frac{m_a}{\mathrm{eV}}\right). \tag{4.3}$$

Substituting it into Eq. (4.2), we expect for the sensitivity of discovery by 3σ to be reachable in

$$T = 0.6\,\mathrm{day} \tag{4.4}$$

for axions with $m_a = 2\,\mathrm{eV}$. Although this value can change by an order depending on the actual performance of the apparatus, reaching this model seemed feasible. However, we were somewhat pessimistic about reaching the GUT axion model, where $E/N = 8/3$, or models with even suppressed axion–photon couplings such as $E/N = 2$. For example, if the axion mass were $m_a = 2\,\mathrm{eV}$, it will take 3 years to reach the same discovery sensitivity for the GUT axion model.

4.3 Sumico research activities

The first measurement to search for solar axions with our axion helioscope was carried out in December 1997. In this phase (Phase I), the gas container was absent and hence the helioscope was operated with vacuum in its conversion region. From the absence of an axion signal, an upper limit on the axion–photon coupling constant was given to be [82]

$$g_{a\gamma} < 6.0 \times 10^{-10}\,\mathrm{GeV}^{-10} \qquad \text{for } m_a < 0.03\,\mathrm{eV} \tag{4.5}$$

at 95% confidence level. This result improved the existing sensitivity to $g_{a\gamma}$ by a factor of 4.5, and it became the first self-consistent experiment which has enough sensitivity to detect such axions that do not violate the solar model itself. The sensitive mass region was limited to $m_a < 0.03\,\mathrm{eV}$, however, because the momentum transfer q is not negligible for heavier axions.

In the second phase (Phase II) [83], we introduced ^{4}He gas into the conversion volume in the magnetic field to make it sensitive to heavier axions. The measurement to search for solar axions was carried out during from July through September 2000. We scanned axion masses up to $m_a < 0.27\,\mathrm{eV}$. Detail of this measurement and the result of analysis are described in Chapter 6.

In the third phase (Phase III) of our program, we developed a more sophisticated gas control system to handle denser ^{4}He gas. A measurement to search for solar axions in the hadronic axion window around 1 eV was carried out from December 2007 through April 2008. It was later continued after repairing the apparatus from July till August 2008. This measurement is described in Chapter 7.

Aside from the solar axion searches, an experiment to search for axions which have celestial origins was carried out from November through December 2000. In addition to a wide-range scan on the celestial sphere to cover its 10%, a tracking measurement was carried out for four compact objects, the galactic center, Sco X-1, Vela X-1, and the Crab nebula [84].

From May till August 2002, another attempt to search for celestial axions was carried out where a soft γ repeater SGR1900+14 was targeted [85].

Furthermore, the telescope mount of the axion helioscope was utilized to search for solar hidden photons. An external hidden photon detector consisting of a parabolic mirror focusing optics, a photomultiplier tube and a light-weight vacuum chamber was attached on the axion helioscope. The measurement was

carried out from October till November 2010 yielding an upper limit on the photon–hidden-photon kinetic mixing angle at the electronvolt energy range [86].

Chapter 5

Experimental apparatus

5.1 Overview

The schematic figure of the axion helioscope is shown in Fig. 5.1. It consists of a superconducting magnet, X-ray detectors, a gas container, and an altazimuth mount. The most notable point of this apparatus is that it is an automated telescope. It was designed to track the sun in order to achieve long exposure time.

The superconducting magnet consists of two 2.3-m long race-track shaped coils running parallel with a 20-mm wide gap between them. The magnetic field between the gap is 4 T perpendicular to the helioscope axis. The coils are kept at 5–6 K during operation. In order to make it easy to swing this huge cryogenic apparatus, two devices are engaged. First, the magnet was made cryogen-free by making two Gifford–McMahon refrigerators to cool it directly by conduction. Second, a persistent current switch was equipped. Thanks to this, the magnet can be freed from thick current leads after excitation, and the magnetic field is very stable for a long period of time without supplying current. Details of the superconducting magnet are given in Ref. [87].

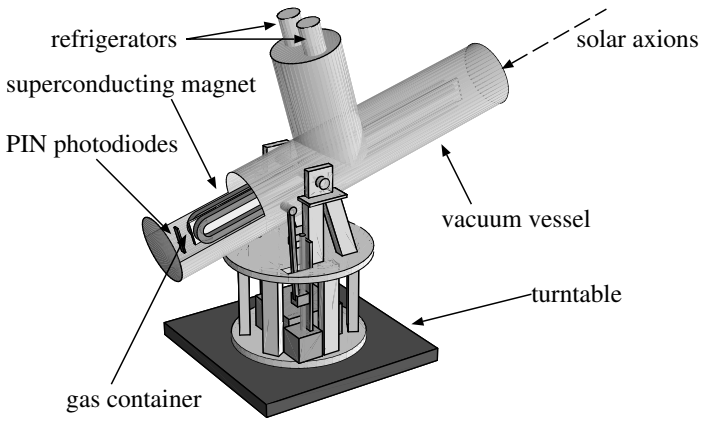

Figure 5.1: The schematic view of the axion helioscope.

The container to hold dispersion-matching gas is inserted in the $20 \times 92\,\mathrm{mm}^2$ aperture of the magnet. Its body is made of four 2.3-m long 0.8-mm thick stainless-steel square pipes welded side by side to each other. The entire body is wrapped with 5N high purity aluminium to achieve high uniformity of temperature. One end at the forward side of the container is sealed with welded plugs and is suspended firmly by three Kevlar cords. The opposite side facing to the X-ray detectors is flanged and fixed to the magnet. At this end of the container, gas is separated from vacuum with an X-ray window which is transparent to X-ray above 2 keV and can hold gas up to 0.3 MPa at liquid helium temperature.

As the X-ray detectors, sixteen PIN photodiodes, Hamamatsu Photonics S3590-06-SPL, are used, whose chip size is $11 \times 11 \times 0.5\,\mathrm{mm}^3$ each. Each chip is mounted on a Kapton film bonded to an Invar plate with cryogenic compatible adhesive. Four photodiodes and the most sensitive portions of the preamplifiers including the first-stage FETs are assembled into an X-ray detector module, and four such modules are used. The X-ray detectors are mounted in a 10-mm thick radiation shielding box made of oxygen-free high conductivity copper (OFHC Cu), which is then surrounded by a lead shield of about 150 mm thick. The copper shield is operated at about 60 K, so that it also functions as a cold finger for the X-ray detectors. Details on the X-ray detector are given in Ref. [88].

The entire axion detector is constructed in a vacuum vessel and the vessel is mounted on an altazimuth mount. Its trackable altitude ranges from $-28°$ to $+28°$ and its azimuthal direction is limited only by a limiter which prevents the helioscope from endless rotation. This view corresponds to an exposure time of about a half of a day in observing the sun in Tokyo at 139° 45' 48" E and 35° 42' 49" N. This is enough for our purpose, since background is measured during the other half of a day. This helioscope mount is driven by two AC servo motors.

Since the effective aperture of the helioscope is narrow, it is crucial to determine its accurate geometry. In order to define the axis of the helioscope, two cross hairs are placed at the edge of the vacuum vessel.

Details on each component are described in the following sections.

5.2 Magnet

5.2.1 Basic design

Design of the magnet was directed by A. Yamamoto of KEK, and it was manufactured by Toshiba Corporation. Main parameters of the magnet are summarized in Table 5.1. Although the designed maximum value for the central magnetic field of this magnet is 5 T, we have operated it with central field of 4 T aiming for stability against magnet quench. For a stable excitation at 5 T, the magnet should be trained further.

From Eq. (3.43), the magnetic field should be perpendicular to the telescope axis. On the other hand, homogeneity of the field is unnecessary in our application. Although the saddle-coil design was more preferable in terms of its larger aperture, we adopted split race-track coil design as shown in Fig. 5.2 which was easier to manufacture and thus relatively inexpensive.

Two race-track coils are paired leaving a gap of 20 mm between them. Each

Magnet:	
Outer dimensions (excluding LHe pipes):	
length	2340 mm
width	168 mm
height	270 mm
Aperture:	
width	20 mm
height	92 mm
Central field	4.0 T(typ)/5.0 T(max)
$B_{\max}$ in coil	5.74 T(typ)/7.18 T(max)
Current	268 A(typ)/336 A(max)
Inductance	15.5 H
Stored energy	560 kJ(typ)/875 kJ(max)
Weight	670 kg
Coils:	
Quantity	2
Shape	racetrack
Conductor	NbTi/Cu
Winding thickness	64 mm
Winding width	50 mm
Cross section area	3.2×10^2 mm^2
Length of the linear section	2100 mm
Inner radius at both ends	50 mm
Outer radius at both ends	100 mm
Gap between coils	20 mm
Volume per coil	14.95×10^4 mm^3
Weight per coil	133.5 kg
Turns per layer	33.5
Layers per coil	54
Turns per coil	1809
Refrigerators:	
Quantity	2
System	2-stage Gifford–McMahon cycle
1st stage cooling power	20 W/each @ 40 K
2nd stage cooling power	0.5 W/each @ 5 K

Table 5.1: Main parameters of the magnet [87].

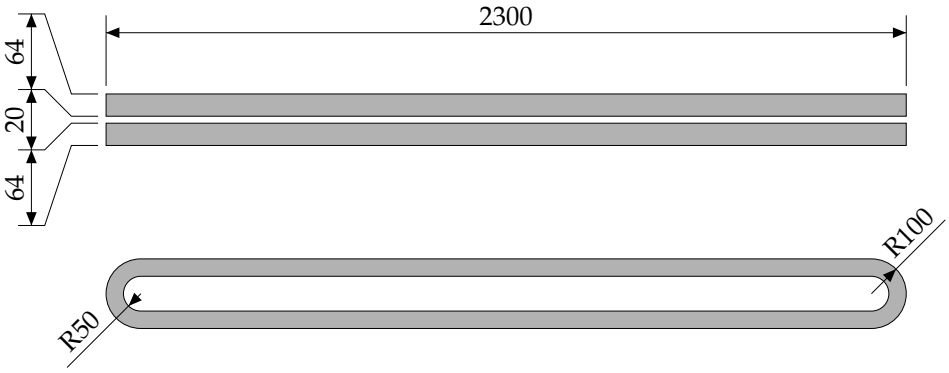

Figure 5.2: Top and side view of the split racetrack coils. Scales are in millimeters.

coil is wound with a copper stabilized NbTi superconducting wire. The gap is held by two 20 mm-thick copper plates sandwiched in the straight sections of the coils. These plates not only support the gap mechanically, but also play as the busbars to transfer heat. Two other copper plates are attached on top and bottom of the coils to enhance thermal contact with them. Each of them is soldered to the gap-holding copper plate perpendicularly to form a T-shaped cross section. The coils and the copper plates are then housed in a stainless steel case which receives the large hoop force acting on the race-track coils.

The gap is not filled with copper at both ends. The converted X-ray passes this aperture from the conversion region to the detector which is outside of the magnet. The stainless steel case has also two apertures at both ends. The size of the aperture of the magnet is 20 mm in width and 92 mm in height. The gap width and the height of the aperture were designed so as not to lose the strength of the field too much while maintaining the area needed for the observation. It is thus slit shaped.

The container to hold dispersion matching gas is inserted through this aperture and is suspended in the $20 \times 92 \times 2300\,\mathrm{mm}^3$ space in the magnet with both ends being supported. In order to minimize the deflection of the gas container, we chose such configuration that the long axis of the aperture becomes vertical, i.e., two coils are put side by side.

Another advantage of this juxtaposed configuration is that both coils are cooled equally by a simple heat transferring topology. Figure 5.3 shows the cooling system of the magnet. The coils are cooled by two DAIKIN V208SC Gifford–McMahon refrigerators by thermal conduction through an annealed copper cold finger. Each refrigerator has two stages; the first stage reaches 40 K whose nominal cooling power is 20 W each, and the second stage reaches 4.2 K whose nominal cooling power is 0.5 W each. They can be inclined up to 30° without severe drop of cooling power. The coils are thermally coupled to the T-shaped copper plates, and the copper cold finger links the 4 K heads, or the second stages, of the refrigerators to the upper piece of the copper plates. In fact, cooling from the upper half of each coil should be enough, since thermal conductivity in a coil is good along conductors. The magnet is kept at 5–6 K during operation.

Two cooling pipes are embedded in the upper and lower pieces of the copper

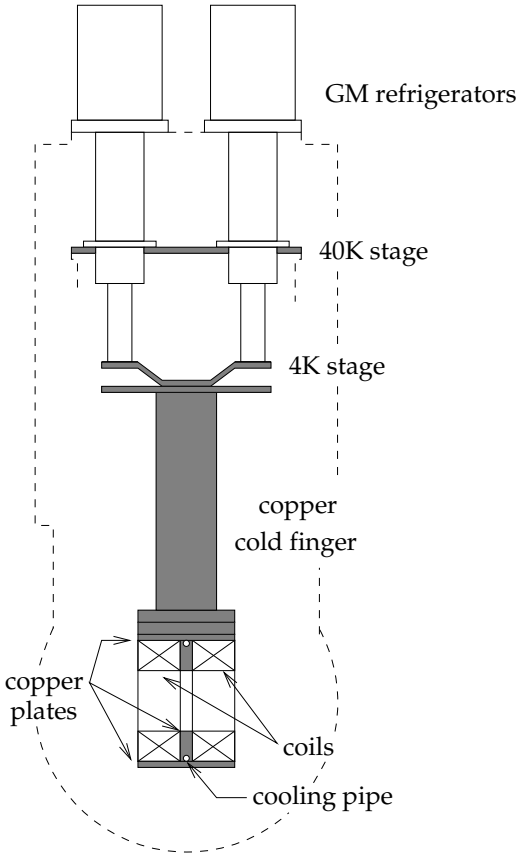

Figure 5.3: Cooling system of the magnet.

plates. They can cool the magnet independently or auxiliary to the refrigerator system by pouring cryogen, e.g., liquid nitrogen or liquid helium. At the exterior of the vacuum vessel, their ends are equipped with Wilson seals. The two refrigerators alone can cool the magnet from room temperature down to the operation temperature in two weeks. However, the magnet was often pre-cooled with liquid nitrogen down to about 100 K in order to decrease attrition of the refrigerators.

5.2.2 Magnetic field

The magnetic field was calculated by a numerical integration of Biot–Savart's law, where the QAGS algorithm of the GNU Scientific Library [89] or the adaptive 21-point Gauss–Kronrod quadrature was used. Figures 5.4 and 5.5 shows the calculated magnetic field, which is to be used in the estimation of the conversion rate in the later analysis. The positions of two Hall sensors SA and SB placed on the case of the magnet are indicated as two white spots in Fig. 5.4. The measured strengths of the field agreed with the numerical calculation within a reasonable range of error.

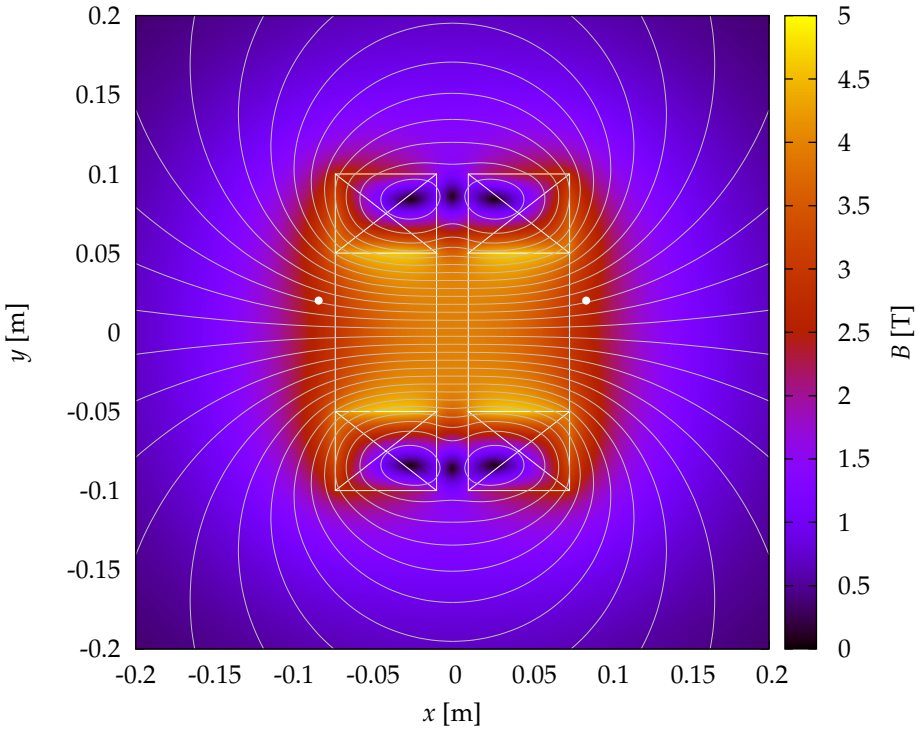

Figure 5.4: Cross section view of the magnetic field on the xy-plane ($z = 0$). The field strength is shown as the color map, the gray curves show the field lines and the white boxes at the center show the coils. The two white spots beside them indicate the positions of two Hall sensors.

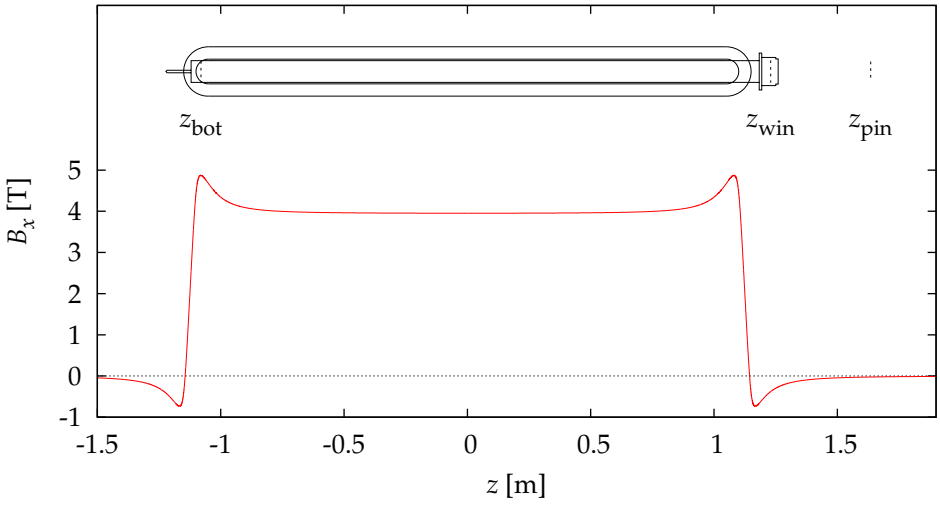

Figure 5.5: The transverse magnetic field along the z-axis. Above it, some important components of the helioscope including the coils, the gas container, and the PIN photodiodes are drawn at their corresponding z-axis positions.

5.2.3 Circuit

Figure 5.6 shows the circuit diagram of the superconducting magnet along with its excitation circuit and the voltage taps being monitored.

Between the 40-K stage and the 4-K stage, high-T_c superconducting rods were used as the power leads. Below the 4-K stage, copper stabilized NbTi superconducting wires were used for wiring.

This magnet is normally operated at persistent current mode where the persistent current switch (PCS) is kept in superconducting and the current leads from the power supply are disconnected. Before the magnet is excited or deexcited, the current leads are connected to the magnet and the PCS is made into normal phase (11 Ω) by a heater attached to it. The PCS was fabricated by S. Mizumaki of The Graduate University for Advanced Studies and its details are described in his PhD thesis [90].

A Hewlett–Packard 6680A System DC Power Supply was used to excite or to deexcite the magnet. Between the power supply and the magnet, a homemade DC breaker circuit was inserted which breaks the circuit on the occasions of a magnet quench, anomalous voltages on the coils as well as on the high-T_c power leads, or a trouble of the cooling system. In the breaker, a Fuji Electric 1DI480A-055 power transistor module was used in conjunction with a Nihon Inter Electronics 250MA60 silicon rectifier which prevents from a coutercurrent to flow from the base to the collector when the supplied voltage is lower than $V_{\mathrm{CE(sat)}}$.

The magnet quench was monitored by a Clear Pulse 8286/N Quench Detector which detects an asymmetry in the voltages of the two coils. When the circuit is broken, the coil current bypasses through the embedded flywheel diodes.

5.2.4 Monitoring system

The strength of the magnetic field and the temperatures of the magnet and the cooling system were monitored regularly throughout from cooling down till warming up of the magnet. In addition to the above, the voltages on the coils and high-T_c power leads were monitored while the magnet was operated.

Two Hall sensors were placed on the stainless steel case of the magnet as already shown in Fig. 5.4. Lakeshore Carbon-Glass Resistor (CGR) thermistors, CGR-1-1000 and partly CGR-1-500, were used mainly in low temperatures below 40 K, whereas Pt-Co resistor thermistors were used in higher temperatures up to room temperature, 300 K. The temperatures of cooling water and the room were also monitored by Tama Electric Corporation type SDT101A Pt resistor thermistors. As shown in Fig. 5.7, all the CGR thermistors are connected in series and a bias current of 10 μA was fed from a current source below 100 K, while a bias current of 100 μA was fed above 100 K. The four-terminal method was used to measure their resistances. The precise value of the bias current was monitored with a 10-kΩ metal film resistor connected in series with the CGR thermistors. The bias currents of 1 mA, 0.25 mA, and 100 mA are fed using similar circuits for the Pt-Co thermistors, the Pt thermistors, and the Hall sensors, respectively.

Figure 5.8 shows the diagram of the data acquisition system for environment monitoring. It was build on a VXIbus system controlled through a Hewlett–

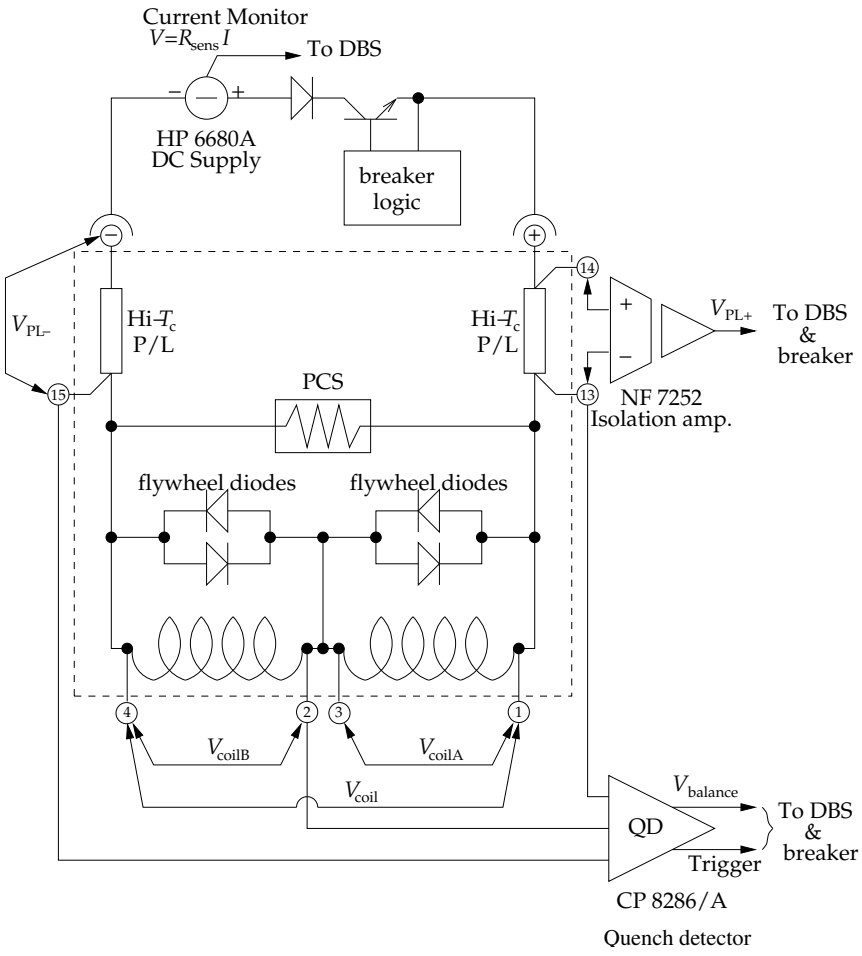

Figure 5.6: Diagram of the magnet excitation circuit. Circled numbers denote the voltage taps being monitored. Only one instance of a isolation amplifier for $V_{\mathrm{PL}+}$ is shown in the diagram. However, same isolation amplifiers are used for $V_{\mathrm{PL}-}, V_{\mathrm{coil}}, V_{\mathrm{coilA}}, V_{\mathrm{coilB}}$, and the current monitor output.

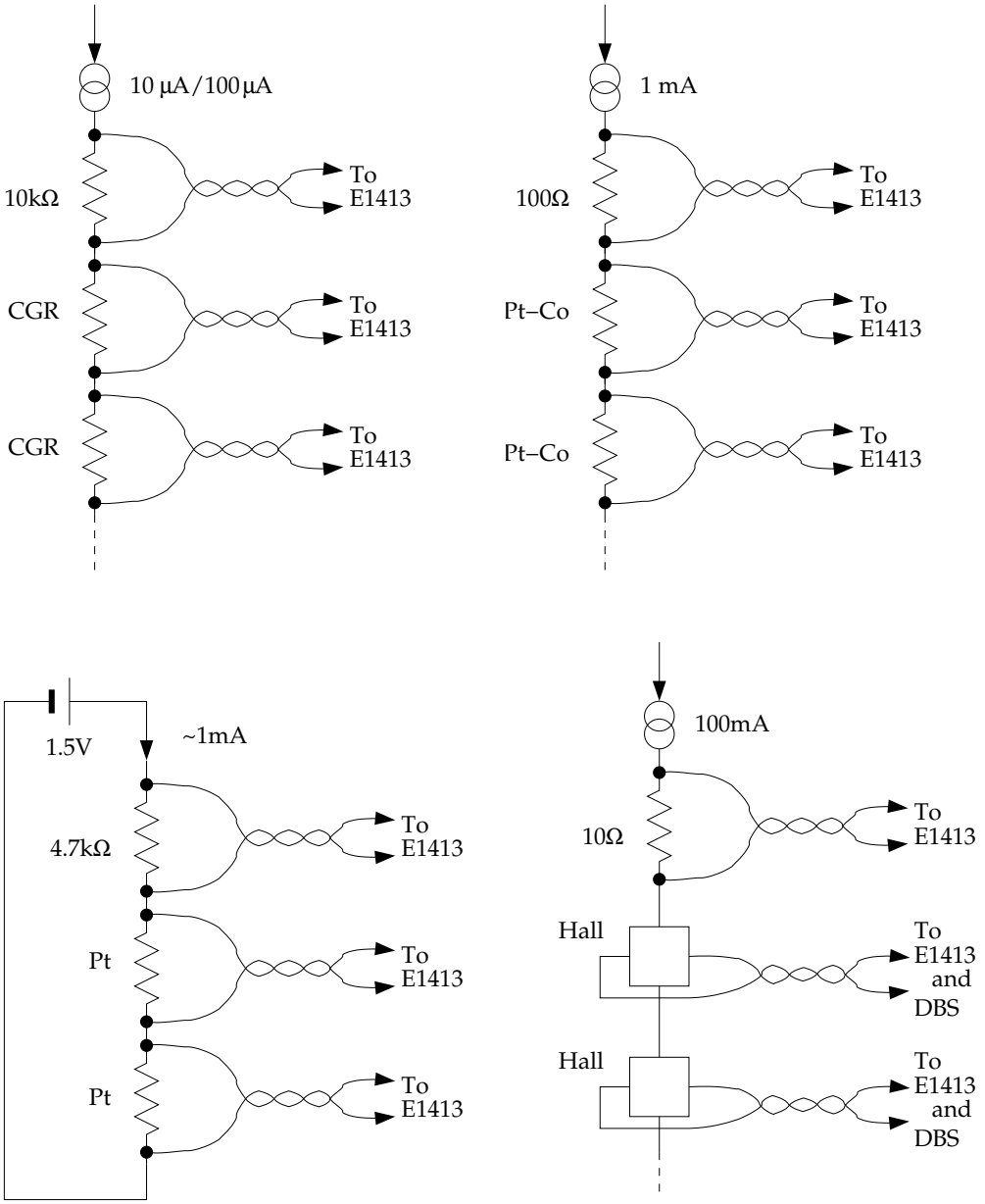

Figure 5.7: Connection to sensors.

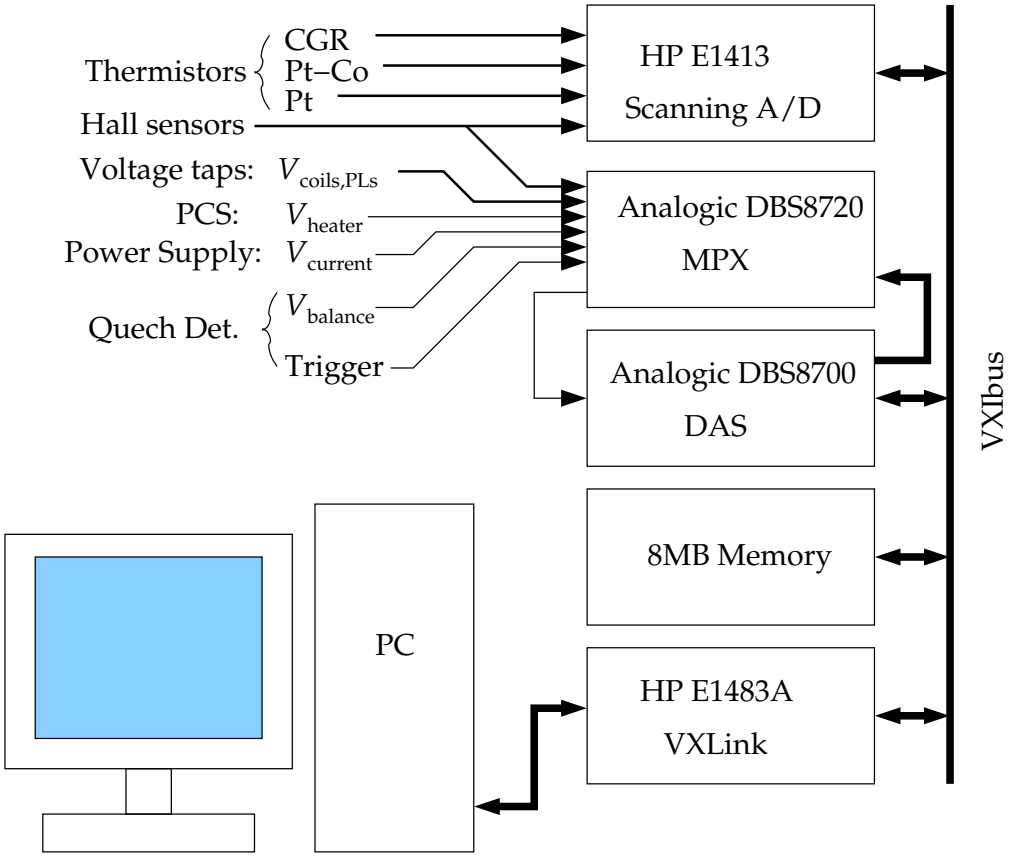

Figure 5.8: Data acquisition system for environment monitoring.

Packard E1483 VXLink VXIbus-ISA adapter. Slow signals such as temperatures were monitored by a Hewlett–Packard E1413 High-Speed Scanning A/D. It has 64 channels of inputs and an auto-ranging/fixed-range high-precision analog-to-digital converter and an on-board averaging feature. For each output voltage from the thermistors, the Hall sensors, and their bias current monitors, the average of thirty-two measurements was retrieved and recorded to the storage in the PC every second.

For the voltage taps, an Analogic DBS8700 Digitizer was used along with an Analogic DBS8720 Multiplexer and an 8-MB VME memory in order to capture the fast transient voltages during quenches. The digitizer continually measures the voltages of eleven points in turn, and stores the measured values in the VME memory. The base sampling rate was set to 11 kHz so that each point was measured every 1 ms. When a quenching of the magnet occurs, the digitizer receives a trigger signal from the quench detector and asserts an interrupt request (IRQ) in the VXIbus. The PC detects it, and 30 seconds later, it retrieves the transient voltages from the VME memory which were measured between 30 seconds before and 30 seconds after the quench. The PC also read the immediate values from the VME memory every second independent of quenches, and logged the values to the disk storage.

NF 7252 Isolation Amplifiers were inserted between the voltage taps and their monitoring electronics, i.e., the VXI digitizer and the breaker logic, in order to protect sensitive electronics from an extraordinary voltage which may appear in the event of a breakage of the flywheel diodes. The quench detector, however, was connected directly to the voltage taps, since it includes its own protection circuit.

The NF 7252 isolation amplifiers had emitted a large amount of switching noise from their input ports which disturbed the precise measurement of temperatures. As a countermeasure to this problem, we wound their input cables around highly permeable torus ferrite cores several times to eliminate the common mode noise.

5.2.5 Excitation and deexcitation procedures

In a normal excitation, we followed the following procedure:

1. First, the PCS was switched to normal state by the PCS heater. The PCS is normally superconducting (closed), and it can be turned into normal state (open), by rising its temperature above 10 K.

2. Then, an excitation voltage was applied on the coil. The supplied voltage should be controlled so as not to induce a quench of the magnet, since the magnet generates heat by the eddy current. We kept the coils below 6 K during excitation.

   Nominally, the magnet can be fully excited in 48 minutes with the excitation voltage of $V_{\mathrm{coil}} = 1.44\,\mathrm{V}$. However, the actual excitation time depended on the condition of the refrigerators.

3. After the target current, 268 A, was reached, we closed the PCS by turning off the PCS heater.

4. Then, we decreased the supplied current gradually to zero until all the coil current to run through the PCS. If we cut off the supplied current abruptly, the magnet would quench originating from the PCS by eddy currents.

5. When the supplied current reached zero, excitation was finished and we were able to disconnect the power leads.

The deexcitation procedure is basically the opposite way. First, the PCS current is cancelled by supplying a current equal to the coil current from the power supply. Then, the PCS is opened and the magnet is deexcited by applying a negative voltage. However, care must be taken here. One can not supply a current which is exactly the same as the coil current. Thus when the PCS opens, a small discontinuous transition must come about.

The load characteristic of the magnet to the power supply changes remarkably depending on the status of the PCS. When the PCS is closed, the load is short-circuited, whereas the load is inductive when the PCS is open. Correspondingly, the power supply has two operation modes: the constant-voltage (CV) mode and the constant-current (CC) mode. The power supply tries to enforce the preset voltage or the preset current on its load, respectively. Therefore, when the PCS is closed, the CC mode is stable, whereas the current becomes

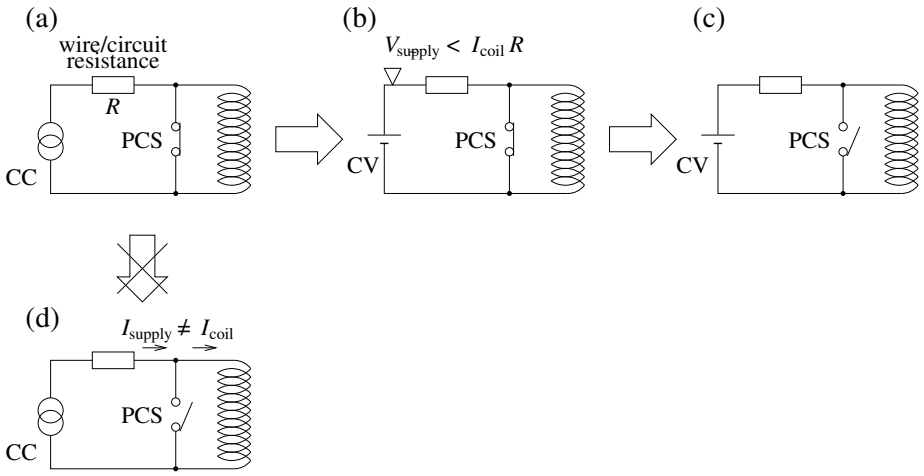

Figure 5.9: When to open PCS during deexcitation? (a) When the supplied current I_{supply} is balanced with the coil current I_{coil}, the power supply is in the CC mode. This state is stable. The power supply in the CC mode is shown with a current source symbol. (b) One can switch its mode into the CV mode by lowering the preset voltage. The power supply in the CV mode is shown with a battery symbol. Although this state is apparently unstable, the change is continuous. Moreover, the power supply is still marginally stable against short circuit, and is considered to be stabilized further by the wire resistance. Here, $I_{\text{coil}}R$ denotes the total voltage drop at $I = I_{\text{coil}}$ symbolically. Actual voltage drop is not linear. (c) By opening the PCS, a small negative voltage would applied on the coil, however, the system is stable against this transition. (d) If the PCS is opened abruptly from State (a), the system will be put into an unstable state. A small disagreement of the supplied current, $I_{\text{supply}} \neq I_{\text{coil}}$, may cause a magnet quench.

relatively unstable under the CV mode, since a small fluctuation of voltage can make a large change in the current. When the PCS is open, on the other hand, the CV mode is stable, whereas, in the CC mode, the power supply can apply the maximum- or minimum permissible voltage to its load trying to adjust the current through the large inductance.

Two modes automatically switch over so as not to exceed neither the preset voltage nor the preset current. Higher bounds of the voltage and the current are thus controlled. For the lower bounds, it can only supply non-negative voltages and non-negative currents actively although they can become negative passively.

If the PCS were opened while the power supply were in the CC mode, and if the actual supplied current were less than the coil current (Fig. 5.9 (d)), the power supply voltage would drop immediately to the minimum 0, which might induce a magnet quench.

In order to carry out deexcitation safely, we devised a somewhat complicated procedure. The basic idea is to transit into the CV mode before opening the PCS, and additionally, to set the preset current large enough to absorb errors.

1. First, we started with the preset current set to 0 A. The preset voltage was set larger than the total voltage drop expected at the target current

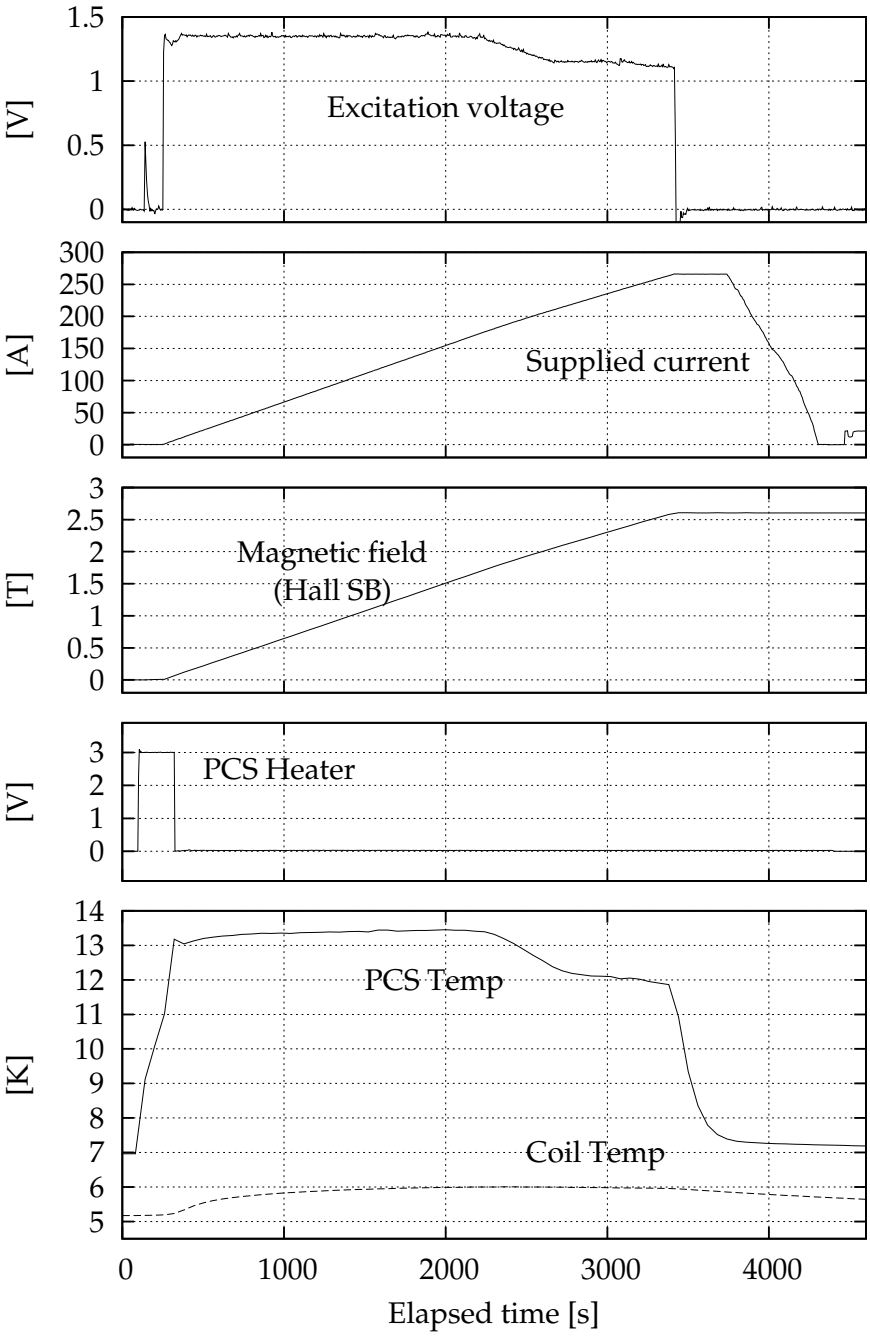

Figure 5.10: Excitation of the magnet. The spike in the excitation voltage at 138 s was considered to be due to the super-to-normal phase transition in the PCS. The bump in the supplied current at the end of the chart is spurious which appears while the power supply is turned off.

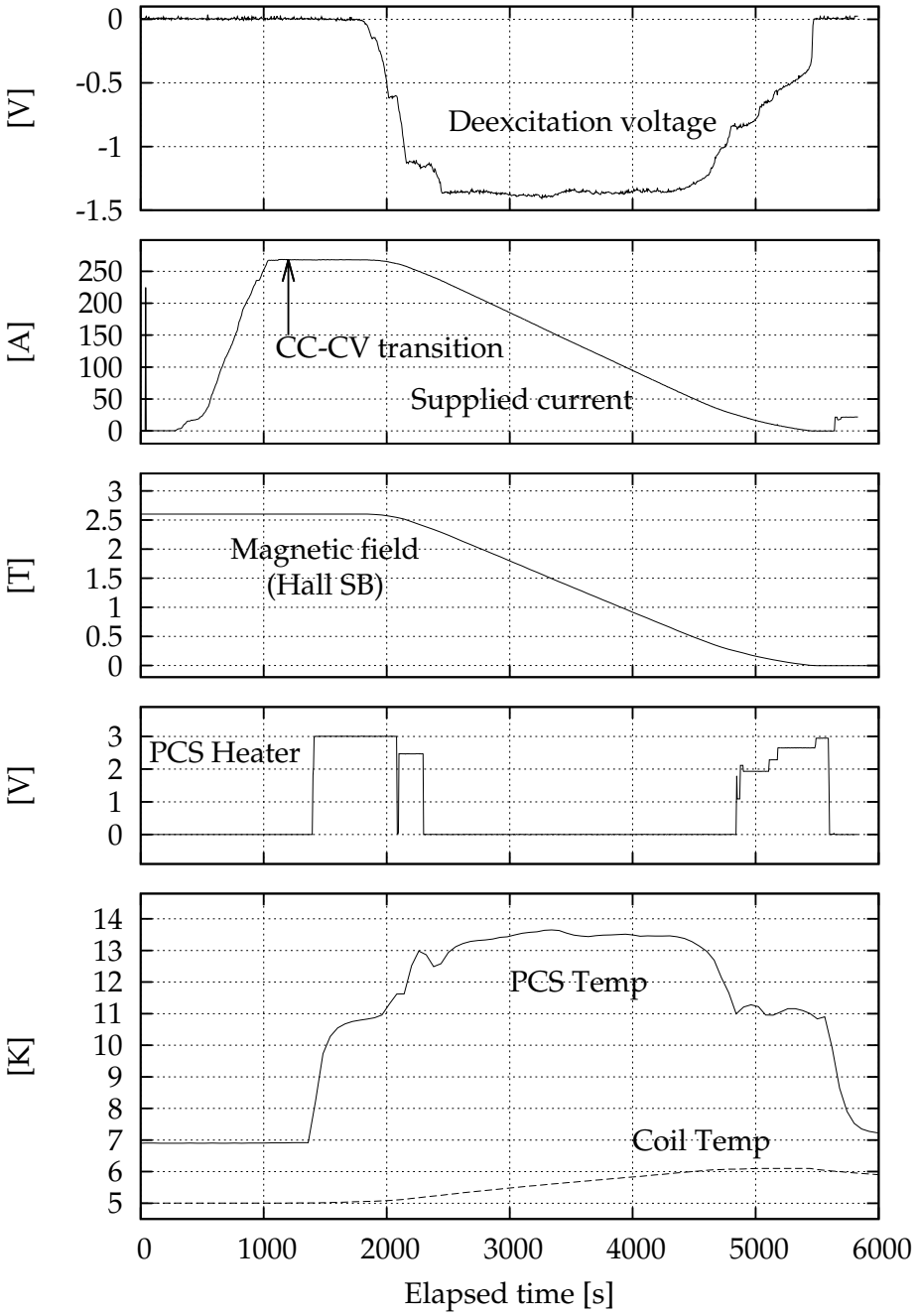

Figure 5.11: Deexcitation of the magnet. No significant anomaly is seen neither at the time of CC–CV transition nor at the super-to-normal transition in the PCS. The cause of the spike in the supplied current at 41 s is unknown. It may be a power up noise from the power supply.

so that it stayed in the CC mode up to the target current.

2. Then the supplied current was gradually increased by increasing the preset current.

3. After the target current was reached (Fig. 5.9 (a)), the preset voltage was lowered until the power supply transited from the CC mode to the CV mode (Fig. 5.9 (b)). The supplied current became slightly smaller than the coil current as a consequence.

4. Then the preset current was increased 1 A larger than the target current. This is to leave a margin of error. Even if the actual supplied current was slightly larger than the coil current, the power supply would remain in the CV mode.

5. The PCS is opened (Fig. 5.9 (c)). The supplied current was slightly smaller than the coil current before opening the PCS. Then it jumped to balance with the coil current by opening the PCS. This jump is, however, safe as long as it does not exceed the preset current. In the meanwhile, a small voltage is applied on the coils, which is too small to induce a quench.

6. By lowering the preset voltage, the magnet was deexcited. Meanwhile, the CV mode was maintained until the end. This deexcitation should be gradual enough not to induce a quench, since the magnet generates heat by the eddy current again.

Figures 5.10 and 5.11 show the traces of an excitation and a deexcitation, where we show the voltage on the coils and the PCS heater, the supplied current, the strength of the magnetic field at a Hall sensor, and temperatures of the coils and the PCS.

5.2.6 Field stability

The persistent current can decay only by the residual resistivity of the magnet. It is controlled well and we observed no evidence of damping of the magnetic field during the measurement. Therefore, we assumed the magnetic field to be constant over time in the analysis.

5.3 Telescope mount

5.3.1 Mechanical description

The telescope mount supports the vacuum vessel in which the magnet is enclosed, and directs it to the aimed direction. Since the acceptance of the detector is very narrow especially when the gas container is installed in the bore of the magnet, the telescope mount should direct the detector toward the sun accurately. We chose the altazimuth design over the equatorial design. The equatorial design is common in small astronomical telescopes. It benefits from simple control of motion by rotating the helioscope around a fixed axis parallel to the axis of the Earth. In the altazimuth design, on the other hand, the helioscope is supported like a seesaw on a turntable. The elevation angle is determined by the inclination of the seesaw and the azimuthal angle is determined

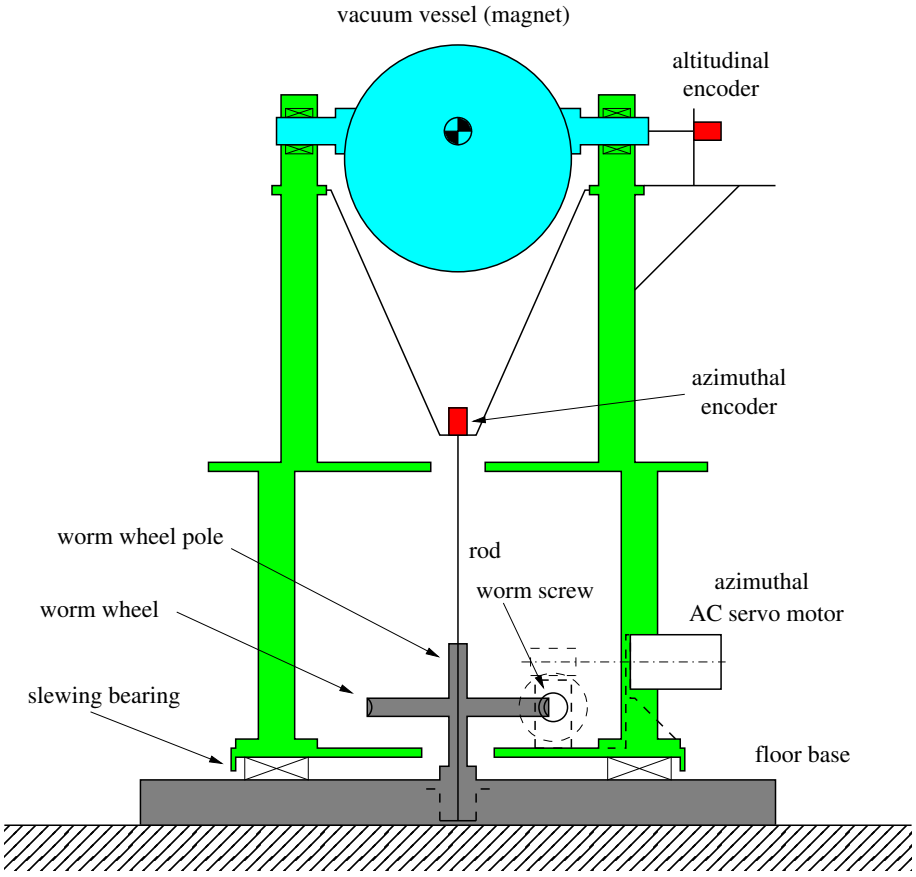

Figure 5.12: Mechanical structure of the telescope mount. Each shaded area corresponds to each co-moving structure. The gray area is fixed on the floor. The green area is the turntable which can rotate horizontally. The cyan area is the telescope body. Two encoders (red) are mounted on the turntable (green), and their axes are connected to the floor base and to the vacuum vessel, respectively. The turntable rotate itself by driving the worm-screw with the AC servo motor (white) against the fixed worm-wheel.

by the rotation angle of the turntable. In our helioscope, the limiting factor is that the inclination of the GM refrigerators should be less than $\pm 30^\circ$ during operation for them to perform normally. It is easier to control the inclination as desired in the latter design. Although the motion in the azimuthal- and altitudinal coordinate is not as trivial as the rotation around the axis of the Earth, it is easily worked out by the computer controlled system.

The trackable range of altitude was restricted to $\pm 28^\circ$ to fulfill the limitation of the GM refrigerators with a margin. There was no limiting factor to the azimuthal range, however, it was restricted to one rotation by installing a limiter switch which prevents the helioscope from endless rotation. This range corresponds to an exposure time of about a half of a day in observing the sun in Tokyo, 35°N, 135°E. This is enough for this experiment, since background was measured during the rest half of a day.

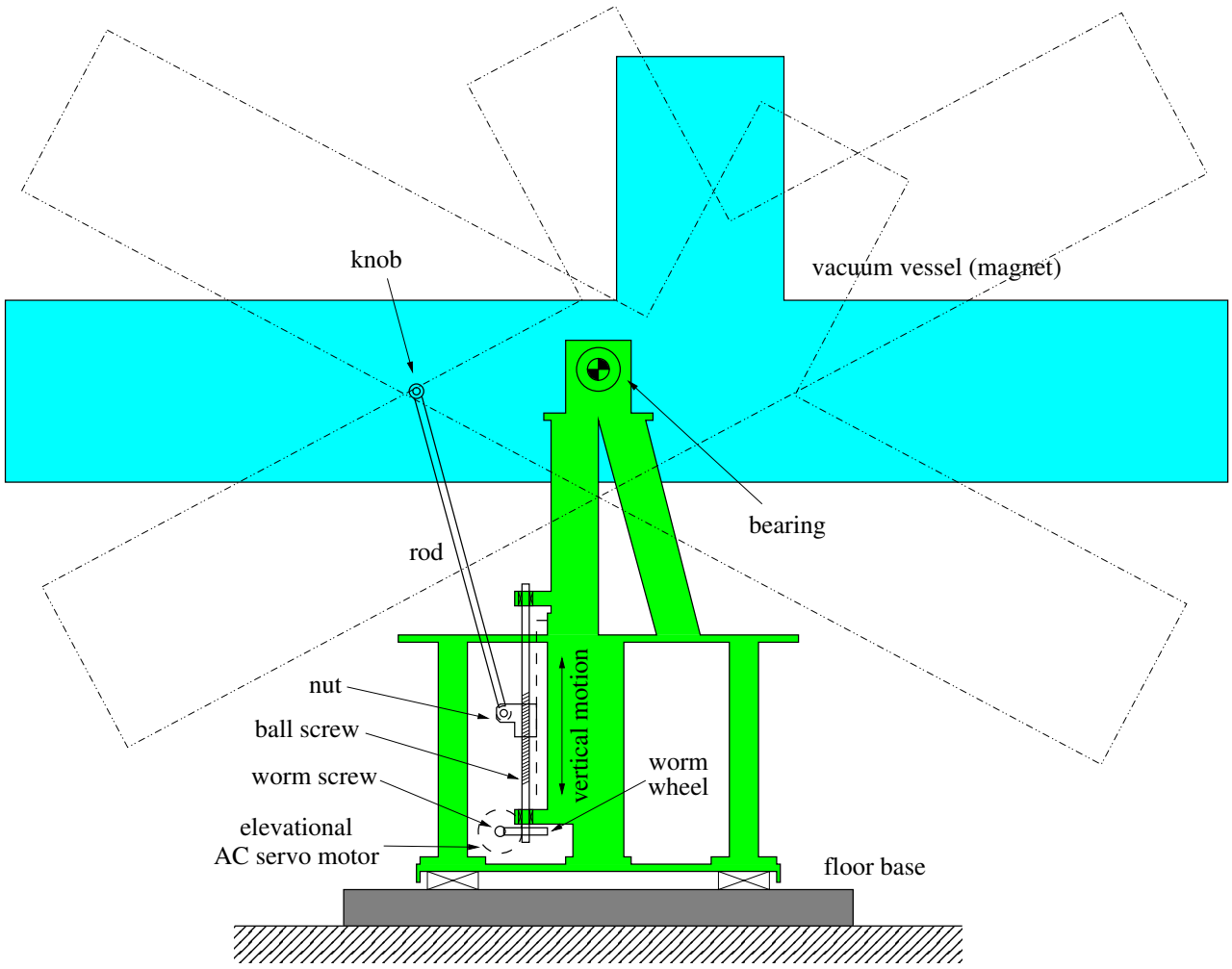

Figure 5.13: Mechanism to incline the helioscope body. The helioscope body can rotate around two bearings which are aligned coaxially in the horizontal direction (the depth direction in the picture). The ball screw driven by the AC servo motor (dashed circle) via a set of worm gear makes a vertical motion of the nut. The triangle of the bearing axis, the nut, and the knob on the vacuum vessel defines the angle of inclination.

Figures 5.12 and 5.13 illustrate the mechanical design of the telescope mount. The turntable can rotate against the ground to the horizontal direction by an NSK 685DBS261y slewing bearing placed between the rotating base and the floor base which is fixed on the ground. The inner diameter of the slewing bearing is 685 mm, and its outer diameter is 889 mm. It had also an external gear though we did not use it for the motion of the turntable as described below. The helioscope body or the vacuum vessel of the magnet is then supported horizontally by two radial ball bearings on the turntable. Their axis is displaced from the center of the main cylinder to go through the barycenter of the helioscope body.

The helioscope mount is driven by two AC servo motors controlled by a computer (PC). Hitachi EPS8 and EPL3TD AC servo motors are used for the azimuthal and elevation motion, respectively. The AC servo motors are preferable since they can rotate smoothly at slow speed, e.g., while tracking a celestial target, and can also rotate at high speed with high torque, e.g., when switching from west to east or east to west. The above motors operate up to 4000 RPM (rotations per minute) at the maximum speed and up to 3000 RPM without decrease in peak torque.

The rotation of the azimuthal motor is reduced by 2400:1 with two-stage worm gears. The final worm-wheel is fixed to the ground through a worm-wheel post of 45 mm in diameter, so that the whole turntable rotates around the post as the motor rotates. The rotation of the elevation motor is also reduced by 60:1 with a single stage worm gear. The rotational motion is then changed to a vertical linear motion by a ball screw and a linear guide. A stainless steel rod joining the nut of the ball screw and a knob on the vacuum vessel is fixing the angle of inclination. The worm gear here is preferable because of its self-locking feature. Since the worm-wheel cannot drive the worm-screw due to the friction, the helioscope stands still even after the motor is powered off.

The azimuthal- and altitudinal angles of the helioscope was monitored by two precision rotary encoders, Canon R-1L Laser Rotary Encoders, whose angular resolutions are 1/324000 rotation or 1.9×10^{-5} radian and their accuracy is better than 20".

The azimuthal encoder is mounted on a V-shaped bridge connecting the two bearing blocks on top of the turntable which hold the vacuum vessel (Fig. 5.12). The shaft of the encoder is fixed to a ϕ6-mm stainless steel rod which is fixed directly on the floor base. Although this rod is co-axial with the ϕ45-mm worm-wheel post, it is going through a bore in the post in order to escape the torsional strain of the post. The altitudinal encoder is mounted on top of the turntable, and its axis is connected to the vacuum vessel through one of the bearing blocks.

The axis of the helioscope was defined by two cross hairs placed on the edges of the vacuum vessel at both ends. Since the rotary encoders only tell us their rotation angles, we need to know their origins. To determine the altitudinal origin, we placed a theodolite in line with the cross hairs, and measured the vertical angle between the helioscope axis and the spirit level on the theodolite. Assuming the setting accuracy of 10" of the spirit level as well as the reading accuracy of 10" of the theodolite, we estimated the angular error of the altitudinal origin of the helioscope as $\delta\theta_{\mathrm{altitude}} = 7 \times 10^{-5}$ radian. The azimuthal origin was determined from the observed direction of Polaris (α-UMi) outdoors. The sun or Polaris are not directly visible from the experimental site on the basement floor. The true north direction was introduced to the experimental site

with the theodolite successively until the theodolite could be placed in line with the cross hairs. In order to minimize azimuthal error involved in this transfer of the origin, multiple reference points were arranged in line between the first point of stellar observation and the helioscope. In addition, we ensured enough distances from each other among the reference points as well as the cross hairs of the helioscope to minimize the effect of the positional error of the theodolite. From the multiple measurements of the mutual angles, we concluded that the angular error of the azimuthal origin at the helioscope was consistent with $\delta\theta_{\rm azimuth} = 7 \times 10^{-5}$ radian.

We measured the amount of pitching of the turntable associated with the motion of the telescope by placing a precision spirit level on the turntable. The turntable is equipped with four leveling blocks at its corners of the floor base, and level of the turntable was optimized by adjusting them. For the residual pitching, a correction was made to the estimated altitudinal direction of the helioscope as a function of azimuthal- and altitudinal angles read from the encoders, although it was already negligibly small. A third order Fourier series was employed as the correction function of the azimuthal rotations and a linear function was used for the elevation motions. They were fit to the measured data by a least squares method. Before correction, the residual pitching of the turntable was as small as 0.28 mrad for the azimuthal rotations and 0.24 mrad for the elevation motions at peak-to-peak. After correction, the residue was 16 μrad (RMS) and 6 μrad (RMS) for the azimuthal- and elevation motions, respectively. By adding them in quadrature, we get $\delta\theta_{\rm altitude} = 1.7 \times 10^{-5}$ radian.

The telescope mount was first built and installed by Nichirei Seiki Kogyo. It needed some rework of parts afterward and we needed to develop some compensation parts for it to work reliably.

5.3.2 Motion control

Figure 5.14 shows the block diagram of the motion control system. Pulses from the rotary encoders are accumulated in two pulse counters in a home-made CAMAC module. The CAMAC bus and its crate controller are shared with the data acquisition system which collects waveform data from the X-ray detector. The counts are read by the PC every 100 ms, and the topocentric directions of the helioscope are calculated from them. In parallel with the motion control of the helioscope, the direction information is recorded to the storage in the PC at intervals every second.

The AC servo controllers are responsible of supplying power to the AC servo motors as well as of setting their rotational angles according to the number of pulses they received. The host computer controls the azimuthal- and elevation AC servo motors through two independent home-made pulse generator CAMAC modules. Each pulse generator sends out a specified number digital pulses continuously at a specified rate. In this manner, once a speed and a number were set by the host computer, each AC servo motor runs at a constant speed automatically until all the pulses are sent out. The pulse generator modules have also some communication registers to get and set the internal states of the AC servo controllers.

As a safety measure, limiter switches to restrict the movement of the helioscope are connected to the home-made pulse generators. The switch circuit was divided into two independent loops corresponding to the azimuthal- and

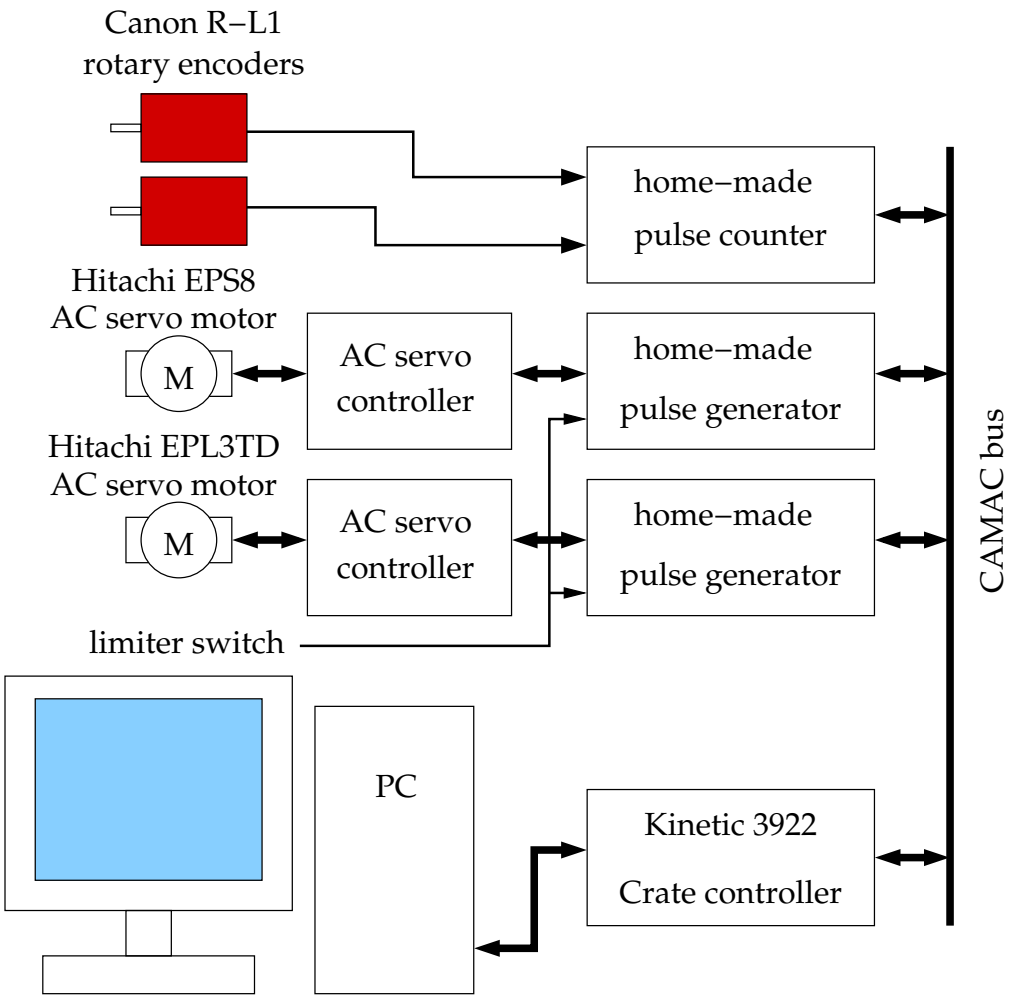

Figure 5.14: Block diagram of the motion control system.

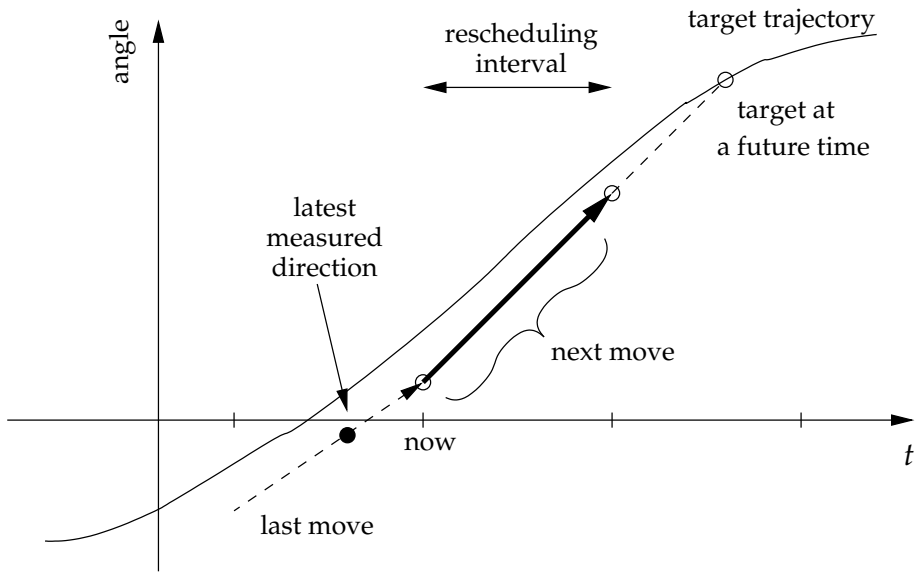

Figure 5.15: Tracking algorithm. The target direction at a point of time in the future is given externally to the motion control program and it is updated regularly while the helioscope is tracking a moving object. The motion control program tries to chase this target.

elevation motions. All the switches are set "normally-on." If a pulse generator detects a circuit break in the loop, it immediately stops the motor which is under its control and get into a trip state. Any intervention by software is intentionally and strictly excluded from this process.

In the host computer, control is carried out individually for the azimuthal- and elevation motions. The angle and the speed for the next short interval are calculated repeatedly based on the latest measured direction of the helioscope and the target direction at a point of time in the immediate future. Figure 5.15 illustrates the tracking algorithm. The target direction is given externally from a separate program which calculates the future positions. The motion control program tries to chase this future target. Therefore, the time length of the prediction acts approximately as the time constant of the motion control during tracking an object. This time length was set to 8 seconds. In addition, both rotational speeds and accelerations are restricted to a safe range. Hence, if the target is far from the current direction, the helioscope starts with a constant-acceleration motion, then keeps the maximum speed until the target get near, decelerates at a constant-acceleration, and catches it exponentially. The interval of rescheduling was set to 1 second at first, but it was later shortened to 0.2 second expecting a smoother motion.

To compute the number of pulses as well as its rate, we need a model of motion, i.e., the expected helioscope direction as a function of the number of pulses sent to the motors. In the static limit, it can be rough as far as the feedback gain is negative. The tracking error of the helioscope would converge to zero, since we are feeding back the measured errors to the motions. In a dynamic context, however, the model of motion should be accurate enough.

Otherwise, errors in the motion model would appear as the tracking error.

The model for the azimuthal angle is trivial. From the number of pulse per rotation of the AC servo motor and the reduction ratio of the worm gear system of the azimuthal motion, it is

$$\theta_{\rm azimuth} = 2\pi n_{\rm pulse,elevation}/N_{\rm ppr}, \tag{5.1}$$

where $N_{\rm ppr} = 7200000$, and $n_{\rm pulse,elevation}$ is the number of pulses sent to the elevation motor controller.

As the model for the elevation motion, we used the joint model shown in Fig. 5.16. Then we find for the (x, y) coordinate of point B as

$$\begin{aligned} x &= x_0, \\ y &= -L_2 \sin(\theta_{\rm altitude} + \beta) - \sqrt{L_1^2 - (x_0 + L_2 \cos(\theta_{\rm altitude} + \beta))^2}, \end{aligned} \tag{5.2}$$

where x_0 is the constant x-coordinate along the linear guide. The mechanical parameters, L_1, L_2, β, and x_0 are listed in Table 5.2. Therefore, the angle of inclination is given by solving the following formula,

$$\begin{aligned} P n_{\rm pulse,altitude} + y_0 + L_2 \sin(\theta_{\rm altitude} + \beta) \\ + \sqrt{L_1^2 - (x_0 + L_2 \cos(\theta_{\rm altitude} + \beta))^2} = 0, \end{aligned} \tag{5.3}$$

where $n_{\rm pulse,altitude}$ is the number of pulses sent to the altitudinal motor controller and $y_0 = -L_2 \sin\beta - \sqrt{L_1^2 - (x_0 + L_2 \cos\beta)^2}$. The overall pitch $P = 1/18000\,{\rm mm}/pulse$ comes from the pitch of the ball screw divided by the number of pulse per rotation of the AC servo motor and the reduction ratio of the elevation worm gear.

The U.S. Naval Observatory Vector Astronomy Subroutines (NOVAS) [91] were used to calculate the solar position. For the earth orientation parameter $\Delta T = {\rm TT} - {\rm UT1}$, we interpolated data from IERS Bulletin A provided by the IERS Rapid Service (USNO, Washington) [92].

The clock of the host computer is adjusted by Network Time Protocol version 3 (NTPv3) [93] synchronizing to a stratum 1 time server in the University of Tokyo. This time server is highly accurate by synchronizing itself to the global positioning satellite (GPS) signal. The NTP daemon[1] adjusts the system clock in small steps so that the timescale is effectively continuous. The estimated accuracy of the clock can be obtained from the NTP daemon, which was usually less than one millisecond and was several milliseconds at worst. This value is negligibly small, since ten milliseconds of error in time corresponds only to $\delta\theta \sim 7 \times 10^{-7}$ radian in solar direction.

5.3.3 Tracking accuracy

The tracking accuracy of the motion control was measured by actually tracking the sun. In Fig. 5.17, we show the measured direction of the helioscope and the deviation from the calculated position of the sun. We observed no evidence of systematic deviation. The root mean squared (RMS) error during a steady tracking period was $\delta\theta_{\rm azimuth} = 6.6 \times 10^{-6}$ radian and $\delta\theta_{\rm altitude} = 6.1 \times 10^{-6}$ radian.

[1] Daemons are a group of software programs which run in background and serve the system for housekeeping works.

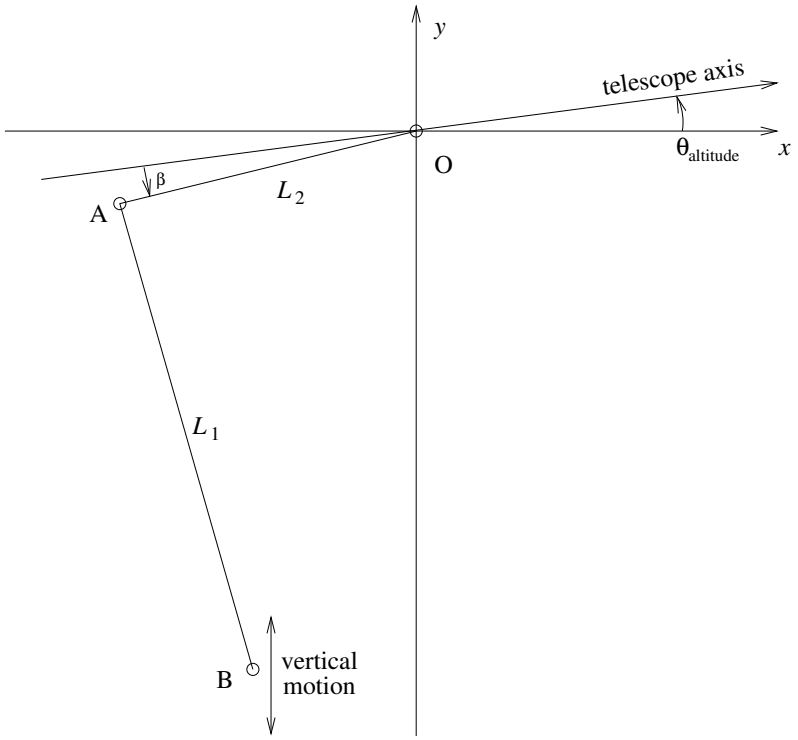

Figure 5.16: The model for the elevation motion of the telescope. Rotating joints/bearings are: O: the center of the elevation motion of the telescope, A: the ball joint on the telescope body, and B: the lower pivot on the vertical moving carriage.

parameter	value	unit
L_1	806	[mm]
L_2	$\sqrt{500^2 + 58^2}$	[mm]
$\tan\beta$	58/500	
x_0	-272.5	[mm]
pitch of ball screw	5	[mm]
worm gear ratio	1:60	
motor pulse per rotation	1500	

Table 5.2: Mechanical parameters in the joint model in Fig. 5.16

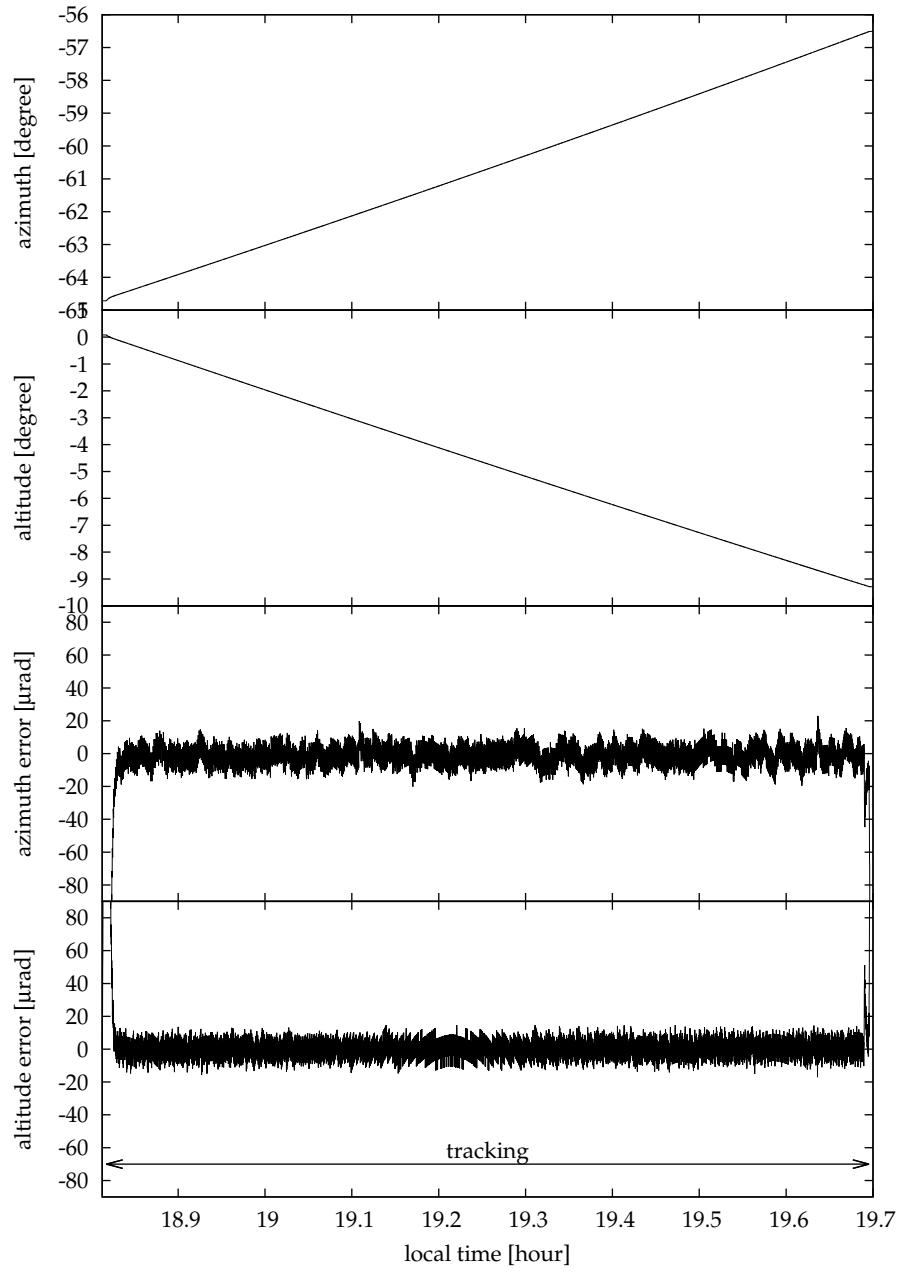

Figure 5.17: Demonstration of the tracking accuracy where the helioscope actually tracked the sun sinking under the horizon.

direction	source of error	estimate [mrad]
azimuth	accuracy of encoder	< 0.10
	origin (north direction)	0.07
	rolling by elevation motion	< 0.05
	motion control	0.0066
	precision of time	< 0.0007
altitude	accuracy of encoder	< 0.10
	origin (level)	0.07
	pitching of the turntable	0.017
	motion control	0.0061
	precision of time	< 0.0007

Table 5.3: Sources of tracking error. The inequality signs indicate that the values are the upper limits.

In Table 5.3, we summarize the sources of the tracking error. One yet undescribed origin is the rolling of the helioscope toward the azimuthal direction by the elevation motion, which is caused by the imperfectness of the level of the horizontal axis on the turntable. Here, we used the value measured in past times. All the estimated errors were much smaller than the size of the axion source, $\delta\theta_a \sim 1\,\mathrm{mrad}$.

5.4 X-ray detector

In this section, we will describe the PIN photodiode array, the preamplifiers attached to it, and the data acquisition system. The radiation shielding which surround the X-ray detector and the calibration source which is placed inside the vacuum vessel are also described here. The obtained signals and their analysis will be discussed elsewhere.

5.4.1 PIN photodiode

An array of sixteen silicon PIN photodiodes is used as the X-ray detector as shown in Fig. 5.18. Silicon PIN photodiodes are suited for this application because:

- They are sensitive to X-rays from a few keV to 10 keV which matches to the solar axion energy spectrum. On the other hand, they are relatively insensitive to background γ-rays of higher energies. However, proper shielding is necessary since such high energy photons form a continuous background by the Compton scatterings.

- They can be operated at cryogenic temperature. As we will see in the later section, this feature helps us to make the system compact. By operating the X-ray detector at sufficiently low temperature, the X-ray detector can be put inside a single cryostat which houses the superconducting magnet and the gas container without additional thermal radiation shielding between them. Gaseous detectors are often used for soft X-ray detection, but they do not possess this virtue.

- They are quite insensitive to magnetic field.
- They have large area-to-cost ratio compared to Ge(Li) or Si(Li) detectors. They are commercially available at relatively low prices and in various sizes and shapes. It is much easier for PIN photodiodes to make a large area detector.
- High purity silicon is a material which is well known for its extremely low content of radioactive elements such as uranium and thorium.

In the course of developing the X-ray detector, two problems arose. A commercial production PIN photodiode, Hamamatsu S3590-06, is mounted in a windowless ceramic case. It turned out that the ceramic used in the case contained 10^{-3}–10^{-2} Bq of radioactive impurities uranium and thorium chain, and β rays from it constituted a continuum in the background spectrum. The ceramic case causes another problem that it shades a part of photodiodes on its back by adding an extra frame around the photodiode chip. Therefore, we used custom PIN photodiodes, Hamamatsu S3590-06-SPL, one of which is shown in Fig. 5.19. A PIN photodiode chip with a area of $11 \times 11\,\mathrm{mm}^2$ and thickness of $500\,\mu$m is mounted on a $300\,\mu$m thick polyimide (Kapton) substrate with silver-filled conductive adhesive.

Downside of using a Kapton substrate is that it has a larger thermal expansion than silicon, which would generate a large force to crack the silicon chip by thermal contraction. In order to prevent the silicon chip from destruction, each Kapton-based PIN photodiode is glued on a Super Invar steel plate with Nitofix SK 230 epoxy resin. Super Invar steel has as small thermal expansion as silicon and large Young's modulus. The Super Invar steel plate is then screwed on an L-shaped acrylic base with brass bolts and spring washers by two threaded holes (ISO M2) on its back as shown in Fig. 5.20. The thermal contraction of the acrylic base is escaped and will not affect the PIN photodiode chip. This acrylic base provides moderate thermal isolation between the copper cold finger at 60 K and the preamplifier cold head which performs best at 130 K. Since the Phase I measurement, a remarkable progress was achieved by a collaborator T. Namba in stabilizing PIN photodiodes against the thermal stress. In fact, all of the sixteen photodiodes worked throughout the Phase II measurement. In contrast, only nine out of sixteen survived in the previous measurement.

Another problem with the X-ray detector was microphonic noise by the vibration of the helioscope which is mainly caused by the back-and-forth motion in the Gifford–McMahon refrigerators. To reduce microphonic noise, connections between the PIN photodiodes and the front-end circuits are kept as short and rigid as possible. In addition, all the parts of the front-end circuit were molded with Stycast 1266 epoxy resin filled with #250-mesh silica (SiO_2) powder with a weight fraction of 55% to prevent vibration in them. This fraction was determined to make its overall thermal expansion comparable to the parts in the mold.

Finally, the remaining microphonic noise was eliminated by recording the waveforms of each event and then by applying numerical pulse shaping to them.

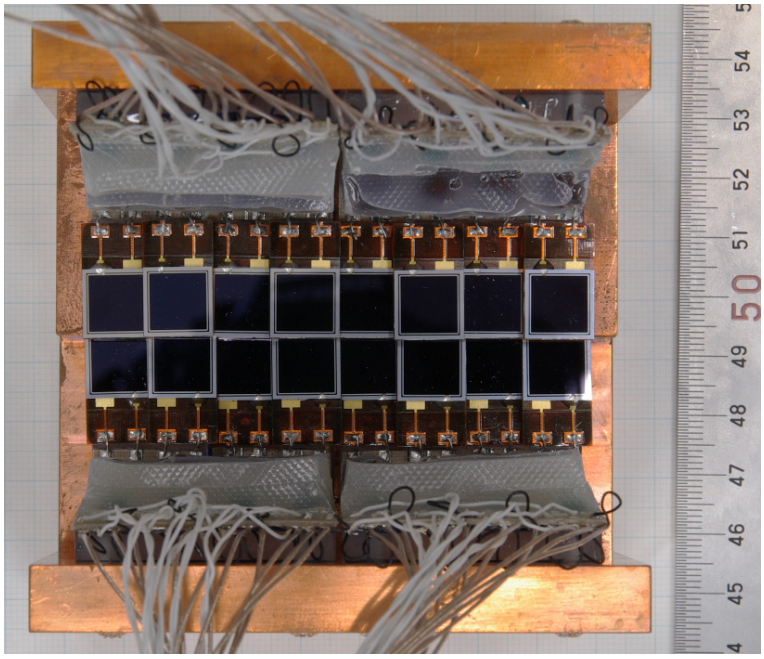

Figure 5.18: The array of the sixteen PIN photodiodes seen from the incident direction. The figures marked on the scales are in millimeters.

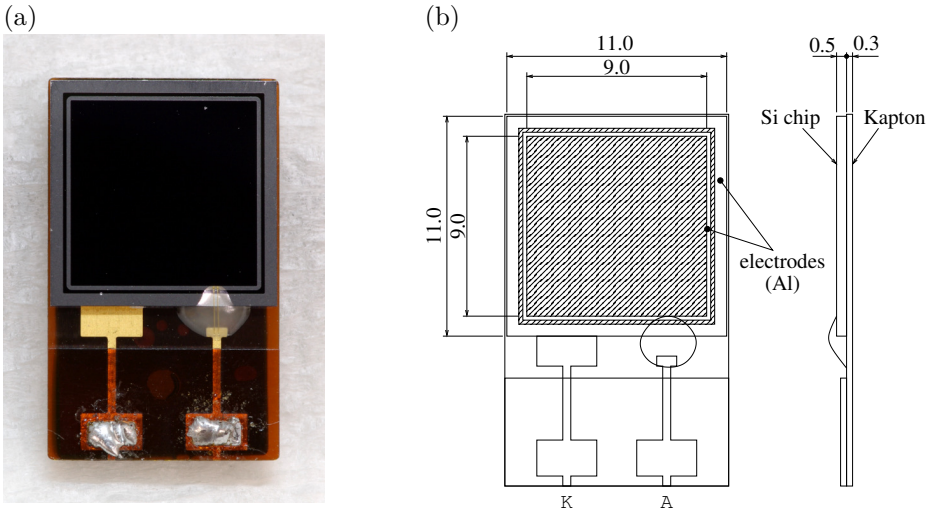

Figure 5.19: (a) Photograph of a Hamamatsu S3590-06-SPL, Kapton based PIN photodiode and (b) its dimensions.

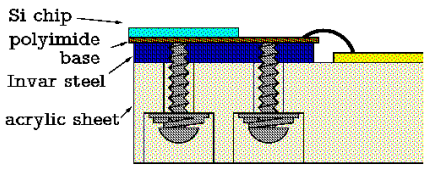

Figure 5.20: PIN photodiode mounted on an Invar steel plate. (Drawing from Ref. [84])

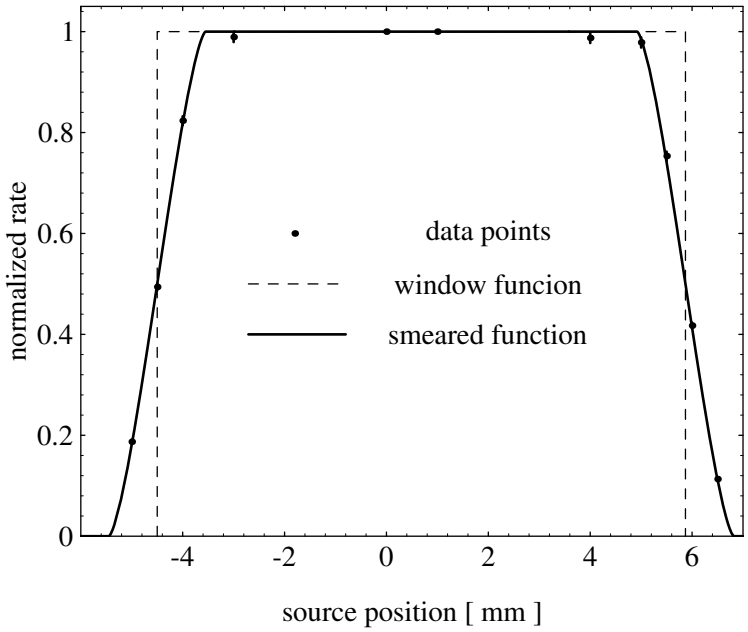

Figure 5.21: Position dependence of the detection efficiency of a S3590-06 PIN photodiode against 5.6-keV X-rays. Data points are shown in points and error bars. The efficiency is normalized at the center point. The solid line shows the best fit function, and the dashed line shows the original unsmeared 'window' function implied by the fit function. (Drawing from Ref. [94])

5.4.2 Measurement of effective area of a PIN photodiode

Each PIN photodiode chip has aluminum electrodes along the four sides on its surface, and the $9 \times 9\,\mathrm{mm}^2$ area inside the electrodes is nominally sensitive to visible light. As an X-ray detector, however, information about its effective area is not officially provided. We measured it by using a collimated ^{55}Fe X-ray source mounted on a micrometer. The source was moved along the center line of the PIN photodiode and the count rate was measured as a function of the source position. Figure 5.21 shows the relative efficiencies, where measured data points are shown in points and error bars. We fit them with a rectangular-shaped 'window' function which was smeared reflecting the circular spot of

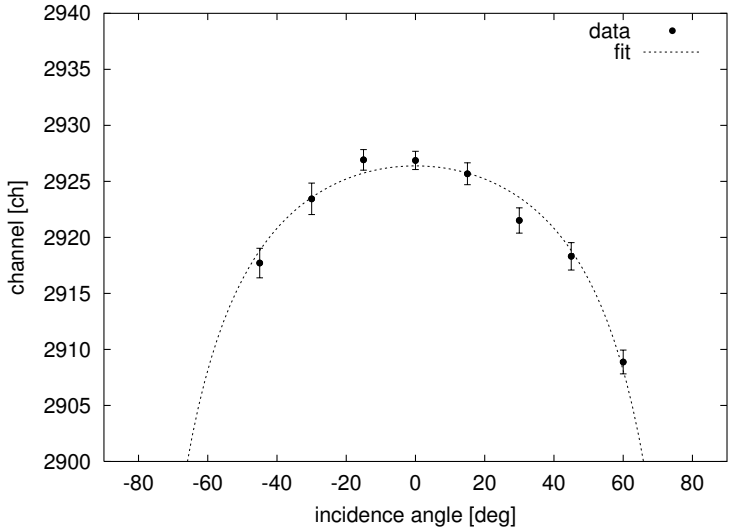

Figure 5.22: Pulse height by α-particle impingements on a PIN photodiode as a function of the incident angle. (Drawing from Ref. [95])

X-rays. Efficiency was assumed to be constant inside the window, and zero outside the window. The absolute efficiency inside the window was measured elsewhere. The solid line shows the best fit function, and the dashed line shows the original unsmeared window function. We found the best fit window width to be 10.4 mm, which showed that not only the $9 \times 9\,\mathrm{mm}^2$ area inside the electrode but also some portion of the underlying layer beneath the aluminium electrode is sensitive to X-rays of 5.6 keV. We conservatively adopted the $9 \times 9\,\mathrm{mm}^2$ area inside the electrode as the estimated effective area.

In the PIN photodiode array, the photodiodes were arranged 3-dimensionally so that they overlapped each other on their electrodes.

5.4.3 Measurement of insensitive layer of a PIN photodiode

There is an insensitive surface layer so-called 'the dead layer' on the detector surface. It consists of the SiO_2 layer as the protective surface and the underlying p^+-layer which would not be depleted. The thickness of the dead layer of an S3590-06 PIN photodiode was measured by making α-particles from an ^{241}Am source impinge on the PIN photodiode in various incident angles [95]. Since respective path lengths of α-particles in the insensitive and sensitive layers depend on their incident angle, the thickness of the insensitive layer can be estimated by measuring pulse heights of α-particles in the PIN photodiode as a function of the incident angle. The range for the 5.486-MeV α-particle in silicon is 24 μm which is much less than the thickness of the PIN photodiode.

We measured spectra for 8 incident angles: 0°, ±15°, ±30°, ±45°, and 60° using a multichannel analyzer (MCA). Figure 5.22 shows the peak channels for the incident angles, where the y-axis denotes the MCA channel number C [ch] which is related to the deposit energy E [keV] by a linear equation, $E = \alpha(C - \beta)$.

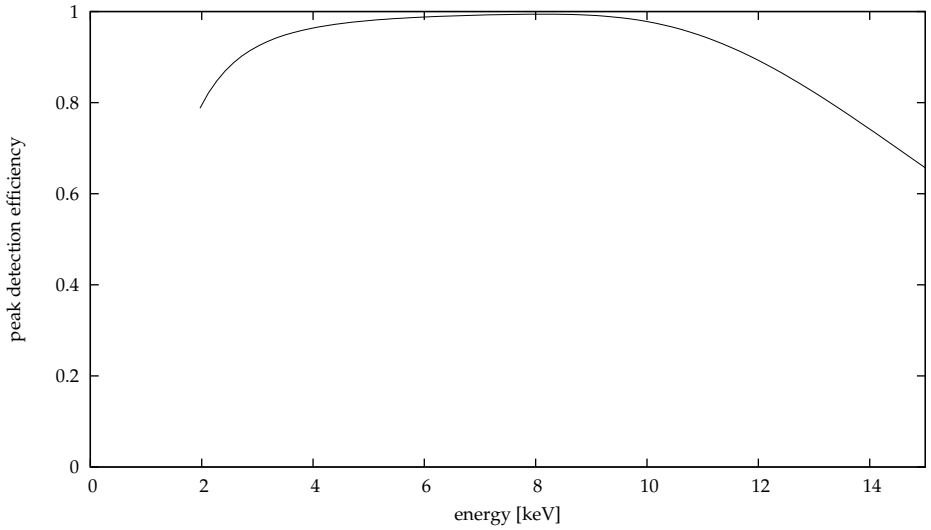

Figure 5.23: Estimated peak detection efficiency of the PIN photodiode.

Thus, data points which are shown as points and error bars are fit by the the following function,

$$C(\theta) = \frac{E_0}{\alpha} + \beta - \frac{1}{\alpha}\frac{\mathrm{d}E}{\mathrm{d}x}\frac{d}{\cos\theta} \tag{5.4}$$

where θ is the incident angle, d is the dead-layer thickness, $E_0 = 5.486\,\mathrm{MeV}$ is the initial energy of α-particles, and $\mathrm{d}E/\mathrm{d}x$ is the stopping power in Si or SiO_2. The best fit function is shown as the dashed line in the figure. We found the dead layer thickness to be $d = 0.31 \pm 0.02\,\mu\mathrm{m}$, if all the dead layer was assumed to consist of silicon. For SiO_2, we got 13% smaller value. The peak detection efficiency of the PIN photodiode within the effective area can be estimated by

$$\epsilon_{\mathrm{pin}} = e^{-\mu_{\mathrm{pe}}d}(1 - e^{-\mu_{\mathrm{pe}}D}), \tag{5.5}$$

where d is the dead-layer thickness, D is the depletion-layer thickness, and μ_{pe} is the photoelectric absorption coefficient. Figure 5.23 shows the estimated peak detection efficiency where the depletion-layer thickness of $D = 500\,\mu\mathrm{m}$ is assumed. We applied 130 V to PIN photodiodes to form full depletion. For the dead-layer thickness, we conservatively used the following upper limit at 95% confidence level

$$d < 0.35\,\mu\mathrm{m}. \quad (95\%\ \mathrm{CL}) \tag{5.6}$$

For the photoelectric absorption coefficient in silicon, we used the following approximation which was obtained by fitting an analytic expression to the data provided by National Institute of Standard and Technology (NIST) [79]

$$\mu_{\mathrm{pe}} \simeq \rho \times (a_0 + a_1 E + a_2 E^2)\left(\frac{E_K}{E}\right)^4 \frac{\exp(-4\xi\tan^{-1}\frac{1}{\xi})}{1 - e^{-2\pi\xi}}, \tag{5.7}$$

where $\xi = \sqrt{E_K/(E - E_K)}$, $E_K = 1.839\,\mathrm{keV}$ the K-edge energy, $\rho = 2.34\,\mathrm{g/cm^3}$ the mass density of silicon, and a_0, a_1, a_2 are model fit parameters: $1.67\ \times$

$10^5\,\mathrm{cm^2g^{-1}}$, $1.37 \times 10^4\,\mathrm{cm^2g^{-1}keV^{-1}}$, and $-6.57 \times 10^2\,\mathrm{cm^2g^{-1}keV^{-2}}$, respectively.

5.4.4 Measurement of geometry of X-ray detector

The positions of the PIN photodiodes were determined relative to the copper shielding box from a photograph taken prior to the installation. First, to know the view point relative to the shielding box, we fitted a 3-dimensional geometric model of the shielding box against the visible vertices of the copper plates in the photograph using the least squares method taking the optical perspective into account. Then, the lateral positions of the photodiodes as well as their in-plane rotating angles were determined relative to the shielding box by fitting the geometric model with photodiodes against the visible vertices or endpoints of the 0.2-mm-thick guard rings on them.

Figure 5.24 shows the original photograph, Fig. 5.25 shows the bird's-eye view of the geometric model, and Fig. 5.26 shows the reconstructed image of Fig. 5.24 from the best fit result.

5.4.5 Data acquisition system

The schematic diagram of the data acquisition (DAQ) system is shown in Fig. 5.27.

The charge pulses from the PIN photodiodes are amplified by home-made charge-sensitive preamplifiers, which are described in the next section. The output of the preamplifiers is digitized using flash analog-to-digital converters (FADCs), REPIC RPC-081's, with a sampling rate of 10 MHz. In parallel to it, each preamplifier output is fed to a shaping amplifier, Clear Pulse CP4026, whose output is bipolar shape with a time constant of 3μs. The output of each shaping amplifiers is then fed to a leading-edge discriminator, Technoland N-TM405, to generate triggers.

The impedance of the preamplifier outputs and the FADC inputs is $50\,\Omega$ matched to the coaxial cables connecting the preamplifier and the DAQ rack, and the input impedance of the shaping amplifier is $1\,\mathrm{k}\Omega$ which is high enough to be negligible.

The trigger signals set a latch in a CAMAC input/interrupt register, Hoshin C005. Then, all the FADCs are stopped at a time $50\,\mu$s after the trigger, and each FADC records waveform of 1024 words for $102.4\,\mu$s until it is stopped. Thus, waveforms of the sixteen preamplifier outputs are recorded simultaneously over $50\,\mu$s before and $50\,\mu$s after each trigger. The $50\,\mu$s delay and 10-MHz clock to the FADC are provided by a Technoland N-TM203, 100-MHz clock generator.

Although shaping amplifiers are used in the system, we use them only to generate trigger signals, and the energy information was obtained solely by an off-line analysis of the preamplifier waveform data. This is because the microphonic noise of the PIN photodiodes was severe and conventional shaping amplifiers did not performed good elimination against such low-frequency noise.

The thresholds of the discriminators were set so that each trigger rate would not exceed $0.1\,\mathrm{s^{-1}}$. The total average trigger rate was about $0.5\,\mathrm{s^{-1}}$ during the Phase II measurement. Precise live time was measured by counting pulses from a home-made 1-kHz clock with a Technoland C-TS 203 CAMAC 80-MHz scaler. The scaler and the trigger system are held by the latch in the input/interrupt

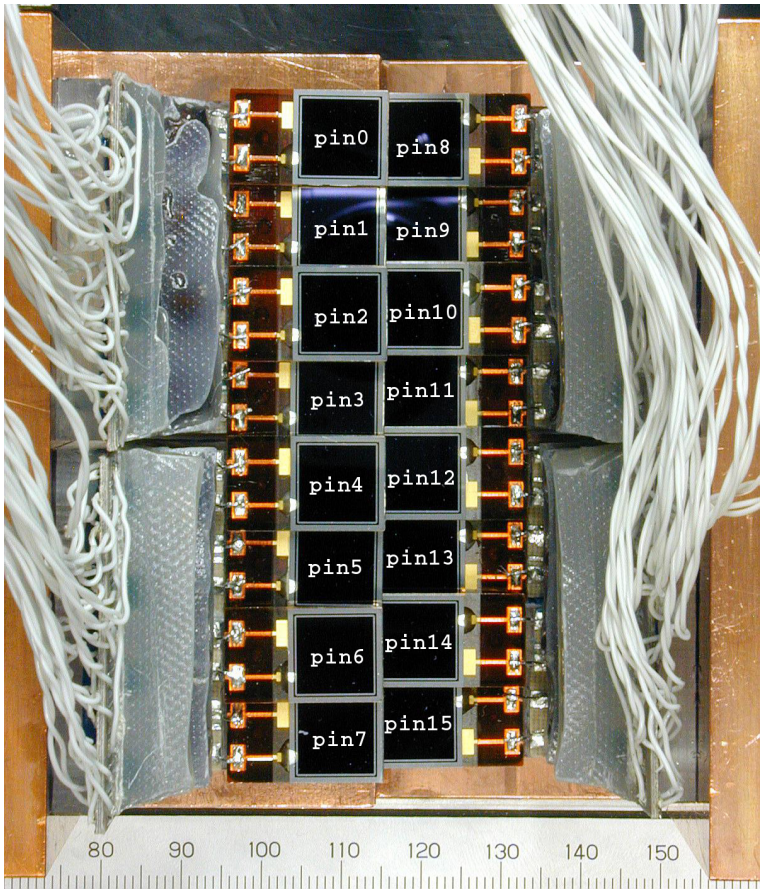

Figure 5.24: Photograph of the PIN photodiodes used to measure their positions.

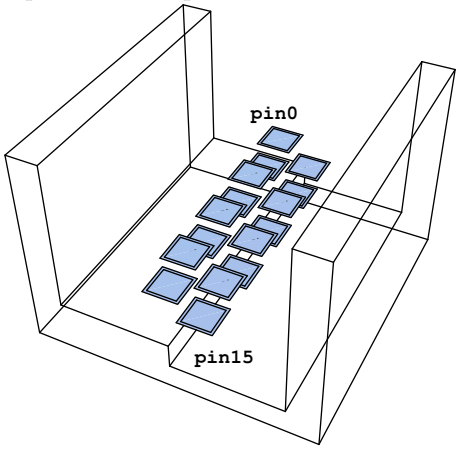

Figure 5.25: Wire-frame model of the copper shielding box used in the fitting. The reconstructed PIN photodiodes are shown together as the opaque squares.

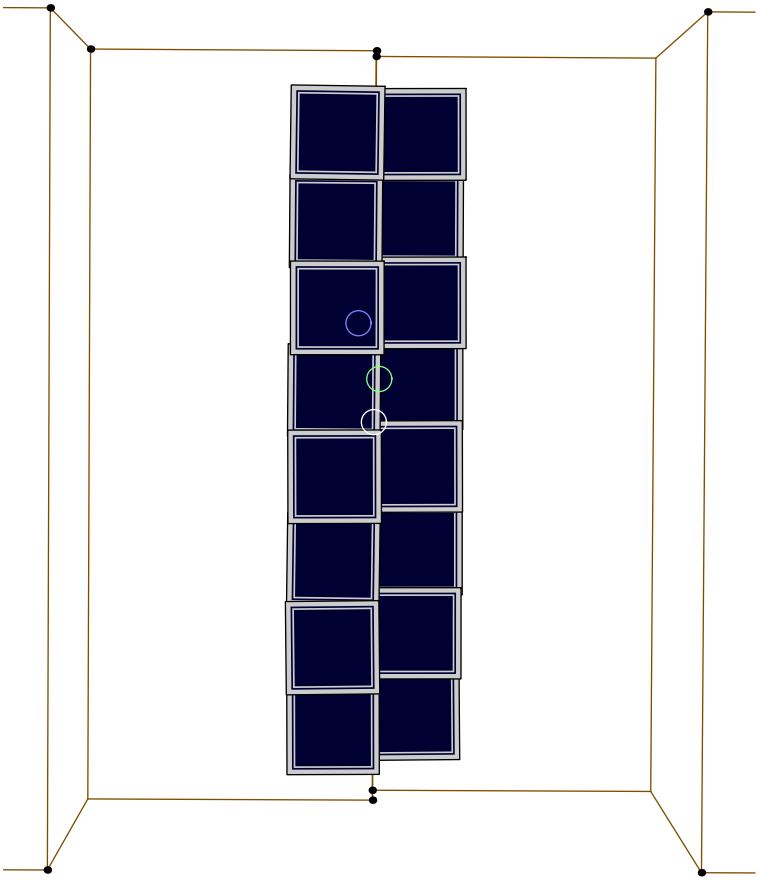

Figure 5.26: Reconstructed image of Fig. 5.24. The open white circle indicates the center of the copper box, the open light green circle shows the optical axis of the camera, and the open light blue circle shows the perpendicular foot on the xy-plane of the view point. The small black circles show the vertices used to determine the view point, the line of sighting, and the rolling angle.

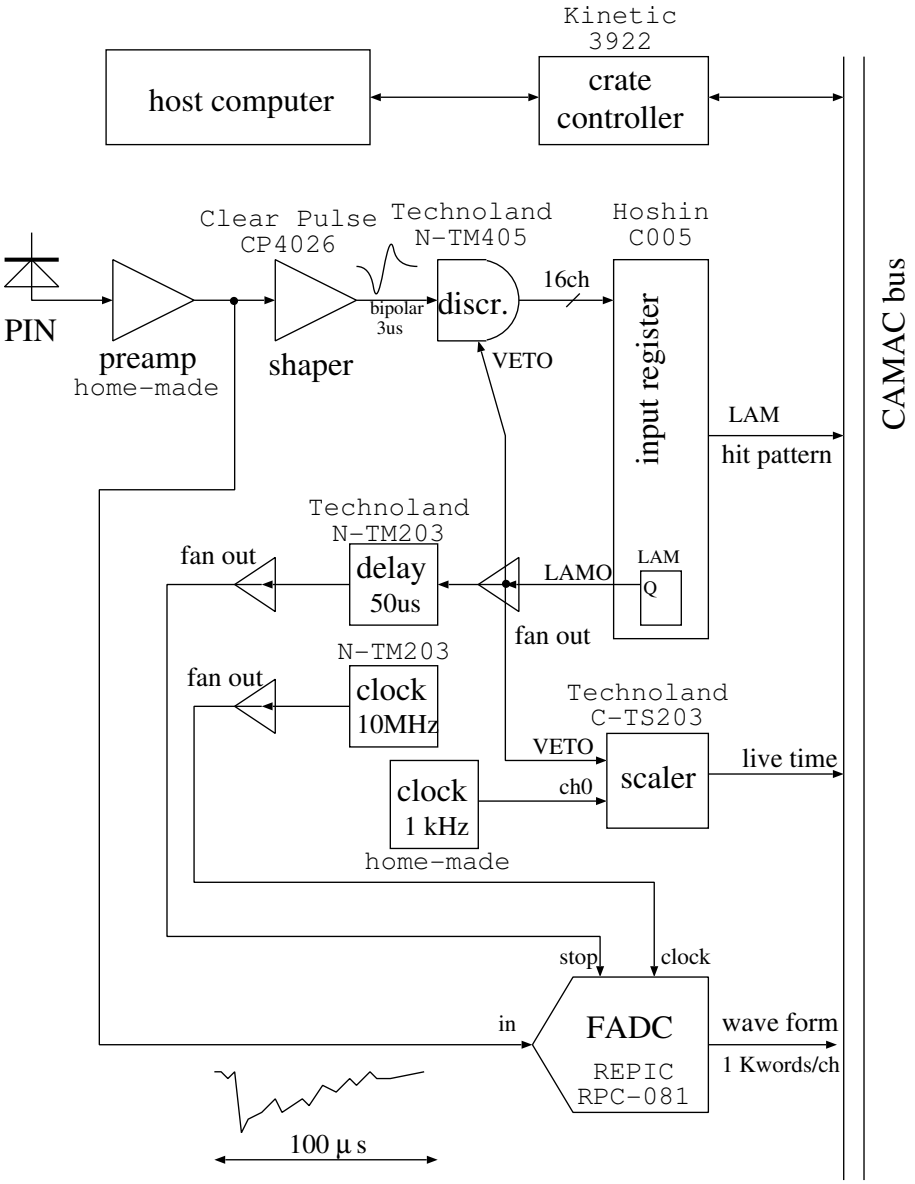

Figure 5.27: Data acquisition system for the X-ray detector.

register until the host computer finishes retrieving data, so that we will not see any latency of the host computer.

The FADCs can also be stopped from the host computer by software. We can obtain waveforms without trigger by this. This feature was used to obtain noise spectra in the preamplifier output, since we need them in the numerical pulse shaping.

5.4.6 Preamplifier

Description

Each preamplifier circuit consists of two parts: the first half is a low-noise charge-sensitive amplifier, and the second half is a linear amplifier named "booster" which adapts the voltage level to its succeeding data acquisition system.

The circuit diagram of the charge-sensitive amplifier is shown in Fig. 5.28. It consists of two parts. One is the "cold head" which is indicated as the area surrounded by a dotted box in Fig. 5.28. It includes a PIN photodiode, a first-stage junction field-effect transistor (JFET), a 5-GΩ feedback resistor, and a local high voltage buffer. It is placed in the copper shield whose temperature is about 60 K. The rest of the preamplifier is called the "back-end". It is placed at room temperature along with the booster amplifiers.

Among various components in a charge-sensitive preamplifier, the first-stage JFET contributes the most to the noise characteristic of the preamplifier. We used low noise JFETs, Hitachi 2SK291, at the first stage. They were selected out of many by their $I_{\rm DSS}$ or the drain current with the gate grounded.

Noise characteristics of discrete transistors disperse chip by chip. In order to obtain lower noise, transistors with larger transconductances g_m are preferred, since the equivalent noise charge (ENC) of an amplifier is given as follows [96]

$$({\rm ENC})^2 = \frac{e^2 k_{\rm B} T R_s C_{\rm in}^2}{2\tau} + \frac{e^2 k_{\rm B} T \tau}{2R_p}, \tag{5.8}$$

where $C_{\rm in}$ is the total input capacitance, R_s is the equivalent series resistance, R_p is the equivalent parallel resistance, and τ is a time constant representing the pulse shaping. We omitted some irrelevant components like $1/f$ noise. In our preamplifier,

$$C_{\rm in} = C_{\rm PIN} + C_{iss}, \tag{5.9}$$

where $C_{\rm PIN} = 30\,{\rm pF}$ is the capacitance of a PIN photodiode, and $C_{iss} = 8.5\,{\rm pF}$ is the input capacitance of the JFET,

$$R_p \simeq R_f, \tag{5.10}$$

where $R_f = 5\,{\rm G\Omega}$ is the feedback resistance, and

$$R_s \simeq \frac{1}{g_m}. \tag{5.11}$$

Among those of the same type, a transistor with larger $I_{\rm DSS}$ gave larger g_m consistently, and measuring $I_{\rm DSS}$ was much easier than g_m.

According to Eq. (5.8), operation at lower temperature is preferable. At too low temperatures, however, freeze out of the main dopant (increase of R_s)

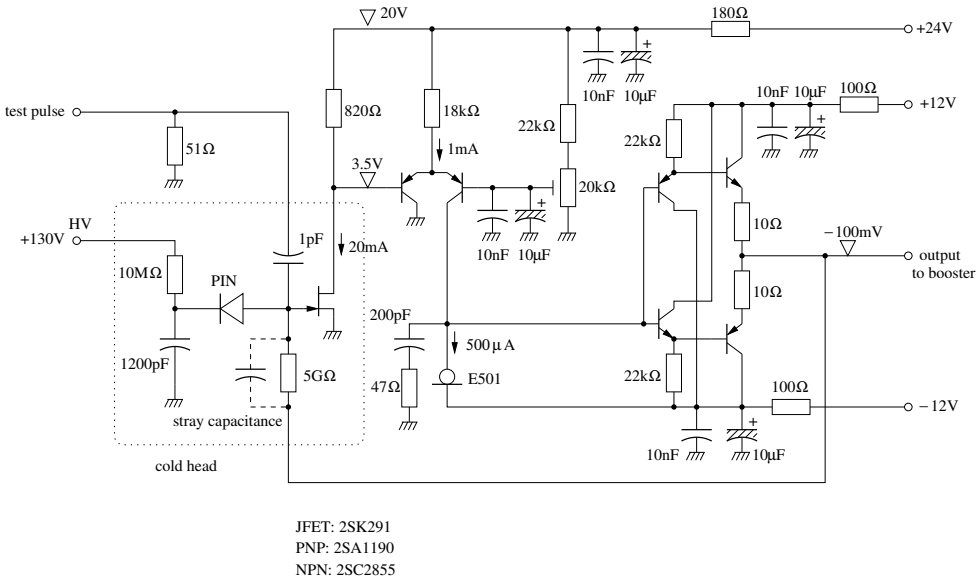

Figure 5.28: Circuit diagram of the charge-sensitive amplifier part of the preamplifier. Typical bias voltages and currents are indicated as triangles and arrows beside the wires, respectively.

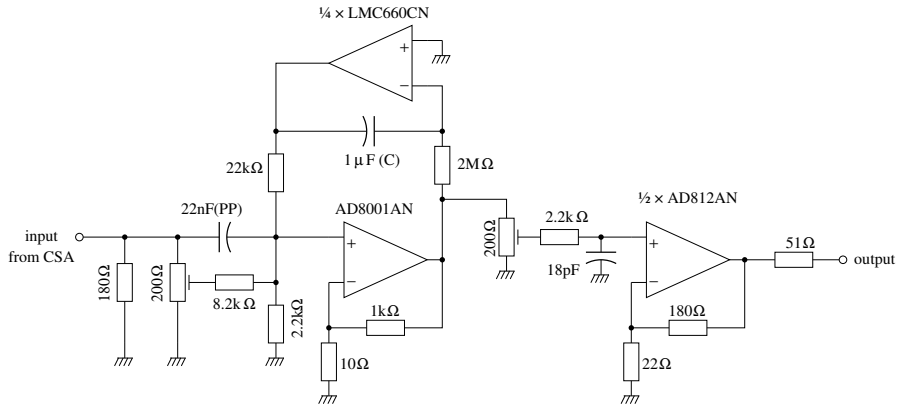

Figure 5.29: Circuit diagram of the booster part of the preamplifier.

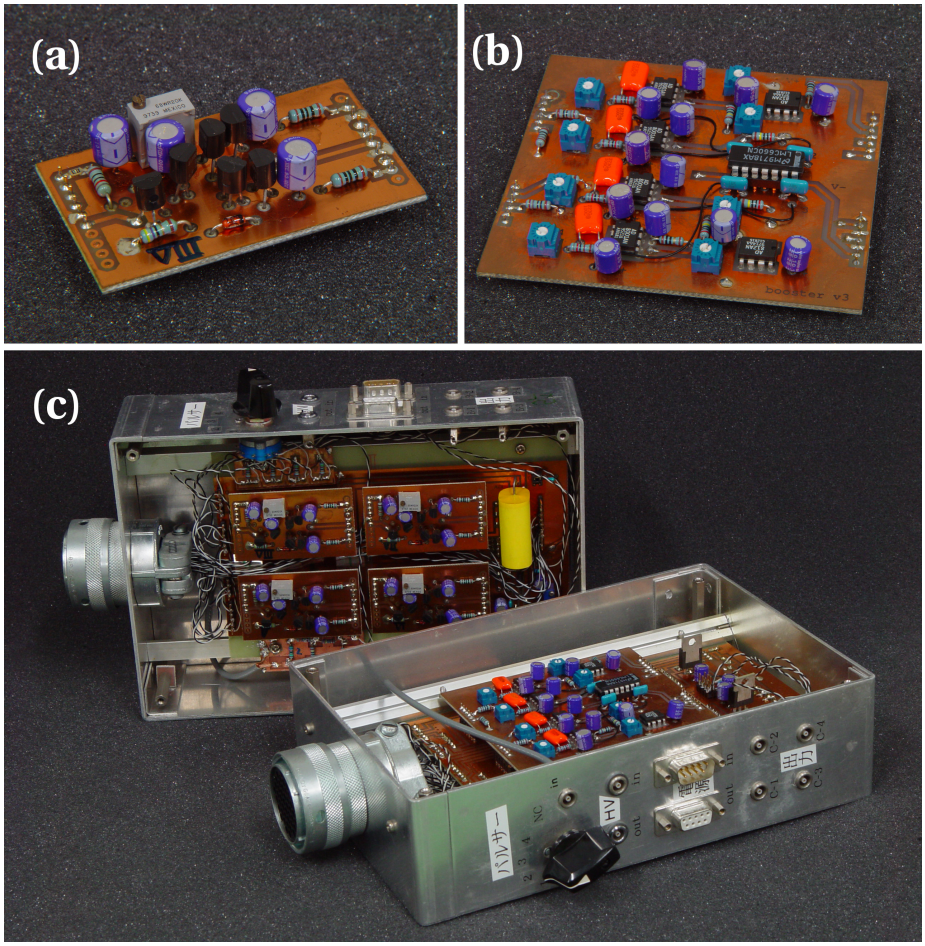

Figure 5.30: Photograph of (a) a charge-sensitive amplifier back-end card, (b) a booster amplifier card, and (c) preamplifier boxes. Four charge-sensitive amplifier cards are mounted on one side of the preamplifier mother board, and a booster card are mounted on the other side. The large yellow device on the mother board is the capacitor of the high-voltage buffer which protect the front-ends of the charge-sensitive amplifiers from a sudden rise/down/disconnection of the high-voltage.

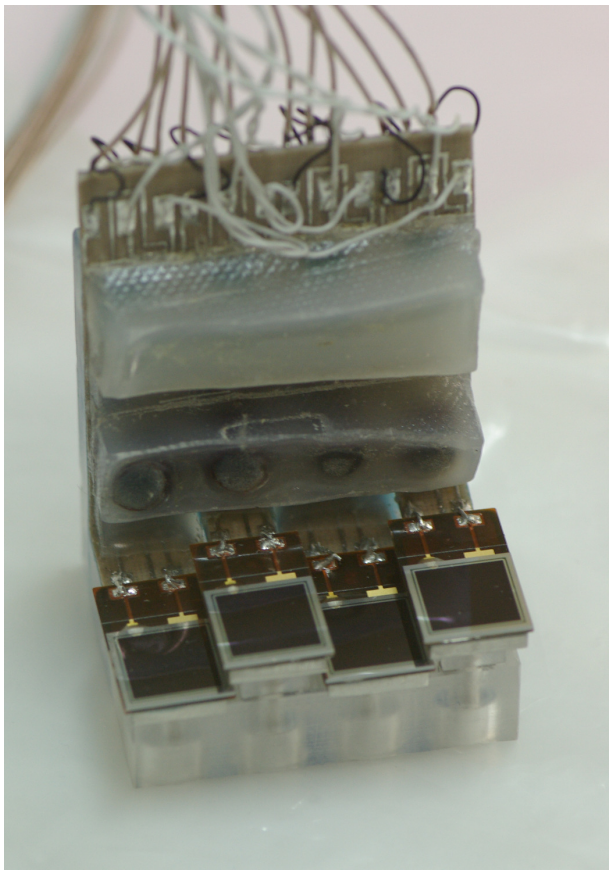

Figure 5.31: Picture of a PIN photodiode X-ray detector module. The cold head part of the preamplifier is molded in epoxy resin and is arranged perpendicular to the PIN photodiodes.

messes up the gain by T [97]. We kept each JFET at about 130 K by a heater made of a ϕ0.1-mm manganin wire wound around it.

The local high voltage buffer consisting of a 100 MΩ resistor and a 1200 pF polyester film capacitor eliminates foreign electric noise entering from the high voltage line.

Each PIN photodiode is DC coupled to the gate of the JFET. The advantage of the DC coupling is that it reduces the number of parts needed in the cold head circuit thus makes it compact and reduces the sources of noise. The drawback is that the leakage current of the PIN photodiode is amplified by the feedback resistor of the charge-sensitive amplifier resulting a DC offset voltage at its output. As we are using large R_f to reduce its thermal noise, leakage current of only $\mathcal{O}(0.1\,\mathrm{nA})$ is allowed. Although the typical leakage current of type S3590-06-SPL is as large as 8 nA at 25°C, it decreases as the temperature goes down. At our operating temperature, 130 K, it is negligibly small.

A picture of an X-ray detector module is shown in Fig. 5.31. One module has four PIN photodiodes and their associated cold head parts of the preamplifier. In order to prevent vibration, the cold head circuits are molded in epoxy resin.

The back-end part of the charge-sensitive amplifier was made into daughter cards. Each card contains one back-end circuit. One of them are shown in Fig. 5.30 (a).

The circuit diagram of the booster is shown in Fig. 5.29. The booster amplifies the output of each charge-sensitive amplifier to fit the input range of the FADCs. They also include pole-zero cancellation network to compress the low frequency components which are rich in microphonic noise. Another aim of the boosters is to strengthen the noise immunity. Since the preamplifier output should be transmitted through 15-m-long coaxial cables until it reaches FADCs, amplification of the signal before the transmission is needed. Four booster circuits are build on a booster daughter card, which is shown in Fig. 5.30 (b).

All the room temperature parts are integrated into four preamplifier boxes attached to the four feedthrough connectors at the access port of the main cylinder. Two of them are shown in Fig. 5.30 (c), where their shieldings are opened to show daughter cards mounted on a mother boards. Other components integrated on a mother board include ±5-V voltage regulators, a 2-minute main high voltage buffer, and a 60-dB attenuator for the test inputs of the charge-sensitive preamplifiers.

Circuit design

In prior to designing the complete sixteen channel preamplifier, the noise power spectrum of a charge-sensitive amplifier was measured by actually mounting a prototypical X-ray detector module to the helioscope. In this measurement, a prototypical preamplifier back-end was used which was designed by F. Shimokoshi and has been used in the early stage of the development of the PIN photodiode X-ray detectors [81]. We did not use the booster amplifiers in this measurement, since they did not exist at this time.

Waveforms are collected for sampling rates of 10 kHz, 100 kHz, 1 MHz, 10 MHz, and 20 MHz using Iwatsu DS-8606 digital oscilloscope. It has a wave memory of 16 Ki words (2^{14} words). Figure 5.32 (a) shows the obtained noise spectrum, where the spectral density of the noise voltage e_n is plotted as a function of frequency. It is separated in five sections by vertical lines. Each section corresponds to the five sampling rates listed in the above. The dotted line in each section indicates the quantization noise given as

$$e_{\mathrm{quantize}} = \frac{\mathrm{LSB}}{\sqrt{6 f_{\mathrm{sampling}}}}, \tag{5.12}$$

which results from the quantization error by the analog-to-digital conversion by the digital oscilloscope. The LSB resolution was 200 μV. Since the absolute minimum noise floor thus dependents on sampling rate, the stair-shaped noise floor which is becoming higher as the sampling rate get lower is spurious. Furthermore, it should be noted that we are seeing a folded spectrum except for the one obtained with the highest sampling rate. Since no anti-aliasing filter was employed except for the intrinsic bandwidth of the front-end of the oscilloscope, noise power at higher frequencies is also contributing to the noise floors of the spectra taken with lower sampling rates.

In order to figure out the main component in the noise spectrum, the integral

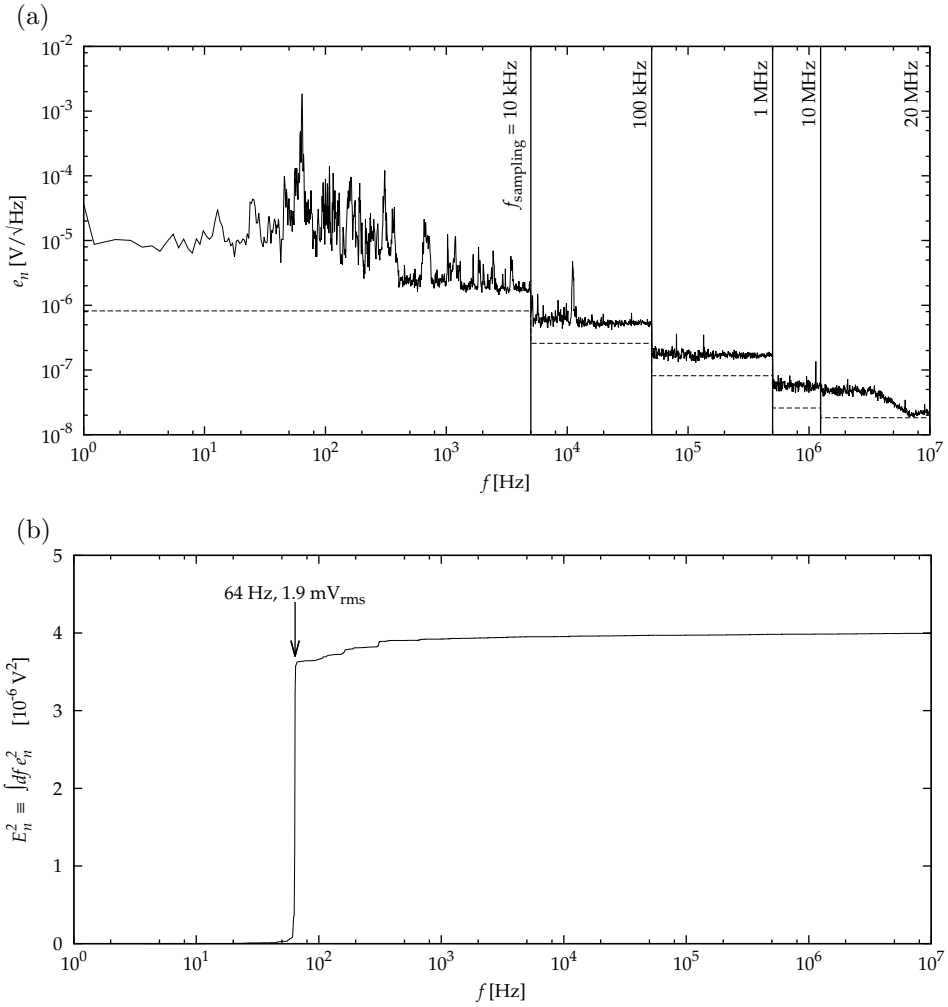

Figure 5.32: (a) Measured noise spectrum at the charge-sensitive amplifier output, where five spectra taken with five different sampling rates are shown side-by-side. The dotted lines indicate the quantization noise by the digital oscilloscope for each sampling rate. (b) Cumulative noise power. The integral of the noise power with respect to frequency is shown as a function of frequency. Each step corresponds to the contribution from each peak in pane (a).

of the noise power e_n^2 with respect to the frequency f was calculated:

$$E_n^2 \equiv \int e_n^2\, df. \tag{5.13}$$

Figure 5.32 (b) shows the cumulative noise power as a function of f. We find that the 64-Hz component with 1.9 $\mathrm{mV_{rms}}$ is obviously dominating the noise spectrum.

The charge gain of a charge-sensitive amplifier is determined by its feedback capacitance. In our circuit, we are utilizing the stray capacitance between the terminals of the 5-GΩ feedback resistor. Although its value depends on the

actual layout of the printed circuit board (PCB), the decay time of the pulse shape of $\tau \sim 2.5\,\mathrm{ms}$ and the charge gain of $70\,\mu\mathrm{V/keV}$ implied $C_{\mathrm{stray}} \sim 0.6\,\mathrm{pF}$ in this measurement. [2]

Considering the typical energies of the axion signal ($\sim 4\,\mathrm{keV}$), the output level of the charge-sensitive amplifier is too small compared to the full-scale range of FADCs of 2 V. The primary purpose of the booster is to fit the signal level to the input range of FADCs. The gain of a booster was designed to be variable around the order of $\mathcal{O}(500)$ so that the full scale becomes about 30 keV altogether.

While amplifying real signals, the booster should compress low frequency components efficiently to prevent the FADC input from overflowing by microphonic noise. As such filter, a pole-zero network was employed which makes an exponential pulse of a long time constant into another exponential pulse of shorter time constant. The exponential waveform is suited for the shaping amplifier which generates triggers. Time constant of 1–3 ms of the charge-sensitive amplifier was made into 50 μs by this filter. Then the 64-Hz noise is expected to be suppressed by 1/20–1/40 relative to signal. The time constant of the pole-zero cancellation network was made adjustable by a pre-set variable resistor.

In order to amplify high speed waveforms precisely, two linear amplifiers employing high-speed current-feedback operational amplifiers were used in series, where the gain of the first and second stages were set to be 100 and 10, respectively. The overall gain was made adjustable by a variable attenuator employing another pre-set variable resistor. However, this variable attenuation mechanism might have been responsible for the slight drift of gain which was observed during long-term measurements.

A DC servo circuit was employed to cancel out the DC offset of each charge-sensitive amplifier as well as the input DC offset voltage of the first stage operational amplifier. A passive low-pass filter whose cut-off frequency is $f = 4\,\mathrm{MHz}$ was introduced as an anti-aliasing filter corresponding to the 10-MHz sampling rate of the FADCs.

The charge-sensitive amplifiers were designed based mostly on the prototypical amplifier designed by Shimokoshi, but some modifications to simplify the circuitry and to stabilize the bias points were made. The parameters of the compensation network of the charge-sensitive amplifier was determined on-site by cut-and-try. Because of the parasitic coupling between the booster output and the front-end, we needed to suppress its gain-bandwidth until the rise time of the preamplifier output deteriorated as slow as 1 μs to settle unwanted oscillations.

5.4.7 Radiation Shield

In order to reduce background by external radiation, the X-ray detector is surrounded by a radiation shielding. It consists of 100-mm thick lead outer shield, 10-mm thick oxygen free high conductivity (OFHC) copper inner shield, and 5-mm thick polymethylmethacrylate (PMMA) lining. The cross section view of the radiation shielding is shown in Fig. 5.33.

The copper shield absorbs γ-rays from ^{210}Pb as well as fluorescent X-rays from lead. It is fixed to the 40-K thermal radiation shield of the magnet and

[2] With the final cold-head design, the decay time and the charge gain was consistent with $C_{\mathrm{stray}} \sim 0.2\,\mathrm{pF}$.

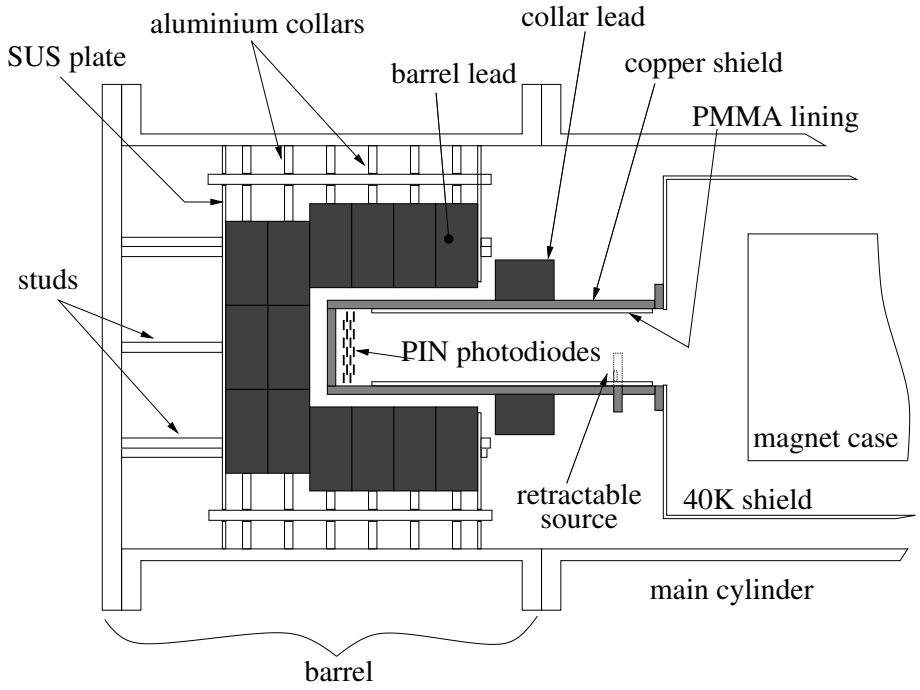

Figure 5.33: Cross section of the radiation shielding and its supporting structure.

its temperature is about 60 K. The X-ray detector is mounted inside the copper shield. This shield is not only a component of the radiation shielding, but also part of the thermal radiation shield, and is also acting as the cold finger for the X-ray detector.

The major part of the lead shield labeled "barrel lead" in the figure is at room temperature. About 300 kg of lead blocks are fixed inside a sub-cylinder labeled "barrel", which is connected to the main cylinder through a JIS V500 vacuum flange. They are supported by stainless steel plates, aluminium collars, and fully-threaded studs penetrating the collars and the blocks. Rest of the lead shield labeled "collar lead" is at 60 K. About 12 kg of lead blocks are placed on the copper shield to cover the opening at the solar side as much as possible.

The inner most PMMA lining was introduced to block 9-keV fluorescent X-rays from the copper surfaces. It is subsectioned into pieces to absorb the large difference in thermal expansion between PMMA and copper. PMMA tiles are fixed on the copper plates with epoxy bolts. Afterwards, this part was replaced with 3-mm thick polychlorotrifluoroethylene (PCTFE) which has larger X-ray absorption in order to widen the clearance around the X-ray path.

5.4.8 Calibration source

Each PIN photodiode was calibrated by 5.9-keV Mn X-rays from a ^{55}Fe source installed in front of them in the midst of the copper shield 307–319 mm away from the PIN photodiodes. The source is manipulated from the outside and is completely retracted behind the shield during observations so as not to increase the background level. Figure 5.34 (a) shows the calibration source mounted on

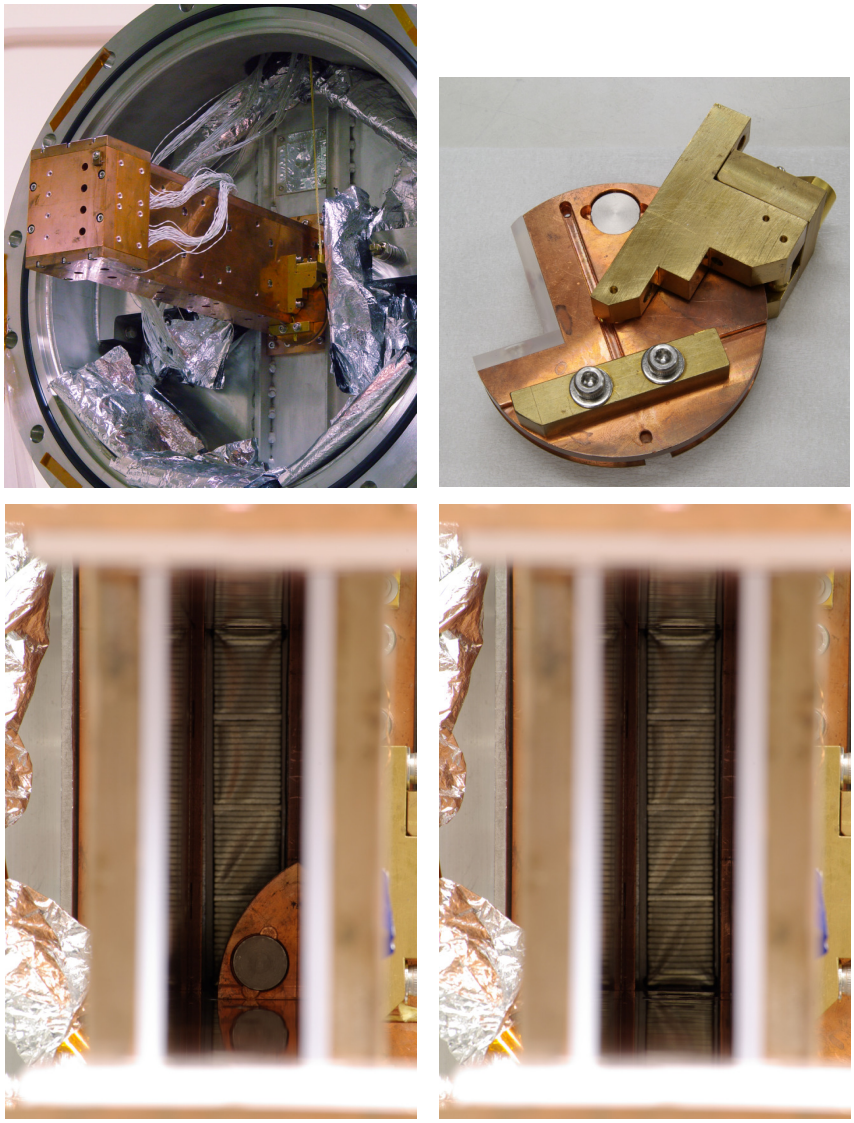

Figure 5.34: (a) An ^{55}Fe calibration source is installed in the midst of the copper shield. (b) The source is on a rotating copper disk, and the right-angled cutaway in the disk becomes part of the inner wall of the copper shield when the source is retracted. (c) The source being exposed or (d) being retracted are viewed from the X-ray detector position.

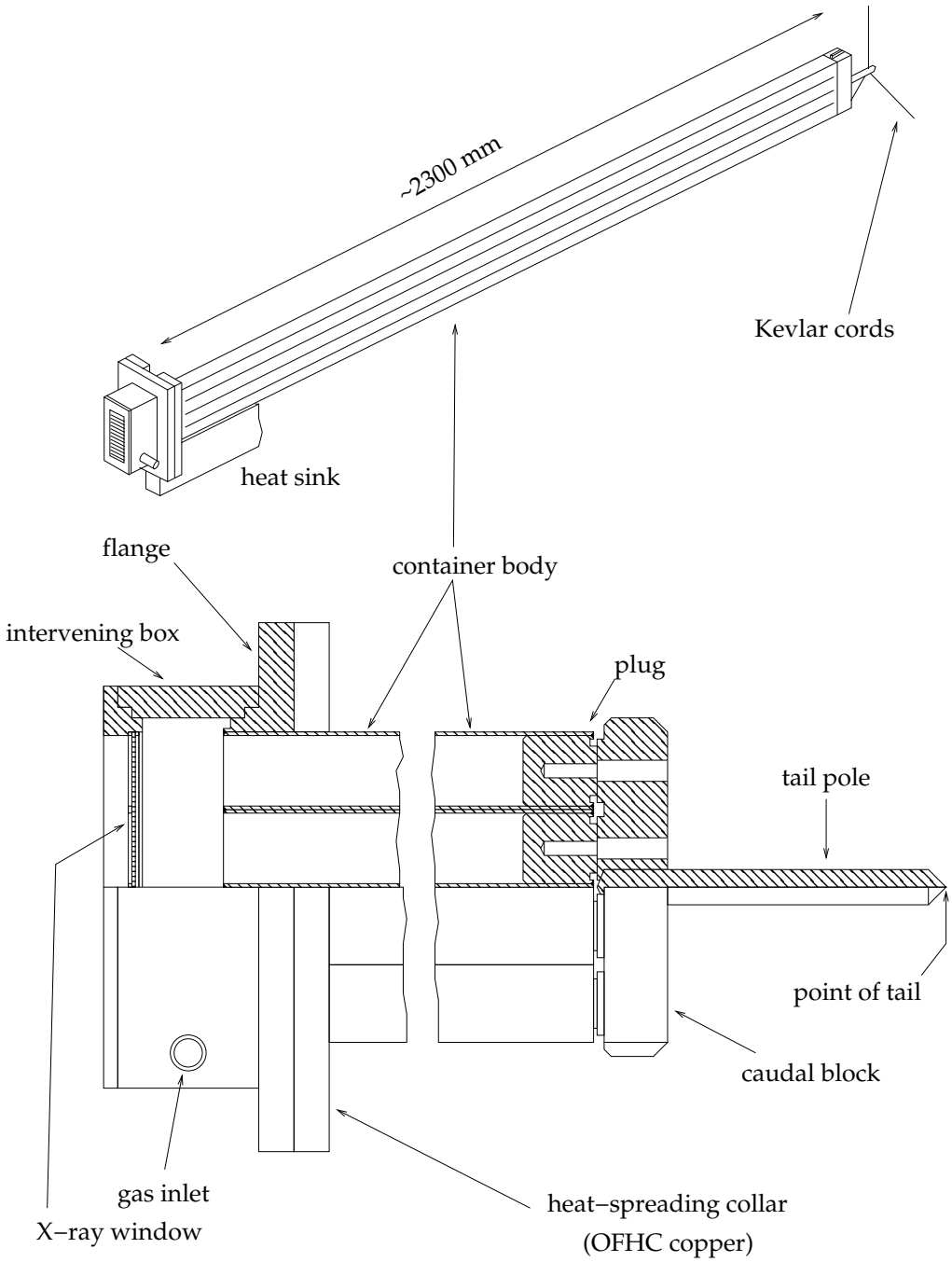

Figure 5.35: The upper figure shows the gas container schematically. The lower half shows the magnified views of its detector-side- and its solar-side structure where its upper half is shown cut-way.

the copper shield, Fig. 5.34 (b) shows rotating mechanism, and Fig. 5.34 (c) and (d) show the source being exposed and being retracted viewed from the X-ray detector position, respectively.

5.5 Gas container

The gas container holds conversion gas which would restore the coherent axion–photon conversion for heavier axions by giving a refractive mass to photons. The container is designed aiming at an axion search experiment up to a few electronvolts including the hadronic axion window.

To achieve this, the following requirements should be fulfilled:

- It should be thin enough to be installed through the $92 \times 20\,\mathrm{mm}^2$ aperture of the magnet.
- It should hold very high density helium.
- The uniformity of the temperature should be $\delta T/T < 2 \times 10^{-4}$, since nonuniformity disturbs coherence.
- The photons generated in the container should reach the X-ray detector.
- It should be leak tight to keep good thermal insulation by the surrounding high vacuum. The required helium leak rate should be less than $10^{-10}\,\mathrm{Pa\,m^3/s}$.

As described in Chapter 4, we decided to operate the gas container at about the same temperature as the magnet. Actually, the magnet temperature is about 5–6 K which is just above the critical temperature of ^{4}He, $T_c = 5.1953\,\mathrm{K}$. If we set the temperature of the buffer gas as the same as the magnet, we can control its pressure within a moderate range while helium gas would not liquefy at any densities. Therefore, the magnet should be the best heat sink for the gas container in our helioscope.

The schematic picture of the gas container is shown in Fig. 5.35. It has a long slender shape to be inserted in the magnet through the $92 \times 20\,\mathrm{mm}^2$ aperture. Its body is made of four 2.3-m long square pipes welded side by side to each other. The square pipes are made of 0.8-mm thick SUS304 stainless-steel. One end of each square pipe is blind-ended with a welded plug. This end becomes the solar side. At the opposite side, four pipes are packed into a rectangular bore of a stainless-steel rectangular flange all together and welded hermetically. This end faces the X-ray detector. The gas container is fixed to the magnet at the detector end with this flange. The solar end is suspended by Kevlar cords so that thermal flow through this end is highly suppressed while, mechanically, the gas container is firmly fixed to the magnet.

The end facing to the X-ray detector is ended with a cryogenic X-ray window. Between it and the flange, a hermetic box with a port to introduce gaseous helium is inserted. Indium sealing is applied to the connection between the flange and the intervening box as well as between the X-ray window frame and the box.

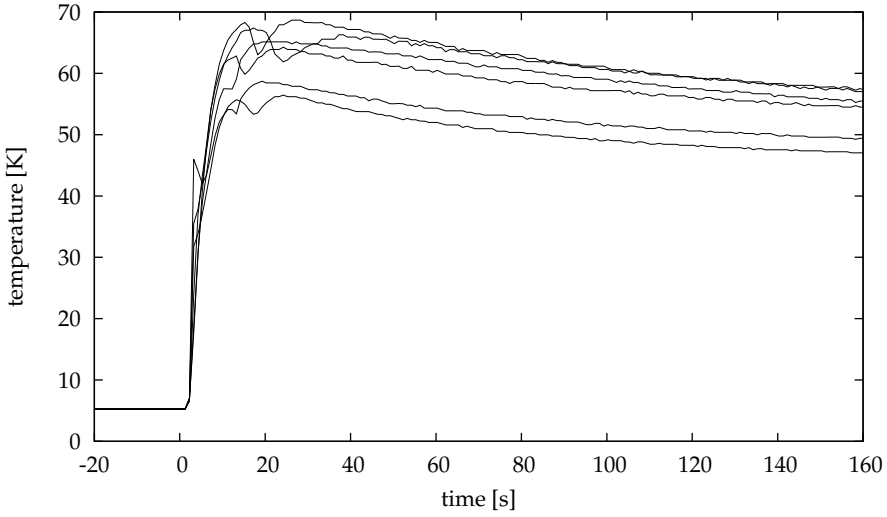

Figure 5.36: Time chart of the temperatures in the magnet before and after a quenching. Six measured points are shown mixed.

5.5.1 Mechanical design of the body

In order to ensure good thermal insulation of the superconducting magnet by the surrounding high vacuum, the gas container should be leak tight. The required helium leak rate should be less than $10^{-10}\,\mathrm{Pa\,m^3/s}$ in total.

At the same time it should robust enough to withstand its internal pressure. In normal operation, the pressure of the buffer gas will not be more than about 1 atmosphere. However, a superconducting magnet can quench suddenly. Considering the increased pressure during this moment, it should withstand some higher pressure. Figure 5.36 shows the measured temperature change of the magnet immediately after a quenching, where six measured points in the magnet are shown mixed. Rise of temperatures was observed 2 seconds after the beginning of the quench. They rose up to 30–50 K within a few seconds after that and reached at their maximum temperatures of 50–70 K twenty seconds later. Ten times of rise in temperature means that the pressure of gaseous helium would increase by about ten times if we did not relief it.

We did not set this extreme pressure for our design value, since we were unable to find an X-ray window with enough transparency which was warranted to withstand such pressure. Instead, we designed the container to withstand at least 3 atmospheres of internal pressure corresponding to the maximum pressure allowed to the X-ray window we used and we left it as a task for the future to invent some mechanism to relief gas at this moment.

In the final design, the cross section of the gas container body was divided into four part as shown in Fig. 5.37 each with rectangular shape of 21.9 mm in height and 17.9 mm in width and the wall thickness was 0.8 mm. The rectangular cross section was selected to maximally utilize the rectangular aperture of the magnet. The maximum stress within the wall is estimated to be

$$\max T_{\mathrm{wall}} \simeq \frac{h'^2 - h'w' + w'^2 + h't}{2t^2} p_{\mathrm{int}} = 9 \times 10^7\,\mathrm{Pa} \tag{5.14}$$

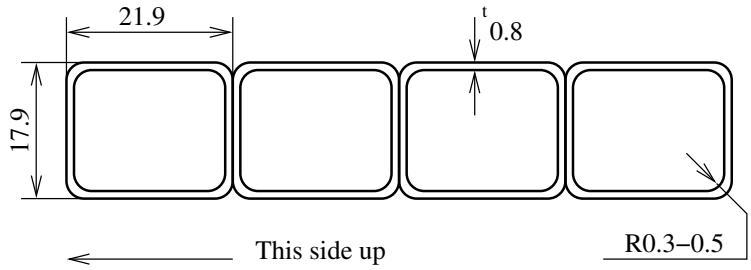

Figure 5.37: Cross section of the gas container body.

at the corners under the internal pressure of $p_{\rm int} = 3\,$atmospheres, where $t = 0.8\,$mm is the wall thickness, $h' = 21.9\,{\rm mm} - 2t$ and $w' = 17.9\,{\rm mm} - 2t$ are the inner height and width of a square tube.

To retain enough strength, SUS304 stainless steel was used. Deformation of the flat surface is then

$$\delta x \simeq \frac{h'^4 + 4h'^3 w' - 4h'^2 w'^2}{32Et^3} p_{\rm int} = 27\,\mu{\rm m} \tag{5.15}$$

at the maximum along the center of each flat surface by the same pressure, where E is Young's modulus of the stainless steel which is typically $E = 1.9 \times 10^{11}\,$Pa at room temperature and slightly higher at cryogenic temperatures.

A disadvantage of this material as the gas container is its low thermal conductivity. We adopted an additional heat conducting layer to get rid of it as described in Section 5.5.2.

Vacuum tightness was achieved by making the body part as a bundle of plain jointless tubes and welding both ends hermetically. Between the flange and the intervening box as well as between the X-ray window and the box, we used indium sealing which provides a reliable vacuum-tight connection at cryogenic temperatures. At the connections for the internal helium pipework, we used Swagelok tube fittings, brazing and soldering depending on the thickness of the tube as well as the allowed working space around them.

5.5.2 Thermal design

If there is a thermal nonuniformity in the buffer gas, the number density N becomes position dependent, and so the momentum transfer, $q = q(z)$. From the ideal gas law and Eqs. (3.19) and (3.26), we find for the influence of the thermal nonuniformity on q as

$$\delta q = \frac{m_\gamma^2}{2E} \frac{\delta T}{T}. \tag{5.16}$$

To estimate the loss of coherence by this, we substituted the first order Taylor series of $q(z)$,

$$q(z) = q_0 + q_1 z + O(z^2), \tag{5.17}$$

into Eq. (3.43). For simplicity, we ignored the absorption by gas, $\Gamma = 0$, and

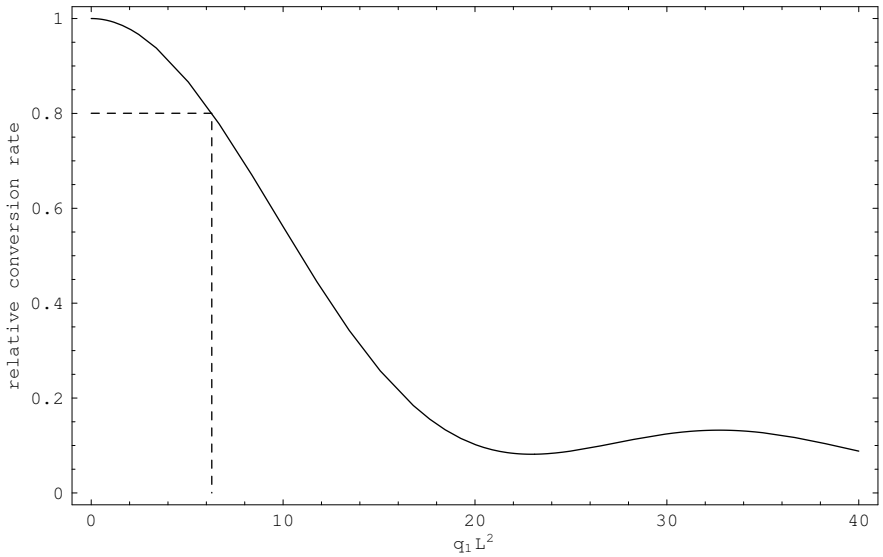

Figure 5.38: Decrease of conversion rate by nonuniformity. The maximum conversion rate $P_{a\to\gamma}$ with a nonuniform buffer gas is plotted relative to the ideal conversion rate $g_{a\gamma}^2 B^2 L^2/4$ as a function of a nonuniformity index $q_1 L^2$, where $q(z) = q_0 + q_1 z$ is the first order Taylor series of the momentum transfer, and L is the length of the magnetic field.

assumed the magnetic field B to be uniform here. Then, we find

$$\max_{q_0} P_{a\to\gamma} = \max_{q_0} \frac{g_{a\gamma}^2}{4} \left| \int_0^L \boldsymbol{B} \exp(iq_0 z + q_1 z^2)\, dz \right|^2 \tag{5.18}$$

$$= \frac{\pi g_{a\gamma}^2 B^2}{4q_1} \left| \mathrm{erf}\left(\frac{L\sqrt{iq_1}}{2} \right) \right|^2, \tag{5.19}$$

where

$$\mathrm{erf}(x) = \frac{2}{\sqrt{\pi}} \int_0^x \exp(-t^2)\, dt \tag{5.20}$$

is the error function. In Fig. 5.38, the shape of this function is plotted as the ratio to the ideal conversion rate (Eq. (3.29)) as a function of a nonuniformity index $q_1 L^2$. For example, with $q_1 L^2 = 2\pi$ which corresponds to the difference of the momentum transfer of $\delta q = 2\pi/L$ from end to end, the maximum conversion rate $P_{a\to\gamma}$ is reduced by 20%. Conversely, if we are to allow up to this amount of incoherence, the allowed nonuniformity of the temperature is

$$\delta T \lesssim \frac{2ET}{m_\gamma^2 L} \sim 1\,\mathrm{mK} \tag{5.21}$$

for the benchmark helium density ($m_\gamma = 2\,\mathrm{eV}$) at $T = 5$–$6\,\mathrm{K}$.

We took two measures to achieve this goal. First, we tried to minimize the thermal flow within the gas container by restricting its thermal contact to a single point. That is, the gas container was made to connect thermally to

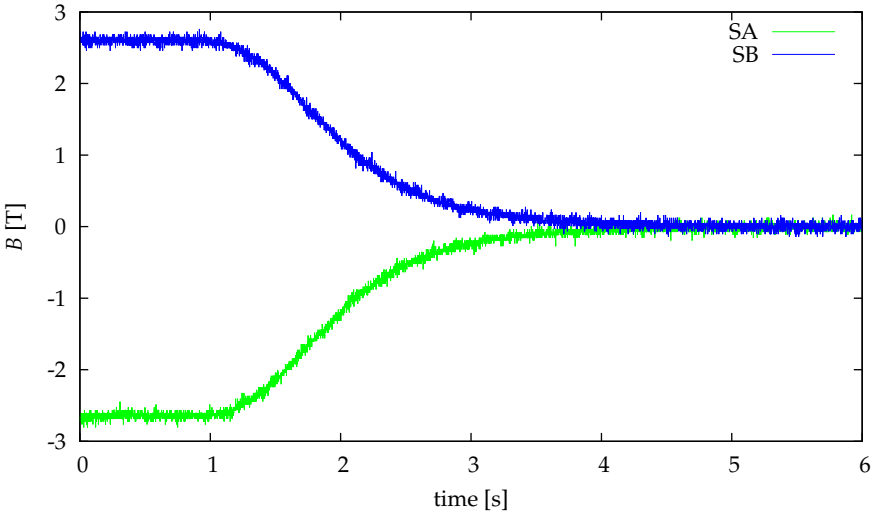

Figure 5.39: Decay of magnetic field during a quenching (exercise) from the full excitation. The abscissa is the relative time in seconds. The ordinate shows the measured magnetic fields at two Hall sensors on the case of the magnet.

the magnet only at the flange at its detector end, and to be thermally isolated at any other surfaces. Second, the container body was wrapped with 5N (99.999%) pure aluminium which is known to be good thermal conductor at the cryogenic temperature. The thermal conductivity of pure aluminium is about $5 \times 10^3\,\mathrm{W/(m \cdot K)}$ at the liquid helium temperature while that of stainless steel SUS304 is only $3\,\mathrm{W/(m \cdot K)}$ at the same temperature [98]. Although the value falls under the strong magnetic field, it will be better than $1 \times 10^3\,\mathrm{W/(m \cdot K)}$ in our environment even with a conservative estimate. (A. Yamamoto, private communication, 1995)

In terms of the thermal conductance, a thicker aluminium layer is preferred. However, the space around the gas container is limited. Finally, we determined the aluminium thickness to be 0.2 mm which was the maximum thickness to retain the container without touching the inner surface of the magnet safely.

Care must be taken against the eddy currents caused by quenchings of the magnet. A collaborator, S. Moriyama gave the first calculation about this eddy currents. Here, the author presents a refined estimation based on more realistic parameters including the measured magnetic field during a quenching.

Figure 5.39 shows the measured magnetic field at two Hall sensors on the case of the magnet during a quenching. It decayed from the full excitation of 2.6 T corresponding to 4 T at the center of the magnet down to zero in a few seconds. The electromotive force by this quick change of the magnetic field induces eddy currents within conductors in and around the magnet.

The pure aluminium is a good electrical conductor, too, by the Wiedemann–Franz law:

$$\frac{\kappa}{\sigma} = LT, \tag{5.22}$$

where κ is the thermal conductivity, σ is the electrical conductivity, and $L = \pi^2 k_\mathrm{B}^2/(3e^2) = 2.45 \times 10^{-8}\,\mathrm{W\,\Omega\,K^{-2}}$ is the Lorenz number. If we assume $\kappa =$

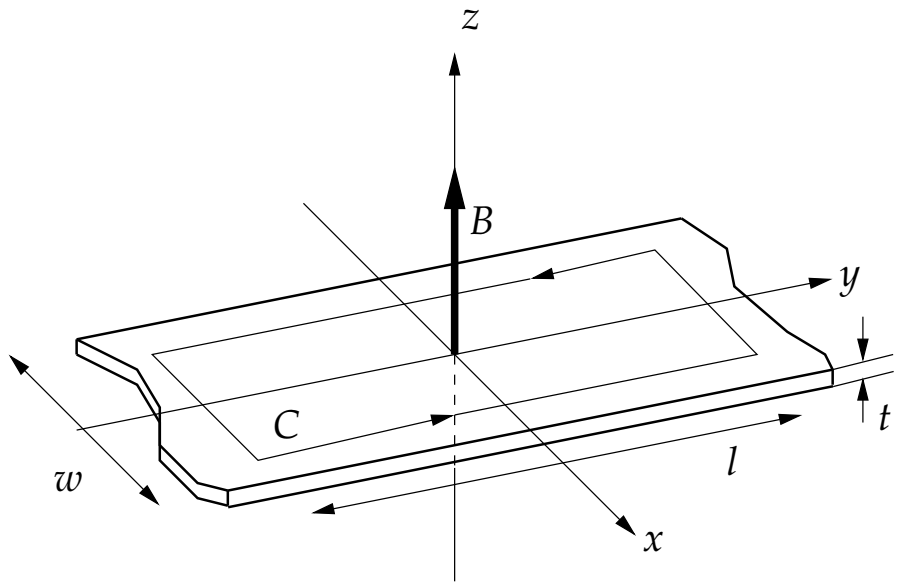

Figure 5.40: Model for the eddy current in the aluminium sheet. A decreasing magnetic field B is applied along the z-axis. The sheet is infinitely long along the y-axis, its width is w, and its thickness is t. A closed curve C has length of l and width of $2x$.

$5 \times 10^3\,\mathrm{W/(m \cdot K)}$ at $T = 5.5\,\mathrm{K}$, we get

$$\sigma = 3.7 \times 10^{10}\,\mathrm{S\,m^{-1}}. \tag{5.23}$$

Large eddy currents are expected within the heat-conducting aluminium layer. With regard to the eddy currents in the stainless steel body, we can ignore them since the stainless steel has only three orders of magnitude less electrical conductivity.

Let us consider the voltage along the closed curve C in an aluminium sheet in Fig. 5.40, where the decreasing magnetic field B is applied in parallel to the z-axis. The sheet is w wide, t thick, and we assume that its length is infinitely long along the y-axis. The closed curve C is l long, symmetric with respect to the y-axis and has $2x$ width, where $2x \leq w$. As an approximation to first order, we ignore the magnetic field by the eddy currents itself which plays as the screening against the change of the magnetic field.

From the symmetry, the current density j should be parallel to the y-axis,

$$\boldsymbol{j} = (0, j, 0), \tag{5.24}$$

anti-symmetric with respect to x,

$$j(-x) = -j(x). \tag{5.25}$$

Since the electromotive force must balance with the voltage drop there,

$$\frac{d}{dt}(2xlB) + 2l\frac{j}{\sigma} = 0. \tag{5.26}$$

Thus we get

$$j = -\sigma \dot{B} x. \tag{5.27}$$

From Fig. 5.39, the steepest descent of the field at the center of the magnet was estimated to be $\max(-\dot{B}) \sim 3\,\mathrm{T\,s^{-1}}$. Using this value, we find for the current density at $x = w/2 = 45\,\mathrm{mm}$, for example, to be

$$j(45\,\mathrm{mm}) = 5 \times 10^9\,\mathrm{A \cdot m^{-2}}. \tag{5.28}$$

From Ampère's law, these amount of current densities will produce a screening magnetic field of about 0.4 T at the center of the sheet assuming $w = 90\,\mathrm{mm}$ and $t = 0.2\,\mathrm{mm}$, for example, which is still weaker than 4 T. This implies that the current approximation is not too bad.

The tensile stress T_{hoop} by the hoop force on the eddy currents comes to the maximum at the center of the sheet. By integrating the Lorentz force on an infinitesimal wire of dx width, l length, and t height with respect to x, we get

$$\max T_{\mathrm{hoop}} = \frac{1}{tl} \int_0^{w/2} Bjtl\,dx = -\frac{1}{8}\sigma B \dot{B} w^2. \tag{5.29}$$

Again from Fig. 5.39, we estimated the maximum value of $-B\dot{B}$ at the magnet center to be as much as $\max(-B\dot{B}) \sim 9\,\mathrm{T^2/s}$. If a flat wide sheet of pure aluminium covering the whole gas container were adopted, i.e., $w = 90\,\mathrm{mm}$, we estimate the maximum stress by the hoop force to be

$$\max T_{\mathrm{hoop}} = 3.4 \times 10^8\,\mathrm{Pa}, \tag{5.30}$$

which is larger than the typical 0.2%-proof stress of annealed aluminium at room temperature, $T_{\mathrm{proof}} = 1 \times 10^8\,\mathrm{Pa}$. That meas that the eddy currents would be so large that it could tear the aluminium sheet during a quenching of the magnet.

The Joule heating can also be problematic. By integrating an infinitesimal Joule heating along C over the whole sheet volume as well as with respect to time, we find for the total energy dissipation per unit length in the aluminium layers of both sides as

$$J/l = \frac{\sigma t w^3}{6} \int \dot{B}^2\,dt \tag{5.31}$$

assuming σ is constant. Using the values: $w = 90\,\mathrm{mm}$, $t = 0.2\,\mathrm{mm}$, and $\int \dot{B}^2\,dt \sim 8\,\mathrm{T^2/s}$ at the magnet center estimated from Fig. 5.39, we get

$$J/l \sim 7 \times 10^3\,\mathrm{J/m}. \tag{5.32}$$

This is certainly large, however, it can be rather an overestimation since σ is also temperature dependent so that the eddy currents would decrease as soon as the temperature rose. At the least, if the above estimated energy dissipation were to be received by the container body without gas its temperature would reach 66 K, and if the same heat were shared with helium gas of the benchmark density ($m_\gamma = 2\,\mathrm{eV}$), it would reach 59 K. In the above estimation, we ignored the small heat capacity of the pure aluminium layers.

A solution to get rid of this large eddy currents is to make the width w smaller. That is to divide a flat wide aluminium sheet into parallel bunch of

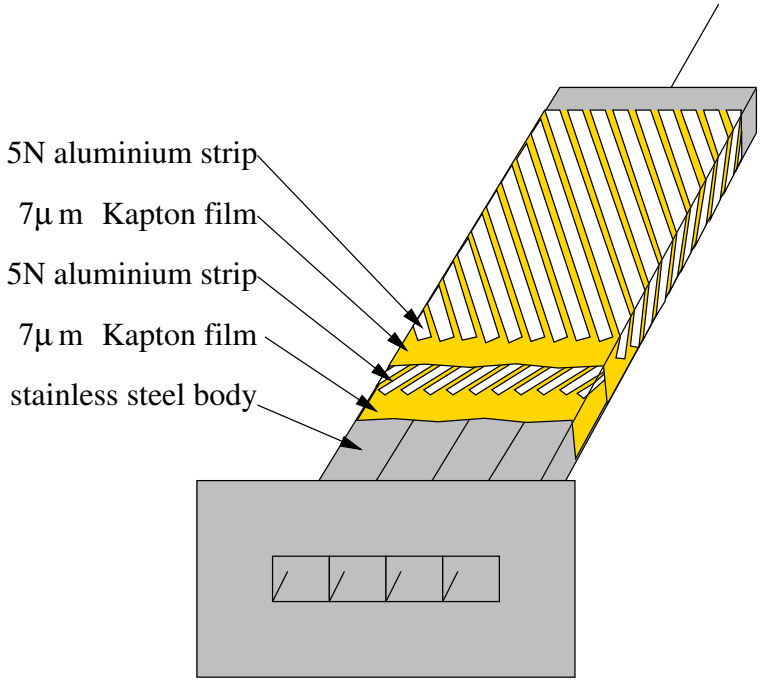

Figure 5.41: Structure of the heat conducting layers. Two layers of heat conducting aluminium layers are formed on the outer surface of the stainless steel body. Each layer consists of twenty strips made of 99.999% pure aluminium. They are wounded helically around the body such that two layers cross over. The stainless body and the aluminium layers are insulated from each other with 7-μm thick Kapton films.

strips. By dividing it into N strips, we will get $1/N^2$ less hoop force and $1/N^2$ less Joule heating. We divided it into strips of 8 mm width. In addition, the thickness was also divided into two to ensure the thermal contact between the strips. They are wound helically around the container body such that two layers cross over as shown in Fig. 5.41. Finally, forty strips made of 5N pure aluminium each with 0.1 mm thickness and 8 mm width are laid in two layers to form a heat conducting layer on the outer surface of the stainless steel body. By way of electric insulation, 7-μm thick Kapton films are inserted between two layers of pure aluminium as well as between the stainless steel body and the first layer aluminium strips. Cryogenic compatible epoxy adhesive, Nitto Shinko Corporation SK-230 was used to bond the layers and to fill the gaps between adjoining strips.

By the above design, the end-to-end thermal conductance of the gas container is estimated as

$$\frac{Q}{\delta T} = 1.4 \times 10^{-2}\,\mathrm{W/K}. \tag{5.33}$$

This means that a heat injection up to $\mathcal{O}(10^{-5}\,\mathrm{W})$ would be allowed at the far end of the gas container. This amount of insulation would be feasible as the temperature differences within the magnet or between the magnet and the gas

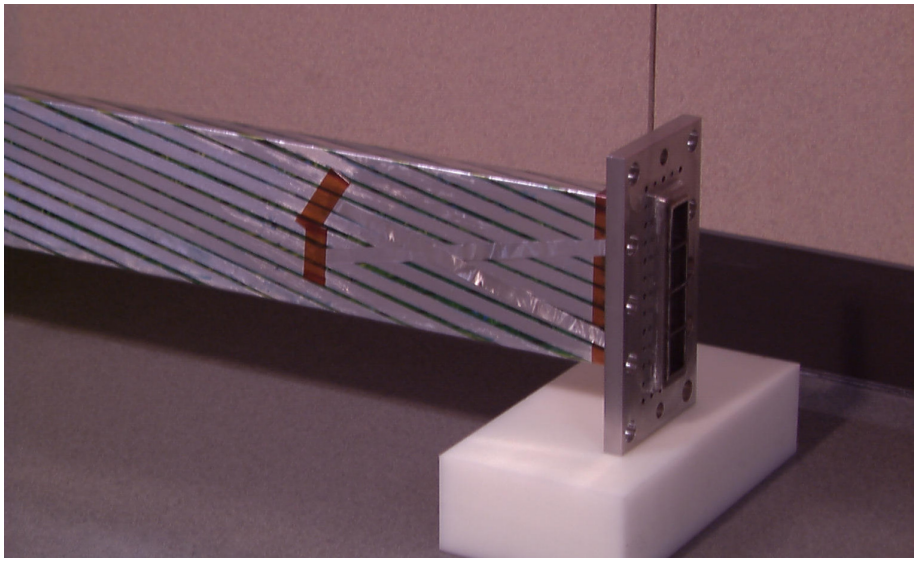

Figure 5.42: Gas container covered with heat conducting 5N aluminium strips. A portion around its flange is shown.

container would be of the order of 0.1 K.

5.5.3 Construction

The stainless steel square pipes are manufactured and welded by Tohsei Kokan Co., Ltd. They are made from annealed SUS304 stainless steel round tubes, made into square cross section by a cold drawing process, and left unannealed to make use of the work hardening by the process. After cutting them into 2.3 m long each, four of them are welded to a square flange together. At the opposite end, each pipe was closed hermetically by welding a plug. Finally, four square pipes were welded side by side to each other at sparse spots to make the entire structure robust. The intervals between the spots are about 230 mm. Tungsten inert gas (TIG) welding was used in all the places.

After its precise outer shape of the stainless steel body was measured, it was covered with the heat conducting aluminium layer as described in the previous section. In Fig. 5.42, we show a portion of the gas container around its flange.

5.5.4 Fixtures

At the detector end, the gas container is fixed to the copper heat-spreading bar of the magnet with its flange. This bar acts as the heat sink. To make thermal contact effectively, a heat-spreading collar made of 10-mm thick oxygen free high conductivity copper plate is inserted between the flange and the magnet. To ensure the thermal contact between them, an indium sheet is sandwiched between the collar and the end surface of the heat-spreading bar of the magnet.

The picture of the fixture at the solar end is shown in Fig. 5.43. This structure restricts the swing motion of the long container body. A 10-mm diameter SUS304 stainless steel pole is sticking out from the solar end of the

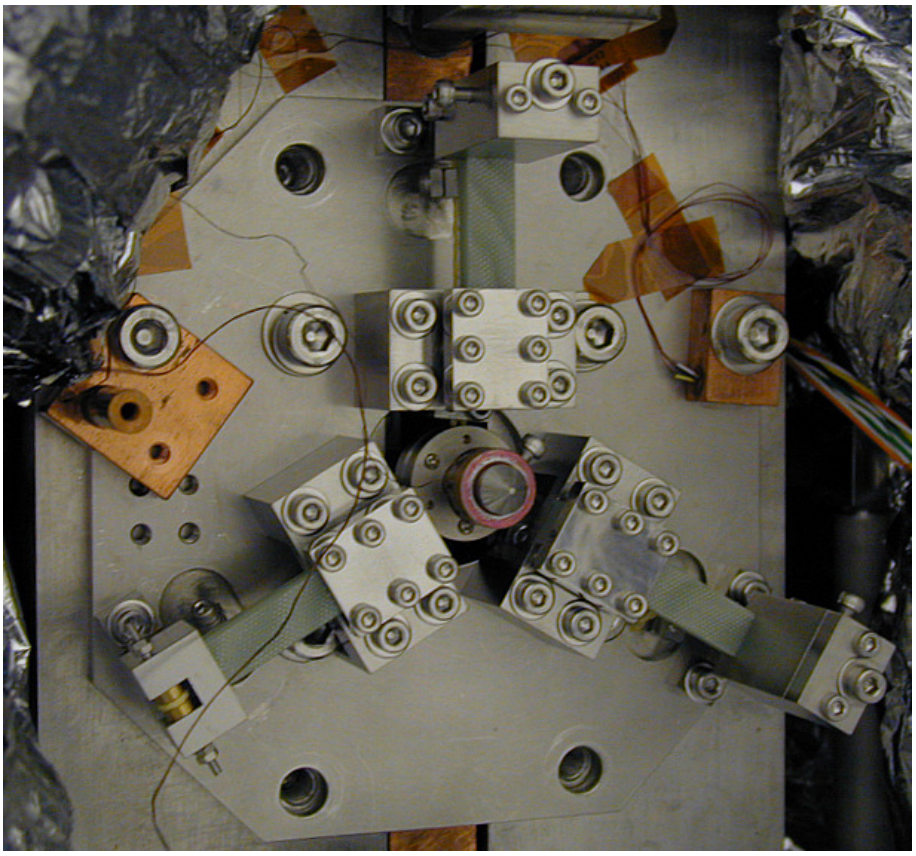

Figure 5.43: Fixture at the solar end. The corn at the center is the pointed end of the ϕ10-mm stainless steel pole sticking out from the gas container. The pole is fixed in the xy direction with a stainless steel collar (rear) which is suspended by three Kevlar cords. The Kevlar cords are behind the G10 flat springs (green) arranged 120° with each other. Each G10 flat spring is fixed on the magnet case with a stainless steel gate-shaped structure at one end (inner). One (left) is ended with a pulley box at the other side. Two of them (top and right) are ended with anchorages of Kevlar cords which are equipped with screws to adjust the position of the gas container. The copper ring on the end of the pole (front) is a heater to measure the total thermal conductance of the gas container. Two copper blocks are a 5-K thermal anchor (larger one) and a heat sink of CGR thermistor T2 (smaller one).

container. It is fixed to the four welded end plugs of the square pipes through a caudal block parts made of SUS304 stainless steel. As a guide for the precise positioning of the gas container, the end of the pole is pointed.

The gas container is suspended by the pole with three 0.8-mm diameter Kevlar cords arranged 120° with each other through a SUS304 stainless steel collar which allows the pole to move freely along the helioscope axis. Since Kevlar has a smaller coefficient of thermal contraction than stainless steel which is the material composing the magnet case, each Kevlar cord is strained by a flat spring made of G10 glass-fibre-reinforced plastics (GFRP). The tension of each cord was adjusted to 100 N at room temperature.

5.5.5 Gas filling system

The gas filling system was drastically changed between Phase II and III. In this section, we describe the gas filling system used in the Phase II measurement. The upgraded gas filling system used in the Phase III measurement is described in Section 7.2.

In the Phase II measurement, we used a simple gas filling system. We employed no countermeasure against over pressure of buffer gas which can occur during a magnet quench. Gas densities were set with a manually operated valve system shown in Fig. 5.44. During the solar tracking- and background measurements, the main valve (V4) is shut off and the pressure controlling part is detached from the helioscope at the ISO KF-25 flange. A Yokogawa MU101-AM1N precision pressure gauge is used to measure the pressure in the gas container.

To ensure the minimal heat injection from it as well as to minimize the volume between 5 K and room temperature, the helium filling pipe inside the cryostat was made minimally thin as shown in Fig. 5.45. Two heat exchangers are inserted between the room temperature part and the gas container. The 40-K heat exchanger is made of a 1/4" copper tube thermally attached to the 40-K shield of the magnet. The 5-K heat exchanger is made of a ϕ3-mm copper tube thermally connected to the heat-spreading collar of the gas container. Between the access port at room temperature and the 40-K heat exchanger, a rigid ϕ6-mm thin-wall stainless steel pipe was used. From there to the 5-K heat exchanger, a rigid ϕ3-mm thin-wall stainless steel pipe was used.

5.5.6 X-ray window

The cryogenic X-ray window was manufactured by Metorex International Oy, Finland. It was designed for this specific application. A photograph of the X-ray window is shown in Fig. 5.46.

It consists of four pieces of $21.88 \times 18.50\,\mathrm{mm}^2$ subwindows, where Metorex C10 type windows are employed. Each subwindow consists of 25-μm beryllium foils coated one side with 1 μm of polyimide to secure gas-tightness, and is supported from the outer side by laser-machined nickel grids whose thickness is 1.5 mm. Shadowing by the nickel grid is about 20% which is limiting the transmission at the high energy region. Figure 5.47 shows the transmission curve for a C10 type window.

The subwindows are sandwiched between two nickel frames and housed in a square outer frame made of SUS304 stainless steel. The frames and subwindows

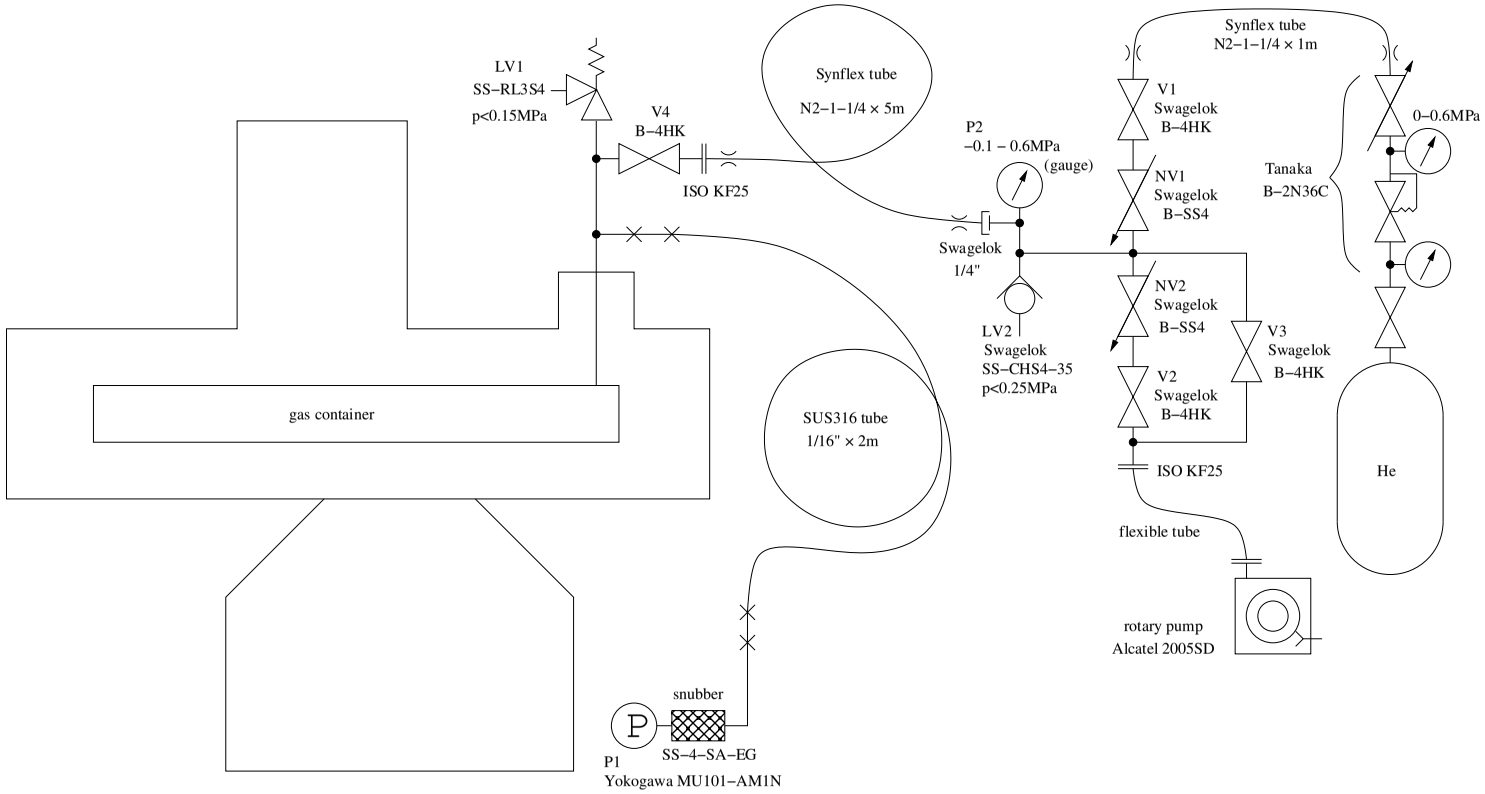

Figure 5.44: Schematic diagram of the manually operated gas pressure control system.

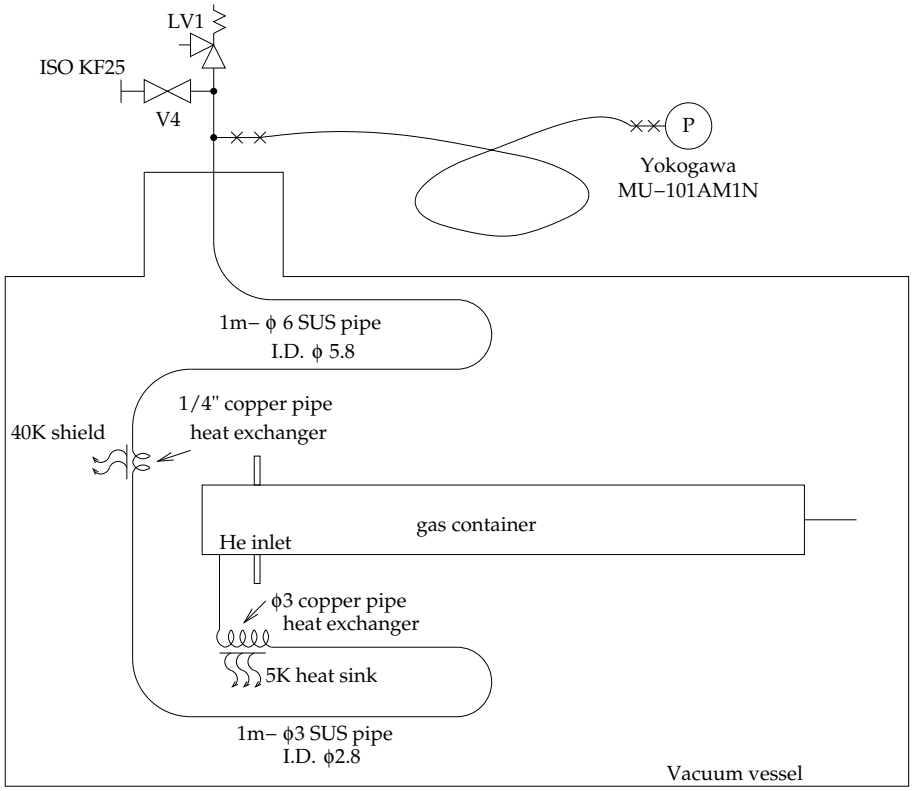

Figure 5.45: Schematic diagram of the helium pipework showing inside the vacuum vessel.

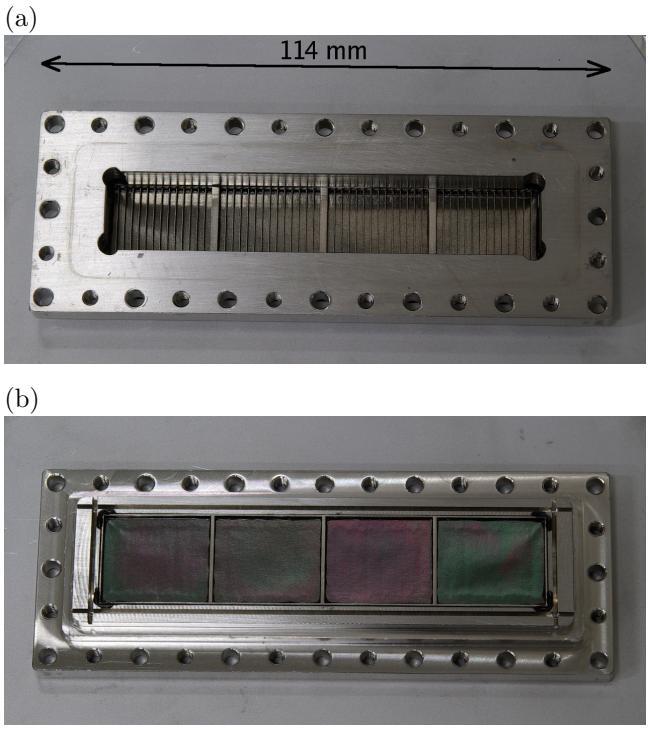

Figure 5.46: Cryogenic X-ray window manufactured by Metorex International Oy viewed from (a) outside (vacuum side) and (b) inside (gas side).

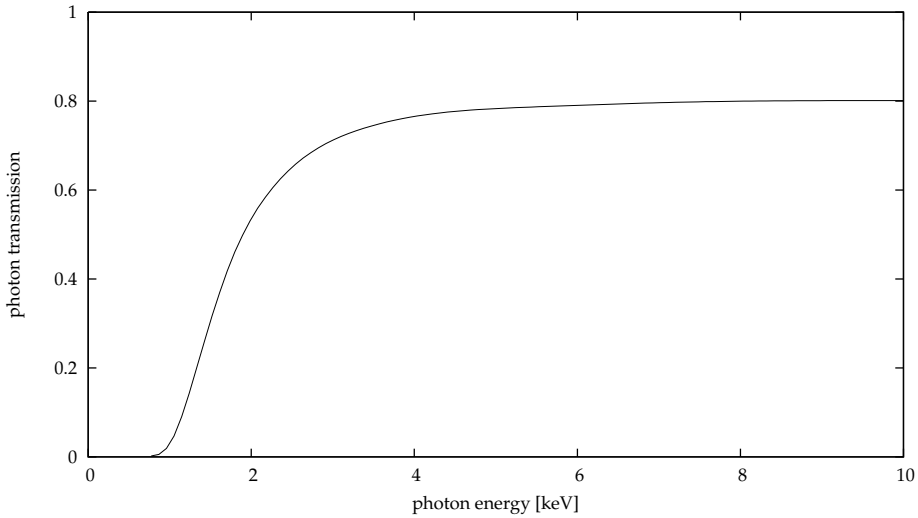

Figure 5.47: Transmission curve of the X-ray window. It is transparent to photons above 3 keV. The high-side transmission is limited by the shadowing by the nickel grid.

are glued with cryogenic compatible epoxy adhesive. In the periphery of the outer frame, steps are made to form indium sealing, with which it couples with the intervening box.

The window can withstand the internal pressure of more than 0.3 MPa. The guaranteed gas tightness through the window is less than 10^{-10} Pa m^3/s for helium at 0.1 MPa differential pressure.

5.5.7 Measurement of gas container geometry

Before the gas container was wrapped with 5N high-purity aluminium heat-conducting layer, the outer shape of the stainless steel container body was measured with a theodolite and with a dial gauge. Outer shapes were sampled at six cross sections marked as Sections 0, 1, 2, 3, 4', and 4, which were positioned at 21 mm, 583 mm, 1143 mm, 1705 mm, 2218 mm, and 2268 mm away from the rear face of the flange, respectively.

Figure 5.48 (a) shows the setup to measure the horizontal bending of the container body. The gas container was laid with the Tube A side up being supported at two points: the bottom of its flange and the tail. In order to minimize the friction, the flange was put on a polyethylene block. The level of the container body was confirmed by putting a spirit level on Tube A in its midst. There, the gradient was less than 10^{-4}. Because of the vertical bending of the container body, however, we were not able to determine the gradient in further accuracy.

Then, a theodolite was set about 3 m away from the tail just above a point on the line passing through the horizontal center mark on the flange and the point of the tail so as to make the station point of the theodolite to come precisely in the vertical plane containing the other two points.

We measured the vertical- and horizontal angles viewed from the theodolite against the top edges of the left- and right sides of Tube A at its five cross sections, Sections 0, 1, 2, 3, and 4', as well as some vertices out of the flange and the caudal block, and the point of the tail. The estimated horizontal bending of the gas container body measured with the theodolite is shown in Table 5.4. The maximum horizontal bending was 0.56 ± 0.20 mm. We have summed the sources of errors in quadrature which are listed in Table 5.5. Among them, the reading error of the theodolite finally dominated the total estimated errors. Thus, the estimated error at Section 0 was relatively large since it was at the farthest about 5 m away from the theodolite.

Figure 5.48 (b) shows the setup to measure the vertical bending of the gas container body. The gas container was laid with the Tube D side up. The level and the height of the gas container was adjusted using shims so that the vertical center mark on the flange and the point of the tail came in the same level plane as the station point of the theodolite. Then, we measured the vertical- and horizontal angles against the center line of the container body at its five cross sections, some vertices out of the flange and the caudal block, and the point of the tail. Here, we used the visual boundary between Tubes B and C as the vertical center of the container body. The result is shown in the right most column of Table 5.4. The vertical bending of the gas container body was 1.02 ± 0.13 mm at the maximum.

We also used a dial gauge to measure the horizontal bending of the gas container body. Figure 5.49 show the setup of this measurement. First, the gas

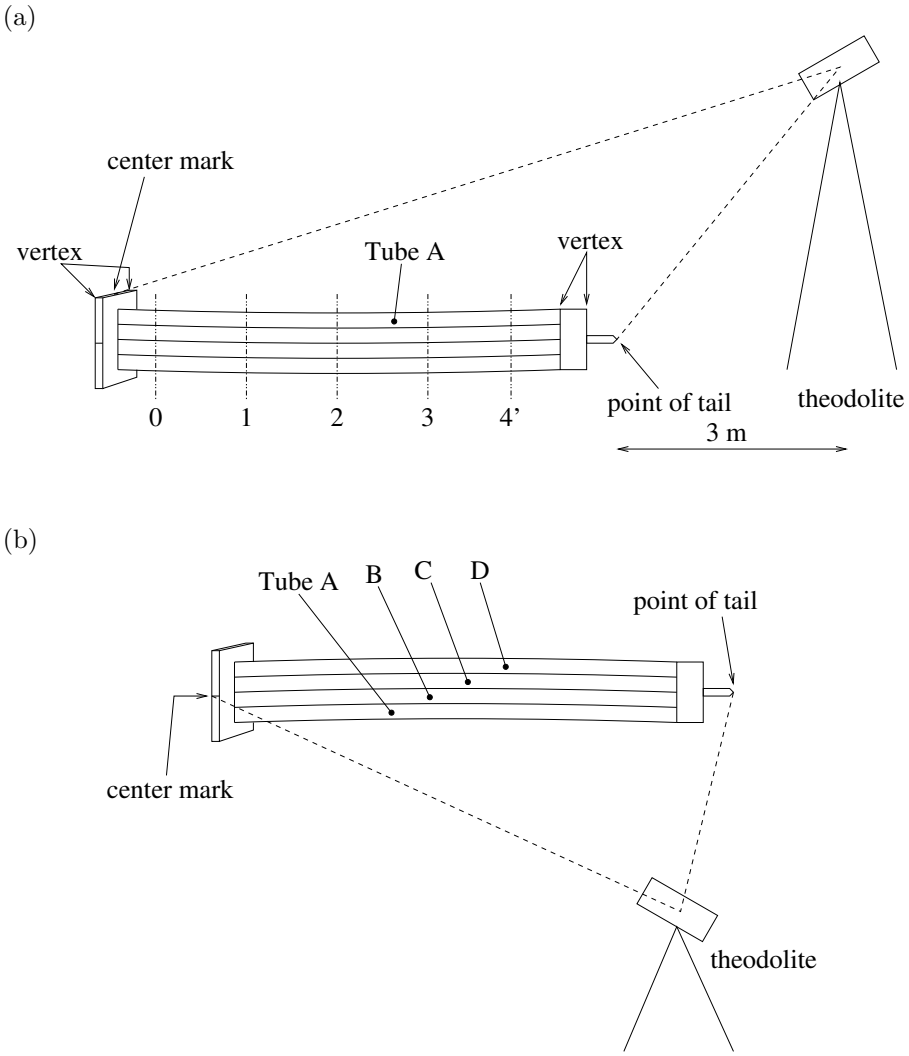

Figure 5.48: Setups to measure (a) the horizontal- and (b) vertical bending of the gas container with a theodolite.

	horizontal		vertical
	(dial gauge)	(theodolite)	(theodolite)
Section 0	-0.05 ± 0.02	$+0.06 \pm 0.31$	$+0.19 \pm 0.14$
Section 1	$+0.34 \pm 0.02$	$+0.37 \pm 0.25$	$+1.02 \pm 0.13$
Section 2	$+0.44 \pm 0.02$	$+0.56 \pm 0.20$	$+0.99 \pm 0.12$
Section 3	$+0.34 \pm 0.02$	$+0.22 \pm 0.17$	$+0.15 \pm 0.12$
Section 4'	—	$+0.02 \pm 0.16$	-0.13 ± 0.12
Section 4	-0.13 ± 0.01	—	—

Table 5.4: Overall bending of the gas container. The vertical bending is common to four tubes, since they are joined side-by-side without gap. The horizontal bending measured with a theodolite is considered to be only valid for Tube A. The horizontal bendings measured with a dial gauge are the average of Tubes B, C and D.

source of error	estimated error
reading error of theodolite	10"
level of theodolite	10"
position accuracy of theodolite by optical plumb	0.3 mm
ambiguity of scribe line on flange	0.05 mm
extrapolation accuracy of vertices	0.1 mm
ambiguity of boundary between Tubes B & C	0.1 mm
ambiguity of side face of a tube	0.1 mm
z-position of cross sections	2 mm

Table 5.5: Sources of error considered in the measurement of the outer shape of the gas container.

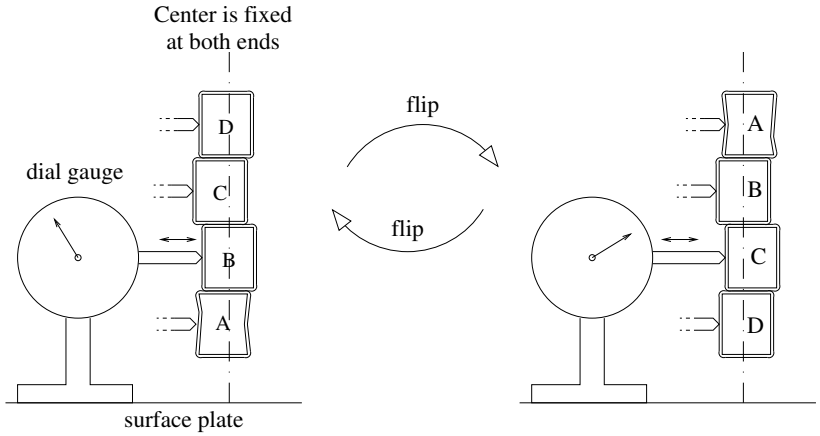

Figure 5.49: Setup to measure the horizontal bending of the gas container with a dial gauge. The gas container was rotated by 180° and the change of the distance from the dial gauge was measured. In the figure, the irregularities are not representing the truth. The actual irregularities are hardly noticeable to the eye.

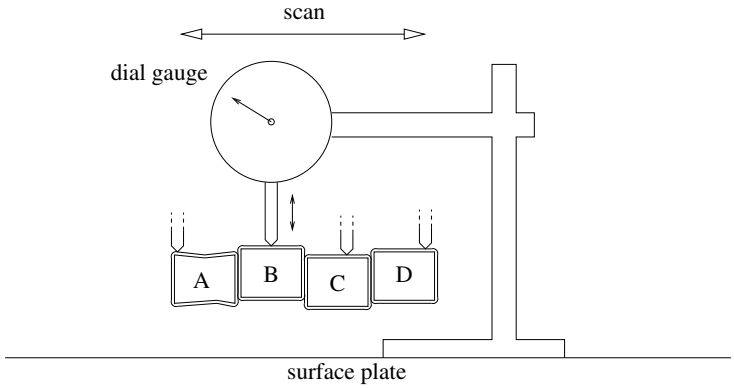

Figure 5.50: Setup to measure the irregularity of each tube. The irregularities are exaggerated.

container was laid with the Tube D side up. We fixed its center by laying the gas container on its flange and its caudal block against fixed walls which are fixed on a surface plate. The dial gauge was also fixed on the surface plate, and the distance between the dial gauge and the side face of the gas container was measured. Then, the gas container was rotated by a half turn, laid likewise but with the Tube A side up, and the change in the dial gauge was recorded. To evaluate the reproducibility of this measurement, the gas container was flipped again to the first position, and the distance was measured. We repeated this set of measurements at each heights at the center of four square pipes along five lines at Sections 0, 1, 2, 3 and 4.

In the above measurement, only the differences between the left side of Tube A and the right side of Tube D, or the right side of Tube B and the left side of Tube C, vise versa, are measured. Therefore, we need to know the proper deviation of each tube among the set of tubes or the irregularities of the side faces of the container body in order to know the bending of the whole container body. Figure 5.50 shows the setup to measure the irregularities of the side faces along the cross section lines with the dial gauge. The gas container was laid flatly and the height was measured along the line of Sections 0, 1, 2, 3, 4 and 4'. This time, the dial gauge was made free to slide on the surface plate. We only used the relative height within each cross section lines for the following calculation. Since the gas container was vertically thin in this position, it sagged considerably by its own weight. Thus the absolute heights are of less values.

Except for Section 4', the horizontal bending of the gas container as well as the proper deviations of each tubes was reconstructed by combining the above measurement of irregularities and the former measurement of the left-to-right differences using the least squares method.

Figure 5.51 shows the horizontal deviations from the reference surfaces including the irregularities and the horizontal bending as a cross section views of the gas container body. Each sub-picture corresponds to each outline at Sections 0, 1, 2, 3, 4', and 4. Two blue vertical lines in each sub-picture indicate the left and right reference surfaces, and the light blue lines beside them correspond to ± 0.5 mm of deviations relative to the reference. In the figure, the horizontal deviations are magnified by five times, since the actual deviations are

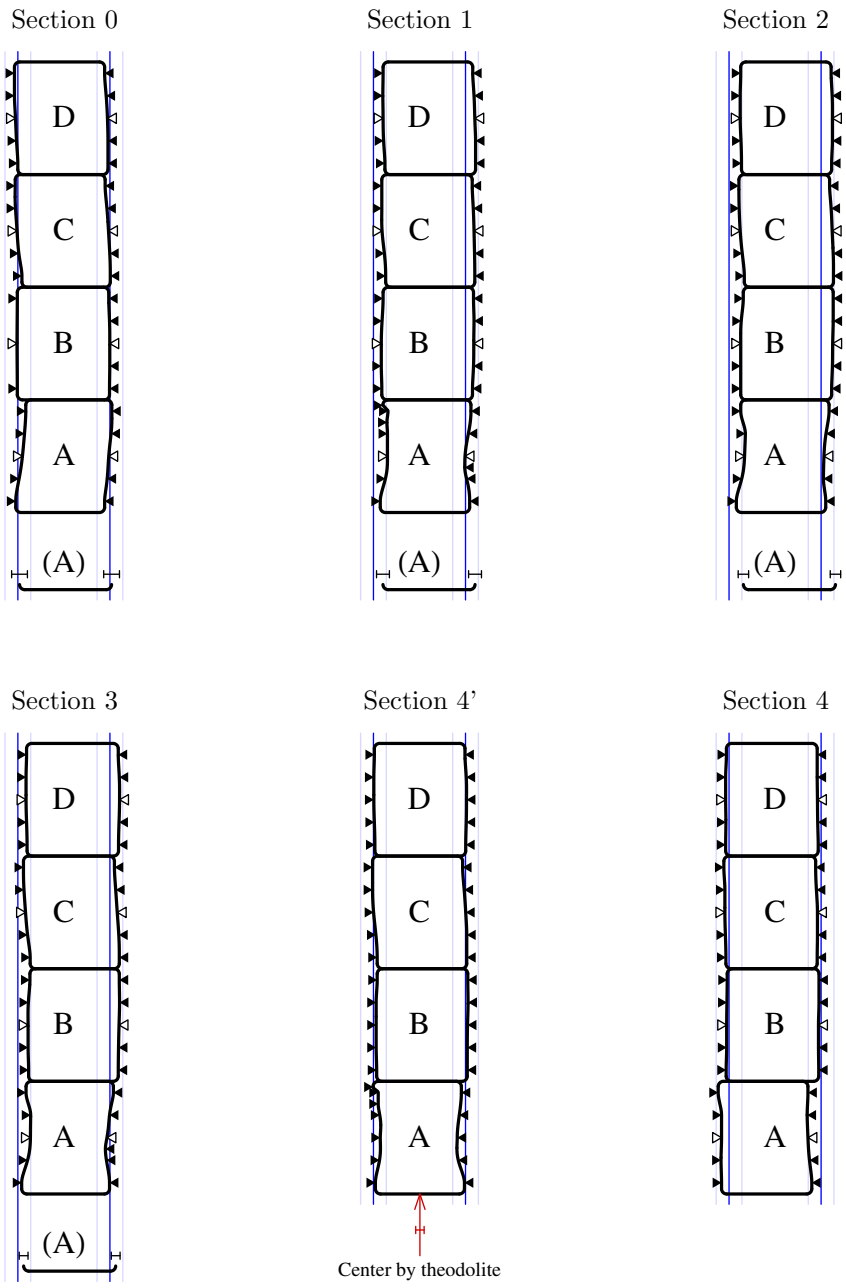

Figure 5.51: Horizontal deviations of the gas container body from the reference surfaces represented as cross section views at Sections 0, 1, 2, 3, 4' and 4. The deviations are magnified by five times. The detail is described in text.

too small to be manifest. The small triangles indicate the sampling points of the measurement of the irregularities. The open triangles indicate the points where the left-to-right differences were also measured.

We can observe that the outline of Tube A is more distorted by bending inwards than the other three. Therefore, we left the pipe width of Tube A as a free parameter, and the mean of Tubes B, C, and D are assumed to have the designed pipe width of 17.9 mm in the fitting. Although the bendings can be obtained with high accuracy with this measurement, it tells nothing about the absolute pipe widths.

The reproducibility of the dial gauge reading was better than 0.04 mm for the same setup and the same position. We used this value, $\delta_{\mathrm{dial}} = 0.04\,\mathrm{mm}$, as the measurement error of the dial gauge. The estimated position error of each sampling points of the dial gauge, the triangles in Fig. 5.51, would be of the order of a few millimeters, since the sampling points were determined by the eye. To account for this error, we conservatively used the dispersion from the center value, the open triangles, of all the sampling points belonging to the same tube as the center. All the errors were added in quadrature. After all, the amount of error for each dial gauge reading at the center of each tube were estimated to be:

$$\delta x_{\mathrm{center}} = \sqrt{\delta^2_{\mathrm{dial}} + \frac{1}{N} \sum_{i \in \text{same tube}} (x_i - x_{\mathrm{center}})^2}, \tag{5.34}$$

where x_{center} is the dial gauge reading sampled at the center of a tube, and $\{x_i\}$ are the other values sampled within the same tube. The best fit result for the horizontal bending at each cross section is shown in Table 5.4, where the values are the averages of Tubes B, C, and D.

For Sections 0, 1, 2 and 3, the Tube-A positions obtained by the theodolite measurement are shown below the cross sections for comparison, where each theodolite result is shown only as the bottom part of the square pipe and it is drawn as if Tube A had the correct width. The error bars at the edges are the estimated errors of the theodolite measurement. Except for Section 2, two independent measurements of the horizontal bending agreed within the error bars. The aberration of Section 2 is still marginal.

For Section 4', the horizontal bending estimated from the theodolite measurement is combined with the irregularity obtained with the dial gauge scan measurement, where the center of the bottom face of Tube A was aligned to the estimated center by the theodolite measurement. The red arrow with a error bar in the figure shows the estimated center of Tube A, where the deviation is also magnified by five times.

5.5.8 Measurement of thermal conductance

Prior to the solar observation, the thermal conductance of the gas container was measured. Figure 5.52 shows the experimental setup for this measurement. The helioscope, or the gas container was directed to the horizon. The tail was heated by a heater with a resistance of 318.7 Ω, and the temperature difference between the tail and the flange was observed by two Lakeshore CGR thermistors, T3 and T4. We did not used the values from thermistor T5, since it showed temperatures 0.5% higher than T3 or T4 when the heater was being switched off.

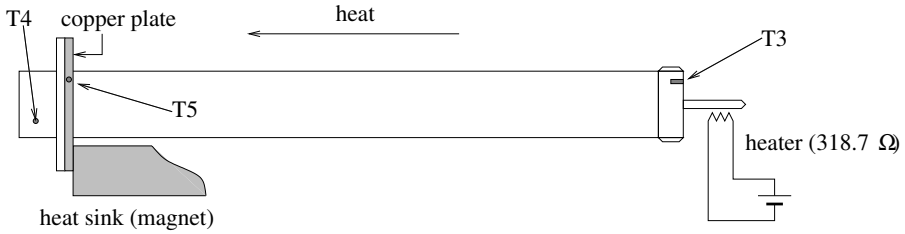

Figure 5.52: Experimental setup for the measurement of the thermal conductance of the gas container.

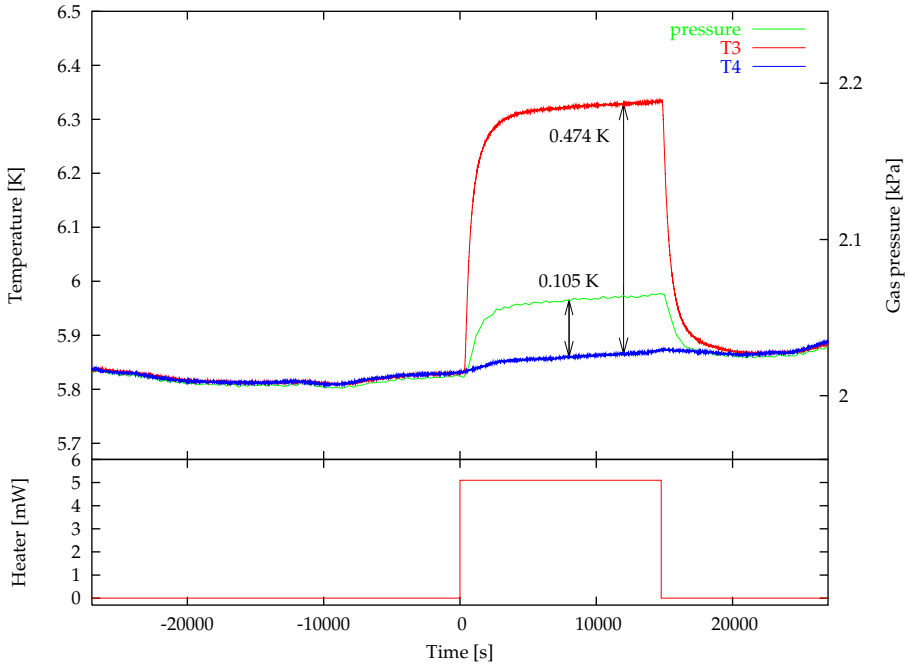

Figure 5.53: Temperature change of the gas container by heat injection at the tail.

It is considered that T5 was thermally decoupled from the subject somehow or other, and that we were seeing spuriously higher temperature by its self heating.

Figure 5.53 shows the temperature change when a heater current of 4 mA was applied under a magnetic field of 4 T, namely the magnet was fully excited. The gas pressure is also plotted in the same figure where the pressure value is scaled so that it indicate the averaged temperature of the gas approximately.

One can observe that T3 and gas (p) had reached to a steady state after 5000 seconds or so. As the temperature step by the heat injection was 0.474 K, the thermal conductance of the gas container is estimated to be

$$\frac{(4\,\mathrm{mA})^2 \times 318.7\,\Omega}{0.474\,\mathrm{K}} = 1.1 \times 10^{-2}\,\mathrm{W/K}. \tag{5.35}$$

Considering that the base temperature was rising gradually during this measure-

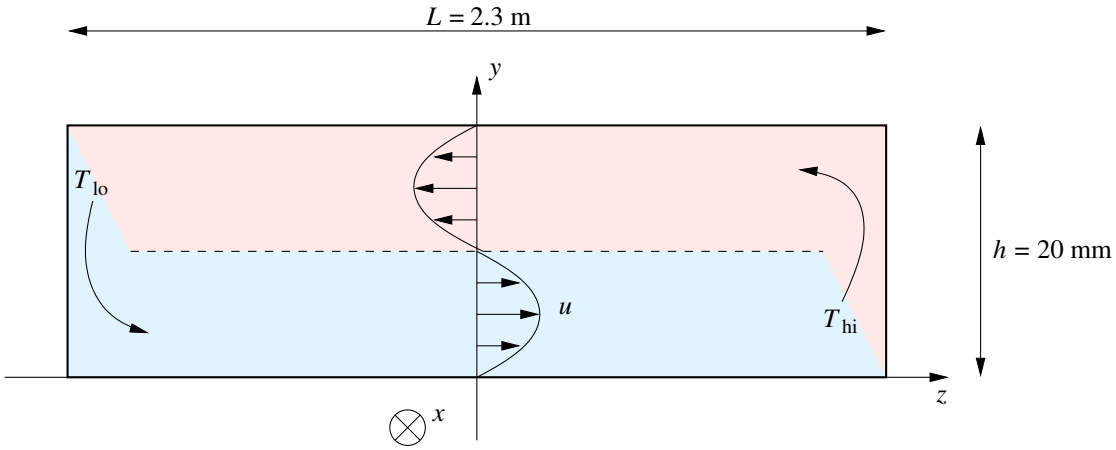

Figure 5.54: Idealized model of convection in the tube.

ment, the thermal conductance can be estimated systematically larger than the truth. However, such effect is practically negligible, since the base temperature rise during the time of relaxation is much smaller than the above temperature step.

Above naive evaluation is very close to the previous conservative estimation, Eq. (5.33), presumably by a coincidence, however, let us consider some side effects here.

Thermal conductance through gas can contribute in parallel to conduction by the gas container. As the thermal conductivity of helium gas at around 6 K is $\lambda \sim 1 \times 10^{-2}\,\mathrm{W/(K \cdot m)}$ [80], the heat transfer by conduction is estimated to be

$$\frac{\dot{Q}}{\delta T} = \frac{4hw\lambda}{L} \sim 7 \times 10^{-6}\,\mathrm{W/K}, \tag{5.36}$$

where $w = 16\,\mathrm{mm}$ is the inner width of the square pipe, and $h = 20\,\mathrm{mm}$ is the inner height. This effect is negligible.

Helium gas in the container might also carry non-negligible heat by convection, since the container was laid horizontally during the measurement. It is difficult to tell the precise heat flow by convection, but we can estimate the order with a simplified model as illustrated in Fig. 5.54. Here, gas is assumed to be vertically split into two layers along each square tube. We assume that the heat exchange between gas and the wall of the container is perfect at the ends, but neglect any other heat exchange. Then, the temperature of gas from the left end through the upper half of the layers is equal to the high side temperature T_{hi}, and that from right end through the lower half is equal to the low side temperature T_{lo}. In each layer, laminar flow is considered to be dominating, where the upper half flows from left to right, and the lower half flows from right to left.

Let us concentrate on the lower laminar flow. When the temperature difference is small, we can safely assume that the density ρ, and the coefficient of viscosity η are constant, and can neglect the effect of gravity. Then, Navier–

Stockes' equation is simplified as

$$\rho\left[\frac{\partial \boldsymbol{u}}{\partial t} + (\boldsymbol{u}\cdot\nabla)\boldsymbol{u}\right] = -\nabla p + \eta\nabla^2\boldsymbol{u}, \tag{5.37}$$

and

$$\nabla\cdot\boldsymbol{u} = 0. \tag{5.38}$$

We will also neglect the friction by the side wall so that the model is symmetric along depth, $\partial_x = 0$. As long as a steady laminar flow is considered, $\partial_t = 0$, $u_x = u_y = 0$. Because the flow is symmetric along the z-axis, $\partial_z \boldsymbol{u} = 0$. Then, the flow which satisfies the boundary condition $u_z = 0$ at $y = 0, h/2$ is trivially given by

$$u_z = \frac{\partial_z p}{2\eta} y(y - h/2), \tag{5.39}$$

where the gradient of pressure $\partial_z p$ is a constant along the flow. The pressure difference which is generating upper and lower flow should balance the density difference between the gas at the two ends:

$$2L\partial_z p = \frac{gh}{2}(\rho_{\rm hi} - \rho_{\rm lo}) \simeq \frac{g\rho h}{2}\left(\frac{T_{\rm lo}}{T_{\rm hi}} - 1\right). \tag{5.40}$$

Thus, we find for the flow rate as

$$u_z = \frac{g\rho h}{8\eta L}\left(1 - \frac{T_{\rm lo}}{T_{\rm hi}}\right) y(h/2 - y). \tag{5.41}$$

The estimated maximum flow velocity is as slow as

$$u_z^{\rm max} = \frac{g\rho h^3}{128\eta L} = 2.5\times 10^{-3}\,{\rm m/s}. \tag{5.42}$$

We can calculate the Reynolds number of this system by

$${\rm Re} = \frac{\rho u_z^{\rm max} h}{\eta} \sim 6, \tag{5.43}$$

which is small enough to support the laminar flow picture. The heat transfer by four lanes of convection is then

$$\dot{Q} = c_p \delta T \times 4N \int_0^w dx \int_0^{h/2} dy\, u_z \tag{5.44}$$

$$= 4.4\times 10^{-4}\,{\rm W}, \tag{5.45}$$

or

$$\frac{\dot{Q}}{\delta T} = 9\times 10^{-4}\,{\rm W/K}, \tag{5.46}$$

where $c_p \sim 5/2R = 21\,{\rm J/K\cdot mol}$ is the specific heat at constant pressure, N is the molar density, and $\delta T = T_{\rm hi} - T_{\rm lo}$. This value is one order of magnitude

smaller than the heat conducted by the container. Friction by the side walls would affect the flow velocity to decrease. Actual temperature distribution will not split into two layers: $T_{\rm hi}$ and $T_{\rm lo}$. Buoyancy of locally warmed or cooled gas would push the flow toward the ceiling and the floor. Thereby, actual flow will more like Z-shaped. This also affect the flow velocity to decrease as well as the effective flow volume which are contributing to heat transfer. Heat exchange between gas and the wall in mid course of the tube will largely suppress the driving force of the convection.

Finally, since thermistor T3 is actually measuring the temperature of the caudal block which is screwed on to the end plugs of the pipes, we will see the contact resistance between the end plugs and the caudal block in series. The amount of step of the gas pressure in Fig. 5.53 implies somewhat better thermal conductance in the reality.

Assuming that gas was nearly in thermal equilibrium with its local temperature of the gas container, the pressure would indicate the average temperature of gas, i.e., the pressure should correspond to the middle point of T3 and T4 temperature. By the second order virial expansion, the gas pressure is given as

$$p \approx NRT(1 + BN + CN^2), \tag{5.47}$$

where T is the temperature, $R = 8.314510\,\mathrm{J/K{\cdot}mol}$ is the gas constant, and B, C are the virial coefficients. According to the estimation described in Section 6.2, $N = 41.65\,\mathrm{mol/m^3}$. The interpolated values of B and C at 5.8 K are $B = -5.58 \times 10^{-5}\mathrm{m^3/mol}$ and $C = 1.286 \times 10^{-9}\mathrm{m^6/mol^2}$, respectively. Thus, the contributions of the first and second order virial terms are small. Neglecting the temperature dependence of the virial coefficients, we can estimate the average temperature as

$$T_{\rm gas} = 2.894\,\mathrm{K} \times \left(\frac{p}{1\,\mathrm{kPa}}\right). \tag{5.48}$$

Figure 5.53 shows that the average temperature of gas estimated as above rose by 0.105 K which is only 22% of T3 − T4. This implies that about half of the measured thermal resistance could be the contact resistance between the container body and the caudal block. Therefore, the actual thermal conductance of the body of the gas container is expected to be about twice as good as the previous estimation. Anyway the designed thermal conductance is considered to be achieved.

5.5.9 Quench exercise

On August 1, 2000, during the Phase II measurement, actual pressure change by a quench of the magnet was measured, where the magnet was forced to quench with helium gas of $41.65\,\mathrm{mol/m^3}$ being held in the gas container. The quench was generated by heating the PCS with its attached heater while the magnet was fully excited.

Figure 5.55 shows the pressure change during the quench. It tripled in two minutes, and reached its maximum in two hours. The pressure rise was fast but not as fast as that of the magnet temperature. The maximum pressure corresponded to the gas temperature of 38 K.

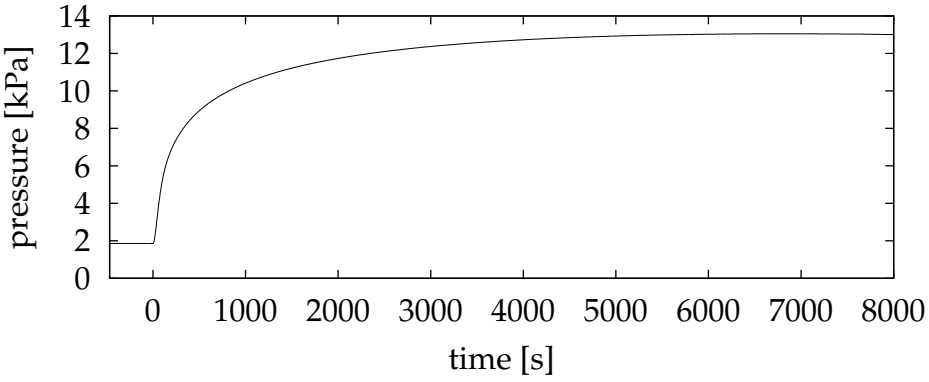

Figure 5.55: Pressure change during a quench.

5.6 Measurement of geometry of the components

The overall effective area of the X-ray detector depends not only on the geometry of the X-ray detector itself, but also on the alignments between the internal components, including the X-ray detector, the X-ray window, and the gas container. They were measured precisely from their exterior using the theodolite while the vacuum vessel of the helioscope was open.

The axis of the helioscope is defined by two cross hairs at the edges of the vacuum vessel. The 3-dimensional position of the vertex of each components can be defined relative to these cross hairs. In addition to the structural vertices, markings on some components to indicate their precise positions are also measured in the same way. The copper shielding box of the PIN photodiode X-ray detector has hairline markings on its back to indicate the center. The gas container has also markings on the surfaces of its flange.

Figure 5.56 illustrates the usage of the theodolite to determine the position of a vertex of a component. By placing the theodolite in line with the cross hairs, we can measure the elevation angle of the helioscope, $\theta_{\rm alt}$. The view point of this position is indicated by V_1 in the figure. From there, we also measured the angles of the vertex, X, in the horizontal and vertical planes, θ_x and θ_y, respectively. The theodolite is equipped with a scope which lets us see the perpendicular foot of the view point, V_1, on the floor downward (optical plumb). By viewing the vertex from another angle, V_2, we can also mark the perpendicular foot of X on the floor. Then, the horizontal distance, L, between V_1 and X was measured with a scale.

From $\theta_{\rm alt}$, θ_x, θ_y, and L, we calculated the position of X in the xy plane with respect to the helioscope axis as:

$$(x, y) = \left(L \sin\theta_x, \frac{L \sin(\theta_y - \theta_{\rm alt})}{\cos\theta_y} \right). \tag{5.49}$$

With respect to the coordinate along z, we used the accumulative depths of designed value of each component since the precision of machining was much higher than the measured values of L and there is no play along this axis except for the indium sealing at both ends of the intervening box.

Since the magnet does not have much reliable markings on it, however, the

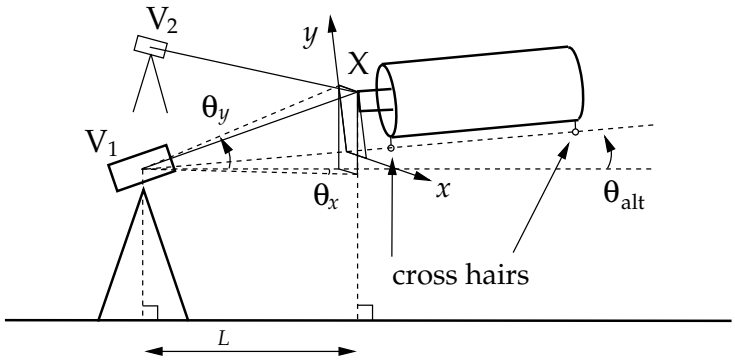

Figure 5.56: Method used to measure the 3-dimensional position of a vertex relative to the cross hairs using the theodolite.

spatial relationship between the magnet and the gas container was determined by measuring the gap around the gas container.

Table 5.6 shows the calculated positions of each component. Instead of their respective vertices, the positions of the gas container and the copper shielding box are expressed as the center positions of their respective end faces and their rotational angles around the z-axis, because of their symmetry as well as their rigid structure. Sources of uncertainty considered in determining these values are listed in Table 5.7, which are summed in quadrature. Rigidity of the positions of the internal components with respect to the helioscope axis against evacuation, cooling, or inclination of the magnet was thoroughly confirmed in past times [94].

z axis values		
PIN photodiodes	z_{pin}	1635.2
X-ray window	z_{win}	1229.4
flange	z_{flange}	1193.2
measured cross-	z_{X_0}	1162.6
sections of pipe	z_{X_1}	600.1
	z_{X_2}	40.0
	z_{X_3}	−522.2
	$z_{X_{4'}}$	−1034.7
	z_{X_4}	−1084.7
end of pipe	z_{bot}	−1079.8
point of tail	z_{spine}	−1222.0

(x, y) values relative to cross hair		
copper shielding box:		
center	$(x_{\mathrm{Cu}}, y_{\mathrm{Cu}})$	$(-0.37 \pm 0.25, 368.76 \pm 0.26)$
tilt	θ_{Cu}	$(-3.04 \pm 1.72) \times 10^{-3}$
gas container:		
flange center	$(x_{\mathrm{flange}}, y_{\mathrm{flange}})$	$(0.19 \pm 0.16, 367.43 \pm 0.16)$
point of tail	$(x_{\mathrm{spine}}, y_{\mathrm{spine}})$	$(0.69 \pm 0.14, 367.26 \pm 0.15)$
tilt	θ_{tube}	$(1.29 \pm 1.22) \times 10^{-3}$

(x, y) values relative to magnet		
flange center	(x, y)	$(0.0 \pm 0.5, -1.0 \pm 0.5)$
point of tail	(x, y)	$(0.0 \pm 0.5, -1.25 \pm 0.5)$

Table 5.6: Geometrical parameters of important vertices. 'Flange' is at the detector side of the gas container. The values of its front face (detector side) are shown below. 'Point of tail' is a reference point at the solar side of the gas container. The conical vertex at the end the pole represents its position.

source of uncertainty	influence	estimate
reading error of theodolite	$\delta\theta$	10"
horizontal distances	δL	0.2 mm
gap measurement	δx, δy	0.5 mm

Table 5.7: Sources of uncertainty in determining the positions of vertices.

Chapter 6

Phase II measurement and analysis

We started the Phase II measurement with a simple gas filling system where no countermeasure against over pressure of the helium gas was employed. Helium filling line inside the cryostat was made minimally thin to ensure the minimal heat injection from it. From safety consideration, we limited the gas density as low as $m_\gamma = 0.263\,\mathrm{eV}$. In this chapter, we describe the details of the measurement where we searched for solar axions in a mass region up to $m_a \lesssim 0.27\,\mathrm{eV}$.

6.1 Phase II solar tracking schedule

During from July 29 through September 1, 2000, we performed a series of measurements searching for solar axions at ten distinct photon mass settings which are listed in Table 6.1. In this measurement, the mass range up to $m_a < 0.27\,\mathrm{eV}$ was scanned. Each run consists of two parts, the solar observation and the background measurement. While the sun is in the trackable range of the helioscope, i.e., $-28^\circ < \theta_{\mathrm{altitude}} < +28^\circ$, it is directed to the sun. For the rest of time, the background spectrum was measured. In the background measurement, the helioscope traced the same trajectory as in the solar observation but in the reverse course in order to minimize systematics. The tracking velocity during background observation was scaled appropriately, since the measurement times of neither solar- nor background observations are not exactly one half of a day.

One day measurement was divided into two parts of 12 hours each: the sunrise runs and the sunset runs. They switched from one to another at 10:30 and 22:30 every day. Although the helioscope can thus continue tracking for solar- or background measurements 24 hours a day, we still needed human intervention to prevent the cables and helium hoses of the refrigerators from tangling around the helioscope. After all, the sunrise runs were performed only on July 30 and 31 over the Phase II measurement, and the apparatus was rested at night otherwise.

Figure 6.1 shows the trace of two-day movement of the axion helioscope during from 22:00 on July 29 through the end of July 31, as an example, where the altitudinal- and azimuthal angles of the helioscope are plotted as functions of time. The solid curves show the direction of the helioscope, and the dotted

molar density	m_γ	live time [s]	
[mol/m^3]	[eV]	solar run	background
4.137	0.083	27318.816	37825.514
8.325	0.118	26430.876	36094.075
12.52	0.144	26502.816	36686.392
16.62	0.166	23330.053	35228.512
20.80	0.186	25741.289	36481.875
25.15	0.204	32623.132	37887.319
29.19	0.220	25943.009	36648.364
33.70	0.237	40476.879	52622.264
37.58	0.250	12995.509	31141.677
($*1$) ditto		12572.399	18515.919
41.65	0.263	54914.123	67681.070

Table 6.1: Table of the gas settings and the live times. The live time values are not corrected for deficit by microphonic noise. The extra row marked by $*1$ is of the period during the down of `pin0` signal. The other rows are of the period while all the photodiodes were working.

curves show the solar trajectory.

Every time after a new gas density was set, the internal ^{55}Fe source was exposed to collect data for energy calibration. They are not only needed to calibrate the energy scale and to study the gain stability, but also to obtain signal template of the waveforms which is crucial in the waveform analysis. Detail of the waveform analysis is discussed in Section 6.3 and the analysis of them as the calibration data is discussed in Section 6.4. They were also used as a guide to discriminate a group of waveforms not of X-ray photons as described in Section 6.6.3.

6.2 Gas densities

In the Phase II measurement, no countermeasure against over pressure of the helium gas was employed. The worst case would happen if air had mistakenly entered the cold helium pipework and had clogged it while the gas container was filly charged. The melting point of nitrogen is 63.14 K and moisture would stay solid up to 273.15 K. Therefore, the maximum density of helium gas was determined so that its pressure is as low as 1 atmosphere even at the melting point of water. Helium gas was charged to the gas container while it was at room temperature. The measured pressure at $T = 291.1$ K was $p = 97.03$ kPa on March 22, 2000. Since helium gas at this state can be treated as ideal gas, the density in the gas container was estimated to be

$$N_{100}^{\mathrm{room}} = 40.09\,\mathrm{mol/m^3}. \tag{6.1}$$

While the magnet was being cooled to its operating temperature, the main valve of the gas container (valve V4 in Fig. 5.44) was shut off and the helium gas was kept confined in the container. On August 2, 2000, the pressure was $p = 1.9$ kPa and the temperature of the gas container was $T = 5.5$ K. In the

following measurements, we set the gas pressure to about the multiples of tenth of this pressure with a manually operated gas controlling system described in Section 5.5.5.

The precise helium densities of each gas settings can be estimated from the measured T, and p using the equation of state. By the virial expansion up to the second order, the relation between gas pressure p and the molar density N at a temperature T is given as

$$p = NRT(1 + BN + CN^2), \tag{6.2}$$

where $R = 8.314510\,\mathrm{J/K \cdot mol}$ is the gas constant, B and C are the first and second virial coefficients. We approximated the temperature dependence of B, and C by

$$B(T) = \frac{b_1}{T} + \frac{b_2}{T^2}, \tag{6.3}$$

$$C(T) = \frac{c_1}{T} + \frac{c_2}{T^2}. \tag{6.4}$$

As the typical temperature and pressure in the Phase II measurement was $T \sim 5.5\,\mathrm{K}$ and $p \lesssim 2\,\mathrm{kPa}$, we picked up the mass density values from the NIST table[80] at 4×5 matrix points, which are combinations of $T = 5.1, 5.3, 5.5$, and

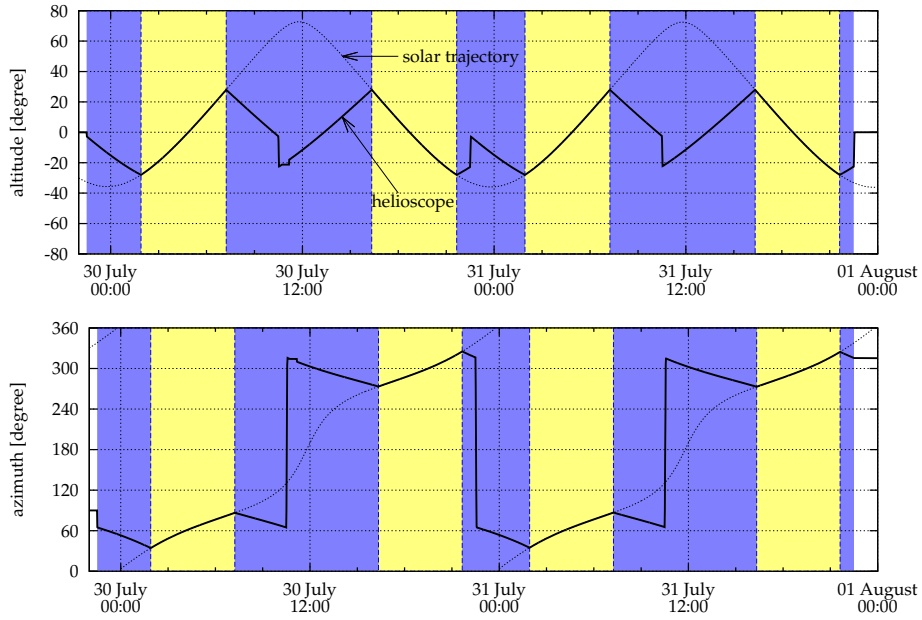

Figure 6.1: Trace of two-day movement of the axion helioscope. The upper figure shows the elevation angle, and the lower figure shows the azimuthal angle. The helioscope direction is shown as the solid curves, and the solar trajectory is shown as the dotted curves. The solar-measurement period is shown as areas shaded with yellow, and the background-measurement period is shown shaded with blue. The small disorder at around 10:40 on 30 July was caused by an abnormal termination of controlling programs by an extrinsic accident.

6.0 K for the temperatures, and $p = 0.010, 0.020, 0.040, 0.060$, and 0.080 MPa for the pressures. Then coefficients b_1, b_2, c_1, and c_2 was determined by a least-squares fitting to these points. The relative deviation of the fit function from data was better than 1.7×10^{-4} at every point of the matrix, which are far better than the estimated uncertainty of the densities in NIST table itself, 0.1% in average and 0.5% at the maximum.

The pressure values were obtained from Yokogawa MU101-AM1N whose nominal precision is 0.02% full scale or 26 Pa. The temperatures of the gas container were obtained from CGR thermistors T3 and T4 which were calibrated by Lakeshore between 4.00–40.0 K at RMS errors of 4 mK and 2.8 mK, respectively. We used the middle point of T3 and T4 as the temperature of gas although they agreed to each other within the range of error. In order to reduce the fluctuation of voltage readings, thirty-two successive measurements were averaged on-board in the Hewlett–Packard E1413 High-Speed Scanning A/D. We retrieved these averaged voltages every second. Furthermore, ten seconds of temperatures before and after each moment of the measurement of pressure were averaged in calculating the gas density.

As a result, the helium density of the fully charged "100% density" setting was determined to be

$$N_{100} = 41.65\,\mathrm{mol/m^3} \tag{6.5}$$

at the operating temperature, which was 3.9% higher than the value estimated at room temperature in Eq. (6.1). The reasons for this disagreement are because:

- The confined volume is composed both of the cold volume including the volume in the container, and of the hot volume including the volume in the pipework at higher temperatures. Since helium would move from the hot volume toward the cold volume as the pressure decreased, the molar density in the container would have increased approximately by their volume ratio, 3.2%.

- As the gas container made of stainless steel thermally contracted, the density would have increased by the rate of volume shrinkage, 0.8%.

When the above corrections are taken into account, two densities agree within the reasonable range of errors.

For 10% through 70%-density runs, the measured temperatures were taken while the magnetic field was applied. Since CGR thermistors are slightly sensitive to magnetic field, we compensated the temperatures for this influence in these runs. Since helium molar density should be constant through the excitation of the magnet, we can use the shift of the apparent molar density during an excitation as the amount to be compensated. As the result, we found that the apparent molar densities calculated at T3 and T4 are shifted by +0.43% and +0.02% under the influence of the magnetic field, respectively. We can compensate this effect without introducing additional errors, since this variation is systematic.

Readings of temperature are also affected by electric noise from the isolation amplifiers which are needed to monitor the coil voltages. The data transfer activity in CAMAC is another source of electric noise which often accompanied with the bulk data transfer from the FADCs. We observed the density shift of

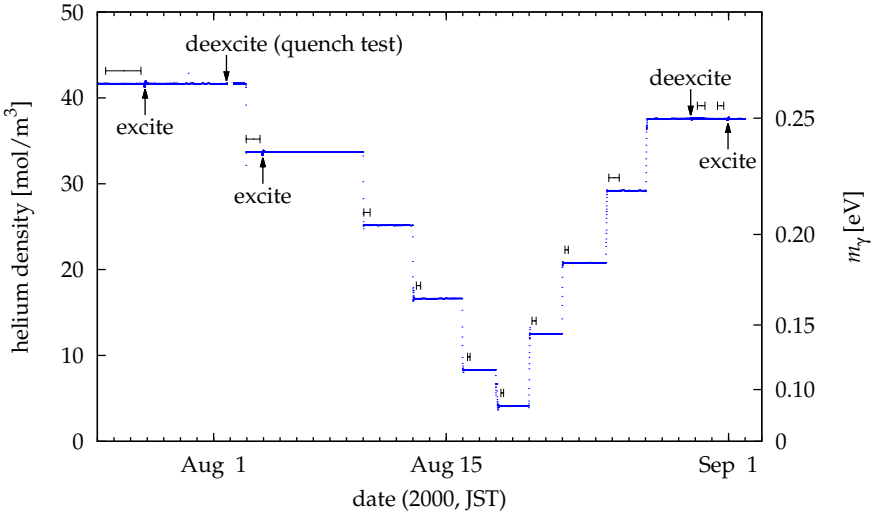

Figure 6.2: Helium density settings and scanned masses. The blue points show the molar densities of helium gas and the corresponding effective photon masses calculated from the pressure- and temperature data of the Phase II measurement. Small bars beside the plot shows the sampled intervals used to determine the final values in Table 6.1.

0.04% as the influence of the former and 0.09% for the latter. Since these shift cannot be considered to be systematic, we counted the former as an additional error of density. Against the latter, we selected data while waveforms from the X-ray detector were not being collected.

Figure 6.2 shows the calculated molar density of helium as well as the corresponding effective photon masses m_γ as a time chart. The final values are obtained by averaging values from clean intervals where FADC data transfers were not running. The sampled intervals are indicated as small bars beside the plot. In Table 6.1, we show the final values of the ten gas settings of the Phase II measurement.

The relative error of the above estimated densities was, e.g., $\delta N/N = 1.5 \times 10^{-2}$ for the 100%-density setting, and $\delta N/N = 1.4 \times 10^{-1}$ for the 10%-density. Among the origins of error, the accuracy of the pressure gauge was dominant:

$$\delta N \simeq \frac{\delta p}{k_{\mathrm{B}} T}. \tag{6.6}$$

Substituting it into Eqs. (3.19) and (3.26), we find

$$\delta q = \frac{4\pi\alpha\delta p}{m_e E k_{\mathrm{B}} T}. \tag{6.7}$$

From Eq. (3.31), the condition that the density error plays negligible role in the conversion rate is

$$\frac{\delta q L}{2} \ll \pi. \tag{6.8}$$

Therefore, the required accuracy to the pressure measurement is

$$\delta p \ll \frac{m_e E k_{\mathrm{B}} T}{2\alpha L} = 120\,\mathrm{Pa}, \tag{6.9}$$

which is fulfilled by our pressure gauge. Let us further emphasize that this error do not affect the coherence of the axion-to-photon conversion unlike the case in the thermal nonuniformity (see Section 5.5.2). Instead the maximum of the conversion rate is just shifted by this error.

6.3 Waveform analysis

Numerical pulse shaping was performed on the raw waveforms from the preamplifiers. We adopted the optimal filter which is a linear filter that would give the optimal S/N ratio for a known signal- and noise spectrum. The optimal filter has a vast area of applications including audio signal processing as well as image processing. For example, application of an optimal filtering algorithm is proposed in Ref. [99] to search for acoustic signals in ocean water produced by ultra-high-energy neutrinos in cosmic rays.

In this numerical pulse shaping method, we calculated the convolution of the optimal filter kernel and a raw waveform to generate the shaped waveform. Then, the energy of an X-ray photon was estimated from the peak value of its shaped waveform. This method gives generally higher energy resolution than other methods including the least squares fitting and it is usually faster to calculate since the calculation is straightforward and hence it requires no iterations. The optimal filter kernel needs to be calculated once from statistical parameters, and convolution needs two fast Fourier transform (FFT) per each waveforms. With this method, we were able to eliminate microphonic noise out of the raw waveforms almost completely.

6.3.1 Optimal filter

We are going to find for a signal of known shape, but unknown amplitude, and unknown position buried in random noise by the maximum likelihood method. After Ref. [99], let us start with a finite discretized data sample, $X = \{X_n\}$, where $n = 0, \ldots, M-1$ is the index with respect to time. Actually, our digital data are finite and discretized. It is considered to be the sum of the signal and random noise:

$$X_n = AS_n^{(m)} + N_n, \tag{6.10}$$

where $S_n^{(m)}$ is the shape of the signal at position m, A is its amplitude, and N_n is the random noise. In pulse shape analysis, $S_n^{(m)}$ is the impulse response function of the system for a unit impulse input at $n = m$, i.e., δ_{nm}. From causality, $S_n^{(m)} = 0$ for $n < m$. There would be some positive or negative peaks, then it would readily fall to zero long enough time after the impulse. Therefore, if M is large enough compared to the time constant of $S_n^{(m)}$, the response function can be defined cyclically without loosing generality as

$$S_n^{(m)} = S_{n-m}, \quad \text{and} \quad S_{n+M} = S_n. \tag{6.11}$$

In order to evaluate the likelihood of the signal presence in the given data, we will look at the distribution function of the random noise. The conditional probability of finding X' in the interval of $[X, X+dX]$ given no signal is related to the distribution function $f_N(X)$ of the random noise by

$$P(X' \in [X, X+dX] | \text{no signal}) = f_N(X)\, dX. \tag{6.12}$$

Likewise, from Eq. (6.10), the conditional probability of finding X' given the signal position m and the amplitude A is

$$P(X' \in [X, X+dX] | m, A) = f_N(X - AS^{(m)})\, dX. \tag{6.13}$$

In general, where the random noise is not perfectly white, the formula of $f_N(X)$ is a hard nut, since there are correlations between the different time bins. In contrast, it is quite straightforward to describe it in the frequency domain where each frequency bin is expected to distribute by a Gaussian:

$$f_{\tilde{N}}(\tilde{X}) = \frac{1}{(2\pi)^{\frac{M}{2}} \prod_k \overline{\tilde{N}}_k} \exp\left[-\frac{1}{2} \sum_k \frac{|\tilde{X}_k|^2}{\overline{\tilde{N}}_k^2} \right], \tag{6.14}$$

where $\tilde{X}$ is the Fourier transform of X:

$$\tilde{X}_k = \sum_n X_n \exp\left[\frac{2\pi i}{M} kn \right], \quad k = 0, \ldots, M-1, \tag{6.15}$$

and $\overline{\tilde{N}}_k$ is the noise spectrum such that $\langle \tilde{N}_j^* \tilde{N}_k \rangle = \delta_{jk} \overline{\tilde{N}}_k^2$. Here, the normalization factor in Eq. (6.14) is determined to fulfill the relation:

$$P(\tilde{X}' \in [\tilde{X}, \tilde{X}+d\tilde{X}] | \text{no signal}) = f_{\tilde{N}}(\tilde{X})\, d\tilde{X}, \tag{6.16}$$

where the interval is defined as $d\tilde{X} = d\tilde{X}_0 d\tilde{X}_{M/2} \prod_{k=1}^{M/2-1} d[\mathrm{Re}\, \tilde{X}_k] d[\mathrm{Im}\, \tilde{X}_k]$ since X is real.

By Eq. (6.11), the Fourier transform of $S^{(m)}$ is given by

$$\tilde{S}_k^{(m)} = \tilde{S}_k \exp\left[\frac{2\pi i}{M} km \right]. \tag{6.17}$$

Substituting the above equation into Eq. (6.13) in the frequency domain, we get

$$P(\tilde{X} \in [\tilde{X}, \tilde{X}+d\tilde{X}] | m, A) = f_{\tilde{N}}(\tilde{X}_k - A\tilde{S}_k e^{\frac{2\pi i}{M} km})\, d\tilde{X}. \tag{6.18}$$

Following the frequentist scheme, the likelihood function is defined as the probability of finding the present data X given the signal position m and the amplitude A. In the frequency domain, it is

$$L(m, A)\, d\tilde{X} \equiv P(\tilde{X} \in [\tilde{X}, \tilde{X}+d\tilde{X}] | m, A). \tag{6.19}$$

Substituting Eqs. (6.14) and (6.18) into it, we find

$$\begin{aligned} L(m, A) &= f_{\tilde{N}}(\tilde{X}_k - A\tilde{S}_k e^{\frac{2\pi i}{M} km}) \\ &= \frac{1}{(2\pi)^{\frac{M}{2}} \prod_k \tilde{N}_k} \exp\left[-\frac{1}{2} \sum_k \frac{|\tilde{X}_k - A\tilde{S}_k e^{\frac{2\pi i}{M} km}|^2}{\tilde{N}_k^2} \right]. \end{aligned} \tag{6.20}$$

The maximum likelihood estimator is given by finding the maximum of L. Instead of maximizing L, we are going to maximize the following log-likelihood function:

$$L' = -\frac{1}{2}\sum_k \frac{|\tilde{X}_k - A\tilde{S}_k e^{\frac{2\pi i}{M}km}|^2}{\tilde{N}_k^2}. \tag{6.21}$$

Apparently, L' is a monotone increasing function of L. Setting the derivative of the above equation with respect to A to zero, i.e., $\partial L'/\partial A = 0$, we find for the optimal amplitude estimate, $\bar{A}^{(m)}$, as a function of m as

$$\bar{A}^{(m)} = \frac{\sum_k \mathrm{Re}(\tilde{S}_k^* \tilde{X}_k e^{-\frac{2\pi i}{M}km})/\overline{\tilde{N}_k}^2}{\sum_k |\tilde{S}_k|^2/\overline{\tilde{N}_k}^2}. \tag{6.22}$$

Let $\{Y_n\}$ be a sequence defined by its Fourier transform:

$$\tilde{Y}_k = \tilde{H}_k \tilde{X}_k, \tag{6.23}$$

where

$$\tilde{H}_k = \frac{M\tilde{S}_k^*}{\overline{\tilde{N}_k}^2} = M\frac{|\tilde{S}_k|^2}{\overline{\tilde{N}_k}^2}\frac{1}{\tilde{S}_k}, \tag{6.24}$$

therefore

$$Y_n = \sum_k \frac{\tilde{S}_k^* \tilde{X}_k}{\overline{\tilde{N}_k}^2} \exp\left[-\frac{2\pi i}{M}kn\right]. \tag{6.25}$$

In other words, $\{Y_n\}$ is a *shaped waveform* which is the result of applying a filter with transfer function of $\tilde{H}_k$ to the input sequence of $\{X_n\}$. Since S_n and $\overline{\tilde{N}_k}^2$ are real and $\overline{\tilde{N}_k}^2$ is symmetric with respect to positive- and negative frequencies, all the elements of Y_n should also be real as well as the filter kernel H_n. Then, the numerator in Eq. (6.22) can be represented using Y_n as:

$$\begin{aligned}\sum_k \frac{\mathrm{Re}(\tilde{S}_k^* \tilde{X}_k e^{-\frac{2\pi i}{M}km})}{\overline{\tilde{N}_k}^2} &= \mathrm{Re}\left[\sum_k \frac{\tilde{S}_k^* \tilde{X}_k}{\overline{\tilde{N}_k}^2} \exp\left[-\frac{2\pi i}{M}km\right]\right] \\ &= Y_m. \end{aligned} \tag{6.26}$$

Substituting Eq. (6.26) into Eq. (6.22), we get

$$\bar{A}^{(m)} = \frac{Y_m}{Z}, \tag{6.27}$$

where $Z = \sum_k |\tilde{S}_k|^2/\overline{\tilde{N}_k}^2$.

It is worth noting that we can, in general, obtain an unphysical value $A < 0$ as a result of the frequentist estimator. In the Bayesian statistics, parameters are restricted to the physical region by the prior probabilities. With constant

prior probabilities in the physical region, we recover the frequentist result except that it is restricted to be physical as:

$$\bar{A}^{(m)} = \max\left(0, \frac{Y_m}{Z}\right). \tag{6.28}$$

The optimal signal position, $\bar{m}$, can be estimated likewise by choosing the value of m such as to maximize L. By substituting A by $\bar{A}^{(m)}$ into Eq. (6.21), we derive

$$L' = -\frac{1}{2}\sum_k \frac{|\tilde{X}_k - \bar{A}^{(m)}\tilde{S}_k e^{\frac{2\pi i}{M}km}|^2}{\tilde{N}_k^2} \tag{6.29}$$

$$= \frac{Y_m^2}{2Z} - \frac{1}{2}\sum_k \frac{|\tilde{X}_k|^2}{\overline{\tilde{N}_k^2}}. \tag{6.30}$$

The above equation means that we can estimate the optimal signal position, $\bar{m}$, and the optimal amplitude, $\bar{A}$, simply by choosing the peak value of the shaped waveform Y:

$$Y_{\bar{m}} = \max\{Y_n\}, \quad \bar{A} = \frac{Y_{\bar{m}}}{Z}. \tag{6.31}$$

If our dataset were noiseless, the deconvolution function $1/\tilde{S}_k$ could reconstruct the original amplitude A from X_n as an impulse or Dirac's delta function:

$$\frac{1}{\tilde{S}_k}\tilde{X}_k = A. \tag{6.32}$$

However, it is not in practice. The transfer function $\tilde{H}_k$ can be expressed as a combination of a filter function and the deconvolution function by

$$\tilde{H}_k = \frac{1}{\tilde{S}_k}\tilde{\Phi}_k. \tag{6.33}$$

The added filter function,

$$\tilde{\Phi}_k = \frac{|\tilde{S}_k|^2}{|\tilde{N}_k|^2}, \tag{6.34}$$

is often called the optimal filter or the Wiener filter and the whole process is called the Wiener deconvolution. When the noise spectrum is white, $|\tilde{N}_k|^2 =$ (constant), $\tilde{H}_k$ resolves into the match filter which gives the cross-correlation of S_n and X_n. The above argument will be generalized to infinite continuous functions in the limit of $t_{\text{sampling}} \to 0$ and $Mt_{\text{sampling}} \to \infty$.

6.3.2 Noise spectrum

The noise spectrum, $\overline{\tilde{N}_k}$, was obtained by gathering the waveforms while there was no physical event. The FADCs can be stopped at any timing from software independently of the trigger system. Such "fake trigger events" were inserted in the record of the usual physical events at a rate of one in ten. Since the hit pattern of the trigger in each event was recorded together with all the sixteen

waveforms, we can easily distinguish fake trigger events by the absence of trigger in them.

The standard deviation of a power spectrum estimated by a discrete Fourier transformation is always 100% of the expectation value at every frequency. In order to reduce this large error, many power spectra were averaged at each frequency.

All the noise spectra of sixteen channels are shown in Fig. 6.3. In these figures, we applied a different preprocessing from the one used to obtain the optimal filter function. As described later in Section 6.3.4, we applied a preprocessing including baseline fixing as well as multiplying by a window function to the waveforms before Fourier transformation. To obtain the optimal filter, we used the combination of the Welch window and the baseline fixing by time derivative. We applied the same preprocessing method to both noise and signal waveforms. As a result of the tricky baseline fixing, the shape of $\overline{\widetilde{N}_k}$ is skewed, which does not represent the real noise spectrum. To obtain the spectra in Section 6.3.4, on the other hand, each waveform was subtracted by the average of the whole waveform. Then, the Hann window was applied to it, which exhibits very low side robes for a somewhat wider peak.

In Fig. 6.3, we can observe that the low frequencies are raised in `pin7`, `pin8`, and `pin15`. These are consistent with the channels with larger microphonic noise. The reason why the noise level is lower in `pin8` than other channels except for the low frequencies is that the amplifier gain is lowered to prevent this channel from overflowing by microphonic noise. Little differences are noticeable in other aspects.

In order to look at the long-term variation of the noise spectra, data sets with more than 500 fake events each were selected. The frequencies were divided into three zones:

- low frequency: $k = 0, \ldots, 7$ ($0 \leq f < 78.125\,\mathrm{kHz}$),
- mid frequency: $k = 8, \ldots, 63$ ($78.125\,\mathrm{kHz} \leq f < 62.5\,\mathrm{kHz}$),
- high frequency: $k = 64, \ldots, 512$ ($62.5\,\mathrm{kHz} \leq f \leq 5\,\mathrm{MHz}$),

and the noise power spectrum was integrated over each three frequency range for each data set. In Fig. 6.4, the noise power of each frequency range is plotted with respect to time for four PIN photodiode channels, `pin1`, `pin7`, `pin8`, and `pin15`. `Pin1` represents the channels with typical noise level. `Pin7`, `pin8`, and `pin15` are channels where microphonic noise is relatively severe as described in the above. The noise power of low-, mid-, and high frequency ranges are shown in red, green, and blue, respectively. Although they are hardly visible, each data is represented as an x–y error bar. The x error bars show the interval contributing to each data set. The y error bars correspond to statistical error estimated assuming stationary noise, where the contribution of each frequency bin was combined in quadrature.

The fluctuation of the data points was larger than the naive statistical estimation. For the typical channels, it was by a factor of 2, 3, and 6 for the low-, mid-, and high frequency ranges, respectively. It was, however, still as small as a few percent of the total in each frequency range.

For `pin7`, `pin8`, and `pin15`, on the other hand, the fluctuation was certainly large in the low frequency range. However, the amplitude of $\overline{\widetilde{N}_k}$ will be cancelled

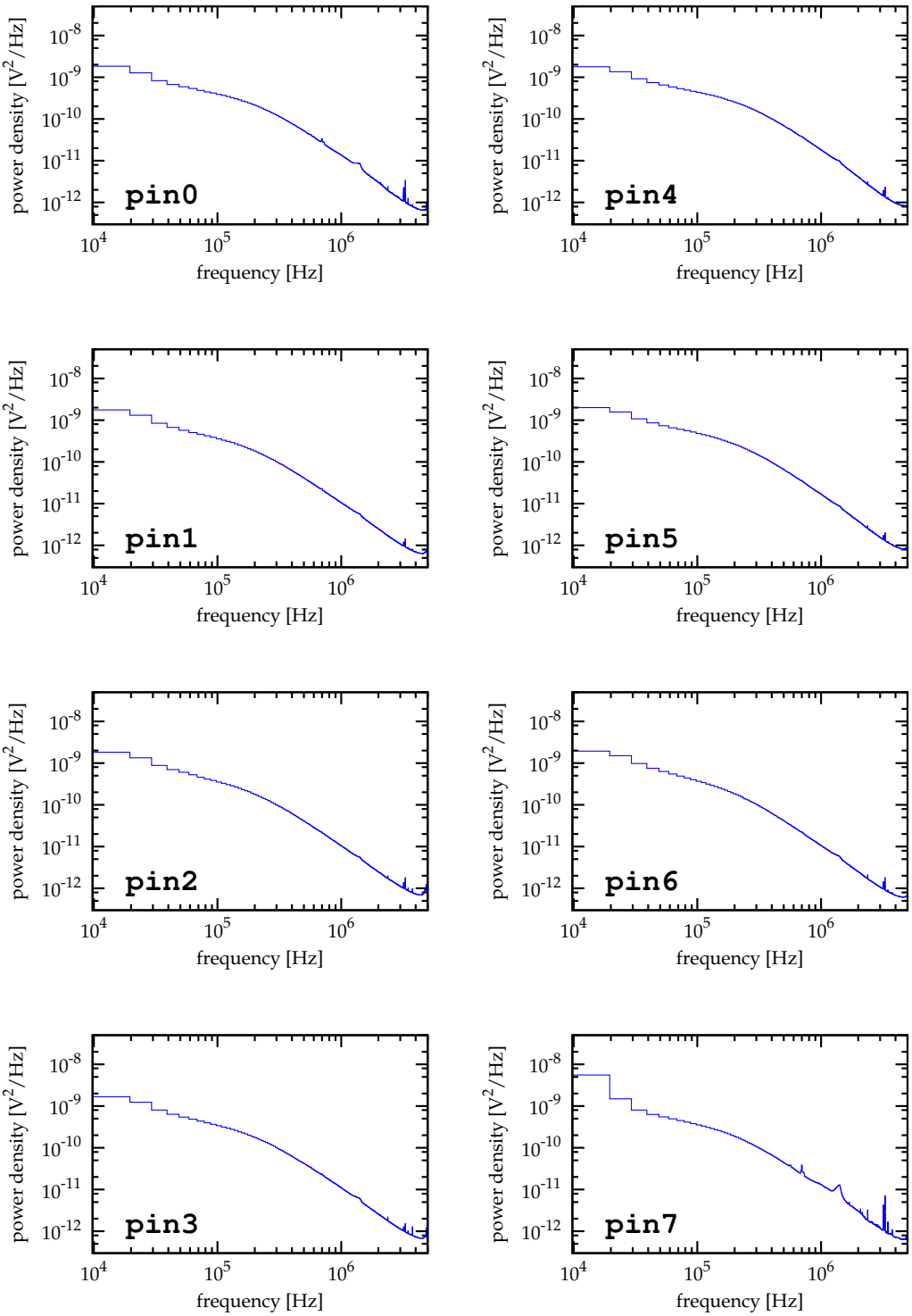

Figure 6.3: Noise power spectra of the PIN photodiodes.
(continued on the next page)

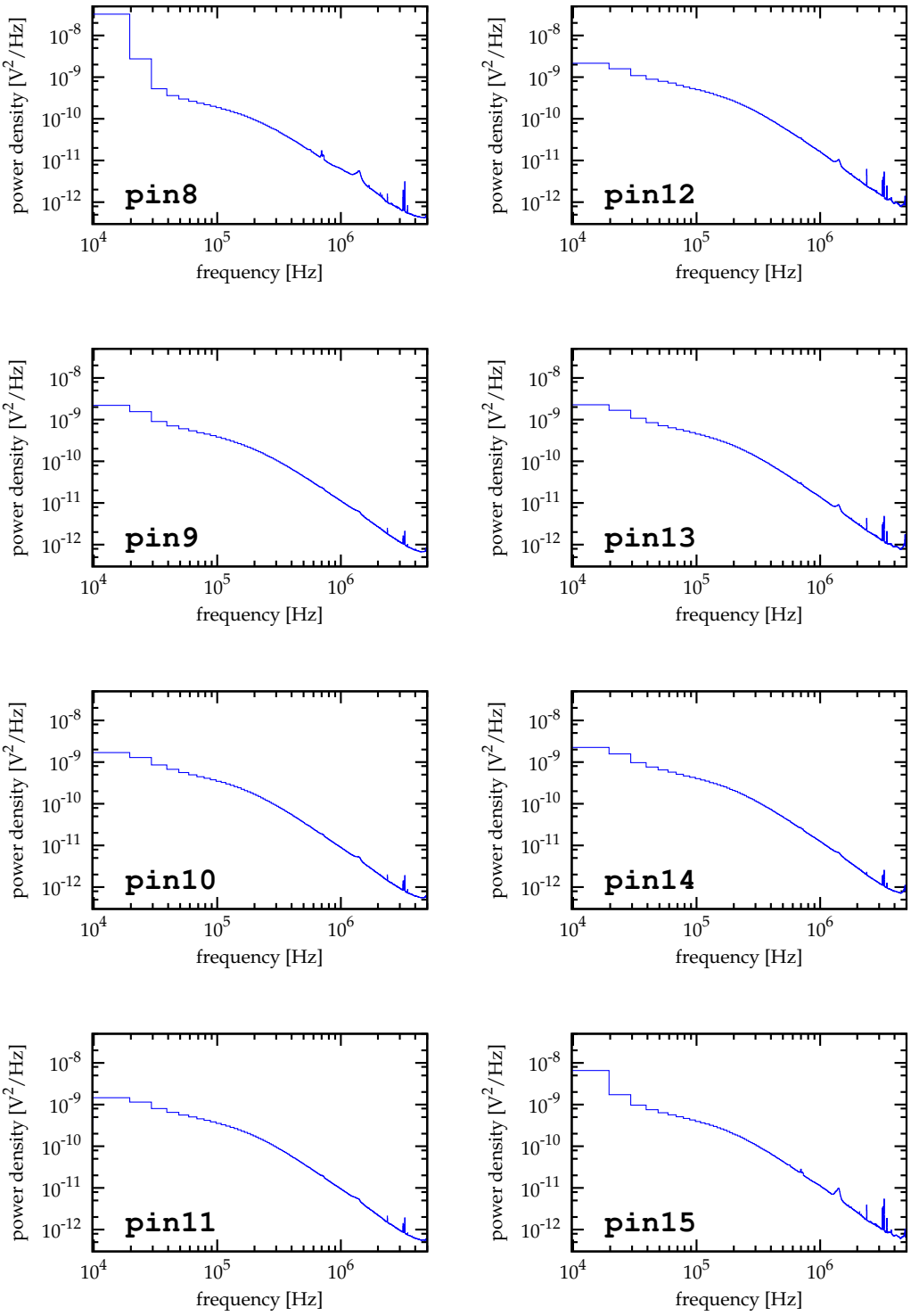

(Figure 6.3 continued)

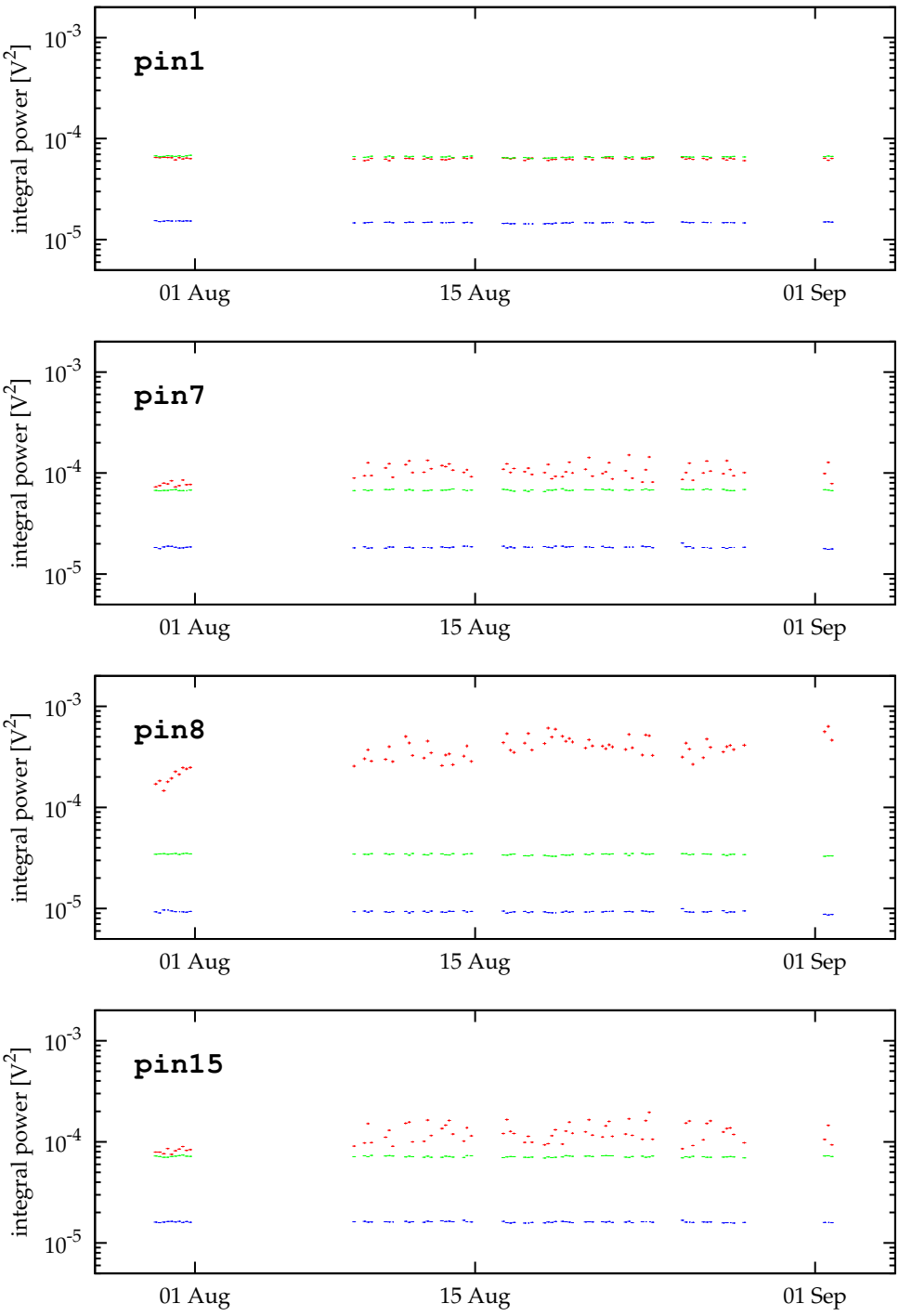

Figure 6.4: Long-term variation of the noise power spectrum is shown for some typical channels. The x-axis is the time of each data set and the y-axis is the power. The red, green, and blue x–y error bars show the integrated noise power of individual data sets in low ($0 \leq f < 78.125\,\mathrm{kHz}$), mid ($78.125\,\mathrm{kHz} \leq f < 62.5\,\mathrm{kHz}$), and high ($62.5\,\mathrm{kHz} \leq f \leq 5\,\mathrm{MHz}$) frequency ranges, respectively.

out in Eq. (6.31). Therefore, this fluctuation of noise level does not affect the estimated energy but only its resolution by making up a not-so-optimal filter. In the analysis, we ignored this time variance and used the $\overline{\widetilde{N}_k}$ value which was calculated by combining all.

6.3.3 Signal template

The expected shape of the signal, S_n, is the impulse response function of the X-ray detector system including the PIN photodiodes, the preamplifier electronics, the cables, and other unknown parasitic elements, although its approximate shape is known by the design of the preamplifier. In this analysis, we measured its actual shape by collecting the waveforms from 5.9 keV manganese X-rays from the ^{55}Fe source. Since each pulse is buried in random noise, many such waveforms should be collected and be averaged at each time.

At the start, however, we cannot sum up the waveforms by the correct timing, since we do not know the actual arrival time of each pulse. Here, we created a less accurate "crude" template first, where the waveforms were simply averaged at each word as it was read from the FADCs. The time line is aligned only by the timing of the discriminators. Thus, each waveform can be out of alignment from its true position by noise and by the pulse height dependency of the trigger timing. Moreover, since we used all the waveforms that were of the channel which hit the trigger system in each event for the sake of simplicity, this crude template can also be contaminated by some unwanted events such as pile-ups, and false triggers caused by noise. The dashed sky-blue curves in Fig. 6.5 shows the crude template of `pin1` as an example.

Then, a crude filter was build based on the crude template, and the waveforms obtained in the calibration run were analyzed using this less accurate filter. According to the peak position estimated by this crude analysis, each waveforms was shifted along the time axis. Thus, the waveforms are now aligned by their

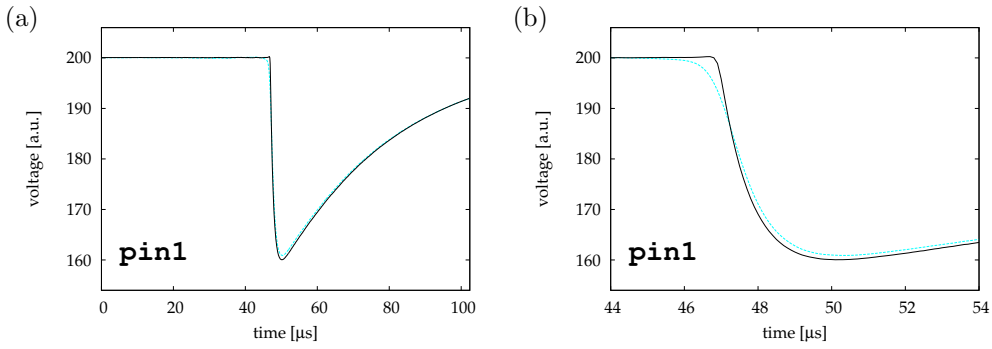

Figure 6.5: An example of the expected shape of the signal. (a) The left figure shows the expected shape of the signal for `pin1`. The dashed sky-blue line shows the crude template which is a naive average of the FADC output, and the black solid line shows the refined template which we used in the analysis. (b) The right figure shows the same curves around the beginning of the pulse. The gradual falling (negative going) of the crude template was clearly improved in the refined template by aligning each waveforms at its expected impulse arrival time.

best timings, since the optimal filter would provide the maximum likelihood estimate not only for the signal amplitude but also for the impulse arrival time. Finally, the refined template was created by averaging the shifted waveforms at each time. We also removed some unwanted events based on the analysis using the crude filter.

The results of analysis by the crude filter are shown in Fig. 6.6. For each channel, three plots are combined sharing the same x-axis which denotes the expected peak height, $\bar{A}$, of each events. The top most plot of each combined plots is the histogram. The blue plots are of the events with triggers and the red plots are of the 'fake-trigger' events, hence of the pure noise waveforms. We can recognize the clear separation between the manganese K X-ray peak (blue) and the pedestal (red). The X-ray peak is attached by a subtle tail component. The values of the peak height, $\bar{A}$, are normalized relative to the signal template, $\{S_n\}$, of each channel. Since the signal template is now an average of the X-ray events, the barycenter of the X-ray peak should come to 1 on the x-axis. However, it is not. This implies that the current estimate of the signal template (crude template) is not accurate enough.

The middle plots are scatter plots of the expected impulse arrival time relative to that of the signal template versus the peak height. By the combination of the K_α and K_β components, the outline of the X-ray peak is a raindrop shape instead of an oval. We can recognize the walk of trigger timing by the peak height evidently in the tail of the X-ray peak.

Here, we would like to comment on the origin of the time axis. In the definition of $\{S_n\}$ in Section 6.3.1, $n = 0$ corresponds to the instant of the impulse. Then, the expected signal position, $\bar{m}$, which is to be calculated from the convolution with the filter corresponds to the expected arrival time of the impulse. However, it is impossible to place the template function at the correct position on the time axis agreeable to its definition, since we do not know the actual arrival time of each γ-ray or X-ray photon. When we form the filter kernel using the signal template described in this section in place of $\{S_n\}$, we will get $\bar{m}$ as the expected impulse arrival time relative to that of the signal template.

In the bottom most plots, we defined an index named "shaped noise power" which indicates how far the waveform is from its ideal waveform. It is defined as the squared sum of the deviation from the expected noiseless shaped waveform, that is

$$\text{(shaped noise power)} = \frac{1}{Z^2}\sum (Y_n - AZ_n)^2, \tag{6.35}$$

where $\tilde{Z}_k = \tilde{H}_k \tilde{S}_k$. We notice that some events exhibit extremely large shaped noise power. These were mainly pile-up events.

In creating the refined template, the waveform of the following minor but unwanted events were excluded from the average:

- Events in the tail component whose pulse heights are too low,
- Events with deformed waveform whose shaped noise powers are too large.

Each X-ray peak in the histograms was fit with two Gaussians corresponding

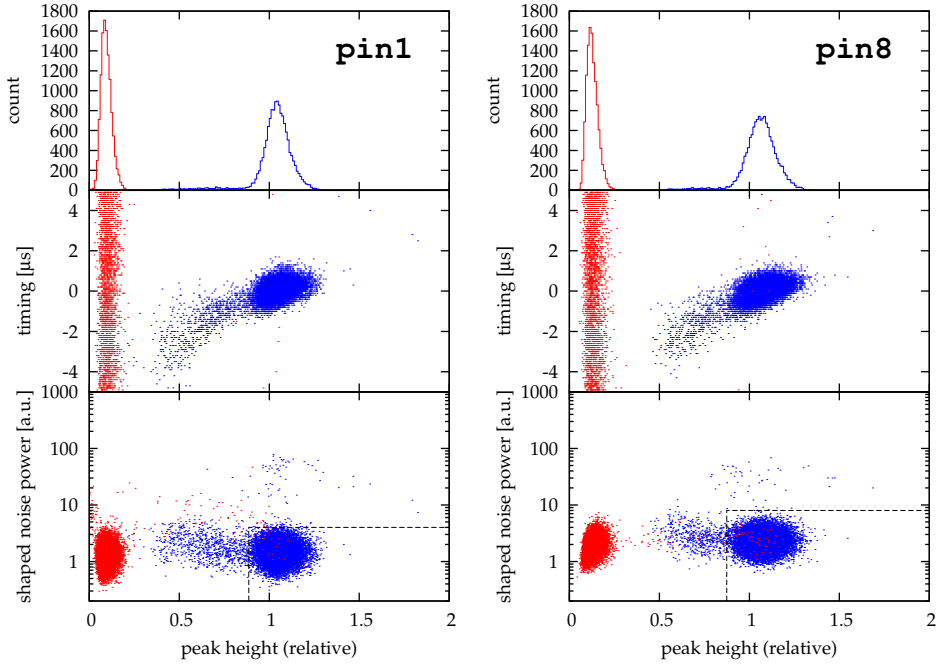

Figure 6.6: Waveform analysis of the ^{55}Fe calibration data using the crude filter for the `pin1` (typical) and `pin8` (worst microphonic) channels. The top most plots are the histograms, where x-axis denotes the expected peak height, $\bar{A}$, of each events, so that the values are relative to the signal template. The blue plots are of the events with triggers and the red plots are of the pure noise waveforms. The middle plots are scatter plots of the expected peak timing versus the peak height. The peak timing is again relative to the signal template. The bottom most plots are scatter plots of the shaped noise power which is described in the text versus the peak height. The dashed lines indicate the selection cut described in the text.

to K_α and K_β as

$$f(A) = \frac{a}{\sigma\sqrt{2\pi}} \frac{1}{\omega_\alpha + \omega_\beta} \times \left[\omega_\alpha \exp\left[-\frac{(A - E_\alpha \mu)^2}{2\sigma^2} \right] + \omega_\beta \exp\left[-\frac{(A - E_\beta \mu)^2}{2\sigma^2} \right] \right], \tag{6.36}$$

where A is the pulse height, $\omega_\alpha : \omega_\beta = 150.5 : 20.3$, $E_\alpha = 5.895\,\mathrm{keV}$, $E_\beta = 6.49\,\mathrm{keV}$, and a, μ, and σ were free parameters. Then, the threshold for pulse height was set 2.7σ below the K_α peak, i.e.:

$$A > E_\alpha \mu - 2.7\sigma. \tag{6.37}$$

The amount of increase of the average peak height by discarding the Gaussian component below this threshold is expected to be

$$9.2 \times 10^{-3} \sigma/\mu + 0.2\,\mathrm{eV} \sim 3\,\mathrm{eV}. \tag{6.38}$$

We will ignore this small error first and will finally calibrate the energy in a different manner as described later.

The threshold for the shaped noise power was determined by the eye. Such arbitrariness would be neutral to the average height of the pulses. The cuts are shown as the dashed curves in Fig. 6.6.

After the event cut, refined templates were generated by averaging waveforms at each "true" time bin where each waveform was shifted along the time axis by its expected impulse arrival time. The black solid curves in Fig. 6.5 shows this new refined template. In Fig. 6.5 (b), we can clearly observe that the gradual falling (negative going) of the pulse head in the crude template was improved to a sharp beginning in the refined template. This implies that the trigger timing variation was properly corrected.

As the adverse effect of shifting the time axis, however, the number of samples contributing to the average at both ends of the sampled period became smaller. To make matters worse, the trigger timings by the discriminators and the voltage level at the ends are correlated by low frequency noise component. Thus, the composition of the waveforms which constituted the average there could be biased. Such effect was observed as the spurious bends at both edges of the signal in `pin8` and `pin15`. The red dashed curve in Fig. 6.7 shows the spurious bends of `pin8`. In other channels, such effect was not significant buried in random noise.

In order to solve this problem, both edges were amended by extrapolating the inner smooth area. Further extrapolation beyond the sampling period enables us to generate arbitrarily shifted signals numerically. We can investigate the influences of the trigger timing variation by this. We will describe this in the later section.

From causality, the pre-pulse signal should be constant. The average in the interval of $[t_1, t_2]$ was extrapolated to $t < t_1$, where the break points were selected at $t_1 = 3.0\,\mu\mathrm{s}$ and $t_2 = 42.9\,\mu\mathrm{s}$. The post-pulse signal was assumed to be a sum of an exponential and a constant. The function was fit in the interval of $[t_3, t_4]$ and was extrapolated to $t_4 < t$, where the break points were selected at $t_3 = 69.4\,\mu\mathrm{s}$ and $t_4 = 99.3\,\mu\mathrm{s}$. Furthermore, to connect the extrapolated function to the original waveform smoothly, each extrapolated function and the

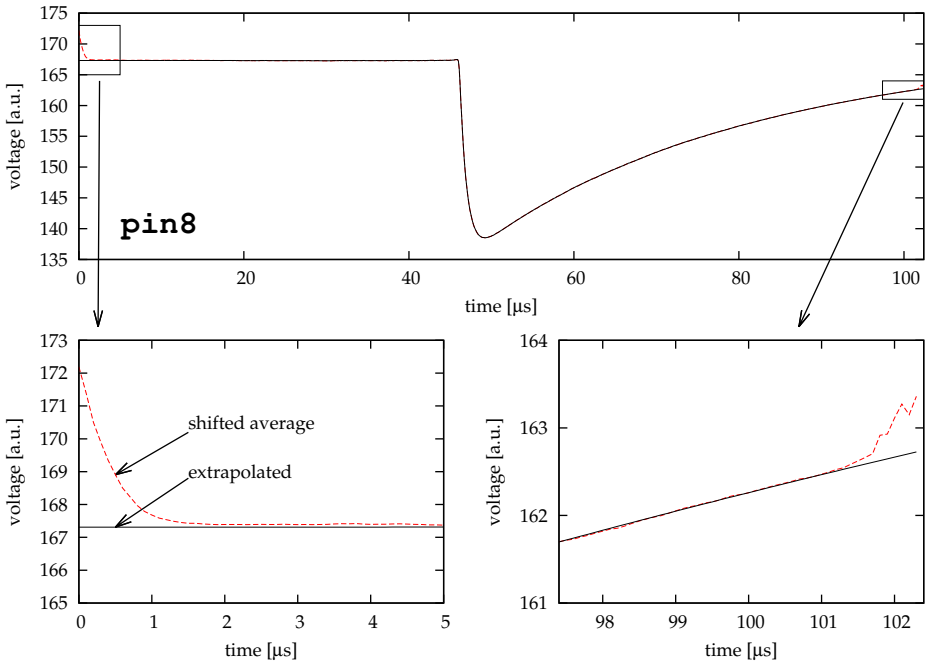

Figure 6.7: Spurious bends appeared at the edges of the `pin8` shifted average signal. The red dashed curve shows the averaged ^{55}Fe signal where each trigger timing was corrected based on the crude filter analysis. The black solid curve shows the final refined template where both edges are amended by extrapolation. The areas at the beginning and ending edges indicated by boxes are shown magnified below. See text for detail.

original waveform were mixed linearly in the intervals of $[t_1, t_2]$ and $[t_3, t_4]$. In summary, we used the following curve as the final refined signal template:

$$f(t) = \begin{cases} b_0, & t < t_1 \\ \frac{t-t_1}{t_2-t_1} b_0 + \frac{t_2-t}{t_2-t_1} g(t), & t_1 < t < t_2 \\ g(t), & t_2 < t < t_3 \\ \frac{t-t_3}{t_3-t_4} g(t) + \frac{t_4-t}{t_3-t_4} \left(b_1 - \exp(-\frac{t-t_0}{\tau}) \right), & t_3 < t < t_4 \\ b_1 - \exp\left(-\frac{t-t_0}{\tau}\right), & t_4 < t, \end{cases} \tag{6.39}$$

where $g(t)$ is the shifted averaged waveform described above, and b_0, b_1, t_0 are the fit parameters. The discrepant baselines, b_0 and b_1, before and after the pulse are to include the long-decay-time ($\sim 1\,\mathrm{ms}$) component which went through the pole-zero-cancellation (PZC) network. This final refined template is shown as the black solid curves in Fig. 6.5. We also show the expected signal waveforms of all the channels in Fig. 6.8.

6.3.4 Baseline fixing and window function

Before applying the argument in Section 6.3.1 to the actual waveform analysis, we fixed the base line since our data contains non-zero indefinite offset. The

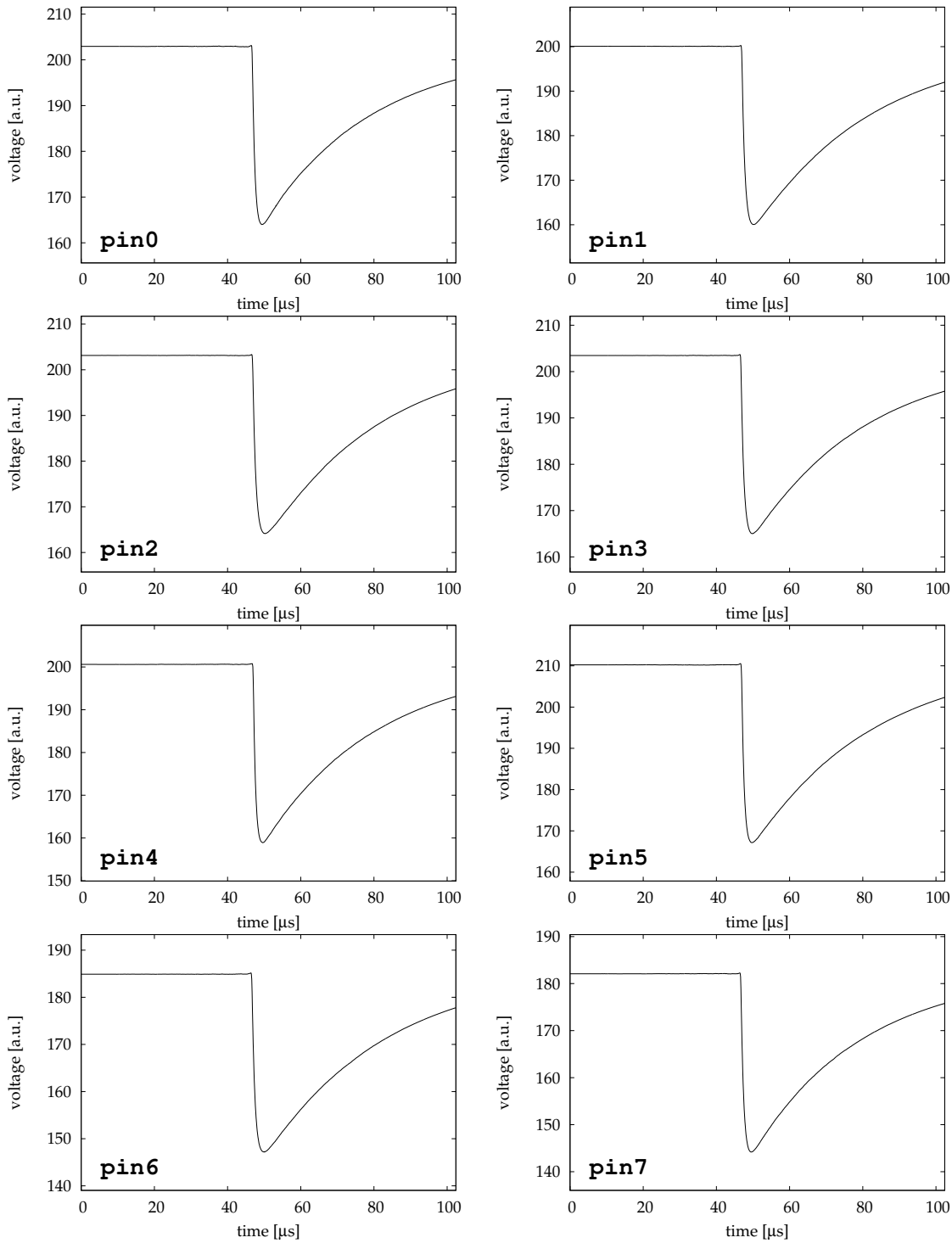

Figure 6.8: Expected signal waveforms of all the channels.
(continued on the next page)

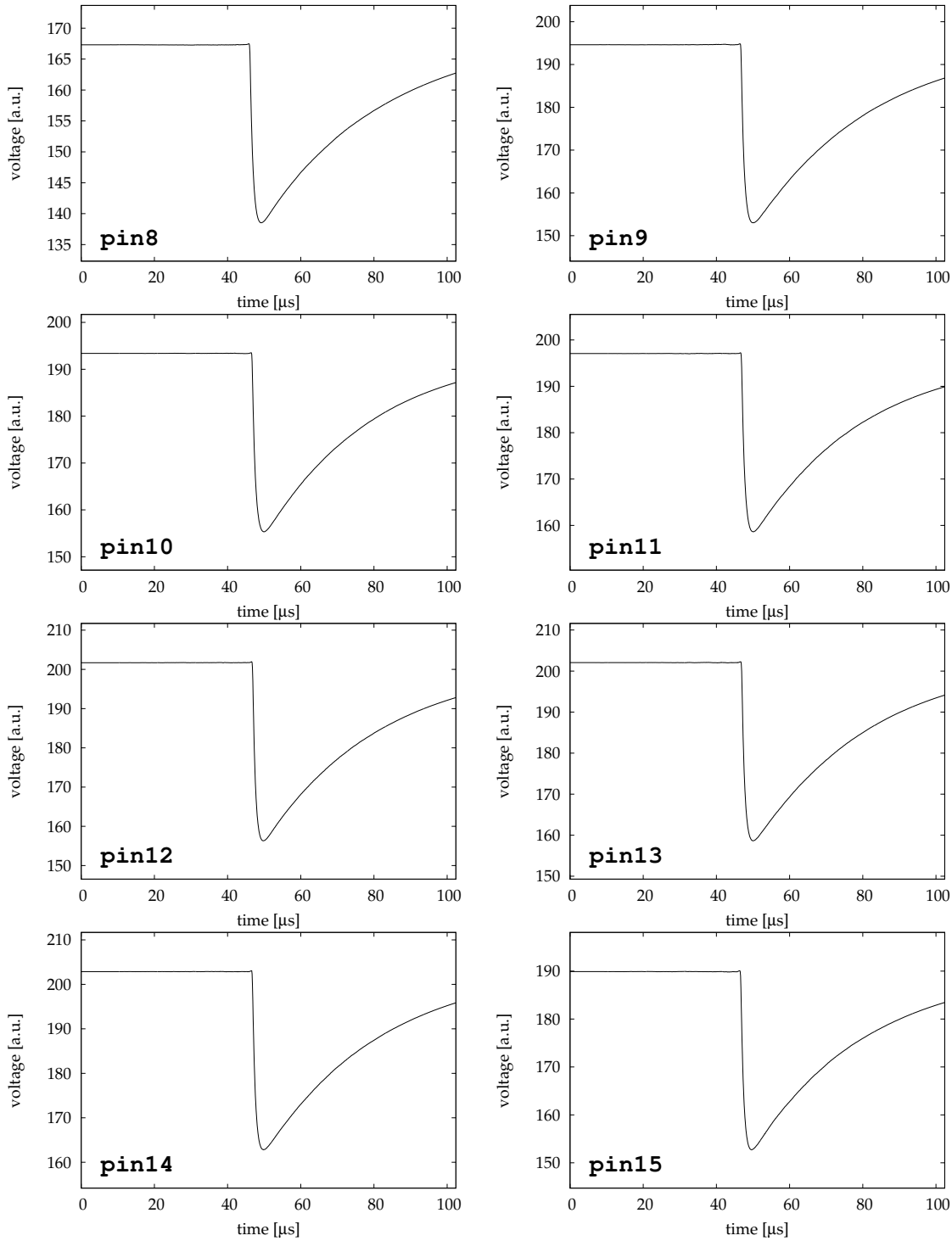

(Figure 6.8 continued)

causes of this offset include the inherent DC offset voltage of the preamplifier outputs, the pedestal settings of the FADCs, and the low frequency components of microphonic noise. Mainly because of the last cause, we can not leave the estimated offset values as constants but we should determine them event-by-event from each waveform data.

The baseline correction was performed before the Fourier transform. If the time interval were infinite, it would only affect the $\omega = 0$ component or the lowest frequencies. However, it is not true in our case, since our interval is finite. As we will see below, we will introduce a window function. By the convolution theorem, we will see the convolution of the true Fourier transform of the original waveform and the Fourier transform of the window function in the frequency domain. Therefore, this indefinite offset can pollute higher frequencies in the process of the Fourier transform.

Three methods of fixing the baseline were examined. In Method A, each waveform was subtracted by the average of the first 128 channels, where is usually filled with pre-impulse signals. In Method B, each waveform was subtracted by the average of the whole waveform. This removes arbitrariness of selecting the pre-impulse region, and will reduce the random fluctuation of the baseline. In exchange for that, the baseline will be made proportional to the signal amplitude instead of zero. Finally, in Method C, the time derivative or the difference of each sequences was used in place of the waveform. It is noteworthy that, in the infinite continuous limit, using the time derivative will produce the identical shaped waveform:

$$X' = \partial_t X, \quad S' = \partial_t S, \quad N' = \partial_t N, \tag{6.40}$$

then

$$\tilde{Y}' = \frac{\tilde{S}'^* \tilde{X}'}{|\tilde{N}'|^2} = \frac{-i\omega \tilde{S}^* \cdot i\omega \tilde{X}}{|i\omega \tilde{N}'|^2} = \tilde{Y}. \tag{6.41}$$

Another problem of applying the arguments in Section 6.3.1 is that our data are too short. Each waveform data are confined within a time window of 102.4 μs which is only comparable with the time scale of the response function instead of virtually infinite intervals.

The Fourier transform of a finite discretized data results in the form of the discrete Fourier transform given by Eq. (6.15). Obviously from Eq. (6.15), it is equivalent to assuming the input data, X_n, or the expected response function, S_n, to be periodic. However, actual waveforms are not periodic but are going forever. The discontinuity from $n = M - 1$ to $n = 0$ is then equivalent to placing a spurious step fixed at $n = 0$ despite the translational symmetry of $S_n^{(m)}$. Accordingly, this spurious step gives rise to a δ-function-like peak fixed at zero in the shaped waveform.

This problem can be remedied by multiplying the input waveform by an appropriate window function, w_j, $j = 0, \ldots, M - 1$, that changes smoothly from zero to unity and then back to zero as j ranges from 0 to $M - 1$. In this analysis, two types of window functions were examined. One is the Welch window defined as

$$w_j = 1 - \left[\frac{j - (M-1)/2}{(M+1)/2} \right]^2, \tag{6.42}$$

and the other is the Hann window defined as

$$w_j = \frac{1}{2}\left[1 - \cos\left(\frac{2\pi j}{M-1}\right)\right]. \tag{6.43}$$

The former is a smooth function which connects to zero at both ends, while the latter is not only continuous to zero at both ends but also continuous by its derivative. In the frequency domain, the former has narrower peak, while the latter has less and rapid-falling side lobes.

Figures 6.9 and 6.10 show the inverse Fourier transform of

$$\tilde{Z}_k^{(m)} = \tilde{H}_k \tilde{S}_k^{(m)}, \tag{6.44}$$

that is the expected shaped waveform for various signal position and various combinations of baseline fixing methods and window functions.

When the signal position is identical with the signal template, then the shape of the "shaped waveform" is almost insensitive to the baseline fixing methods or to the selection of the window function. It depends more on the PIN photodiode channels. In channels with a typical noise, e.g., `pin0`, it becomes a simple cusp shaped curve. While, in `pin8` where microphonic noise is relatively severe, the peak becomes sharper and there are significant undershoots on both sides of the peak. In the combination of Method B and the Welch window, we can observe the tendency to warp toward positive in the periphery even when the signal position is at zero. There are also some small bumps. Such deformation is less significant when the Hann window is combined.

In the cases when the signal position is off the center, Method A shows a distinct convergence of the side lobes which do not deviate far from zero, until the signal overlaps the first 128 channels. With regard to its shape, however, it becomes more asymmetric as the signal position gets away from the center. In the extreme where the signal overlaps the first 128 channels, it deforms into a sinusoid-like curve.

The asymmetry of the shaped waveform in Method B when the signal position is off the center resembles to the case of Method A. What is worse is that its side lobes converges worse than Method A.

In Method C, the shaped waveform is less deformed. The side lobes on both sides are smooth and the left-right symmetry of the cusp is not much affected by the signal position. When the signal position is off the center, their side lobes tend to sag toward negative a little more than Method A although the amount is still acceptable.

Although their side lobes look to converge better when the Hann window was selected, the peak height also diminishes rapidly as the signal position gets away from the center. Thus, we can not profit by the good convergence of the Hann window in terms of the S/N ratio.

Figure 6.11 shows some energy spectra and histograms of the estimated signal positions obtained by analyzing all the calibration data during Phase II measurement for some combinations of window functions and baseline fixing methods. The peak in each energy spectra corresponds to Mn K X-rays from a ^{55}Fe source. The plot contains only the data which are of the channels which hit the trigger system. From the histograms of the signal positions, we found that most trigger timings came within the interval of $\pm 2\,\mu$s relative to the template.

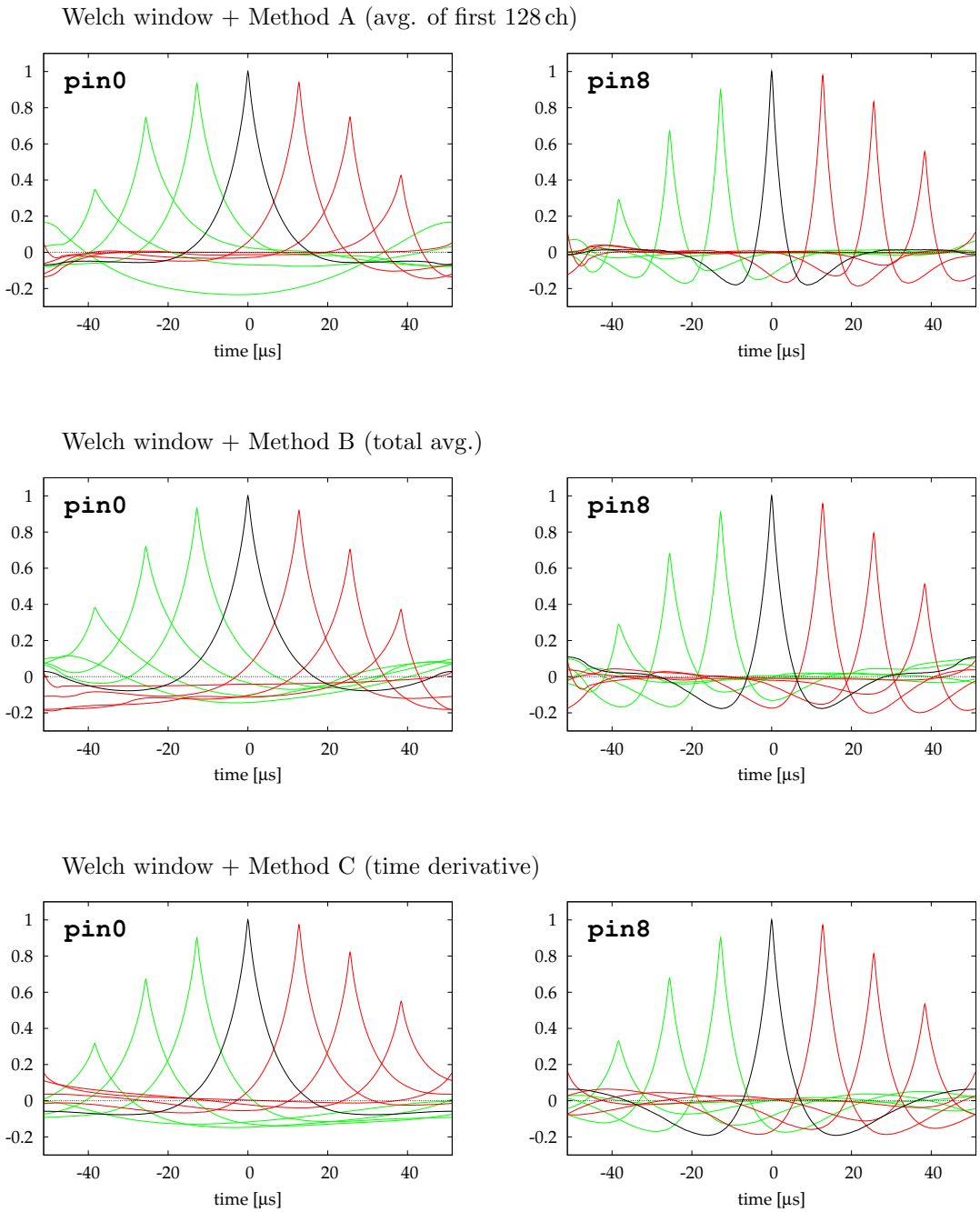

Figure 6.9: Comparison of shaped waveforms by changing the baseline fixing methods, where the Welch window is applied to the three baseline fixing methods. `pin0` has a typical noise character, and `pin8` exhibits relatively large microphonic noise.

Hann window + Method A (avg. of first 128 ch)

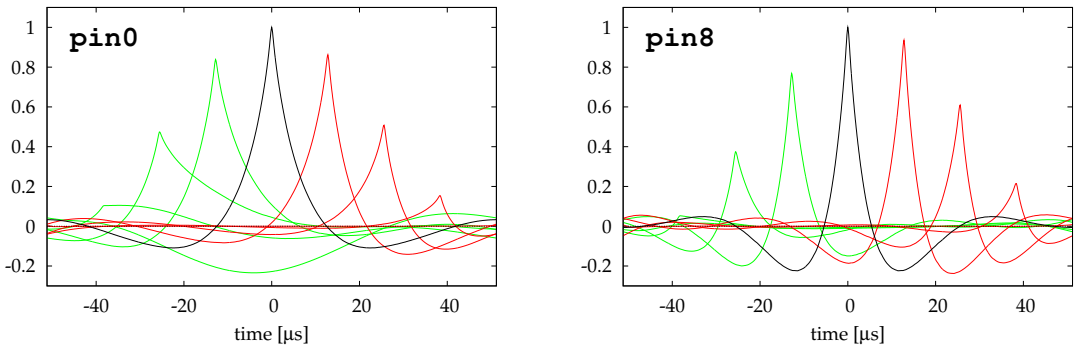

Hann window + Method B (total avg.)

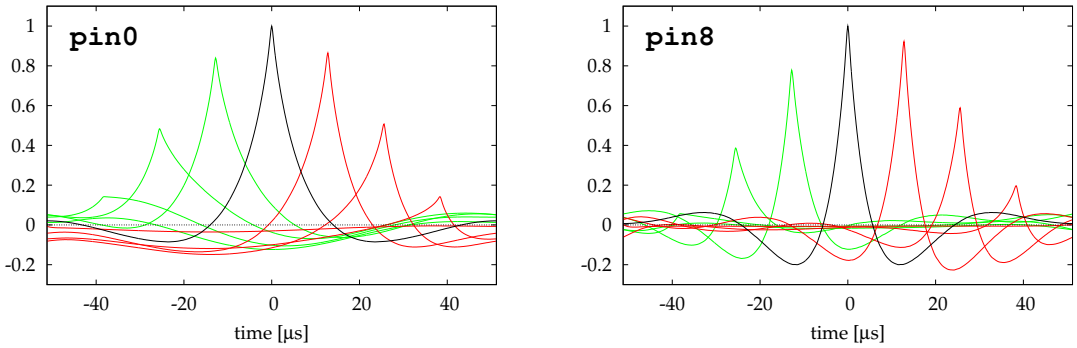

Hann window + Method C (time derivative)

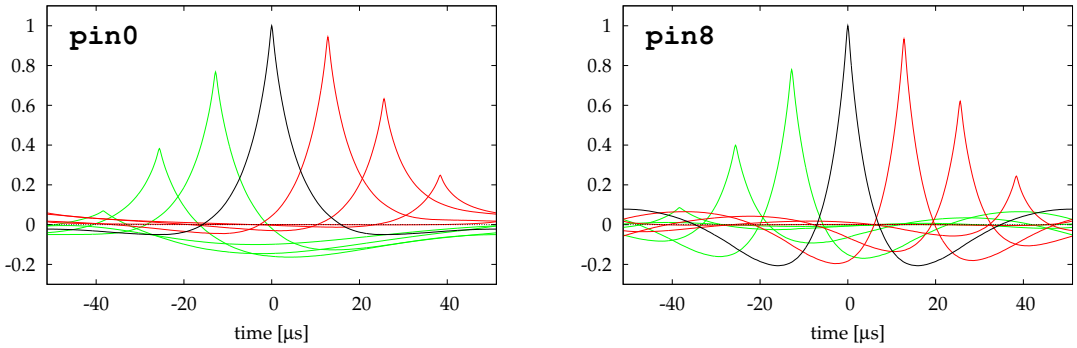

Figure 6.10: Comparison of shaped waveforms by changing baseline fixing methods, where the Hann window is applied to the three baseline fixing methods.

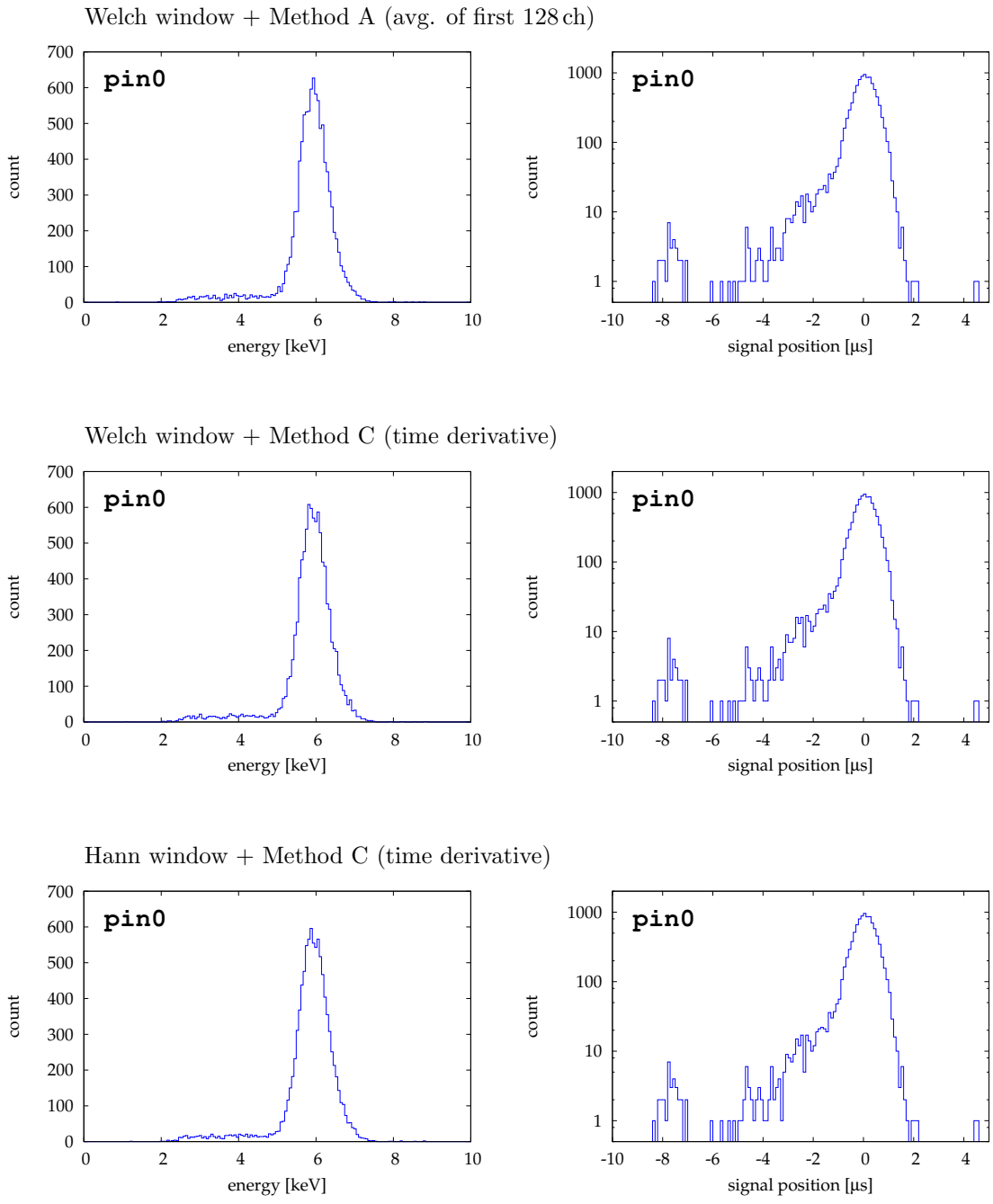

Figure 6.11: Comparison of histograms by changing window functions and baseline fixing methods. The ^{55}Fe calibration data were analyzed using various combinations of window functions and baseline fixing methods. Energy spectra and histograms of expected signal positions are shown for some combinations. They are almost identical independently of the preprocessing methods.

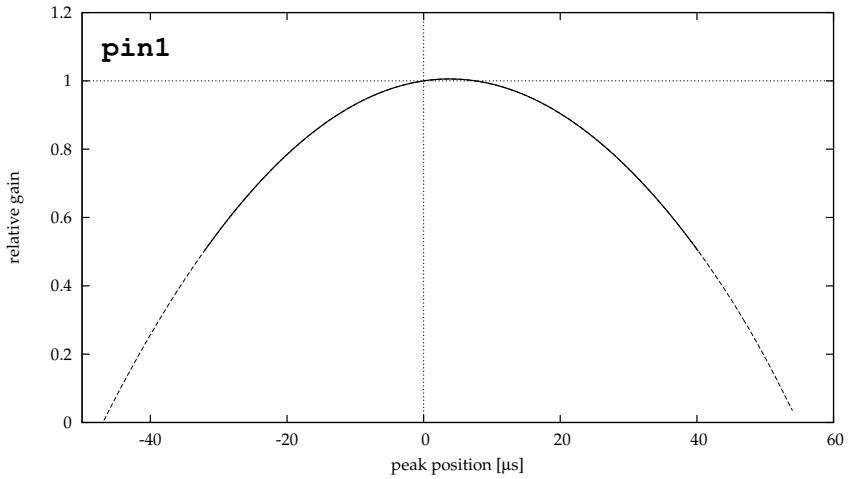

Figure 6.12: Example of a timing compensation function. The relative gain of the waveform analysis for the channel `pin1` is plotted as a function of the expected peak position. We used only the interval which is drawn in a solid curve.

As a result, little differences were observed between the variations of window functions or baseline fixing methods. In the analysis, we used the combination of the Welch window and baseline fixing by time derivative or Method C.

6.3.5 Trigger timing dependence

In this waveform analysis, we are analyzing pulse shapes within a finite interval of only 102.4 μs. Furthermore, we are multiplying them by the Welch window which is unity at the center but falls to zero toward the edges. As a result, the signal gain of the pulse height is no longer uniform against the time shift as the idealized arguments in Section 6.3.1. Instead, it changes as a function of the signal position as we observed in Fig. 6.9.

In order to compensate for the signal position dependence of the peak height analysis, we first calculated the expected shaped waveform, $Z_n^{(m)}$, for various signal position, m, then, we created a table of the peak height and the peak position of them for each channel. The compensation was performed in reverse by dividing the expected peak height of each event by the compensation coefficient which is to be found at the expected peak position in the table.

The result was that the obtained peak position agreed with the input signal position until the signal was shifted near to the ends of the sight. For example in the `pin1` channel, the signal position was reproduced in the interval of $-469 \leq m \leq 546$ or $-46.9\mu\text{s} \leq \delta t \leq 54.5\mu\text{s}$. Moreover, regarding the positive m, this agreement continued beyond the wrap-around boundary, $m = 512$. This fact makes sense since the falling edges of the pulses is positioned a bit left to the center of the sampling interval. Therefore, we used the interval where the signal position was reproduced. We also required the analyzing gain to be more than 50% relative to the value at $m = 0$. This latter condition was always more stringent than the condition to reproduce the signal position.

channel #	fiducial signal position [μs]
pin0	$-32.3 \leq \delta t \leq 40.2$
pin1	$-32.1 \leq \delta t \leq 40.2$
pin2	$-32.3 \leq \delta t \leq 40.1$
pin3	$-32.0 \leq \delta t \leq 40.4$
pin4	$-32.2 \leq \delta t \leq 40.3$
pin5	$-31.8 \leq \delta t \leq 40.5$
pin6	$-31.7 \leq \delta t \leq 40.6$
pin7	$-33.9 \leq \delta t \leq 39.0$
pin8	$-32.8 \leq \delta t \leq 39.6$
pin9	$-32.1 \leq \delta t \leq 40.2$
pin10	$-32.1 \leq \delta t \leq 40.3$
pin11	$-32.0 \leq \delta t \leq 40.4$
pin12	$-32.2 \leq \delta t \leq 40.3$
pin13	$-32.2 \leq \delta t \leq 40.2$
pin14	$-32.1 \leq \delta t \leq 40.2$
pin15	$-34.0 \leq \delta t \leq 39.0$

Table 6.2: List of the acceptable ranges for the signal positions relative to the templates, or the fiducial intervals.

Figure 6.12 shows one of such compensation coefficient plotted as a function of the signal position. Fiducial interval is indicated as the solid curve. Table 6.2 shows the fiducial intervals of all the channels.

Finally, we will discuss the influence of the signal position dependence of the gain on the waveform analysis. Since the timing compensation was done after the peak was determined, the estimated signal position could have been attracted toward the gain maximum. This bias is still acceptable since real signals are expected around $m \sim 0$ where the trigger is and the gain maximum is also at around $m \sim 0$. We were too much egalitarian about the estimate of the signal position in Section 6.3.1 just to simplify the argument. At around $m \sim 0$, the gain is quite stable and thus insensitive to the signal position. Furthermore, if the signal were free from noise, the cusp of the shaped waveform reproduces the signal position quite well. The only concern remains in the cases when the original pulse height was as small as the noise level, where a crest of noise near $m \sim 0$ can be misidentified as the peak. This counts for nothing because we will not use such events near the noise level.

6.3.6 Linearity

Since the pulse height analysis involves the maximum function, it is non-linear in nature whether the method used is numerical or electronic. When the signal is large enough where noise can be negligible, the pulse height is proportional to the strength of the real signal. At the low energy extreme, however, the expected value of 'the pulse height' converges to the crest value of the noise.

In order to see this non-linearity, we generated a series of simulated signals by adding the template waveform to a set of noise waveforms by various amplitudes. Figure 6.13 (a) shows some examples of such simulated signals. By applying the identical waveform analysis to the simulated signals, we obtained a set of peak

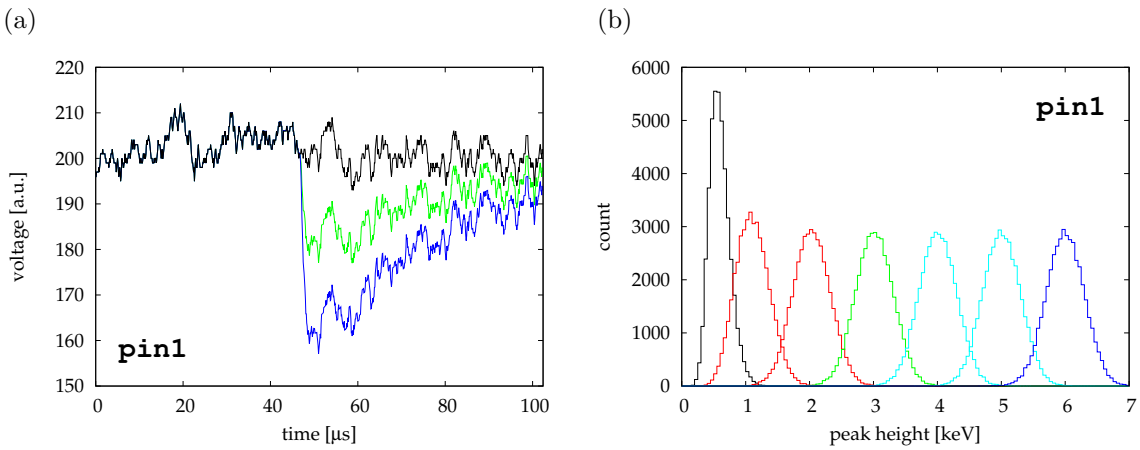

Figure 6.13: (a) Example of simulated waveforms corresponding to 3 keV (green) and 6 keV (blue) are plotted along with the original pure noise waveform (black). (b) Change of energy histogram by the addition of expected signal of various amplitude to a set of noise waveforms.

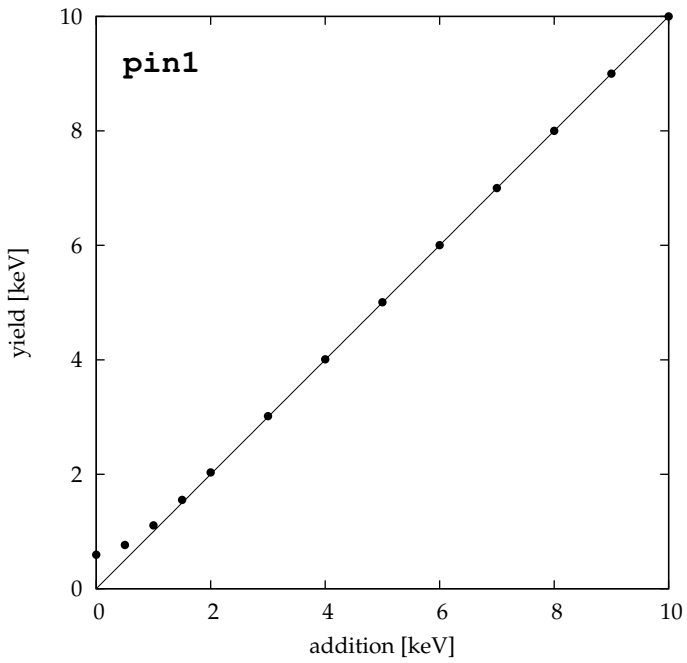

Figure 6.14: Linearity test of the peak height analysis for the `pin1` channel as an example. The x-axis shows the input, i.e., the amount of the added signal in the simulated waveforms, and the y-axis shows the output, i.e., the yield of the peak height analysis. The diagonal line shows the relation when the output were identical with the input.

channel #	$\bar{\mu}$	χ^2_μ/ndf	$\chi^2_{\mu M}$/ndf
pin0	1.0029 ± 0.0008	48.0/11	34.5/10
pin1	1.0024 ± 0.0006	56.7/12	40.3/11
pin2	1.0025 ± 0.0006	24.1/12	4.9/11
pin3	1.0020 ± 0.0006	48.6/12	37.8/11
pin4	1.0031 ± 0.0006	53.0/12	22.6/11
pin5	1.0027 ± 0.0006	40.3/12	18.8/11
pin6	1.0040 ± 0.0006	51.2/12	12.1/11
pin7	1.0029 ± 0.0007	28.9/12	10.1/11
pin8	1.0027 ± 0.0007	27.8/12	14.4/11
pin9	1.0020 ± 0.0007	20.1/12	10.6/11
pin10	1.0028 ± 0.0006	24.4/12	5.1/11
pin11	1.0017 ± 0.0006	17.9/12	11.1/11
pin12	1.0021 ± 0.0006	25.8/12	13.6/11
pin13	1.0014 ± 0.0006	18.3/12	13.1/11
pin14	1.0023 ± 0.0006	96.4/12	82.6/11
pin15	1.0028 ± 0.0007	44.5/12	30.4/11

Table 6.3: Statistics of ^{55}Fe peak positions.

heights for each amount of addition. As shown in Fig. 6.13 (b), the more we added, the larger the peak height became. In Fig. 6.14, the yielded peak heights are plotted as a function of the amount of addition for pin1 as an example. Other channels showed almost the same appearances. As the peak height of each simulated signal is statistically dispersed, the mean value for each amount of addition is used as the value of the yield. Their statistical errors are about 1.5 eV each which is invisibly small on the graph. Non-linearity was observed in the low energy region. At 2 keV, however, the discrepancy between the inputs and the outputs were smaller than 50 eV. Above that energy, the outputs were almost identical with the inputs and non-linearity was negligible.

6.4 Energy calibration

Figure 6.15 shows the long-term evolution of the manganese K X-ray peak positions in the energy spectra while the ^{55}Fe calibration source was viewed.

In the course of the Phase II measurement, the pin0 channel was found to be giving out no signal since September 1. Thus, we excluded this channel from the analysis of the final run starting from this day. This seems to be a connector problem, since we observed a very weak signal during the down time and the problem resolved spontaneously while we were investigating the cause.

Each X-ray peak was fit by two component Gaussians, Eq. (6.36), using the log-likelihood method assuming the Poisson distribution of the number of events. Unlike the analysis in Section 6.3.3, the gain walk by the trigger timing dependence was corrected this time as described in Section 6.3.5. The y-axis is normalized against the signal template assuming that it corresponds to the weighted average energy of the manganese K X-ray, 5.9657 keV. If the estimation of the signal template were exact, points in Fig. 6.15 would gather along the line, $y = 1$, aside from the small error estimated in Eq. (6.38).

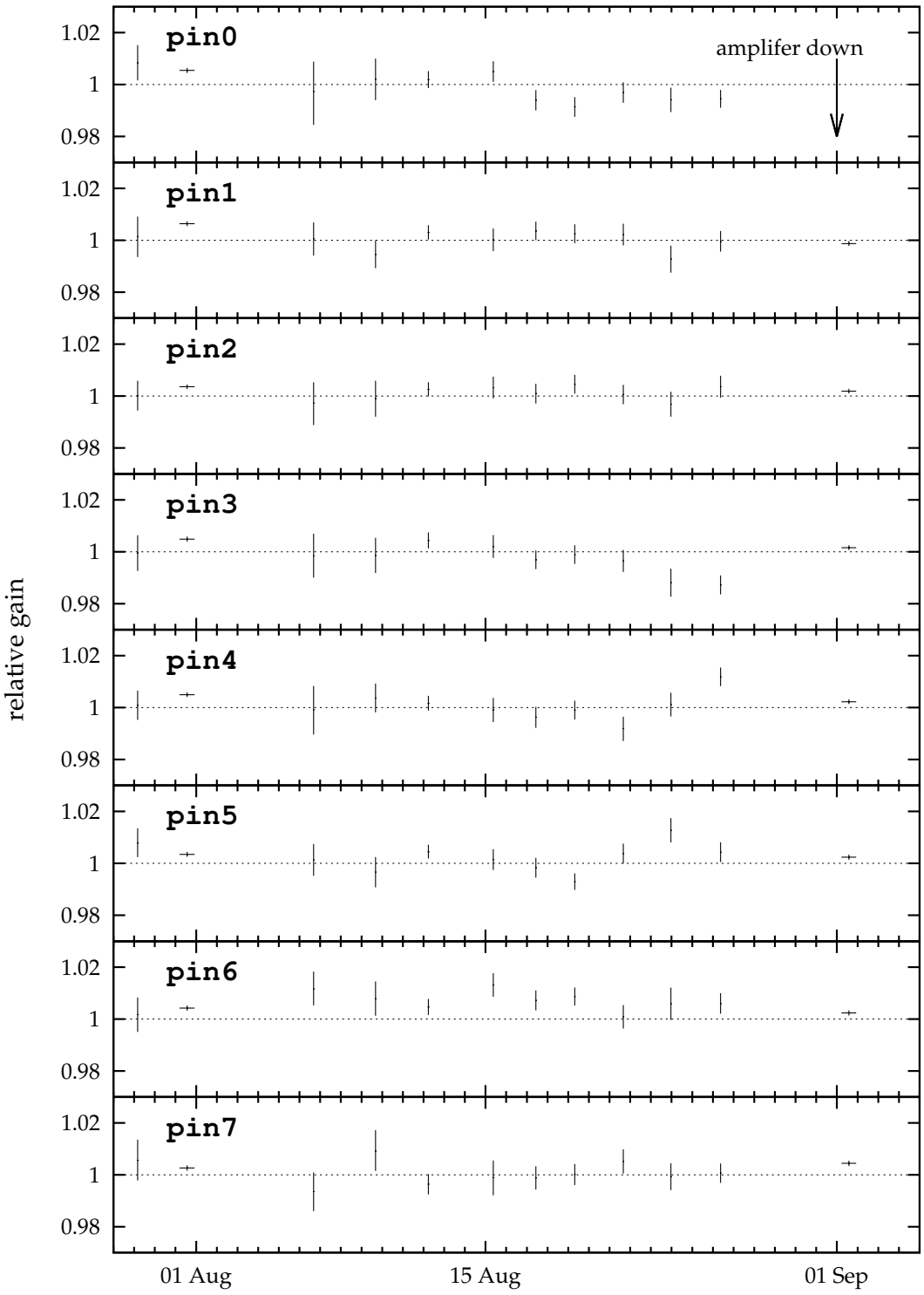

Figure 6.15: Long-term evolution of the ^{55}Fe peak position.
(continued on the next page)

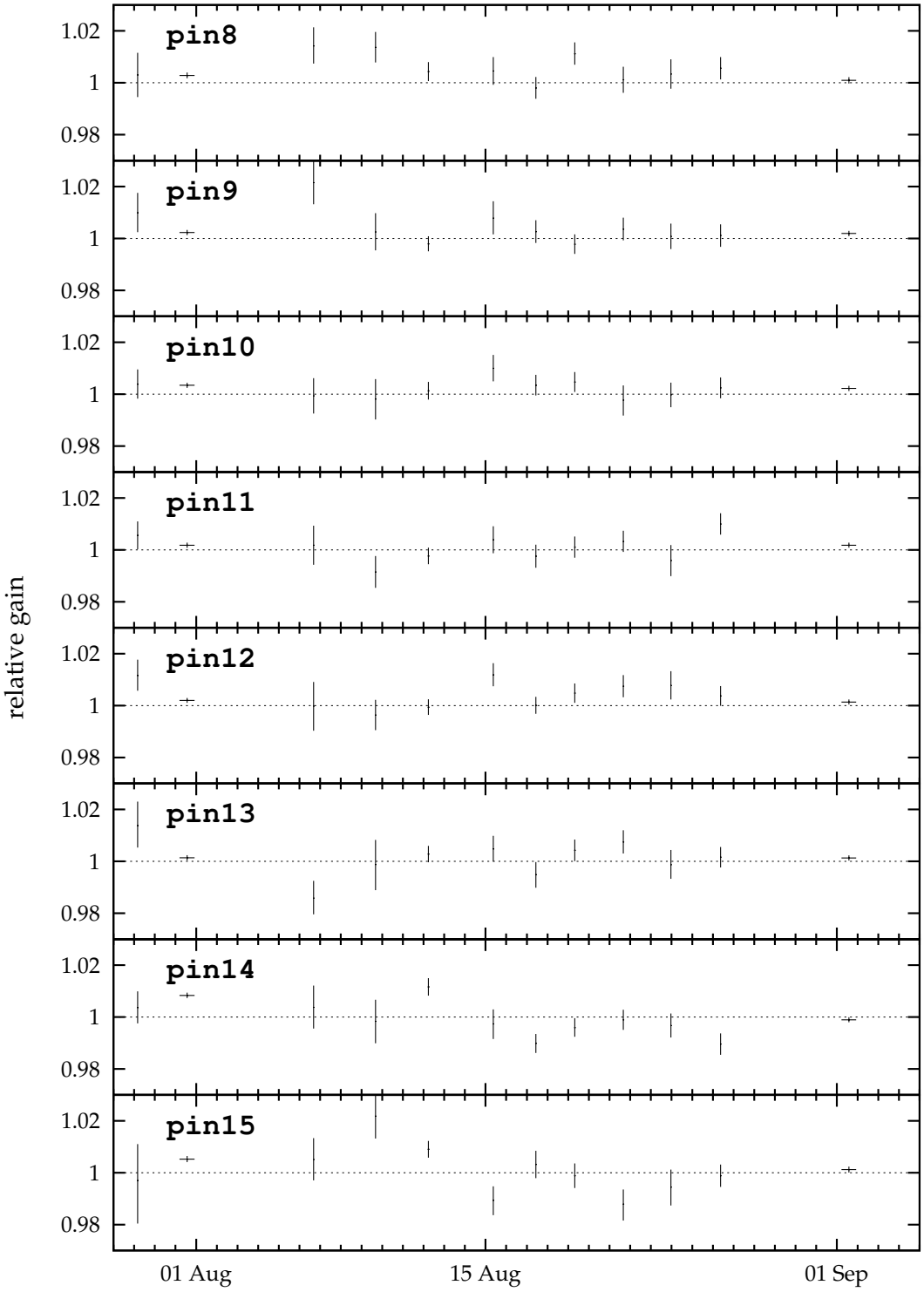

(Figure 6.15 continued)

channel #	$\bar{\sigma}$ [keV]
pin0	0.322 ± 0.005
pin1	0.304 ± 0.003
pin2	0.318 ± 0.003
pin3	0.315 ± 0.004
pin4	0.317 ± 0.003
pin5	0.311 ± 0.003
pin6	0.347 ± 0.004
pin7	0.350 ± 0.004
pin8	0.356 ± 0.005
pin9	0.317 ± 0.004
pin10	0.326 ± 0.004
pin11	0.310 ± 0.004
pin12	0.316 ± 0.004
pin13	0.319 ± 0.004
pin14	0.325 ± 0.004
pin15	0.358 ± 0.005

Table 6.4: Energy resolution of each PIN photodiode.

In Table 6.3, some statistics including the weighted average

$$\bar{\mu} = \frac{\sum_i \mu_i/\delta\mu_i^2}{\sum_i 1/\delta\mu_i^2}, \tag{6.45}$$

the χ^2 value calculated from the deviations from the theoretical expectation, 1,

$$\chi^2_\mu = \sum_i \left(\frac{\mu_i - 1}{\delta\mu_i}\right)^2, \tag{6.46}$$

and the χ^2 value calculated from the deviations from $\bar{\mu}$,

$$\chi^2_{\mu M} = \sum_i \left(\frac{\mu_i - \bar{\mu}}{\delta\mu_i}\right)^2 \tag{6.47}$$

are tabulated by each channel.

The values of $\chi^2_{\mu M}$/ndf were larger than expected from random error, which implies that the gains of the amplifiers could be drifting. The obtained $\bar{\mu}$'s were slightly larger than the expectation, however, their agreements were better than %0.4. This implies that our signal templates are fairly accurate as the estimation of the true signal.

Although there remains slight doubt of some gain drifts, larger random errors will be brought to analysis if we are to calibrate energies of each run individually. Instead, we used common $\bar{\mu}$ values throughout the Phase II measurement.

Table 6.4 shows the energy resolution of each channel, where each weighted average of the fitted values of σ,

$$\bar{\sigma} = \frac{\sum_i \sigma_i/\delta\sigma_i^2}{\sum_i 1/\delta\sigma_i^2}, \tag{6.48}$$

is calibrated using $\bar{\mu}$ of the corresponding channel.

In the later analysis, we used the worst value at the `pin15` channel,

$$\sigma_{\rm pin} \leq 0.358\,{\rm keV}, \tag{6.49}$$

instead of applying the individual resolution to each channel.

6.5 Trigger efficiency

Measurement of the efficiencies that the discriminators generate trigger signals to incoming pulses, $\epsilon_{\rm trig}$, was done on July 28, August 2, August 6, August 15, August 28, and September 3, 2000 while the normal data acquisitions were stopped due to the setting of new gas densities. A modified DAQ system shown in Fig. 6.16 was employed to the measurement. Pulses from a precision pulser, ORTEC 448, were fed to the test pulse input of the preamplifier of the channel to be measured through a built-in 60-dB attenuator in the preamplifier box. Their waveforms were also monitored through a home-made inverting amplifier by a FADC of one of the other channels, which was `pin15` in testing `pin0` through `pin7` and `pin0` in testing `pin8` through `pin15`. Figure 6.17 shows the circuit diagram of the home-made inverting amplifier, which is a simple inverting amplifier preceded by a non-inverting amplifier of gain 2. Its input impedance was made high enough and the stub line was minimized not to disturb the test pulses. This monitoring channel (`pin0` or `pin15`) was isolated from the trigger generating path so that it would not generate any triggers. Additionally, discriminator outputs from the rest channels were masked in the input register. In this manner, we ensured that the triggers generated in this setup consisted only of that coming from the channel being tested. Number of pulses sent during a live period was counted by the scaler which usually measures the live time.

In Fig. 6.18, a typical inverted pulser waveform observed at the monitoring channel is shown along with the signal waveform by it. In order to reject events which were caused by random noise, the inverted pulser waveforms were examined. Thanks to their low noise content, cut was straight forward. Events with voltage step less than 5 divisions in FADC reading were rejected as noise events. One event in which the edge of the test pulse was observed at $t = 79.3\,\mu$s was also rejected since the trigger was not caused by the test pulse but by random noise which preceded it. In any other events with test pulses, their edges were observed between $40\,\mu{\rm s} < t < 50\,\mu{\rm s}$. Finally, we selected 512,668 events out of 515,815 in total. Figure 6.19 shows the measured trigger efficiency of each channel, where the pulse height is expressed in terms of the equivalent photon energy in the abscissas.

Assuming the Gaussian distribution of the peak heights for pulses of an energy E after the shaping amplifiers and its standard deviation σ independent of the energy would be a good approximation since their variances are dominated by electronic noise. Then the trigger efficiency is expected to be

$$\epsilon_{\rm trig}(E) = \frac{1}{2}\left[{\rm erf}\left(\frac{E - E_{\rm th}}{\sqrt{2}\sigma}\right) + 1\right], \tag{6.50}$$

where $E_{\rm th}$ is the threshold of the discriminator. For each PIN photodiode channel, $E_{\rm th}$ and σ was determined using the log-likelihood method where the binomial distribution was assumed for the number of triggers counted in the measurement. The fitted model functions are shown in the same figures in sold

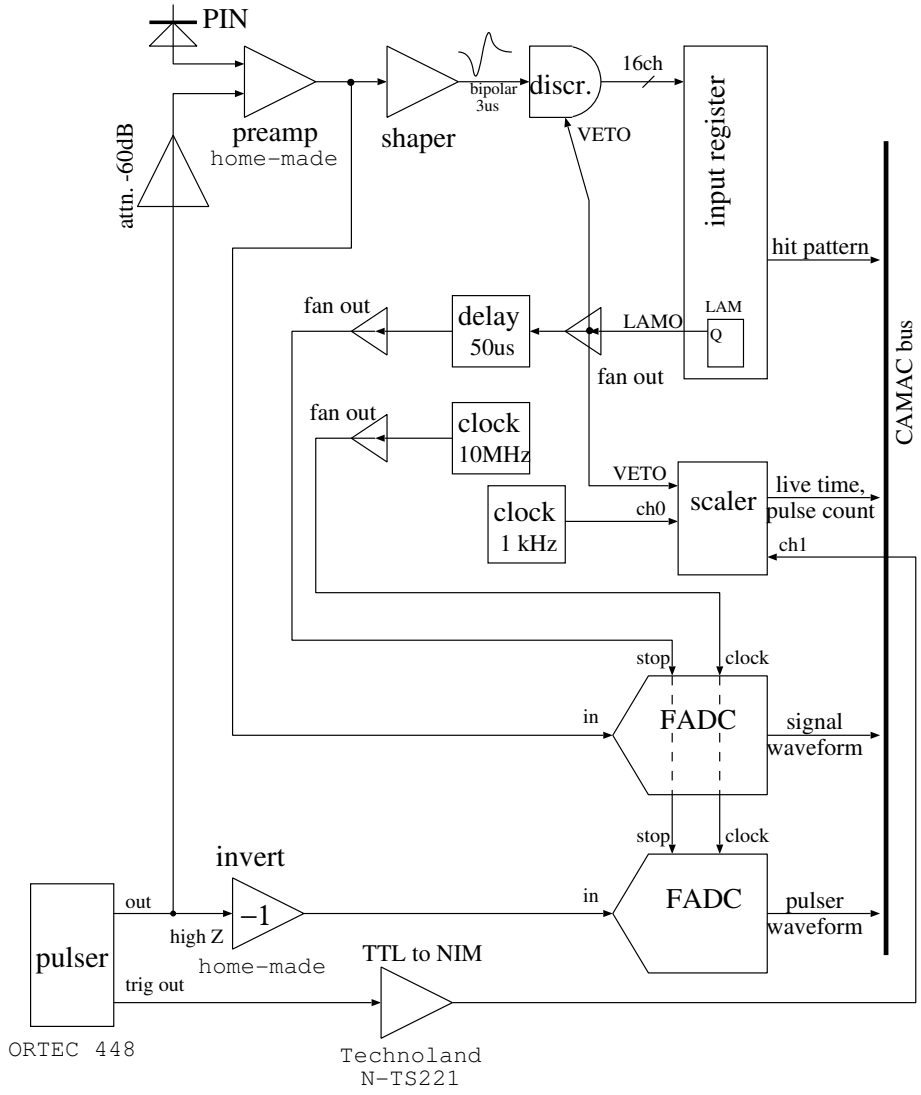

Figure 6.16: Data acquisition system set-up used to measure the trigger efficiency.

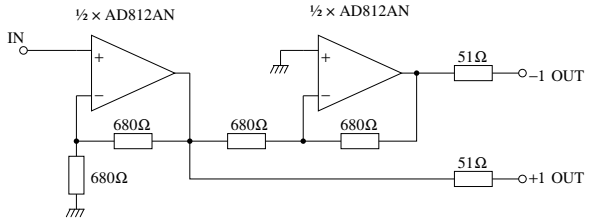

Figure 6.17: Circuit diagram of the inverting amplifier. The non-inverting output was not used in the measurement.

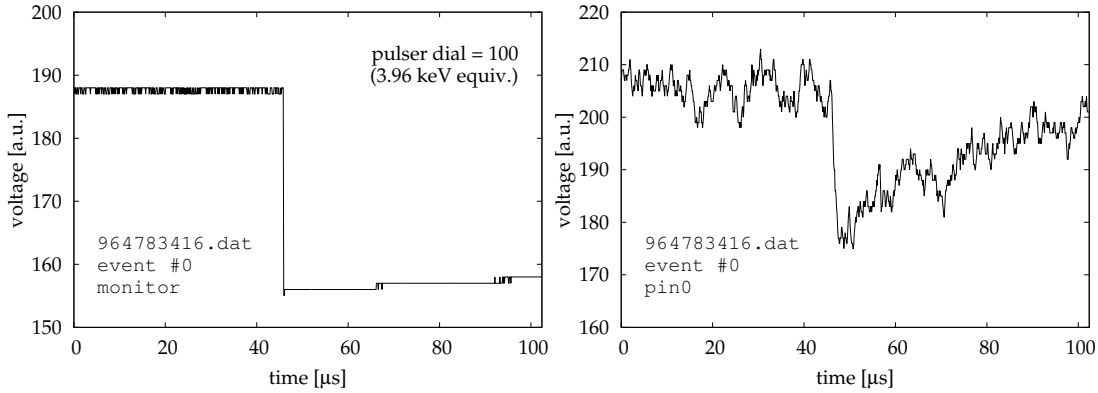

Figure 6.18: Example of a typical inverted pulser waveform (left) seen at the monitoring FADC and the resulting preamplifier signal (right) are shown. In this example, a test pulse whose pulse height was equivalent to a photon of 3.96 keV was injected to the test pulse input of `pin0`.

curves. In the later analysis, we used the worst value at the `pin8` channel which was $E_{\rm th} = 3.545\,\text{keV}$ and $\sigma = 0.520\,\text{keV}$.

6.6 Event selection

An event selection was performed to exclude unwanted events containing corrupted waveforms as well as those events which are apparently not originating from solar axions, e.g., multiple hit events. To determine the selection criteria, we investigated 490,839 inclusive background events which were taken when the calibration source was not exposed and the helioscope direction satisfied the background condition, i.e., $|\theta_{\rm altitude}| > 0.163$ and $|\theta_{\rm azimuth}| > 0.041$. They are "inclusive" because no condition was required to the gas density nor to the mode of the tracking program. Apparently, this data set lacks signals originating from solar axions.

6.6.1 Event selection by waveform signature

Figure 6.20 shows some examples of unwanted waveforms. We named such waveforms that went out of the range of the FADC input to the negative- or positive voltages as the under- or overflowed waveforms, respectively. These

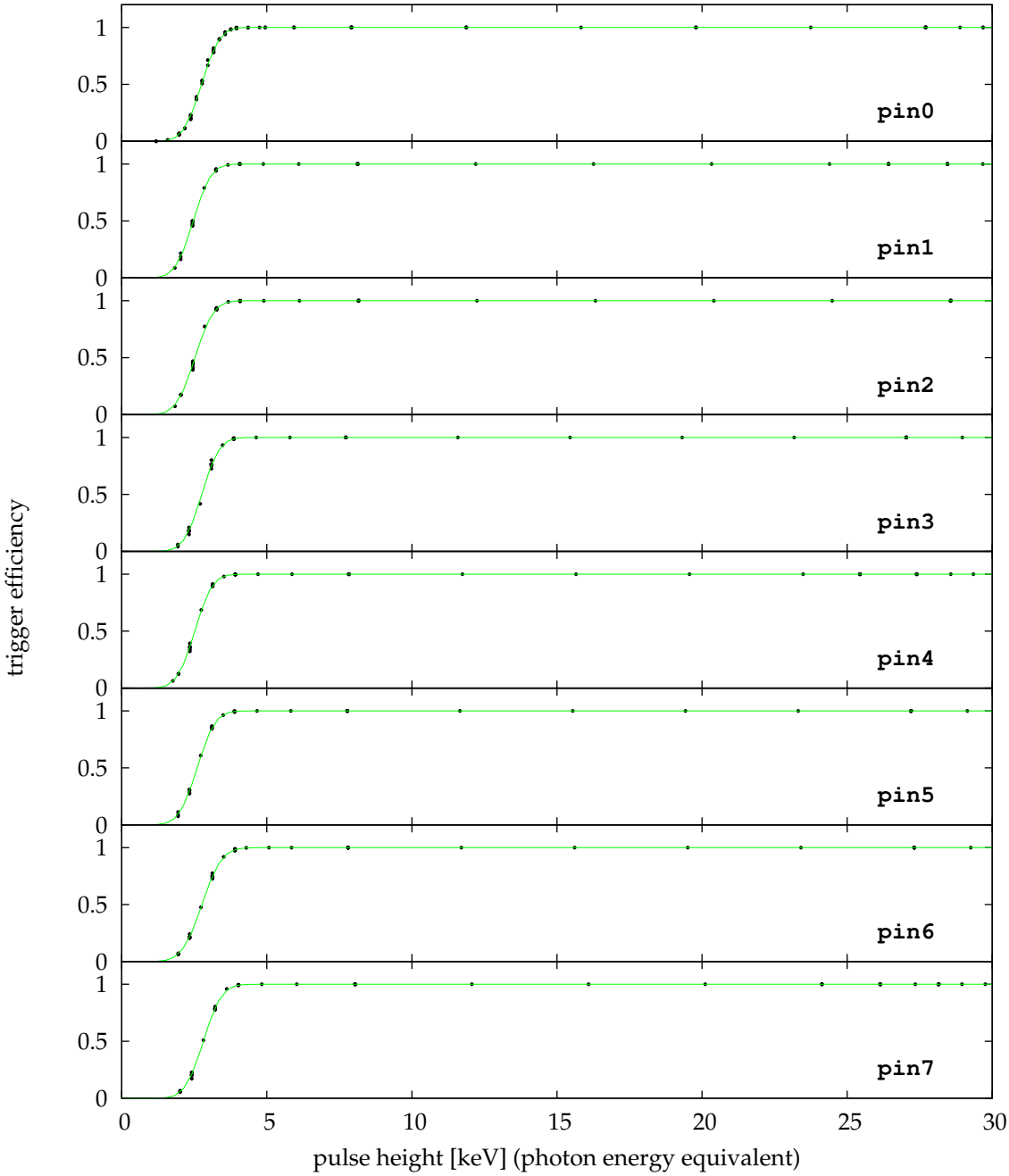

Figure 6.19: Trigger efficiency of each channel. The fitted model function is shown as the solid green curves.

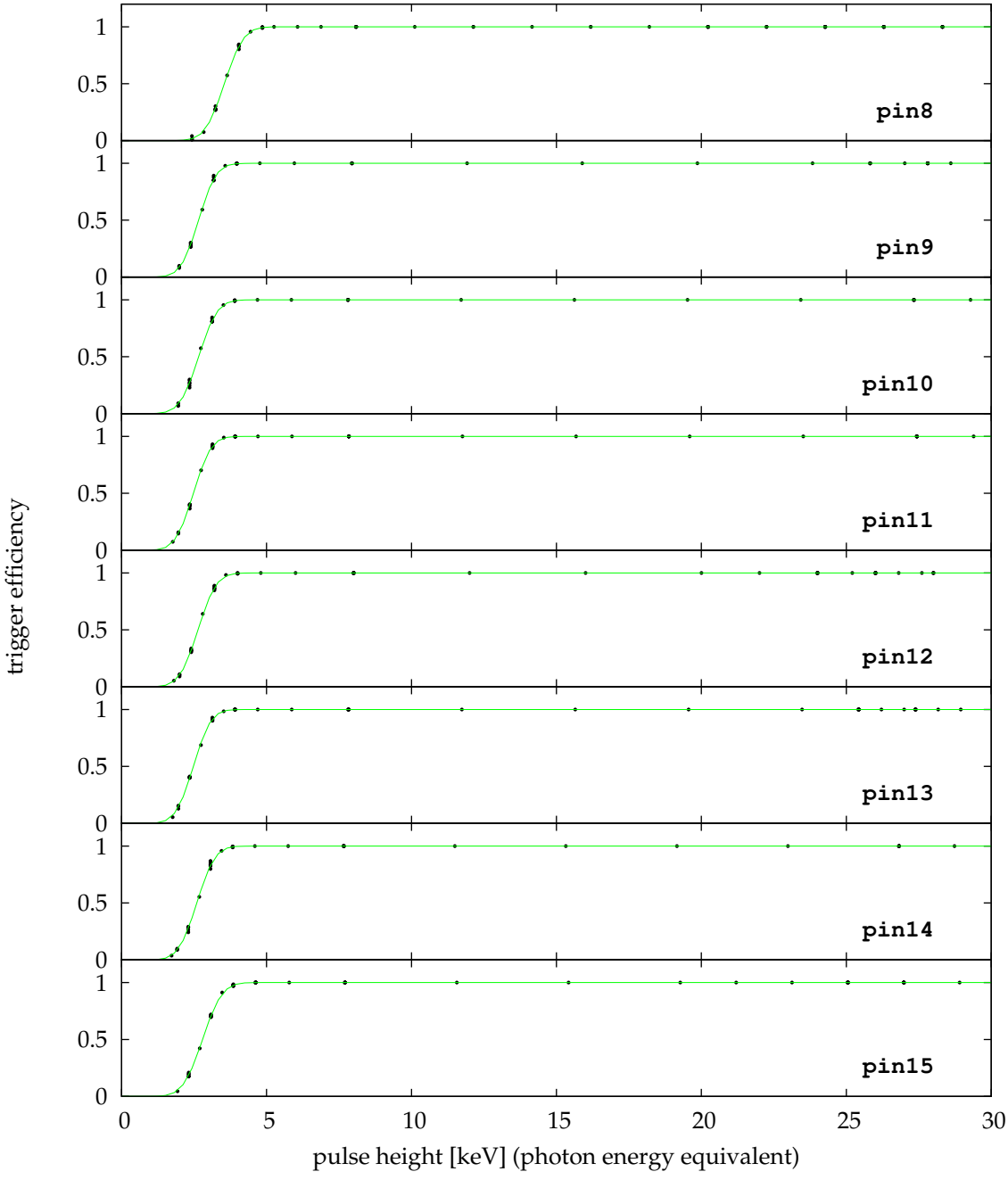

(Figure 6.19 continued)

clipped waveforms do not contain enough information about their total energy. In REPIC RPC-081 FADC, under- or overflows are saturated to the lowest possible value 0, or the highest possible value 255, respectively. Therefore, we treated any waveforms containing 0 or 255 as one of its data to be under- or overflowed ones.

Normal pulses are expected to have negative polarities as exemplified in Fig. 6.20 (a). Most of the underflowed waveforms are considered to be caused by giant signals which are too large to fit into the input range of the FADCs. Figure 6.20 (b) shows one of such giant pulses. The overflowed waveforms, on the other hand, often appeared as clipped "positive" pulses as shown in Fig. 6.20 (c). These are considered to be caused by crosstalks in the preampli-

(a) Ordinary `good` event

(b) Underflowed by a `giant` pulse

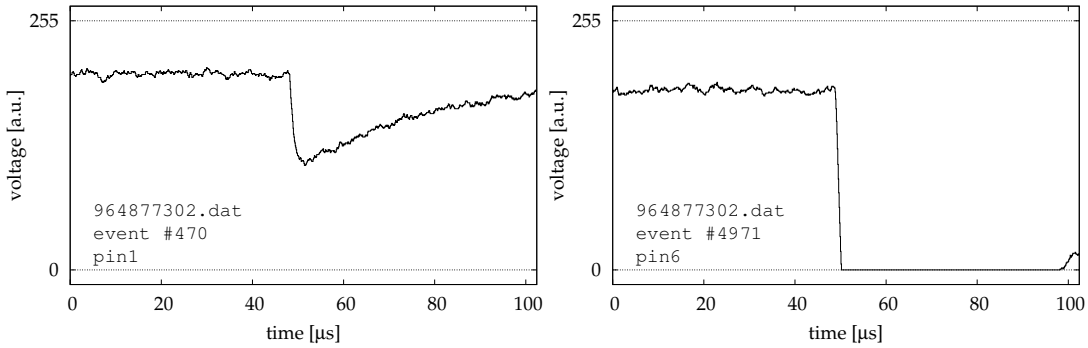

(c) Negative crosstalk of a `giant`

(d) Bipolar crosstalk of a `giant`

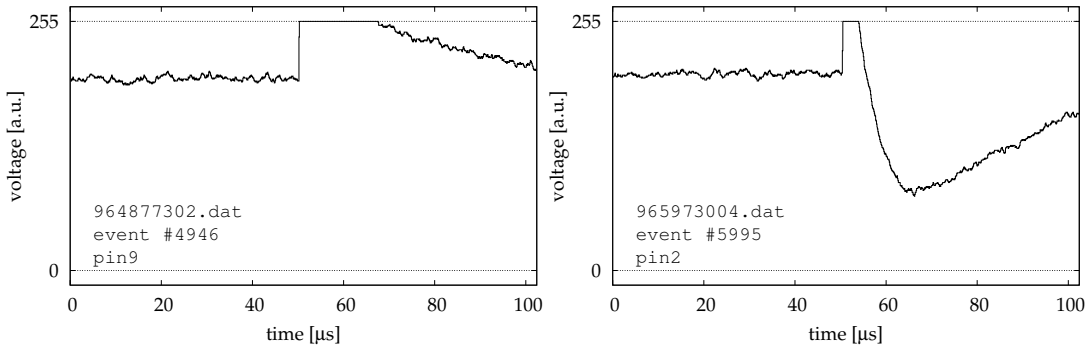

Figure 6.20: Examples of waveforms of unwanted events are shown along with an ordinary waveform as a comparison (Fig. (a)). Waveforms are sometimes clipped by underflowing (Fig. (b)), overflowing (Figs. (c), (d), (e), (f)) the FADC range, or both (Fig. (g), (h)). Fair amount of events contained slow-rise-time pulses (Fig. (i)), which were though rarely seen in the calibration runs. This implies that these events are not resulting from gamma rays. These bad events were systematically removed by their signature.

(continued on the next page)

(e) Overflowed by `microphonic` noise

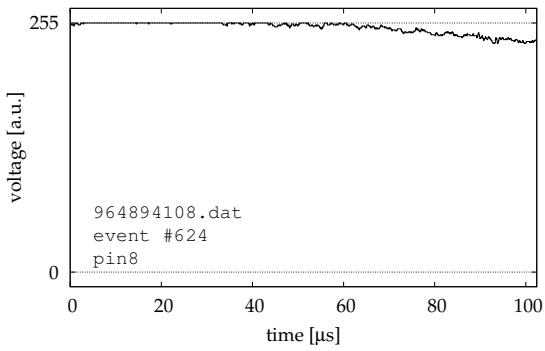

(f) Ordinary pulse in `microphonic`

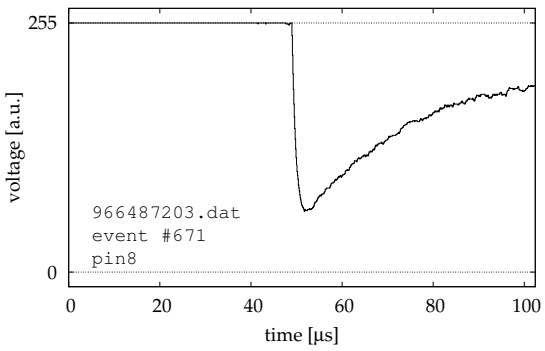

(g) Giant pulse in `microphonic`

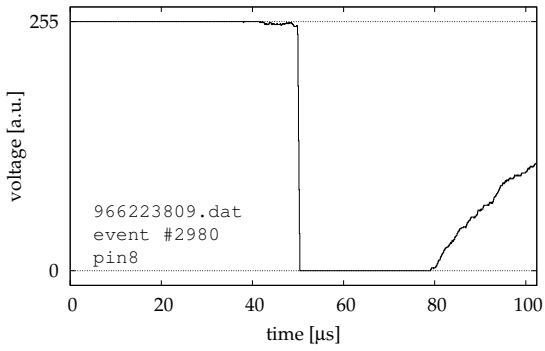

(h) `Giant` bipolar crosstalk

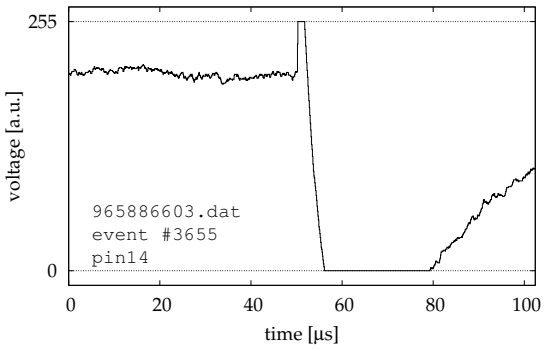

(i) `Slow`-rise-time pulse

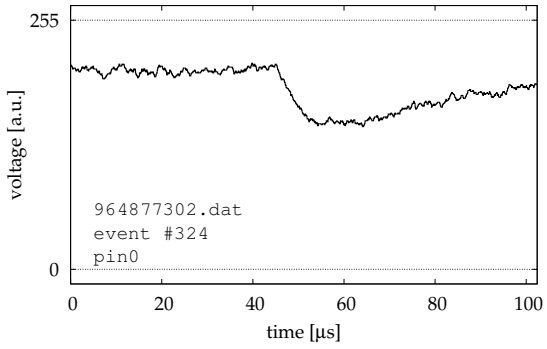

(Figure 6.20 continued)

o	u	t	$\mathcal{G}$	#	category	comment
–	–	–	X		—	Ignored
–	–	✓	–	395,152	$*1$	Candidates for `good`
–	–	✓	✓	60	`giant`	Multiple hit event, `giant` in other channel
–	✓	–	–	48	`giant`	Solitary giant, but late trigger
–	✓	–	✓	16,481	`giant`	Multiple giants
–	✓	✓	–	75,101	`giant`	Solitary giant
–	✓	✓	✓	26,373	`giant`	Multiple giants
✓	–	–	–	11,679	`microphonic`	
✓	–	–	✓	41,215	$*2$	Various crosstalks & microphonics
✓	–	✓	–	299	`microphonic`	
✓	–	✓	✓	1	`microphonic`	Eye-scanned
✓	✓	–	–	0	—	No events
✓	✓	–	✓	261	`giant`	Bipolar crosstalk
✓	✓	✓	–	110	`giant+mic`	Giant in microphonic
✓	✓	✓	✓	32	`giant+mic`	Giant in microphonic

Table 6.5: Event categorization by waveform flags. Each column shows the presence of each flag in a waveform, the number of waveforms which matched each flag patterns, concluded event categories, and some comments. Symbols `o`, `u`, and `t` denote the presence of overflow-, underflow-, and triggered flags, respectively. Symbol $\mathcal{G}$ denotes the presence of one or more accompanying giant pulses in that event, i.e., underflow flags in the other channels. Two cases marked as $*1$ and $*2$ contain events from multiple origins and require further investigation.

fiers, since they always accompanied one or more giant negative pulses in their neighboring channels. The crosstalk pulses sometimes appear in bipolar shape as shown in Fig. 6.20 (d). Part of the ordinary- or giant negative pulses can be common-mode crosstalks. However, they are hardly indistinguishable in shape. Their existence is implied by the fact that giant pulses often appear plurally in an event.

Another cause of the overflowed waveforms are the baseline fluctuations notably by microphonic noise, one is exemplified in Fig. 6.20 (e). Microphonic noise sometimes corrupts normal pulses (Fig. 6.20 (f)) or giant pulses (Fig. 6.20 (g)). The chances that microphonic noise has produced underflowed waveforms is expected be rare in our set up, since the DC baselines of the preamplifier outputs were set near the upper bound of the FADC range at around 200/256. There was about four times larger room below the baselines than above them.

In order to categorize waveforms systematically, each waveform was labeled with some flags according to their apparent characteristics. Any waveforms that accompanied trigger signals on those channels were attached with the `t`-flag for 'trigger'. By any occurrences of under- or overflow, the `u`-flag for 'underflow' and/or the `o`-flag for 'overflow' were attached to the waveforms. Table 6.5 shows the categorization based on the flag patterns. In the table, the $\mathcal{G}$ pseudo-flag for 'Giant' does not indicate any characteristics of the waveform of interest itself,

but it indicates that one or more waveforms with the u-flag present in the other channels of the same event.

From the above discussions, any good events are expected to be contained in the group flagged only "t" and without any other flags. Waveforms flagged "tu" = t + u or "tu$\mathcal{G}$" are considered to be caused by giant pulses. In the same way, waveforms flagged "t$\mathcal{G}$" themselves may be normal waveforms, however they are mark as "giant" in the table because the events containing them are to be excluded because of the giants in the other channels. We ignored waveforms without any flags in this selection.

The underflowed large pulses without corresponding triggers, i.e. those with "u", "u$\mathcal{G}$", "ou", or "ou$\mathcal{G}$", may look bizarre because these waveforms should actually possess enough pulse heights to activate the discriminators. This phenomenon occurs because the discriminators are vetoed right after the first arrival of a trigger in each event —please refer Fig. 5.27— so that there are chances that the leading edge of a large enough pulse can lag behind the veto caused by a trigger from another channel.

Waveforms both with under- and overflows but without triggers flagged "ou" or "ou$\mathcal{G}$ consisted of bipolar crosstalks as exemplified in Fig. 6.20 (h). In fact, all of these waveforms accompanied giant pulses in the other channels. In other words, we saw no occurrences of "ou", but all of them were "ou$\mathcal{G}$". This fact endorses the conclusion that all of these waveforms belonged to this category. In bipolar crosstalks, the waveforms go positive once, and their falling edges are late enough to lag behind the veto signals generated by the first trigger from one of the other channels. Therefore, it is hardly probable for bipolar crosstalks to appear as "tou$\mathcal{G}$".

All of the $32 + 110$ waveforms flagged "tou" and "tou$\mathcal{G}$" were eye-scanned and confirmed to belong to giant pulses tainted by microphonic noise as exemplified in Fig. 6.20 (g). Rest of the waveforms with o-flag but without $\mathcal{G}$ are considered to be tainted by microphonic noise. The single waveform flagged "to$\mathcal{G}$" was also eye-scanned and confirmed to be an ordinary pulse tainted by microphonic noise. The 41,215 waveforms flagged "o$\mathcal{G}$" were a mixture of microphonic events and various crosstalks. Further investigation is required to discriminate microphonics from crosstalks in them.

Among the events consisting only of waveforms flagged "t", those with multiple pulses in different channels at once were excluded. In other words, an event can be good if it contains one and only one waveform flagged "t" and flags on the other channels should be none. Since events induced by solar axions are expected to be extremely rare, multiple hits must be a sign of background including cosmic ray showers and cascade decays of natural radioactivities. The crosstalk between channels could be another cause of the multiple hit events. However, the observed crosstalk was so small that it was not noticeable without any giant pulses. Therefore, we can safely assume that any crosstalk events which triggered multiple channels at once were already excluded as being bad because of giant pulses.

6.6.2 Multiple hit rejection using pulse height analysis

We used not only the trigger hit pattern information but also the pulse height information to remove multiple-hit events. Since the discriminators are vetoed right after the first occurrence of a trigger in each event, it may have missed

some late pulses. We set out a set of thresholds for each channel and marked every event as multiple hit if one or more peak heights exceeded the thresholds in the other channels.

To determine the thresholds, we picked up all the waveforms without flag from the 395,152 candidate events for `good`. Figure 6.21 shows the peak height spectra and the scatter plots of the peak timings versus the peak heights. The peak heights are plotted in terms of the equivalent photon energy based on the energy calibration using ^{55}Fe. They are not corrected for the gain walk by the trigger timing. The timings are relative to the signal templates. The bin widths of the histograms are 20 eV, and the vertical scales in them are logarithmic.

Two distinctive components are observed in each plots. One in the majority is the pedestal peak component which settles at the bottom of the energy scale but is less restricted in the timing scale. The other is of the silent true pulses which have missed trigger. They range over wide energies, however, their timings are not going too far from the center, $t \sim 0$. Although we have only small statistics, the number of silent pulses between 2–5 keV was $n_{\rm miss} \sim \mathcal{O}(1\,\text{waveform/keV/PIN})$ in the given data set.

For each channel, we determined the threshold, $E_{\rm th}$, so that the expected number of true pulses which are to be dropped and that of mere noises which are to be counted mistakenly as pulses become on a par. We assumed that the distributions of the silent pulse components can be extrapolated to lower energies using constant functions, $f(E) = n_{\rm miss}$, and that those of the higher sides of the pedestal peaks can be extrapolated using exponential functions, $f(E) = n_{\rm miss} \exp[(E_x - E)/E_d]$. Then, $E_{\rm th}$, is obtained by solving:

$$n_{\rm miss} E_{\rm th} = \int_{E_{\rm th}}^{\infty} n_{\rm miss} \exp \frac{E_x - E}{E_d}\, dE, \tag{6.51}$$

or

$$E_{\rm th} = E_d \exp \frac{E_x - E_{\rm th}}{E_d}. \tag{6.52}$$

The vertical dashed lines in Fig. 6.21 indicate the obtained thresholds. Data above the thresholds are shown in crosses, and those below them are plotted in dots in the scatter plots.

We found 142 events in the test data which were to be excluded by this cut.

6.6.3 Rejection of slow-rise-time pulses

Fair amount of events contained slow-rise-time pulses which were though rarely seen in the calibration data using the ^{55}Fe source. An example of such pulses is shown in Fig. 6.20 (i). Although we have not assigned the cause yet, absence of such pulses in the calibration data implies that they are not resulting from gamma rays.

The rise time of an ordinary pulse is 1.2–1.6 μs to go up from 10% to 90% of its pulse height, which is dominated by the time constants of the preamplifiers. In slow-rise-time pulses, on the other hand, it ranges from 4 to 15 μs and is typically 8 μs.

When the duration of maximum of the weight function of waveform shaping is shorter than the charge collection time, the resulting pulse heights become

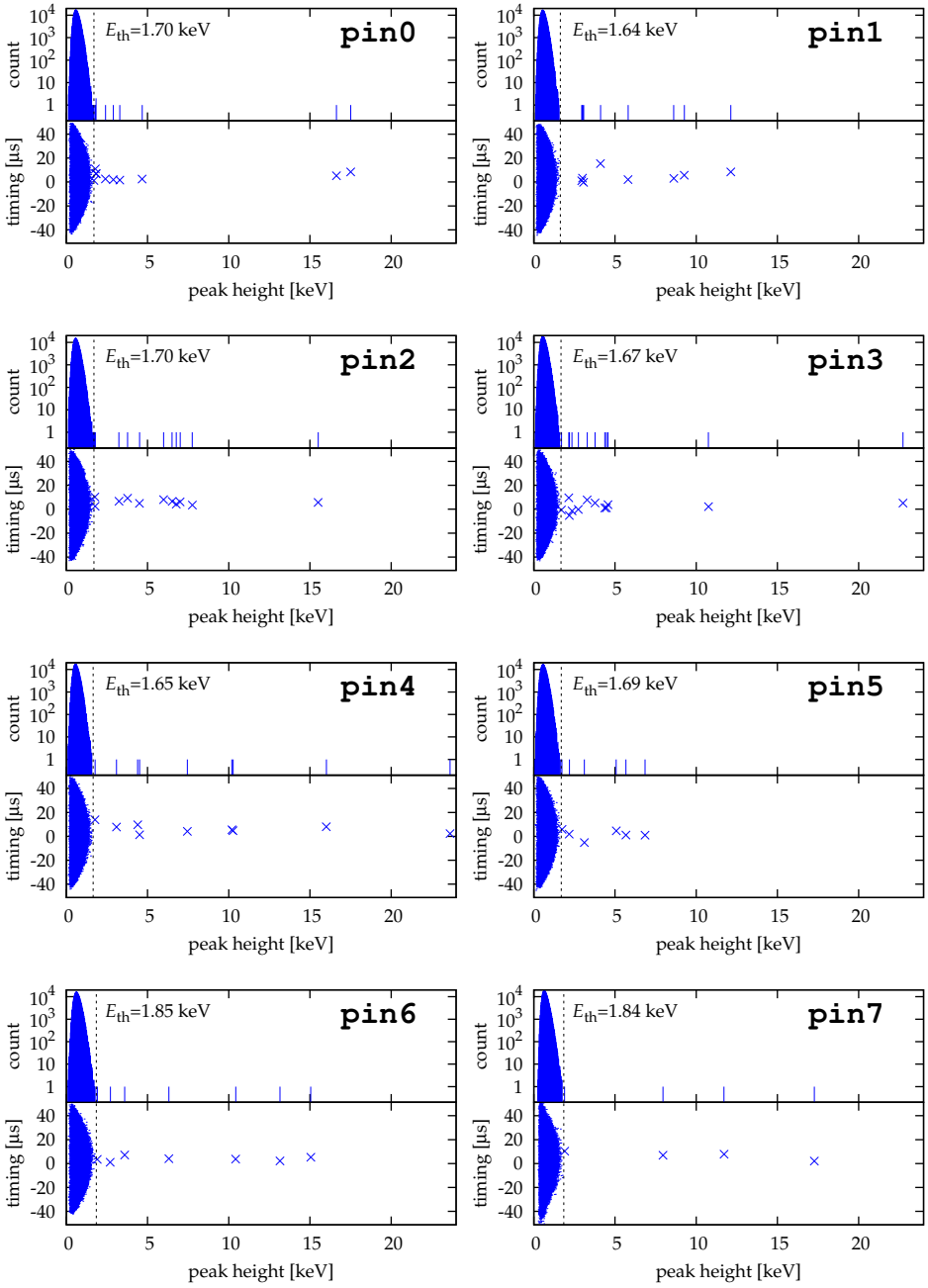

Figure 6.21: Analysis of the waveforms without flag. The upper halves are the peak height spectra, and the lower halves are the scatter plots of the peak timings versus the peak heights. The timings are shown relative to the signal templates, and the heights are plotted in terms of the equivalent photon energy. The peak heights are not corrected for the gain walk by the trigger timing. Data above the thresholds are plotted in crosses.

(continued on the next page)

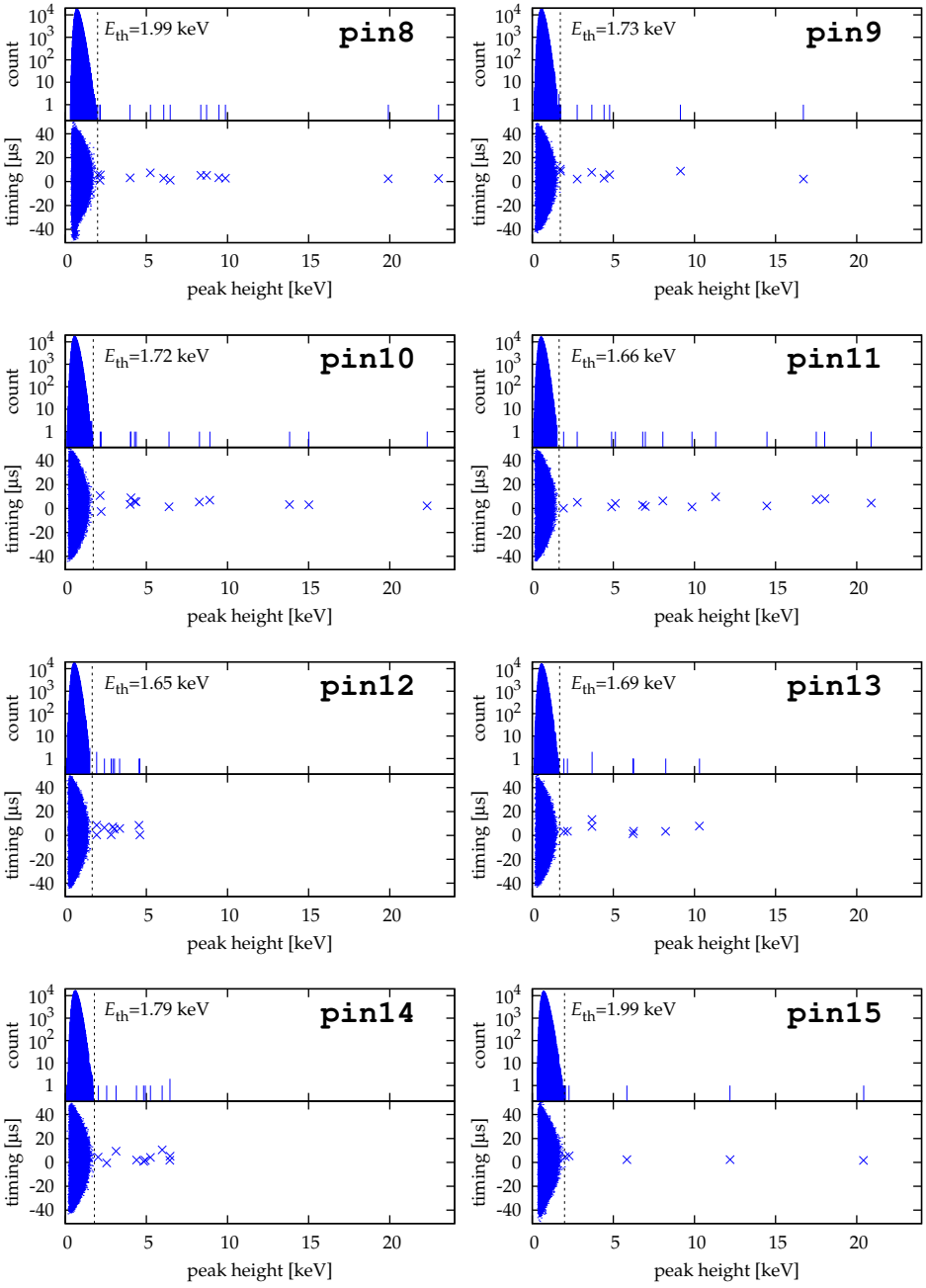

(Figure 6.21 continued)

lower than expected from their total energy losses. This falloff is called the "ballistic deficit". As shown in Fig. 6.9, the waveforms after shaping in our analysis have pointed top shapes. This means that we cannot expect these slow-rise-time pulses to contribute to any meaningful spectrum, since we cannot expect their peak values to reflect their total energy losses. Furthermore, broad continuum of background can be spuriously compressed into the low energy region by the ballistic deficit, where the region of interest is.

In this analysis, instead of regaining the true total energy losses, we excluded these events systematically by their signatures and estimated the loss of efficiency by the selection.

Direct measurement of the rise time of a pulse is not easy except for very large pulses because of noise inseparable from the signal. Instead, we emulated the gated integrator shaper [100] by integrating the shaped waveforms over 12.8 μs, or 128 channels in the time bin. Slow-rise-time pulses would regain some of their ballistic deficit by this integration. The integration interval was chosen to cover the typical slow rise times. From the convolution theorem, definite integral in the time domain is equivalent to multiplying the Fourier transform of a window function defined as

$$w(t) = \begin{cases} 1 & \text{for } -T/2 < t < T/2, \\ 0 & \text{otherwise} \end{cases} \tag{6.53}$$

in the frequency domain, where $T = 12.8\,\mu$s is the integration interval. We prepared a set of modified filter functions and used it in digital filtering in place of the optimal filter functions:

$$\tilde{H}'_k = \tilde{H}_k \tilde{w}_k. \tag{6.54}$$

Figure 6.22 shows the scatter plot of the ballistic recovery rates versus the peak heights. The horizontal axis of each plot shows the peak height of each shaped waveform in terms of the equivalent photon energy based on the energy calibration using ^{55}Fe. They are not corrected for the gain walk by the trigger timing. The vertical axis show the peak height of the integrated waveform divided by that of the normal optimal filter. The gains of the integrated filters are normalized by the template waveform so that ordinary pulses will appear at around 1. Slow-rise-time pulses will appear at higher bands. Plots in the left side are of the candidates for `good` events in the inclusive background data after rejection based on flag pattern analysis and rejection of the multiple hit events. The right ones are of the calibration data where 5.9-keV manganese X-rays from a ^{55}Fe source were observed.

In the plots of background data, we find three distinctive groups in each plot. Most of the points are in the pedestal component mainly below 2 keV. They are the crest values of pure electronic noise where noise has triggered one of the discriminators by accident. Although appropriate energy thresholds may depend on channels, we set a common threshold to discriminate this component at $E \leq 2.5$ keV. In the later analysis, we will discuss the fiducial energy range which is to be contained in this cut. The second group is the horizontal band at ratio of 1, and the third group is the more diffused horizontal band which is centered at around ratio of 1.4. Naturally, the second one is the group of normal pulses which we will use in the later analysis, and the third one is the slow-rise-time pulses which are to be excluded.

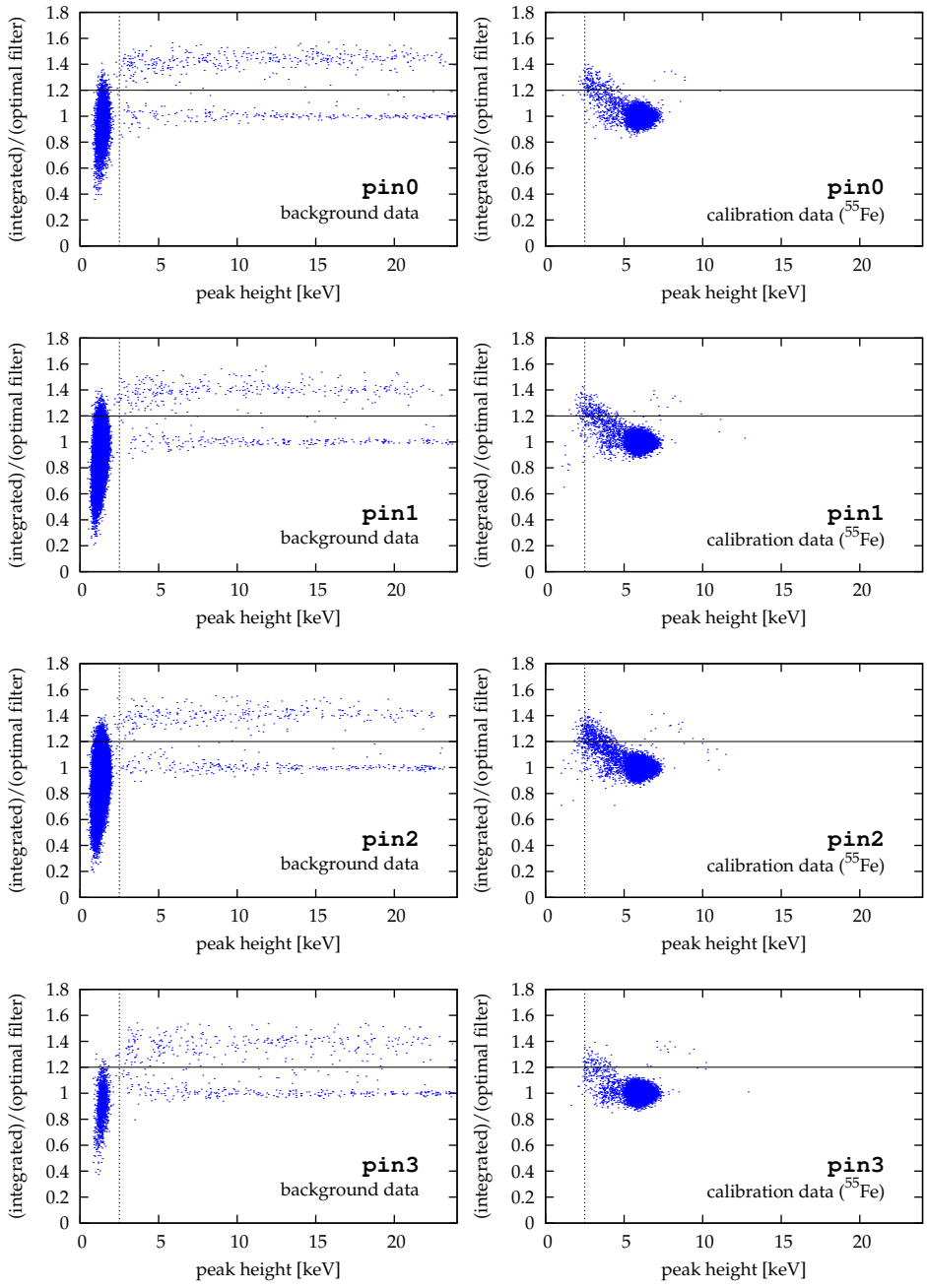

Figure 6.22: Scatter plots of the ballistic recovery rates versus the peak heights. The left figures show the candidates for `good` events in the inclusive background data, and the right ones show the calibration data using a ^{55}Fe source. The data above the horizontal line in each plot were excluded as slow-rise-time pulses. The vertical dotted line indicates the low energy cut to exclude pedestal components.
(continued on the next 3 pages)

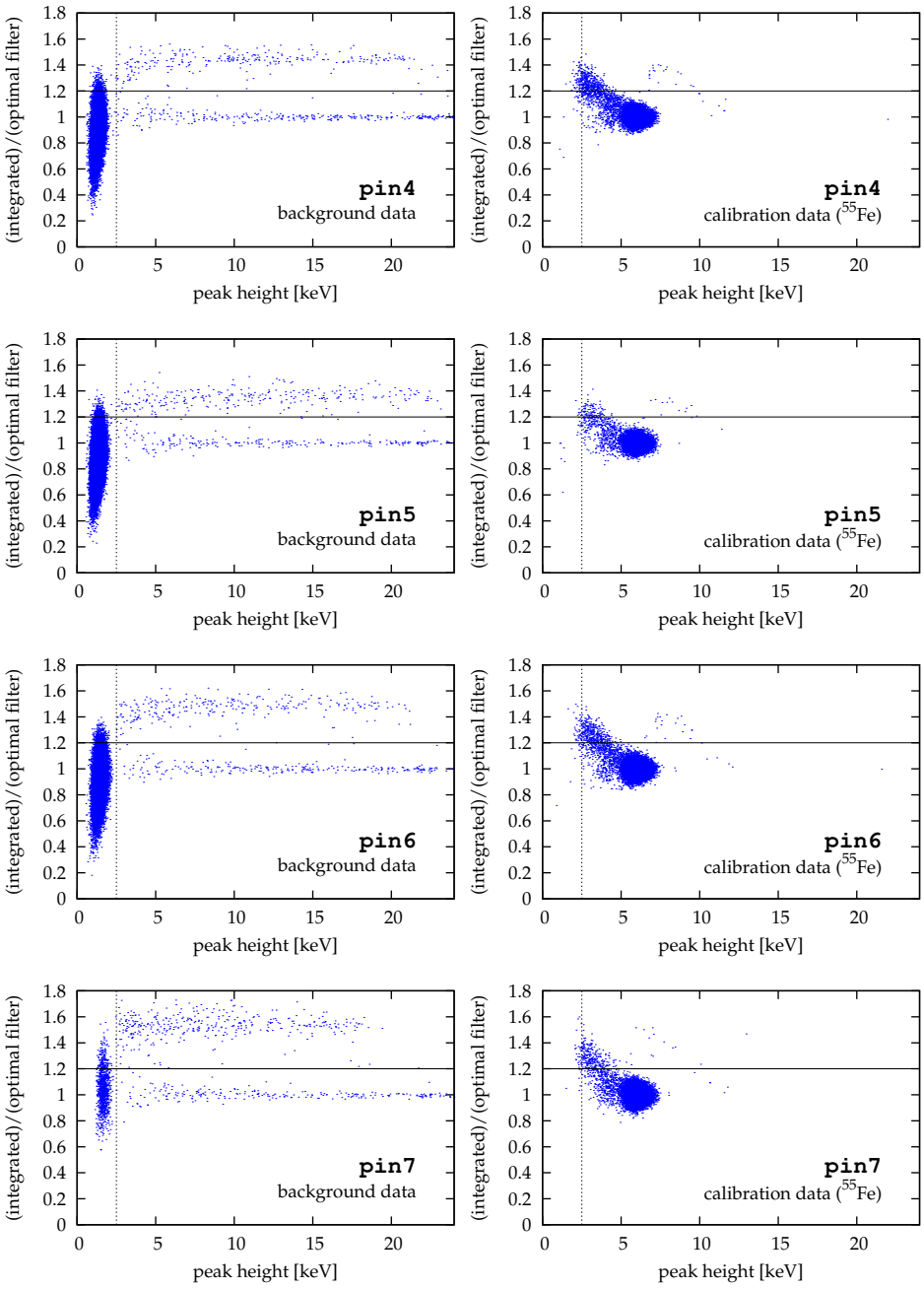

(Figure 6.22 continued)

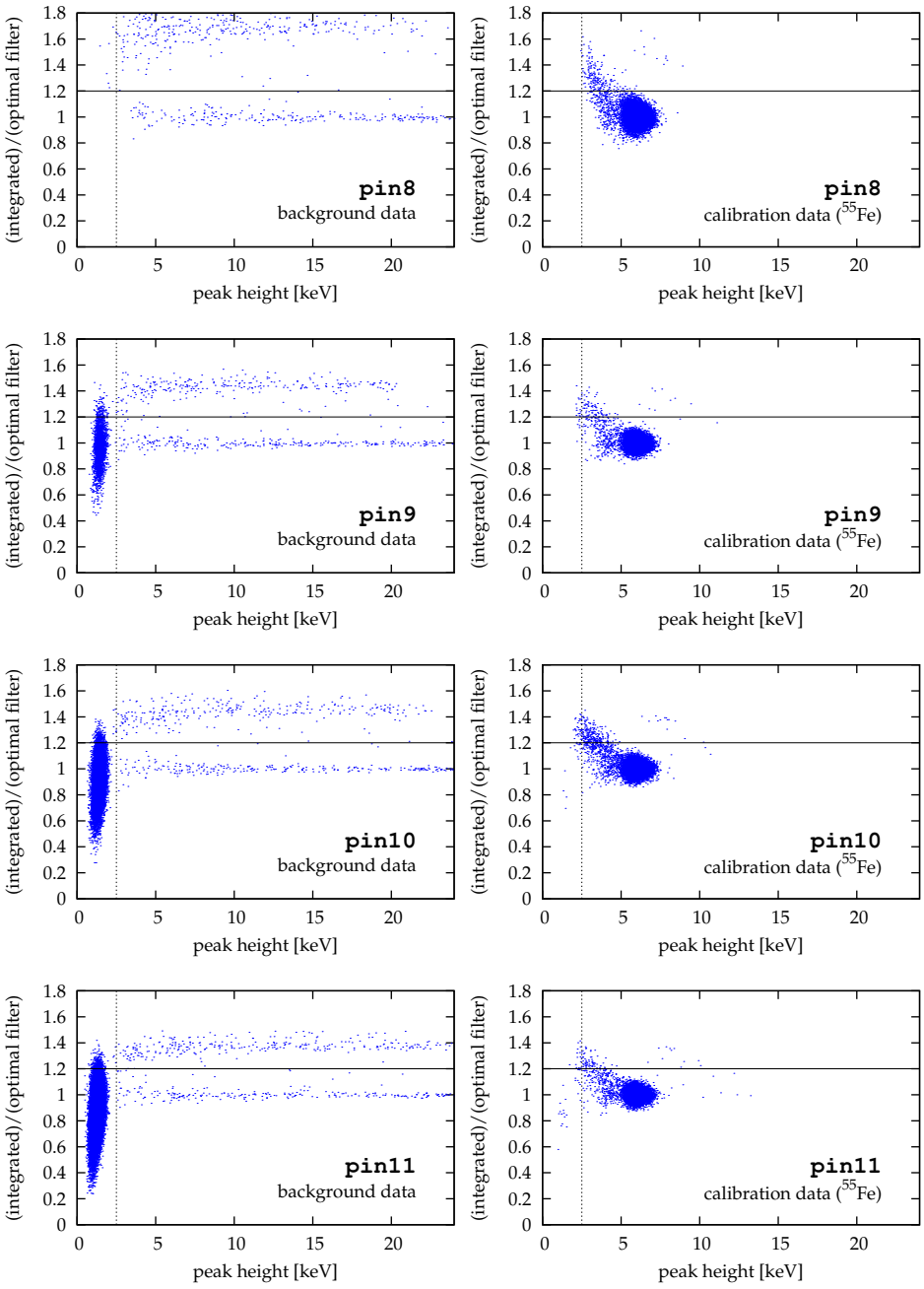

(Figure 6.22 continued)

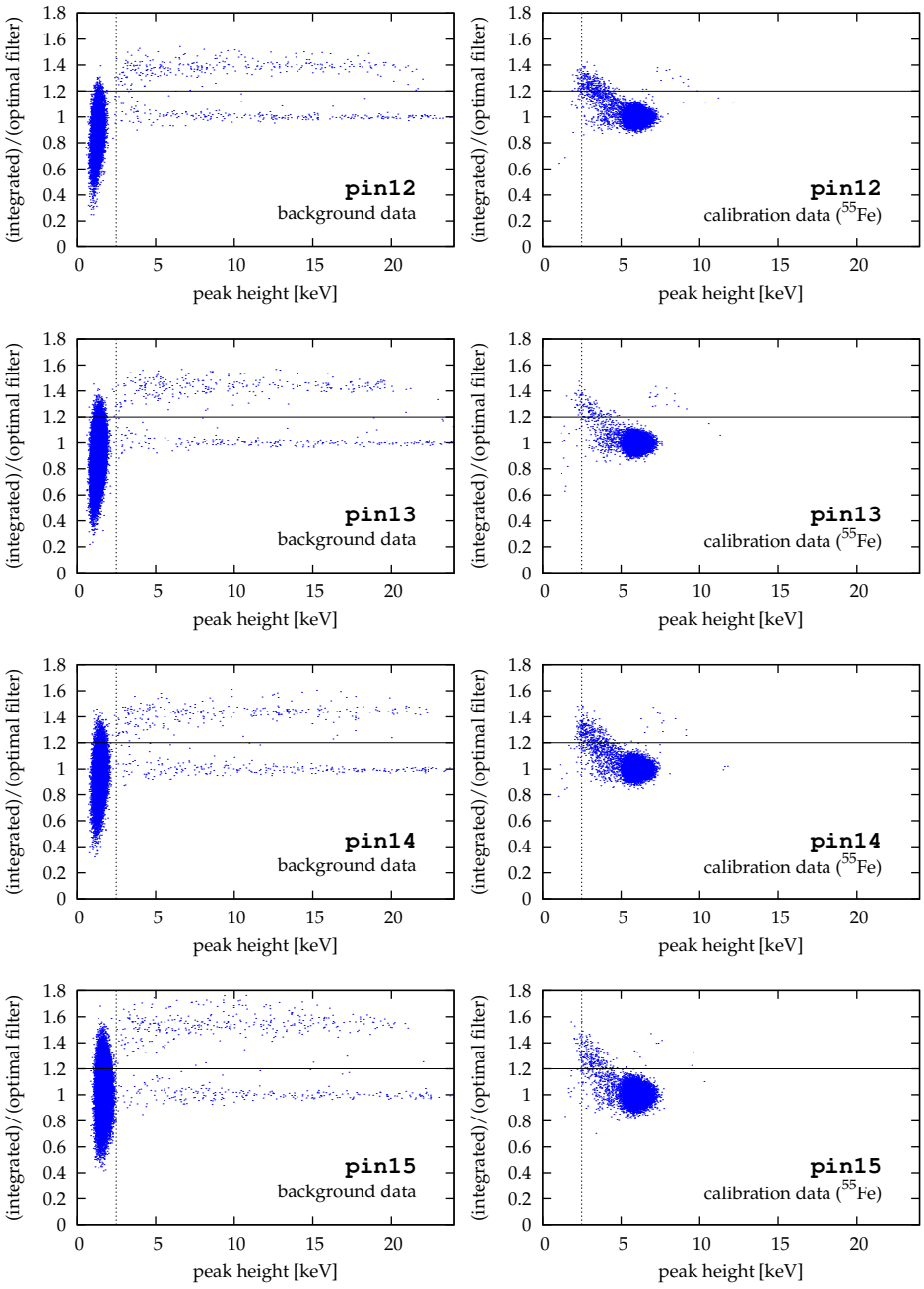

(Figure 6.22 continued)

From the plots, we determined the threshold for the slow-rise-time pulses by the eye to be 1.2. Out of 383,478 candidates for `good` events in the inclusive background data, 373,924 events (97.5%) were in the pedestal component below $E < 2.5\,\mathrm{keV}$, 4,841 events (1.3%) were categorized to slow-rise-time pulses, and 4,713 events (1.2%) remained as `good` pulses.

In the plots of calibration data, we find a single group in each plot whose center of the energy is at 5.9 keV and that of peak height ratio is at 1. The egg shape of the dense area is due to the weak resolution of the K_α and K_β components. Unlike the background data, we find no separate group for slow-rise-time pulses. Instead, we find a thin fin shaped tail extending toward upper left and left direction from the dense area.

Although the K-fluorescent yield of manganese is only $\omega_K = 0.314$ [101], the measured dead layer of the silicon PIN photodiode is thick enough to decelerate most of its energy from 5.2-keV Auger electrons from the ^{55}Fe source. Therefore, we can assume that we are seeing pure photons in these plots. Out of 231,627 events in the calibration data, 3,892 events were found to have the peak height ratio larger than 1.2. From these values, we estimated the loss by this cut to be

$$1 - \epsilon_{\mathrm{cut}} = (1.68 \pm 0.03) \times 10^{-2}. \tag{6.55}$$

The fact that we found only intermediate tail component instead of a separate group at around ratio of 1.4 in the calibration data implies that these slow-rise-time pulses are related to the surface zone, where the electric field is weaker and the electron/hole traps may be denser than the bulk zones. Considering the structure of the PIN photodiode, we can further speculate that slow-rise-time pulses in the background data are produced in the thicker rear surface zones.

6.6.4 Trigger timing cut

As discussed in Section 6.3.5, before applying compensation to the gain dependence by the signal position, we required the timing to fall within the fiducial interval defined in Table 6.2. Since we found no events outside them in the 4,713 remaining candidates for `good` events, we will ignore the loss by this cut entirely. In fact all points are contained within a narrow band between $-4.4\,\mu\mathrm{s} \le t \le 3.1\,\mu\mathrm{s}$. In Fig. 6.23, we show a scatter plot of the signal positions versus the energies in the upper pane, and a histogram with respect to the signal positions in the lower pane. The fiducial interval is indicated as an arrow with both heads. Although the fiducial interval varies slightly by the signal channel, we showed the inner most interval of all in the figure.

6.6.5 Live time deficit by microphonics

In this section, we will re-examine the measured live time and estimate the amount of correction to it.

Each record of an event contains the time between the last DAQ ready and the DAQ busy after a detection of a trigger in millisecond accuracy by counting the 1-kHz clock pulses. The live time is measured by integrating these 'atomic' live times during a measurement. Dead time caused by the DAQ system is correctly taken into account this way.

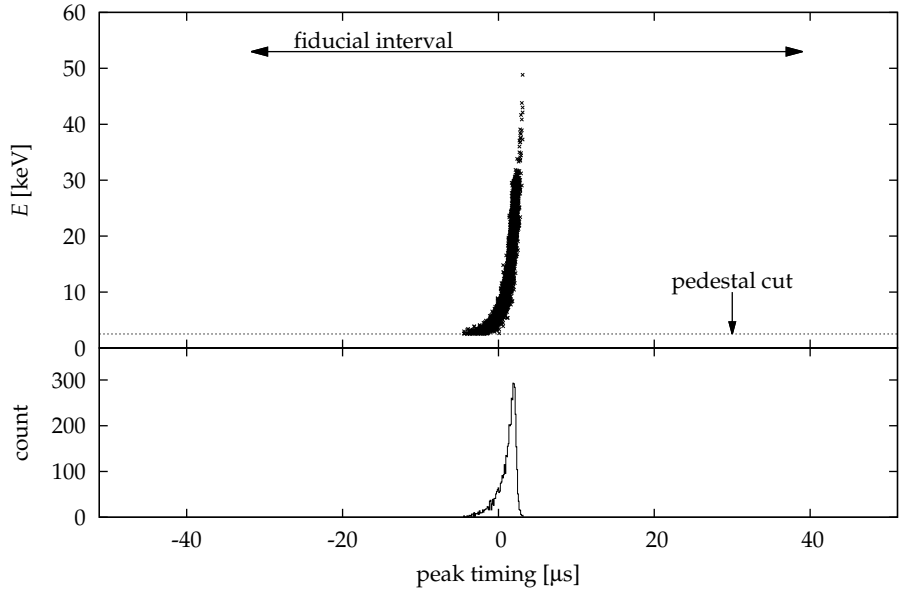

Figure 6.23: Peak timings of the `good` events. In the upper pane, the peak timings versus the peak heights are shown as a scatter plot. The timings are plotted relative to the signal templates, and the heights are plotted in terms of the photon energy. We observe no events below 2.5 keV because of the pedestal cut applied beforehand. In the lower pane, a histogram with respect to the timings is shown.

In the above sections, we have excluded some bad events. In most cases, we should add in their atomic live times even when we discard the events for some reasons, since if they, e.g., cosmic ray hits or decays of radioactive nuclei, had not happened, the 1-kHz clock would have continued counting. Therefore, the live time should be carried-over. Whereas, the intervals should be treated as the dead time while microphonic noise had brought the signal out of the input range of FADCs, since we would not see any normal signals during that periods.

The correct dead time can not be obtained naively by rejecting the atomic live times in the events already categorized as "`microphonic`" in Section 6.6.1. It is because remnant microphonics can still reside in the waveforms flagged "$\mathtt{o}\mathcal{G}$" which are the mixtures of crosstalks and microphonics. Furthermore, we have no information of the waveform between triggers. Thus, we can not tell exactly how much of the measured time was dead during this periods. In this analysis, we estimated this dead time statistically.

Let us assume that the rate of dead time by microphonic noise is constant, p_{mic}, and that triggers are independent of microphonic noise. Then the probability of seeing m waveforms which were tainted by microphonic noise at each trigger in N events should obey the binomial distribution:

$$\mathrm{Binom}(m; N, p_{\mathrm{mic}}) = \binom{N}{m} p_{\mathrm{mic}}^{m} (1 - p_{\mathrm{mic}})^{N-m}. \tag{6.56}$$

The former assumption is not absolutely true as we see it in the following, however, the same discussion holds true as far as the variation is not extreme

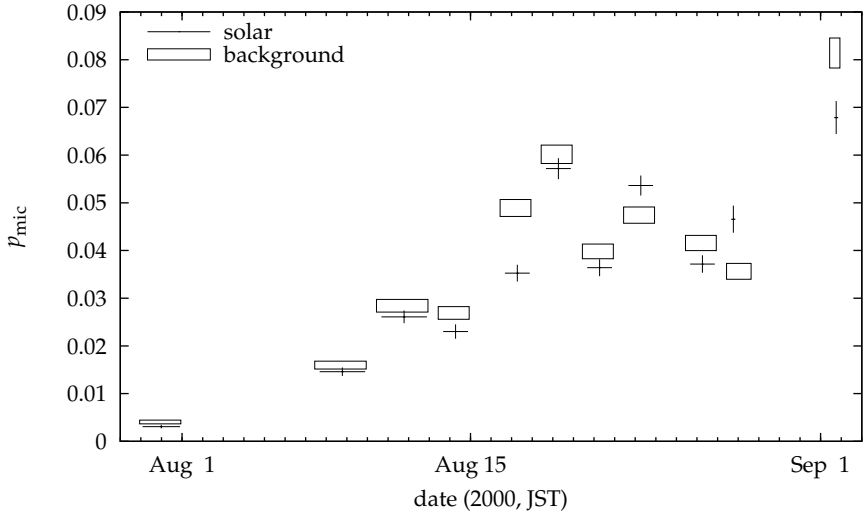

Figure 6.24: Time variation of the ratio of the dead time $p_{\rm mic}$, which is caused by microphonic noise. Values of $p_{\rm mic}$ are plotted for each sets of solar-tracking and background measurements, where crosses correspond to the solar observations, and open boxes correspond to the background measurements. The horizontal axis is the date in local time and the vertical axis shows $p_{\rm mic}$ which are indicated by their center. The heights of the vertical lines or the boxes denote the statistical errors, and the widths of the horizontal lines or the boxes show the interval which contributed to each data.

during a measurement and its time scale is much longer than the intervals between events. The latter is conservative since we will expect lower sensitivity by counting more microphonic events if their triggers are caused by microphonic noise.

Now, let us concentrate on the events without any giant pulses. We have already sorted out all such events in Section 6.6.1, and can tell whether an event is tainted by microphonic noise or not from their waveform signatures. Then, let $N_{\not G}$ be the number of events without any giant pulses, and let $N_{{\rm mic}\not G}$ be the number of events tainted by microphonic noise in them. Apparently, the absence of a giant pulse is independent of the presence of microphonic noise. From Eq. (6.56), therefore, we find for the probability of obtaining $N_{{\rm mic}\not G}$ out of $N_{\not G}$ events given $p_{\rm mic}$ as

$$P(N_{{\rm mic}\not G}, N_{\not G}|p_{\rm mic}) = {\rm Binom}(N_{{\rm mic}\not G}; N_{\not G}, p_{\rm mic}), \tag{6.57}$$

which gives the expectation value for the ratio of the microphonic dead time as

$${\rm E}[p_{\rm mic}] = N_{{\rm mic}\not G}/N_{\not G}. \tag{6.58}$$

In the later analysis, we left $p_{\rm mic}$ as a free parameter and used Eq. (6.57) to incorporate the statistical knowledge of the $p_{\rm mic}$ into consideration.

Finally in this section, we show the time variation of $p_{\rm mic}$ in Fig. 6.24. The $p_{\rm mic}$ values were obtained by $p_{\rm mic} = N_{{\rm mic}\not G}/N_{\not G}$ for each sets of solar-tracking and background measurements individually. The value was not at all constant

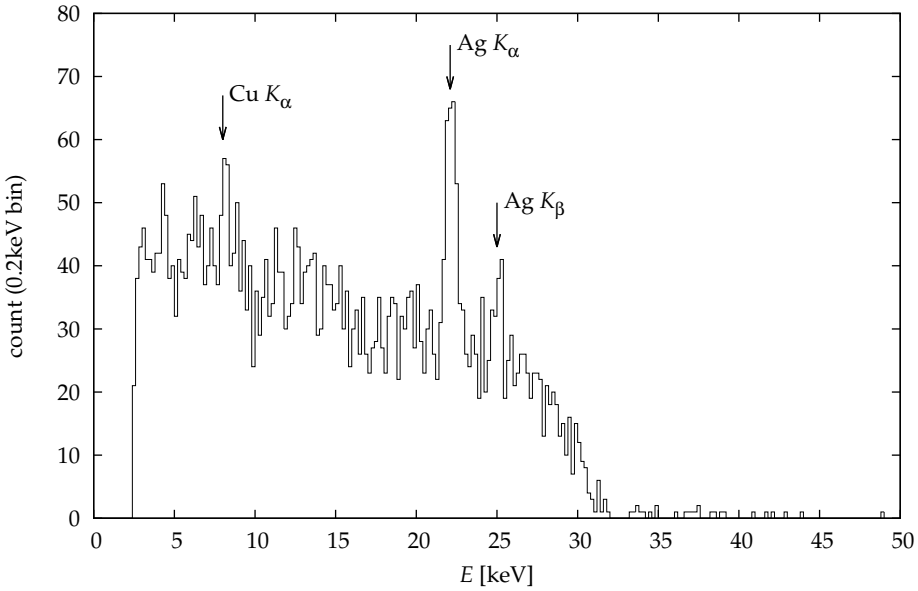

Figure 6.25: Background energy spectrum.

throughout the Phase II measurement. Therefore, we should determine p_{mic} individually not only for each distinct gas density settings but also for solar-tracking and background measurements. However, the variation was slow and moderate enough so that it allows us to justify the above discussion where we expect the same binomial distribution of microphonic events by using the average of p_{mic} over a single run.

category	# of events	comment
`giant`	95166	Signal too large. (FADC underflow)
`microphonic`	11816	FADC overflows by microphonic noise.
`multi`	146	Multiple hit at once.
`down`	233	Ignored `pin0` events during its down time.
`pedestal`	373924	Signal too small, $E < 2.5\,\mathrm{keV}$.
`slow`	4841	Slow-rise-time pulses.
`good`	4713	
total	490839	

Table 6.6: Numbers of events by categories in the inclusive background data. In mixed cases, the upper categories are taking precedence over lower ones in this table. For example, those events both with `giant` and `microphonic` waveforms in them are counted as `giant`.

6.6.6 Summary of the background analysis

Finally in this section, we summarize the result of the analysis of 490,839 events in the inclusive background data during the Phase II measurement.

In Table 6.6, the number of events in each category is summarized. In Fig. 6.25, the energy spectrum of the `good` events are shown. The steep falloff below 2.5 keV is due to the cut to remove pedestal events. The upper bound at around 30 keV is due to underflow of the FADC inputs. Events with energy deposit more than it were categorized to `giant` events. Among them, however, the amplifier gain of `pin8` was set exceptionally lower, which caused some events with higher energies up to about 50 keV.

The sharp silver K_α X-ray peak is evident, and the silver K_β and copper K_α X-ray peaks are marginally noticeable. Their appearance is quite understandable, since silver paste is used on the back contact of the PIN photodiode chips and copper is used in the radiation shield as well as the conductor on the plastic film substrate of the PIN photodiodes. Furthermore, their appearance strongly supports the validity and precision of the current energy estimation. We fitted the silver K_α X-ray peak with a sum of constant continuum b and two Gaussians corresponding to $K_{\alpha 1}$ and $K_{\alpha 2}$ as

$$f(E) = b + \frac{N}{\sigma\sqrt{2\pi}} \frac{1}{\omega_{\alpha 1} + \omega_{\alpha 2}} \times \left[\omega_{\alpha 1} \exp\left[-\frac{(E - E_{\alpha 1}\mu)^2}{2\sigma^2} \right] + \omega_{\alpha 2} \exp\left[-\frac{(E - E_{\alpha 2}\mu)^2}{2\sigma^2} \right] \right], \quad (6.59)$$

where N is the number of silver K_α events, $E_{\alpha 1} = 21.9903\,\mathrm{keV}$, $E_{\alpha 2} = 22.16292\,\mathrm{keV}$, and $\omega_{\alpha 1} : \omega_{\alpha 2} = 53.0 : 100$. The result was consistent with the overall relative gain error of

$$(\mu - 1) = (2.5 \pm 1.6) \times 10^{-3}, \quad (6.60)$$

and the overall energy resolution at 22 keV of

$$\sigma = 0.300 \pm 0.039\,\mathrm{keV}. \quad (6.61)$$

Compared to the values in Table 6.4, we observed no sign of broadening of the peak at this energy. Thus we used the constant energy resolution σ_{pin} in the later analysis.

As shown in Fig. 5.23, the peak efficiency of the PIN photodiode is expected to drop above 10 to 15 keV. However, the continuum of the background looks relatively flat up to the cut-off at 30 keV. This implies that the contribution of low energy γ rays to the continuum might be small and that the main component might be consisting of the Compton scatterings of high energy γ rays.

6.7 Analysis of Phase II waveforms

We followed exactly the same procedure which was described in Section 6.6 in analyzing the waveform from the PIN photodiodes taken during both the solar tracking- and the background runs. In prior to that, each event in each gas density setting was classified into the solar tracking-, the background-, and the uncertain ones according to the measured direction of the helioscope.

The measured direction of the helioscope is recorded every second. An event was classified to the solar tracking event, if the helioscope was directed to the sun as precise as

$$|\delta\theta_{\rm altitude}| < 5 \times 10^{-5} \text{ and } |\delta\theta_{\rm azimuth}| < 5 \times 10^{-5} \tag{6.62}$$

at two adjacent recorded points immediately before and after the event. Likewise, we required the helioscope to be directed far enough from the sun by

$$|\delta\theta_{\rm altitude}| > 0.163 \text{ and } |\delta\theta_{\rm azimuth}| > 0.041 \tag{6.63}$$

for the background events. The remaining uncertain events were excluded from the analysis.

The above condition for the solar tracking events given in Eq. (6.62) was made intentionally stringent in order to reject any unanticipated mechanical disturbance to the helioscope. However, it is yet easily satisfied by the motion control system of the helioscope during the steady tracking. The background condition, Eq. (6.63), was determined so that the topocentric aspect of the sun would not enter inside the magnet aperture seen from the PIN photodiodes. As in the tracking system, we used the NOVAS package to calculate the solar position, where we interpolated data from IERS Bulletin A for the earth orientation parameter, ΔT.

In addition, we rejected the interval between 10:18:00 and 18:41:50 JST, August 11 2000, or the Modified Julian Dates of 51767.05417 and 51767.40405, while the system clock was going wrong by $-13.8\,\mathrm{s}$ because of a trouble in the network connectivity.

By integrating the atomic live times bound to each event, we get solar-tracking and background live times for each gas density setting as already shown in the third and the fourth columns of Table 6.1. The values shown there are not corrected for the live time deficit by microphonic noise yet.

By counting good events by their estimated energies, we get solar-tracking- and background energy spectra for each gas density setting.

6.8 Interpretation

6.8.1 Expected axion signal or Detection efficiency

In order to evaluate the observed energy spectra, we need to estimate the expected axion signal taking account of the detection efficiency of the detector.

Leaving the energy resolution out of consideration, the expected differential event rate or the energy spectrum is given by

$$\begin{aligned} R &\equiv \frac{d^2N}{dt\,dE} \\ &= \epsilon_{\rm cut}(E)\epsilon_{\rm trig}(E)\epsilon_{\rm win}(E) \iint \epsilon_{\rm pin}(E,x,y)\frac{d\Phi_\gamma}{dE}(E,x,y)\,dx\,dy, \end{aligned} \tag{6.64}$$

where $\epsilon_{\rm cut}(E)$ is the cut efficiency of the waveform analysis for a given photon energy E, $\epsilon_{\rm trig}(E)$ the trigger efficiency, $\epsilon_{\rm win}(E)$ the transmission efficiency of the X-ray window, $\epsilon_{\rm pin}(E,x,y)$ the detection efficiency of the PIN photodiodes at position (x,y), and x, y are the axes of the orthogonal coordinate perpendicular

to the helioscope axis. In this coordinate frame, the x-axis is defined horizontal with respect to the ground directed from left to right when viewed from the rear of the detector. The z-axis is defined parallel to the helioscope axis directed from the sun to the detector, and the y-axis is perpendicular to both of them directed upwards, but is not necessarily normal with respect to the ground. The origin, $(x, y, z) = (0, 0, 0)$, is placed at the center of the magnet.

The photon flux on the PIN photodiodes is then given by

$$\frac{d\Phi_\gamma}{dE}(E, x, y) = \int P_{a\to\gamma}(x, y, \vec{r}_s, q) \frac{d^2\Phi_a}{dE\, d\vec{r}_s}(E, \vec{r}_s)\, d\vec{r}_s, \tag{6.65}$$

where $\vec{r}_s$ is a point of the axion source in the solar core. Since the photon absorption in gas is negligible for the gas density adopted in the Phase II measurement, the conversion probability is then given simply by

$$P_{a\to\gamma}(x, y, \vec{r}_s, q) = \frac{g_{a\gamma}^2}{4} \left| \int_{\text{visible}} \vec{B}_\perp(x', y', z') e^{iqz'}\, dz' \right|^2, \tag{6.66}$$

where (x', y', z') is the coordinate of a point on the line connecting the view point, (x, y, z_{pin}), and the axion source, $\vec{r}_s$, and $\vec{B}_\perp$ is the magnetic field component perpendicular to the line of integral. The very small angle between the z-axis and the line of integral is ignored. Let us emphasize that the integration interval with respect to z' is limited to the range which is directly visible from the view point. For simplicity and conservatism, we required end-to-end clearance to the direct visibility of the integration interval and assumed $P_{a\to\gamma} = 0$ where there are any obstacles in the way between the PIN photodiodes and the end of the gas container. Let $d\epsilon_{\text{geom}}/d\vec{r}_s$ be the geometric efficiency density defined as

$$\frac{d\epsilon_{\text{geom}}}{d\vec{r}_s} = \begin{cases} \frac{d^2\Phi_a}{dE\, d\vec{r}_s} \Big/ \frac{d\Phi_a}{dE} & \text{if directly visible end-to-end,} \\ 0 & \text{otherwise.} \end{cases} \tag{6.67}$$

It is a function of x, y, and $\vec{r}_s$ assuming that the shape of the axion source is independent of E. Apparently, the integrated geometric efficiency ϵ_{geom} is a function of (x, y) and is independent of $\vec{r}_s$. It is $\epsilon_{\text{geom}} = 1$ if all the axion source region is visible from the view point to the end of the gas container, and $\epsilon_{\text{geom}} = 0$ if it is completely occulted. Then, we can factor out $\vec{r}_s$ dependence from the integral in $P_{a\to\gamma}$ as well as from the axion flux density. Equation (6.65) is simplified as

$$\frac{d\Phi_\gamma}{dE} = \epsilon_{\text{geom}}(x, y; \boldsymbol{g})\, \frac{d\Phi_a}{dE}(E) \cdot \frac{g_{a\gamma}^2}{4} \left| \int \vec{B}_\perp(x', y', z') e^{iqz'}\, dz' \right|^2, \tag{6.68}$$

where $\boldsymbol{g}$ represents dependence on a specific geometric configuration. The integral interval with respect to z' is end-to-end regardless of the intervening materials namely from the detector to the end of the gas container.

We have already discussed the transmissivity of the X-ray window, $\epsilon_{\text{win}}(E)$, in Section 5.5.6. The detection efficiency of the PIN photodiodes, $\epsilon_{\text{pin}}(E, x, y)$, has been discussed in Section 5.4.3, but it is position dependent in the current context. We can redefine ϵ_{geom} to incorporate the position dependence of ϵ_{pin}, and make ϵ_{pin} position-independent again.

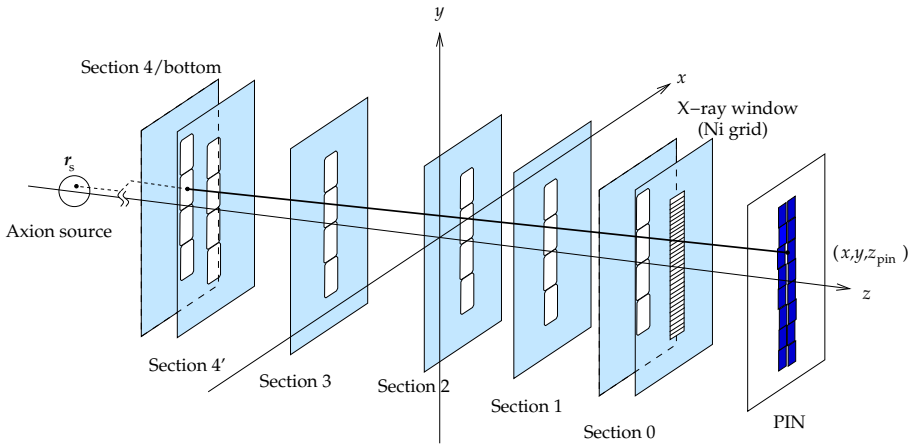

Figure 6.26: Geometric model used in the Monte Carlo simulation.

Finally, let us introduce the normalized differential axion flux to simplify the following discussion:

$$\frac{d\hat{\Phi}_a}{dE} \equiv \frac{1}{g_{a\gamma}^2}\frac{d\Phi_a}{dE}. \tag{6.69}$$

Then we get

$$R = \frac{g_{a\gamma}^4}{4}\epsilon(E)\,\frac{d\hat{\Phi}_a}{dE}(E) \times \iint\left\{\int \frac{d\epsilon_{\rm geom}}{d\vec{r}_s}(x,y,\vec{r}_s;\boldsymbol{g})\,d\vec{r}_s \times \left|\int \vec{B}_\perp(x',y',z')e^{iqz'}\,dz'\right|^2\right\} dx\,dy, \tag{6.70}$$

where ϵ is the overall efficiency defined by

$$\epsilon(E) \equiv \epsilon_{\rm cut}(E)\,\epsilon_{\rm trig}(E)\,\epsilon_{\rm win}(E)\,\epsilon_{\rm pin}(E). \tag{6.71}$$

In the following, we examine the remaining factors.

6.8.2 Effective area and photon flux on PIN photodiodes

It is difficult to calculate the multiple integral in Eq. (6.70) taking into account the shading of photons. Furthermore, it is also difficult to estimate analytically the amount of uncertainty brought by the geometric errors into the expected axion signal rate. To solve these problems, we used the Monte Carlo method, where not only the variables of integration but also the geometries are modified randomly. Each geometric parameter was given a Gaussian distribution whose deviation is equal to its estimated error. But some were given truncated Gaussian distributions since there were mechanical limits.

In the geometric model of the simulation, PIN photodiodes and the supporting nickel frames of the X-ray window were represented as planar masks of zero thickness which are perpendicular to the z-axis for simplicity. Likewise, the

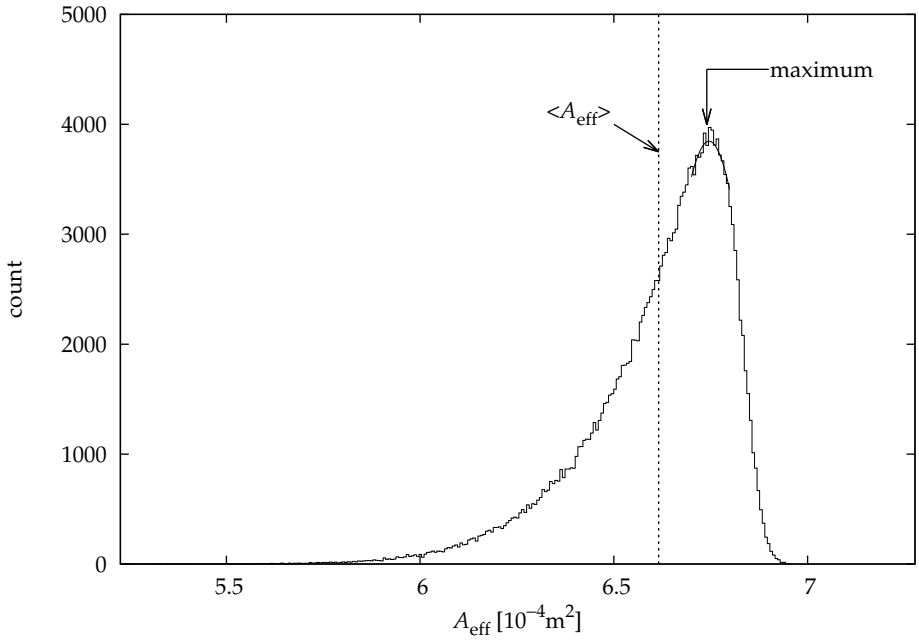

Figure 6.27: Distribution of the effective area, $A_{\rm eff}$. The vertical dashed line shows the ensemble average and the solid curve at the peak corresponds to the smooth function assumed in the text.

inner surfaces of the gas container were represented as six planar masks corresponding to the six measured cross sections. Although the mask of Section 4 sits several millimeters behind the bottom surfaces of the blind-ended plugs where the interior of the gas container ends, we required rays of photon-axion mixture to pass through this mask as the substitute for the walls around the plugs.

The 0.30-mm-width thin nickel grids of the X-ray window were also reproduced in this simulation model. Since the transmission curve shown in Fig. 5.47 already contains the shadowing of 20% by them, we corrected the transmission efficiency, $\epsilon_{\rm win}(E)$, for it in the later analysis to reproduce the net transmission. Figure 6.26 shows the schematic drawing of the geometric model used in the Monte Carlo simulation. We traced each line of integral along z' in Eq. (6.70) or each ray of photon-axion mixture backwards from a randomly chosen point on the detector plane at $z = z_{\rm pin}$ in a rectangular area, $x \in [-10\,{\rm mm}, 10\,{\rm mm}]$ and $y \in [-41\,{\rm mm}, 41\,{\rm mm}]$, to a randomly chosen point in the spherical solar axion source at $z = -215R_\odot$ with a radius of $r = 0.2R_\odot$. We assumed that axions are emitted homogeneously within the sphere for simplicity.

Figure 6.27 shows the distribution of the overall effective area

$$A_{\rm eff}(\boldsymbol{g}) = \iiint \frac{d\epsilon_{\rm geom}}{d\vec{r}_s}\, d\vec{r}_s\, dx\, dy \tag{6.72}$$

for $N_{\boldsymbol{g}} = 2 \times 10^5$ geometric configurations, where $N_{\boldsymbol{r}} = 5 \times 10^5$ photon-axion mixtures were traces in each configuration. The Mersenne-Twister random generator [102] was used in the simulation. We found its ensemble average and its

standard deviation were

$$\langle A_{\rm eff}\rangle \pm \delta A_{\rm eff} = (6.616 \pm 0.185) \times 10^{-4}\,{\rm m}^2. \tag{6.73}$$

The distribution was considerably asymmetric, and the maximum likely value was

$$A_{\rm eff,likely} = (6.746 \pm 0.002\,({\rm stat.})) \times 10^{-4}\,{\rm m}^2 \tag{6.74}$$

assuming a smooth distribution.

Unfortunately, however, the converted X-rays are not irradiating the unshaded area uniformly since the magnetic field is not perfectly uniform in our apparatus. To introduce its influence, we examined the following normalized conversion rate by a numerical integration,

$$\begin{aligned} I_1(x,y,q) &\equiv P_{a\to\gamma}/g_{a\gamma}^2 \\ &= \frac{1}{4}\left|\int_{z_{\rm bot}}^{z_{\rm win}} \vec{B}_\perp e^{iqz'}\,dz'\right|^2, \end{aligned} \tag{6.75}$$

where $z_{\rm bot} = -1078.3\,{\rm mm}$ and $z_{\rm win} = 1229.4\,{\rm mm}$. Here, we ignored the residual oscillation after the X-ray window where the gas density is out of tune, i.e., $m_a \neq m_\gamma = 0$, and the magnetic field is much smaller than the inside.

By an approximation to first order, I_1 is equivalent to the power spectrum of a rectangular function. It has the maximum at $q = 0$ and decays by $1/q^2$ oscillating with a period of $4\pi/L$ like Eq. (3.31). Because of the soft edge of the magnetic field at the detector side, however, actual I_1 is expected to decay faster than the simple rectangular case above a certain large q. At the solar side, on the other hand, because of the end of the pipe, the integration must start at $z_{\rm bot}$ where the magnetic field is still strong. This will result in a persistent component which only decays by

$$I_1 \simeq \frac{|B_\perp(z_{\rm bot})|^2}{4q^2} \qquad \text{(for very large } q\text{)}. \tag{6.76}$$

From this view, the number of q's to be calculated can be restricted. From the length of the magnet, $L = 2.3\,{\rm m}$, I_1 will not change much by a shift of q by an amount smaller than

$$\delta q \ll \frac{1}{L} = 0.86 \times 10^{-7}\,{\rm eV}. \tag{6.77}$$

Considering the variance of $\delta L \sim 10\,{\rm mm}$ of the run length in the magnetic field contributing to the total signal, the oscillation of I_1 at high q's is expected to be smoothed out above

$$q \gg \frac{4\pi}{\delta L} \sim 2.5 \times 10^{-4}\,{\rm eV}. \tag{6.78}$$

Furthermore, the finite energy resolution also affects the oscillation by q to be smoothed out, since q depends on E by $q \simeq (m_a^2 - m_\gamma^2)/2E$. Assuming the typical energy of $E \sim 4\,{\rm keV}$ and the energy resolution of $\sigma_{\rm pin} = 0.358\,{\rm keV}$, we can neglect the oscillation at

$$q \gtrsim \frac{4\pi}{L}\frac{E}{\sigma_{\rm pin}} \sim 6 \times 10^{-6}\,{\rm eV}. \tag{6.79}$$

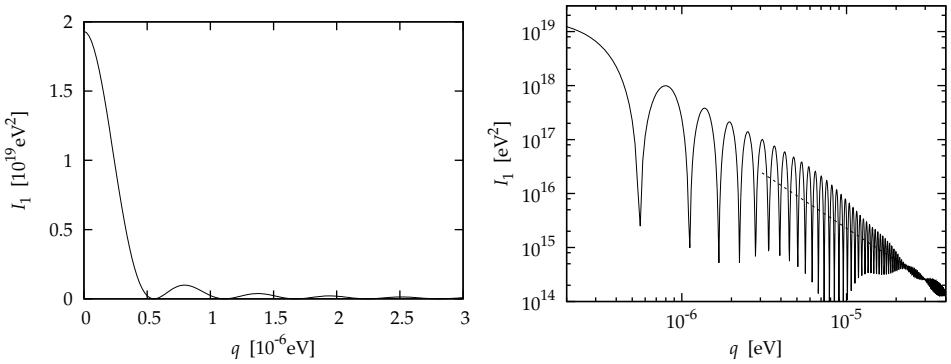

Figure 6.28: Normalized conversion rate, $I_1 = P_{a\to\gamma}/g_{a\gamma}^2$, along the line crossing the magnet center is plotted as a function of the momentum transfer, q. The left figure shows the region near the peak at $q = 0$, and the right one shows a logarithmic plot for the wider region. The dashed line indicates the asymptotic $1/q^2$ function used in $q \geq 4 \times 10^5$eV.

For such high q's, it will be safe to approximate it as Eq. (6.76). Finally, we performed the numerical integrations of Eq. (6.75) for q from 0 up to 4×10^{-5}eV in $\Delta q = 2 \times 10^{-8}$eV steps and for (x, y) in 0.5-mm mesh. In the integration, the QAWO algorithm of the GNU Scientific Library [89] was used, which subdivides the integration interval adaptively until a satisfactory accuracy is achieved and applies a 25-point Clenshaw–Curtis integration rule or a 15-point Gauss–Kronrod integration depending on the width of each subinterval. Thus the magnetic field $\vec{B}$ for selected combinations of (x, y, z) were calculated where the (x, y) values were of the 0.5-mm mesh and the z values were selected by the algorithm.

Figure 6.28 shows the calculated I_1 as a function of q along the line which crosses the center of the magnet, $(x, y) = (0, 0)$, as an example. Figure 6.29 shows I_1 as a function of x and y on the detector plane for $q = 0, 10^{-6}$eV, and 10^{-5}eV. The effective areas of the PIN photodiodes are shown as white open squares, where all the measured geometric values are assumed error free. Let us emphasize that we are seeing the PIN photodiodes from their back in these figures since we are using a Cartesian coordinate frame explained above where the z-axis directed from the sun to the detector.

In the same figure at its right most, the map of the ensemble average of the position-dependent geometric efficiencies, $\langle\epsilon_{\rm geom}\rangle$, is shown to indicate the patches which are actually contributing. They were obtained by counting the following amounts in the Monte Carlo simulation for small patches of $\Delta x \times \Delta y$:

$$\langle\epsilon_{\rm geom}\rangle = \frac{1}{N_{\boldsymbol{g}}\Delta x\Delta y}\sum_{\boldsymbol{g}}\int_{x-\Delta x/2}^{x+\Delta x/2}dx\int_{y-\Delta y/2}^{y+\Delta y/2}dy\int d\vec{r}_s\frac{d\epsilon_{\rm geom}}{d\vec{r}_s}. \tag{6.80}$$

Here, we can find that they are limited to $\langle\epsilon_{\rm geom}\rangle \lesssim 80\%$ by the thin nickel grids of the X-ray window. The blurred edges are mainly due to the broadening of the axion source.

Likewise, by averaging I_1 over (x, y) on the whole detector surface and over many possible sets of the geometric parameters varied by their uncertainties, we

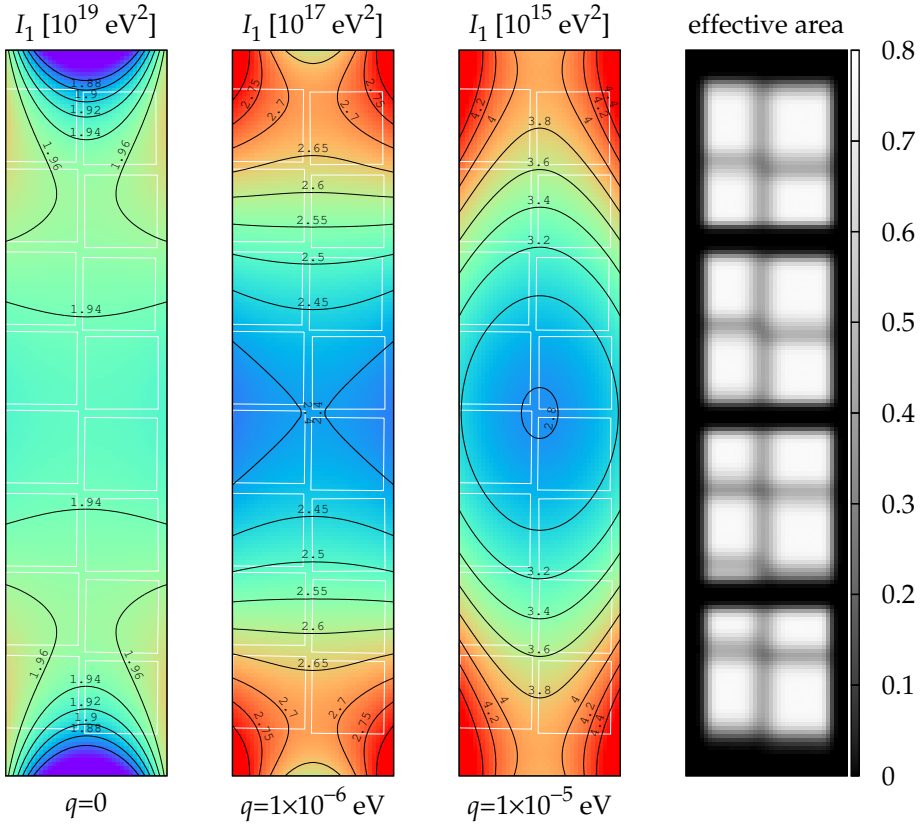

Figure 6.29: Maps of the normalized conversion rate, $I_1 = P_{a\to\gamma}/g_{a\gamma}^2$, on the xy plane of the magnet coordinate frame are shown for $q = 0, 10^{-6}$eV, and 10^{-5}eV. Regions where I_1 is about or equal to its ensemble average, $\langle I_1 \rangle$, are shown in green. Regions where I_1 are less or more than that are shown bluish or reddish. The effective areas of the PIN photodiodes are shown as white open squares. The right most figure shows the map of the ensemble averages of the geometric efficiencies of the corresponding areas.

can obtain its ensemble average, $\langle \bar{I}_1 \rangle$ as a function of q. Regions where $I_1 \simeq \langle \bar{I}_1 \rangle$ are shown green in the I_1 maps in Fig. 6.29. Regions where I_1 is less or more than $\langle \bar{I}_1 \rangle$ are shown bluish or reddish, respectively.

At $q = 0$, where the helioscope is the most efficient, we find no significant deviations from the uniformity of I_1 within the effective area. They are $+1\%$ and -3% at the maximum and the minimum only at the edges. At higher harmonics of q, on the other hand, non-uniformities due to the different run lengths in the magnetic field become evident. Because of the symmetry of the non-uniformities, however, we can still expect that their influences on the total signal rate will be less sensitive to the geometric errors, and that the geometric errors will affect the total signal rate mainly through the uncertainty of the effective area.

By the Monte Carlo method, we obtained the integral of I_1 with respect to x, y, and $\vec{r}_s$. Let I_2 be it written formally as

$$I_2 \equiv \iiint \frac{d\epsilon_{\rm geom}}{d\vec{r}_s} I_1 \, d\vec{r}_s \, dx \, dy, \tag{6.81}$$

which is a function of q and the geometry of the apparatus. Then Eq. (6.70) can be rewritten:

$$R = g_{a\gamma}^4 \, \epsilon(E) \, \frac{d\hat{\Phi}_a}{dE}(E) \, I_2(q; \boldsymbol{g}). \tag{6.82}$$

Figure 6.30 exemplifies the distributions of I_2 for $N_{\boldsymbol{g}} = 2 \times 10^5$ and $N_{\boldsymbol{r}} = 5 \times 10^5$ for the same set of q's. As expected, they are almost identical with the distribution of the effective area, $A_{\rm eff}$, in Fig. 6.27.

The above prediction is further supported by the much narrower distributions in Fig. 6.31, where the distributions of the averaged normalized conversion rate,

$$\bar{I}_1 \equiv \frac{I_2}{A_{\rm eff}}, \tag{6.83}$$

of $N_{\boldsymbol{g}} = 4 \times 10^4$ and $N_{\boldsymbol{r}} = 10^6$ are shown for the same set of q's. In Fig. 6.32, the standard deviations of the distributions, $\delta \bar{I}_1$, are plotted as a function of q in a dashed curve, along with their ensemble average,

$$\langle \bar{I}_1 \rangle = \frac{1}{N_{\boldsymbol{g}}} \sum_{\boldsymbol{g}} \bar{I}_1, \tag{6.84}$$

in a solid curve. We find that the deviations are four orders of magnitude smaller than the ensemble averages for small q's which are dominant within the scanned mass ranges, or that $\delta \bar{I}_1 \leq 2 \times 10^{-4} \langle \bar{I}_1 \rangle$ up to $q \leq 4.2 \times 10^{-7}\,\mathrm{eV}$. At higher q's, they are still typically three orders of magnitude below the ensemble averages. Therefore, we ignore these small deviations and assume that the uncertainty in I_2 by the geometric errors is fully caused by the uncertainty of the effective area as

$$\delta I_2 = \delta A_{\rm eff} \langle \bar{I}_1 \rangle. \tag{6.85}$$

The term $\delta A_{\rm eff}$ is independent of q and $\langle \bar{I}_1 \rangle$ is independent of a particular geometric configuration. In the later analysis, we used the calculated values of

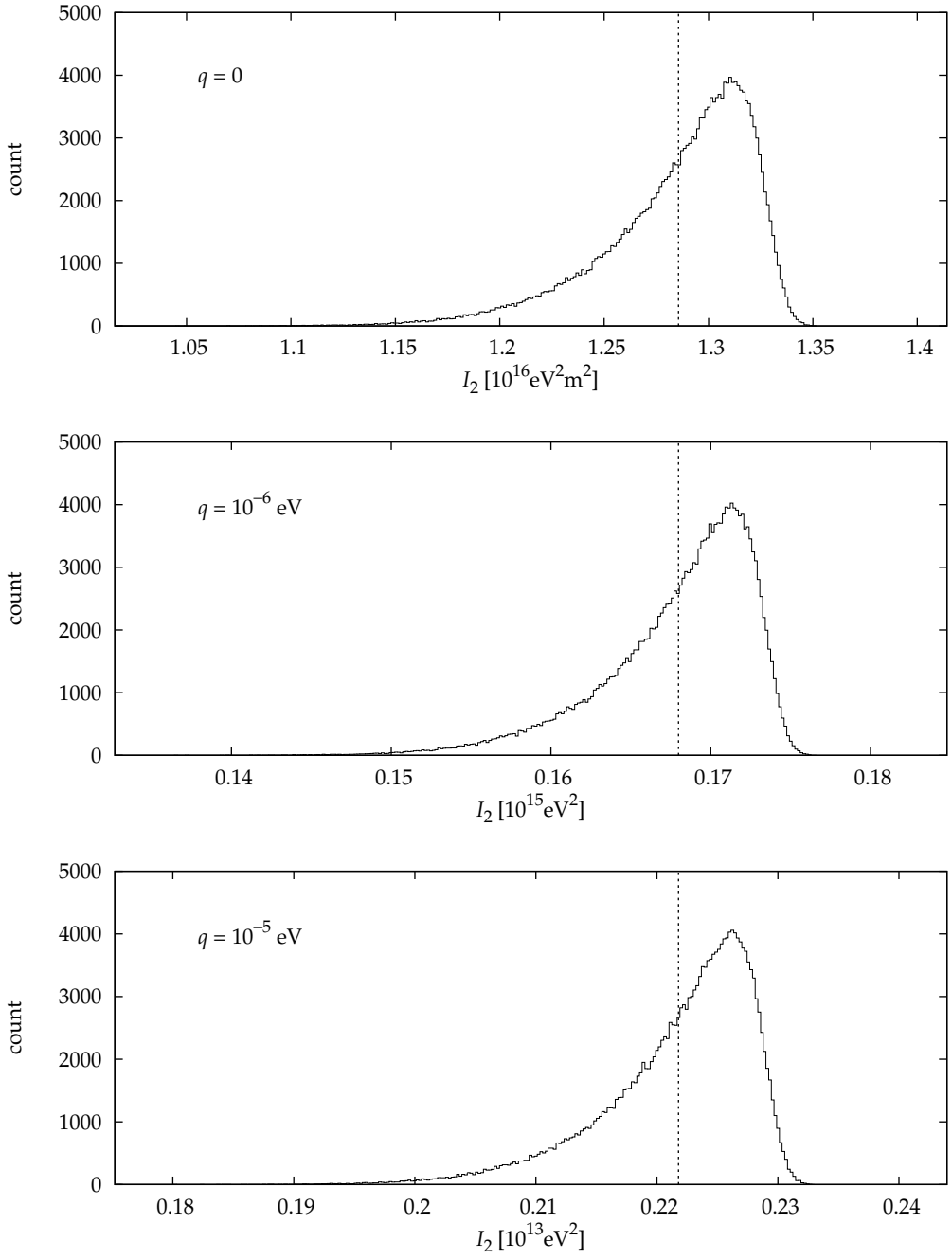

Figure 6.30: Distribution of the integrated normalized conversion rate, I_2, for $q = 0$, $10^{-6}\,\mathrm{eV}$ and $10^{-5}\,\mathrm{eV}$. The vertical dashed line shows the ensemble average.

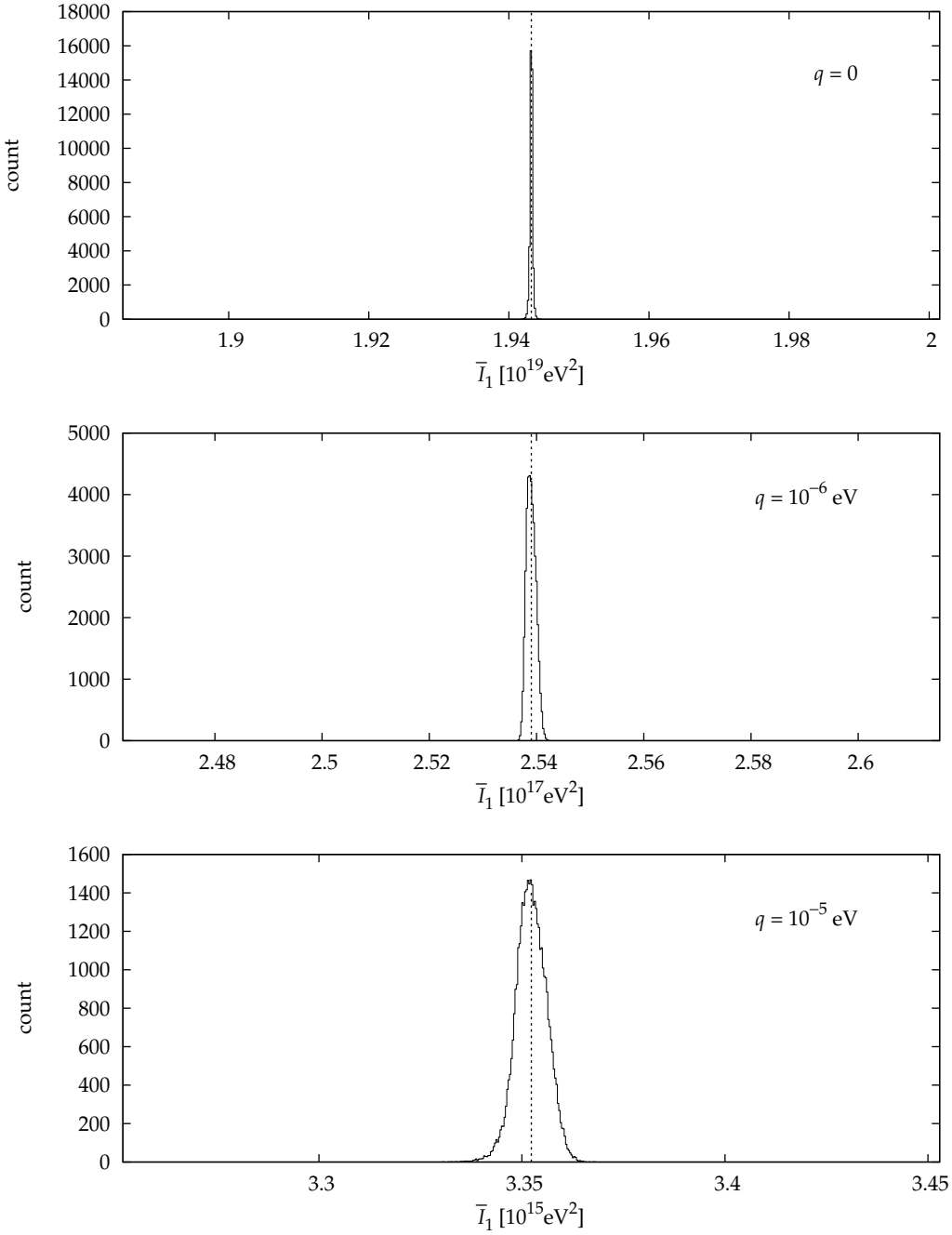

Figure 6.31: Distribution of the averaged normalized conversion rate, $\bar{I}_1 = I_2/A_{\rm eff}$, for $q = 0$, 10^{-6} eV and 10^{-5} eV. The vertical dashed line shows the ensemble average. The plot range is fixed to $\pm 3\%$ of the ensemble average for three of them.

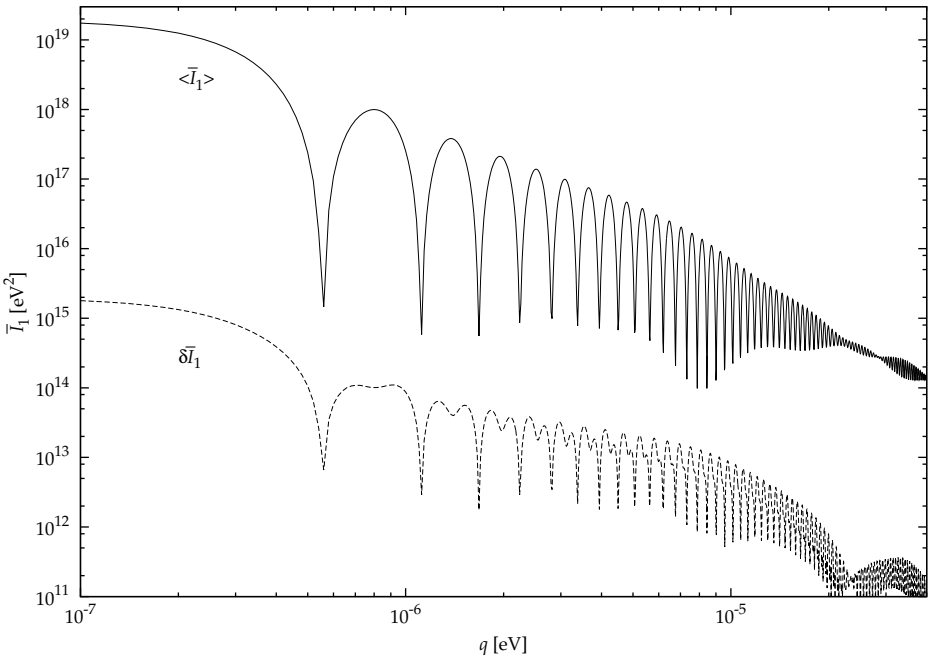

Figure 6.32: Ensemble averages and standard deviations of the averaged normalized conversion rate, $\bar{I}_1$, are plotted against q. The solid curve shows the ensemble average of many geometric configurations, $\langle \bar{I}_1 \rangle$, and the dashed curve shows the standard deviation, $\delta \bar{I}_1$.

$\langle \bar{I}_1 \rangle$ as the only factor that depend on q and $A_{\rm eff}$ as the only factor that depends on the geometry.

Let us define a more physically sensible symbol instead of $\langle \bar{I}_1 \rangle$:

$$\hat{P}_{a\to\gamma} \equiv \langle \bar{I}_1 \rangle. \tag{6.86}$$

Equation (6.70) is then

$$R(E) = g_{a\gamma}^4 A_{\rm eff}(\boldsymbol{g})\, \epsilon(E)\, \frac{d\hat{\Phi}_a}{dE}(E)\, \hat{P}_{a\to\gamma}(q). \tag{6.87}$$

For the period while the `pin0` channel was down, we carried out a same kind of Monte Carlo simulation and confirmed that the effective area was as good as $A_{\rm eff}^{\not{\rm pin0}} = 0.918 A_{\rm eff}$.

6.8.3 Comparison of the expected signal with the measured data

In Fig. 6.33, the expected energy spectra of the axion signal at the X-ray detector are plotted for mass differences of $\Delta m^2 = m_a^2 - m_\gamma^2 = 0$, $(0.05\,{\rm eV})^2$, $(0.07\,{\rm eV})^2$, $(0.15\,{\rm eV})^2$, and $(0.3\,{\rm eV})^2$, where $A_{\rm eff} = 6.746 \times 10^{-4}\,{\rm m}^2$ is assumed, and smearing by the limited energy resolution of $\sigma_{\rm pin}$ is considered.

In practice, both the solar tracking- and background data contain background. Since we have no reasonable model for the theoretical shape of the background spectrum, we binned both data into histograms and compared them bin-by-bin. Naturally, the narrower the bin width is, the more information we will obtain from the shape of the spectrum. With narrower bin width, however, we get more free parameters which should be determined at the same time. Considering the energy resolution, the bin width narrower than $\Delta E \lesssim 0.5\,{\rm keV}$ would not bring us more information. Furthermore, we need enough number of events in each bin to compare them in a statistically meaningful manner. Finally, we used $\Delta E = 1\,{\rm keV}$ in this analysis.

In Fig. 6.34, one of the energy spectra of the solar observation is shown together with the background spectrum, where $m_\gamma = 0.263\,{\rm eV}$, as an example. Actually, there are ten such sets of spectra corresponding to the gas density settings and one extra set corresponding to the period while the `pin0` channel was down. We searched for an excess of an axion signal in these spectra following the method of maximum likelihood. The smooth curve in the figure represents an example for the expected axion signal where we assumed $\Delta m^2 = 0$ and $g_{a\gamma} = 6.6 \times 10^{-10}\,{\rm GeV}^{-1}$, which corresponds to the upper limit at $m_a = 0.263\,{\rm eV}$ estimated as follows.

Let $N_{ij}^{\odot}$ be the number of events in the i-th energy bin, $E \in [E_i, E_{i+1})$, obtained in the solar tracking run of the j-th gas density setting, and $N_{ij}^{\rm bg}$ be that of the corresponding background run. The bin widths are taken to be uniform: $E_{i+1} - E_i = \Delta E$. We assume that the background rate at each energy bin is equal in both runs but may have changed in a longer period during which the gas density was modified. Considering the energy resolution of $\sigma_{\rm pin}$, the expected values of $N_{ij}^{\odot}$ and $N_{ij}^{\rm bg}$ are:

$$\mathrm{E}[N_{ij}^{\odot}] = T_j^{\odot}(1 - p_{\rm mic}^{j\odot}) \left[b_{ij} + \int_{E_i}^{E_{i+1}} dE \int_0^\infty dE' C_i e^{-\frac{(E'-E)^2}{2\sigma_{\rm pin}^2}} R(E') \right] \tag{6.88}$$

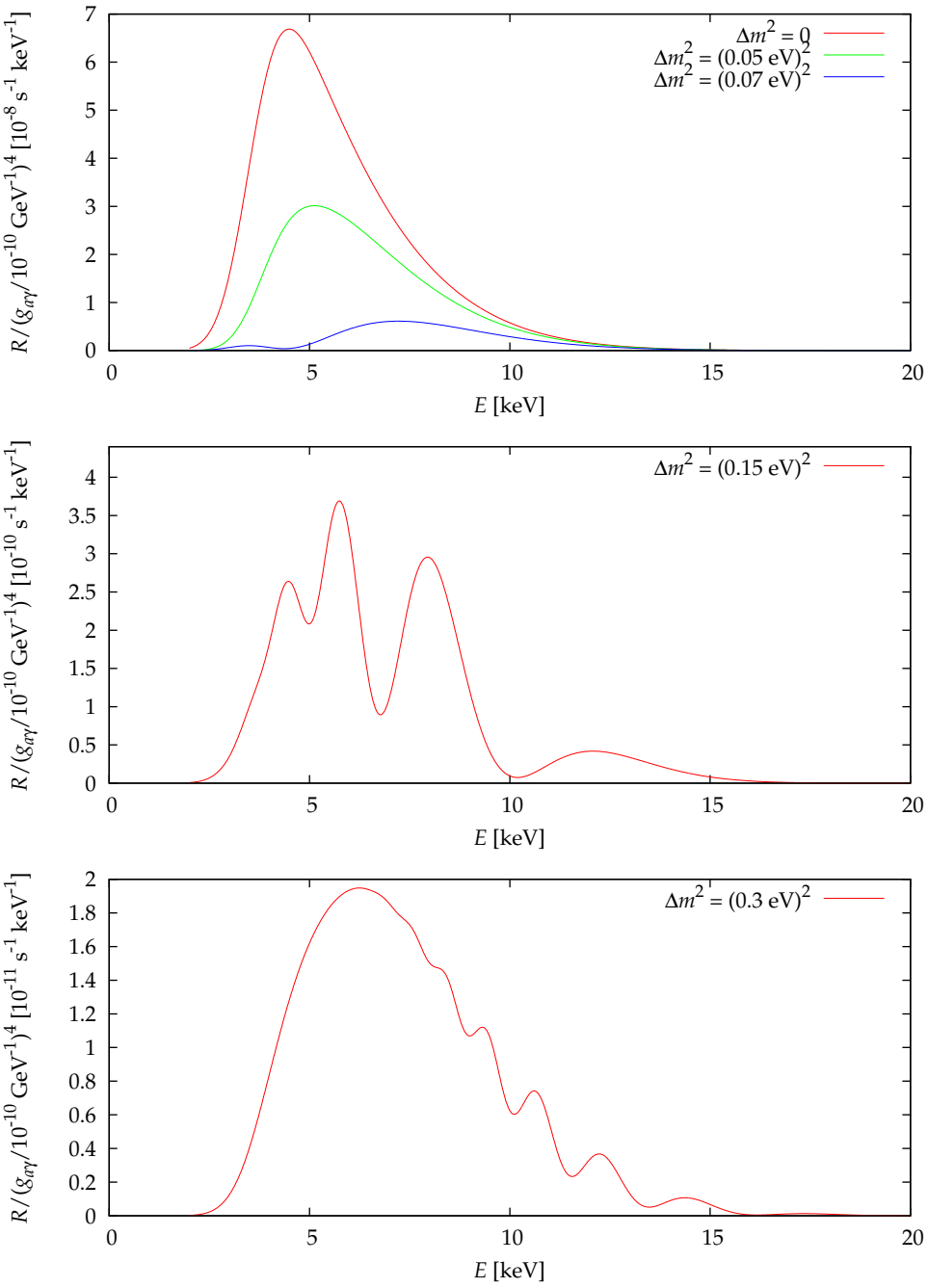

Figure 6.33: Expected energy spectra of the axion signal at the X-ray detector for various mass differences.

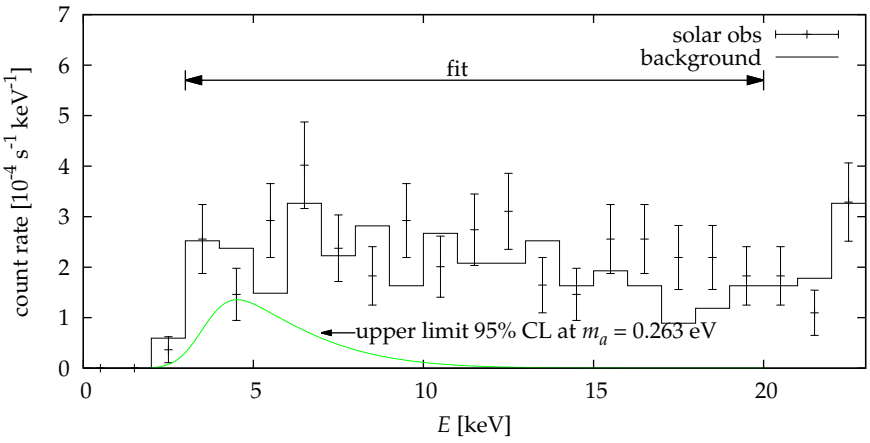

Figure 6.34: Example of the measured energy spectra. The error bars show the solar observation and the solid step line shows the background spectrum when the gas density was tuned to $m_\gamma = 0.263\,\mathrm{eV}$. The vertical axis shows the count rates, where the live times are corrected for the deficit by microphonic noise following the procedure described in the text. The smooth curve shows the expected axion signal before binning where we assumed $\Delta m^2 = 0$ and $g_{a\gamma} = 6.6 \times 10^{-10}\,\mathrm{GeV}^{-1}$. This $g_{a\gamma}$ value corresponds to the upper limit at 95% confidence level at $m_a = 0.263\,\mathrm{eV}$.

and

$$\mathrm{E}[N_{ij}^{\mathrm{bg}}] = T_j^{\mathrm{bg}}(1 - p_{\mathrm{mic}}^{j,\mathrm{bg}})b_{ij}, \tag{6.89}$$

where $T_j^{\odot}$ and T_j^{bg} are the 'crude' live times of the measurements without correction for the live time deficit by microphonic noise, $p_{\mathrm{mic}}^{j\odot}$ and $p_{\mathrm{mic}}^{j,\mathrm{bg}}$ are the expected dead time ratio by microphonic noise in them, b_{ij} the yet-unknown background rate in i-th energy bin, and C_i the normalization constant which is

$$C_i \simeq \frac{1}{\sigma_{\mathrm{pin}}\sqrt{2\pi}} \tag{6.90}$$

for $E_i \gg \sigma_{\mathrm{pin}}$. Substituting Eqs. (6.87) and (6.90) into Eq. (6.88) we get

$$\mathrm{E}[N_{ij}^{\odot}] = T_j^{\odot}(1 - p_{\mathrm{mic}}^{j\odot})\left[b_{ij} + \frac{g_{a\gamma}^4 A_{\mathrm{eff}}(\boldsymbol{g})}{\sigma_{\mathrm{pin}}\sqrt{2\pi}} \int_{E_i}^{E_{i+1}} dE \int_0^{\infty} dE' \right.$$
$$\left. \times\, e^{-\frac{(E'-E)^2}{2\sigma_{\mathrm{pin}}^2}}\, \epsilon(E')\, \frac{d\hat{\Phi}_a}{dE}(E')\, \hat{P}_{a\to\gamma}(q')\right]. \tag{6.91}$$

It follows from the above expected values, the likelihood function or the probability of finding our present data including the number of `microphonic`

events given m_a, $g_{a\gamma}$, $\{b_{ij}\}$, $\{p^{j\odot}_{\rm mic}\}$, $\{p^{j,{\rm bg}}_{\rm mic}\}$ and $A_{\rm eff}$, is

$$\begin{aligned} L \equiv P(&\{N^{\odot}_{ij}\}, \{N^{\rm bg}_{ij}\}, \{N^{j\odot}_{{\rm mic}\not g}\}, \{N^{j,{\rm bg}}_{{\rm mic}\not g}\}| \\ &m_a, g_{a\gamma}, \{b_{ij}\}, \{p^{j\odot}_{\rm mic}\}, \{p^{j,{\rm bg}}_{\rm mic}\}, A_{\rm eff}, \{N^{j\odot}_{\not g}\}, \{N^{j,{\rm bg}}_{\not g}\}) \end{aligned} \tag{6.92}$$

$$\begin{aligned} = &\prod_j^{m_\gamma} \prod_i^{\{E_i\}} {\rm Pois}(N^{\odot}_{ij}, {\rm E}[N^{\odot}_{ij}])\ {\rm Pois}(N^{\rm bg}_{ij}, {\rm E}[N^{\rm bg}_{ij}]) \\ &\times {\rm Binom}(N^{j\odot}_{{\rm mic}\not g}; N^{j\odot}_{\not g}, p^{j\odot}_{\rm mic})\ {\rm Binom}(N^{j,{\rm bg}}_{{\rm mic}\not g}; N^{j,{\rm bg}}_{\not g}, p^{j,{\rm bg}}_{\rm mic}), \end{aligned} \tag{6.93}$$

where ${\rm Pois}(k, \mu)$ is the Poisson distribution function:

$${\rm Pois}(k, \mu) = \frac{\mu^k e^{-\mu}}{k!}, \tag{6.94}$$

$N^{j\odot}_{\not g}$ and $N^{j,{\rm bg}}_{\not g}$ are the numbers of events without any `giant` pulses, $N^{j\odot}_{{\rm mic}\not g}$ and $N^{j,{\rm bg}}_{{\rm mic}\not g}$ are the numbers of `microphonic` events in them, and ${\rm Binom}(n; N, p)$ is the binomial distribution function. Data from the eleven different settings were not analyzed separately, but were combined by multiplying all of their likelihood functions.

Here we have five species of unknown parameters: m_a, $g_{a\gamma}$, b_{ij}'s, $p_{\rm mic}$'s, and $A_{\rm eff}$. With regard to m_a, we fixed its value during the fitting, and scanned the m_a space repeating the estimation of the rest parameters for various m_a values. We can not estimate $g_{a\gamma}$ and $A_{\rm eff}$ independently only from the spectrum data, since they are incorporated in the expected signal rate, $R(E)$, in the form of $g^4_{a\gamma} \times A_{\rm eff}$. However, the knowledge about the possible values of $A_{\rm eff}$ is given elsewhere through the geometrical measurement of the apparatus and the following Monte Carlo simulation. On the contrary, we know nothing a priori but they are non-negative about $g_{a\gamma}$ or b_{ij}'s, nor about $p_{\rm mic}$'s of which we know only that they lie between 0 and 1.

Let $f(A_{\rm eff})$ be the probability density function of $A_{\rm eff}$ whose distribution is given in Fig. 6.27. In general, frequentist statistics does not define such a quantity as the probability of finding a value of a parameter or the *prior probability* of a parameter. However, if we regard the measurement of geometry $\boldsymbol{g}$ as a separate experiment, we can incorporate it by extending the likelihood function. The extended likelihood function is then given as

$$L^* = L\, P(\boldsymbol{g}|A_{\rm eff}). \tag{6.95}$$

The first term L is the identical likelihood as in Eq. (6.92). The second term, on the other hand, make less sense since we do not have an analytic model function for that yet.

Instead of finding a reasonable function for it straightforwardly, we estimated it utilizing idea from the Bayesian statistics. By using Bayes' theorem,

$$\pi(A_{\rm eff}|\boldsymbol{g}) = \frac{P(\boldsymbol{g}|A_{\rm eff})\pi(A_{\rm eff})}{\int P(\boldsymbol{g}|A_{\rm eff})\pi(A_{\rm eff})\, dA_{\rm eff}}, \tag{6.96}$$

where

$$\pi(A_{\rm eff})\, dA_{\rm eff} = P(\hat{A}_{\rm eff} \in [A_{\rm eff}, A_{\rm eff} + dA_{\rm eff}]) \tag{6.97}$$

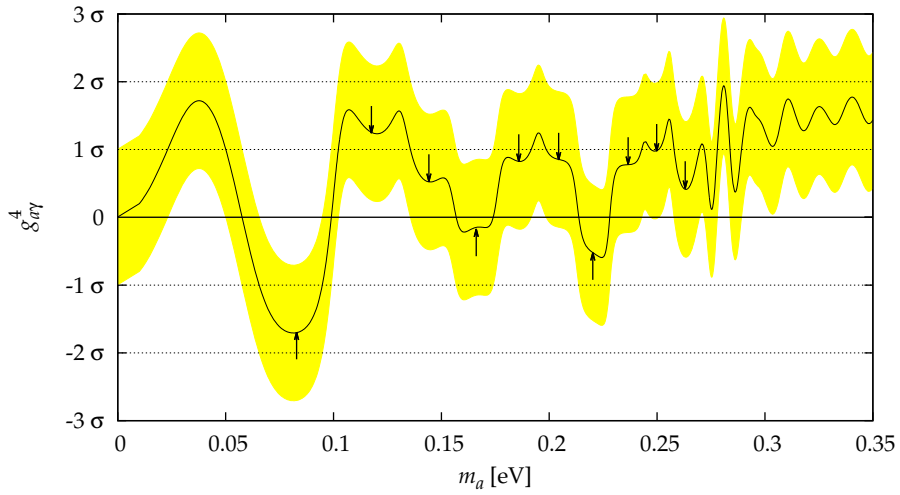

Figure 6.35: The amount of excess of the axion signal in terms of its significance. The best-fit estimates of $g^4_{a\gamma}$ divided by their errors are plotted as a function of m_a. The solid curve shows the best-fit values, and the shaded area shows the one-standard-deviation ranges from there. Ten small arrows indicate the positions of the effective photon masses, m_γ, set in the Phase II measurement.

is the initial prior probability density of $A_{\rm eff}$ before the measurement of geometry was carried out,

$$\pi(A_{\rm eff}|\boldsymbol{g})\, dA_{\rm eff} = P(\hat{A}_{\rm eff} \in [A_{\rm eff}, A_{\rm eff} + dA_{\rm eff}]|\boldsymbol{g}) \tag{6.98}$$

is the updated degree of belief for $A_{\rm eff}$ after the geometry measurement, and the hat sign on $\hat{A}_{\rm eff}$ shows the unknown true value of $A_{\rm eff}$. One may equate $\pi(A_{\rm eff}|\boldsymbol{g})$ with $f(A_{\rm eff})$. We are assuming that we knew nothing about the value of $\hat{A}_{\rm eff}$ but it was non-negative before the geometry measurement, i.e.,

$$\pi(A_{\rm eff}) = \begin{cases} \text{constant} & \text{for } A_{\rm eff} \geq 0 \\ 0 & \text{otherwise.} \end{cases} \tag{6.99}$$

Thus we expect $P(\boldsymbol{g}|A_{\rm eff})$ to be

$$P(\boldsymbol{g}|A_{\rm eff}) \propto f(A_{\rm eff}) \tag{6.100}$$

for $A_{\rm eff} \geq 0$, and undefined otherwise.

From Eqs. (6.95) and (6.100), we find for the extended likelihood function which is proper to be maximized as:

$$\begin{aligned} L^* = f(A_{\rm eff}) \prod_j^{m_\gamma} \prod_i^{\{E_i\}} & \mathrm{Pois}(N^{\odot}_{ij}, \mathrm{E}[N^{\odot}_{ij}])\ \mathrm{Pois}(N^{\rm bg}_{ij}, \mathrm{E}[N^{\rm bg}_{ij}]) \\ & \times \mathrm{Binom}(N^{j\odot}_{\rm mic\mathcal{G}}; N^{j\odot}_{\mathcal{G}}, p^{j\odot}_{\rm mic})\ \mathrm{Binom}(N^{j,\rm bg}_{\rm mic\mathcal{G}}; N^{j,\rm bg}_{\mathcal{G}}, p^{j,\rm bg}_{\rm mic}). \end{aligned} \tag{6.101}$$

The energy region of $E = 3$–$20\,\mathrm{keV}$ was used for fitting. As a result, we found no significant excess for any m_a. As mentioned earlier, the expected axion signal

scales with $g_{a\gamma}^4$. Figure 6.35 shows the amount of excess of the axion signal in terms of its significance, where the best-fit estimates of $g_{a\gamma}^4$ divided by their errors are plotted as a function of m_a. When it is measured, the amount of excess can be positive or negative by statistical error although it should be non-negative theoretically. Therefore, negative excesses or negative estimates of $g_{a\gamma}^4$ in Fig. 6.35 are quite natural.

Then, we estimated upper limits on $g_{a\gamma}$ at 95% confidence level following the Bayesian scheme:

$$0.95 = \frac{\int_0^{(g_{a\gamma}^{\rm UL95})^4} L^*|_{g_{a\gamma}^4=\tau}\, d\tau}{\int_0^{\infty} L^*|_{g_{a\gamma}^4=\tau}\, d\tau}. \tag{6.102}$$

Figure 6.36 shows the limit plotted as a function of m_a. The previous limit given by the Phase I measurement, the limit inferred from the solar age consideration, and the $g_{a\gamma}$–m_a region predicted by the preferred axion models [30] are plotted in the same figure for comparison.

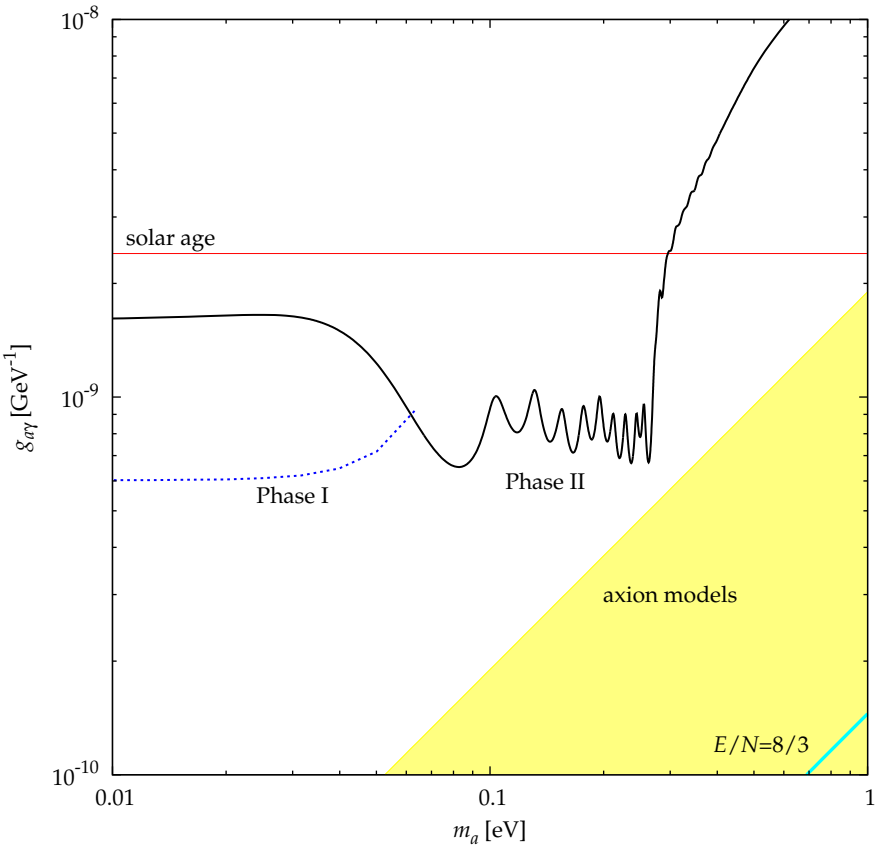

Figure 6.36: The upper limit on $g_{a\gamma}$ as a function of m_a is plotted. The new limit given by the Phase II measurement is shown in solid curve. The dashed curve (blue) shows the previous limit given by the Phase I measurement and the horizontal solid line shows the limit inferred from the solar age consideration (red). The shaded area (yellow) corresponds to the preferred axion models [30] and the diagonal line (cyan) at the corner to the case when a GUT ($E/N = 8/3$) is assumed.

Chapter 7

Phase III measurement and analysis

A new series of measurements was carried out with buffer gas of higher densities aiming at a search for solar axions in the hadronic axion window. However, since we had not completed the gas relief system which can be reset without shutting down the cryogenic system, the highest density was limited so that the gas pressure would not exceed the maximum pressure allowed for the one-time relief system even during a magnet quenching.

In late 2007, the first series of the measurement was started for 10 gas-density settings and the mass range of $0.96\,\mathrm{eV} < m_a < 1.00\,\mathrm{eV}$ was scanned. It was handed over to the second series, which terminated unintentionally due to multiple failures of the apparatus. Before the termination, we carried out measurements to search for solar axions for 24 gas-density settings and the mass range $0.84\,\mathrm{eV} < m_a < 0.96\,\mathrm{eV}$ was newly scanned. A collaborator R. Ohta successfully revived the axion helioscope and started the third series or the Phase III *plus* run, where the mass range of $0.79\,\mathrm{eV} < m_a < 0.84\,\mathrm{eV}$ was newly scanned. The first series is reported in Ref. [103]. The third series or Phase III *plus* is reported in Ref. [104].

In this chapter, we will describe what was renewed in this measurement including the new determination of the azimuthal origin, and some upgrades to the apparatus. Then we will report detail of the second series of the Phase III measurement, and the result where the first series is combined.

7.1 Move of the site

Due to a reconstruction of the housing building, the helioscope had to move to a new experimental site on the 2nd basement at 139° 45' 47" E and 35° 42' 49" N in the same campus, where the azimuthal origin was newly measured. Two marks aligning on a meridian are placed on the floor using a SOKKIA G-1 gyroscope by an expert. The nominal accuracy of the north origin by this method is $\delta\theta_{\mathrm{azimuth}} = 8$" or $4 \times 10^{-5}\,\mathrm{radian}$. The axis of the helioscope is directly visible from a point about 1 m above one of these marks. By measuring the angle between the meridian and the helioscope axis with a theodolite, we determined the azimuthal origin of the helioscope. The sun nor any stars are

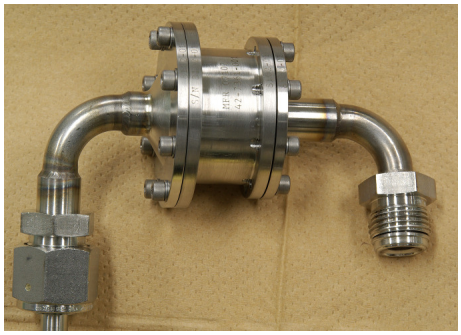

Figure 7.1: The cryogenic precision burst disc from Hydrodyne. It works at 5 K and protects the X-ray window from overpressure.

directly visible from the laboratory.

We followed exactly the same procedure used in Phase II in determining the altitudinal origin as well as in correcting the measured altitude for the pitching of the turntable associated with its motion by redoing all the necessary measurement.

7.2 Phase III upgrade

7.2.1 Safety system

One of the most notable upgrade in this phase is the introduction of the safety system which exhausts helium gas to avoid destruction of the X-ray window in case of rapid temperature increase due to a quenching of the magnet. The gas introduction pipe should be thin enough to minimize the heat injection into the gas container, while it should be thick enough to have the necessary flow rate to relief pressure before destruction. In order for them to coexist, gas filling line should be separated from the exhaust line and the relief system must work at 5 K. Although a resetable pressure relief device was not developed successfully, we introduced a cryogenic rupture disc and the corresponding exhaust line.

Figure 7.1 shows the cryogenic precision burst disc purchased from Hydrodyne. It operates at 5 K. Its designed break pressure is 0.248 MPa and it is helium leak tight at that temperature. We used Mitsumoto Rasenkan Kogyo Co., Ltd. 3/8" thin-wall stainless steel flexible tubes to connect the exhaust port of the rupture disc and the intermediate connection at 40 K as well as to connect the 40-K connection and the access port at room temperature. Flexible tubes were used, since their thin and wrinkled wall structure minimizes the thermal conduction through them. In order to prevent elongation and destruction by internal pressure, we reinforced them with Kevlar over-braids. The helium exhaust line is normally evacuated to vacuum. Renovation of the internal pipework to adapt it to helium of higher densities was lead by Y. Akimoto although the cryogenic rupture disc had been purchased earlier.

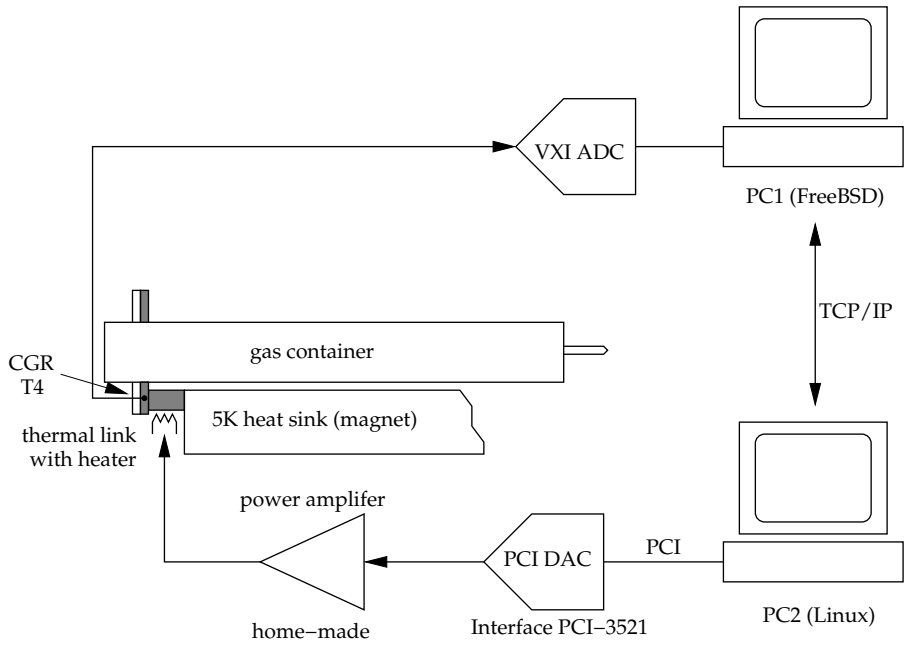

Figure 7.2: Schematic diagram of the temperature control system.

7.2.2 Temperature stabilization system

The cooling power of the Gifford–McMahon refrigerators fluctuated by time and the angle of inclination. At the high densities in the Phase III measurement, it was crucial to keep the gas temperature constant to achieve the required uniformity.

Figure 7.2 shows the schematic diagram of the temperature control system. A thermal link made of a 10-mm-thick copper block is inserted between the magnet and the heat-spreading collar of the gas container which is made of a 10-mm-thick OFHC copper plate. The thermal link is attached with a heater made of ϕ0.1-mm manganin wire wound around it. A PC which differs from the main PC controls the current through the heater via an Interface Corporation PC-3521 digital-to-analog converter PCI-bus card and a simple home-made power amplifier. The current is calculated based on the difference between the target temperature and the temperature at CGR thermistor T4 which is embedded in the heat-spreading collar plate. The proportional-integral (PI) control is adopted to keep the T4 temperature constant. The measured deviation from the target temperature was ± 1 mK at the maximum. Since temperatures are read by the VXI system connected to the main PC, the temperature information was made available via TCP/IP network.

7.2.3 Pressure control system

In place of the manually operated gas pressure control system which was adopted in the Phase II measurement, a computer controlled system was developed by Ohta along with the temperature stabilization system. Its schematic diagram is shown in Fig. 7.3. A HORIBA STEC PV-1101 piezo valve (PV1) is used

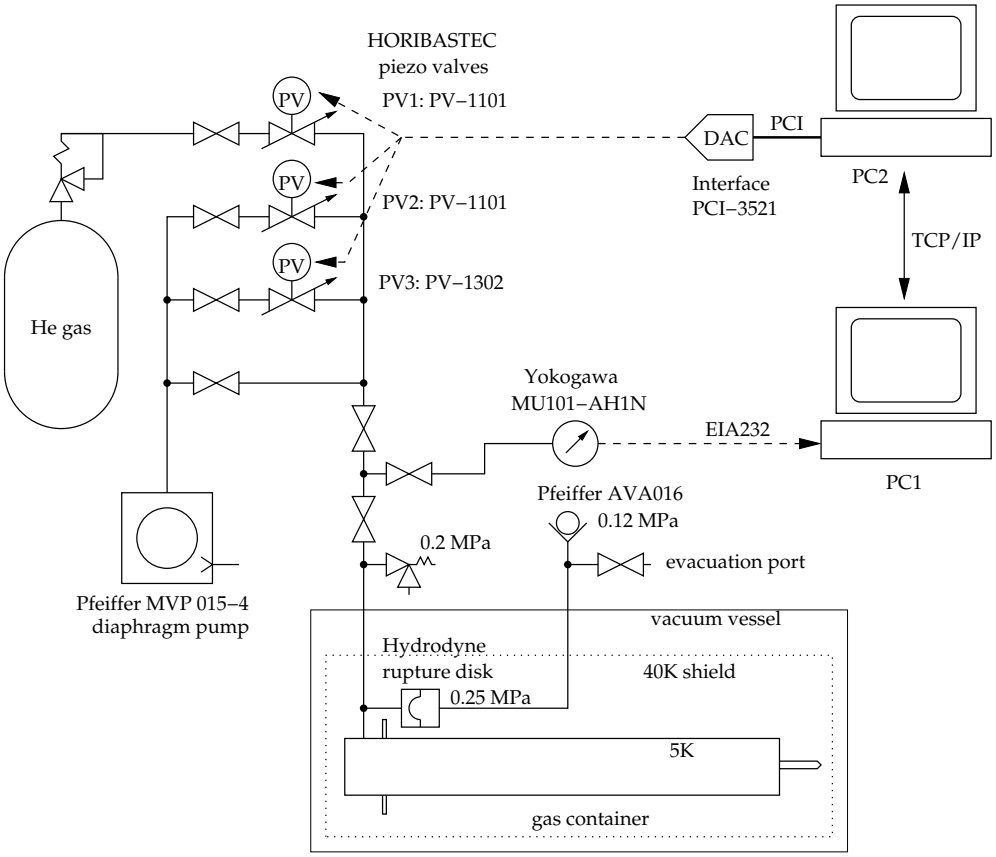

Figure 7.3: Schematic diagram of the computer controlled gas filling system

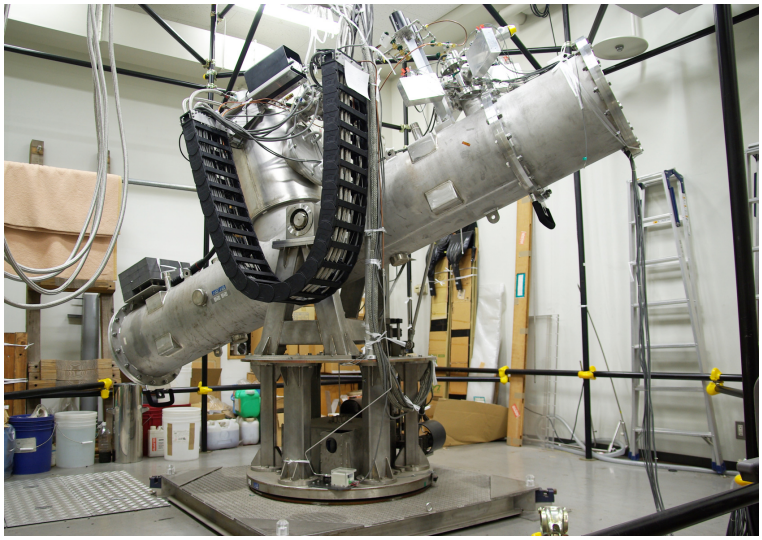

Figure 7.4: Sumico viewed from its left-hand side. The black caterpillar-like structure is a part of the cable handling system for the vertical movement.

to inject helium gas and a PV-1101 (PV2) and a PV-1302 (PV3) are used for suction. PV3 has a higher flow rate than PV2 and is used to reach lower pressures below 10 kPa. Three piezo-valves are controlled by PC2 through the other channels of the identical digital-to-analog converter to the temperature stabilization system. Again pressure gauge output is regularly read by the main PC (PC1) through an EIA 232 serial line, the information is retrieved from it via TCP/IP network.

7.2.4 Other upgrades

In addition to the above, the inner most polymethylmethacrylate (PMMA) lining of the radiation shielding was replaced with thinner polychlorotrifluoroethylene (PCTFE) lining, which widened the clearance inside the copper inner shield by a few millimeters. A cable handling system was introduced to the vertical movement, with which duration of unmanned operation of the telescope was extended from a few hours to a half of a day if switching between east and west was required or to a few months if only sunrises or sunsets were tracked. In this measurement, the helioscope was directed to the east and only sunrises were tracked. Since the cable handling system for the horizontal movement was not completed before the measurement, the azimuthal range was restricted to about 60 degrees for its unmanned operation. The picture of the cable handling system is shown in Fig. 7.4. Some PIN photodiodes which seemed defective after the previous measurement were replaced. However, the same level of stability as in the previous measurement was not achieved. Sufficient training was required to build a reliable X-ray detector module.

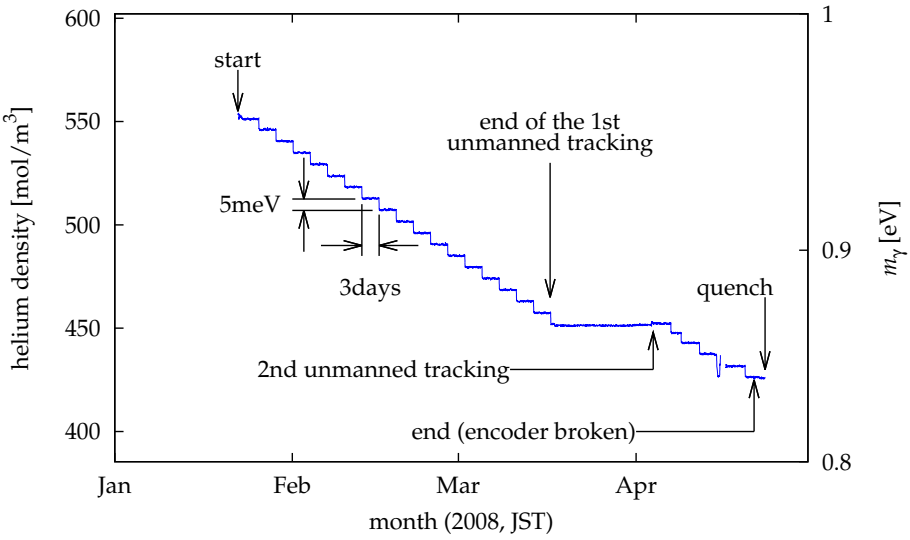

Figure 7.5: Helium densities and the corresponding effective photon masses.

molar density	m_γ	live time [s]	
[mol/m^3]	[eV]	solar run	background
425.8	0.841	8726.817	33122.496
431.1	0.846	25362.813	97561.713
437.1	0.852	25916.684	97863.703
442.4	0.857	24209.316	91178.546
447.2	0.862	16724.156	62828.999
451.7	0.866	23543.709	92698.519
457.1	0.871	22070.878	84977.102
462.8	0.877	20242.818	78517.882
468.3	0.882	20508.113	79185.428
473.8	0.887	18916.877	73595.788
479.3	0.892	19569.124	74852.579
484.8	0.897	18788.295	72368.718
490.3	0.902	18801.649	71656.780
495.8	0.907	18985.843	71630.732
501.3	0.912	18343.668	68041.102
507.0	0.918	18126.204	67753.036
512.5	0.923	18022.376	66218.357
518.0	0.928	18468.133	68035.751
523.3	0.932	17805.490	63160.975
529.0	0.937	18683.594	66060.173
534.6	0.942	19309.984	65930.354
540.2	0.947	18650.869	63162.373
545.9	0.952	19801.929	67513.763
550.9	0.957	20626.335	68302.259

Table 7.1: Table of the gas settings and the live times.

7.3 Scanned masses

On January 22, 2008, the second series of the Phase III measurement was started, and it terminated unintentionally on April 20 due to a failure of a direction sensing encoder and a subsequent quench of the magnet.

The molar density N of helium gas was determined from the measured temperature and the pressure using virial expansion of 3rd order with respect to pressure and 4th order with respect to temperature as:

$$p = NRT\left(1 + \sum_{i=1}^{3}\sum_{j=0}^{4} c_{ij} p^i T^j\right), \tag{7.1}$$

where the coefficients c_{ij} were determined by fitting the data of helium-4 property from NIST [80].

Figure 7.5 shows the calculated molar density of helium and the corresponding effective photon masses as a time chart and the final values for measured mass values are summarized in Table 7.1.

7.4 Analysis

This time, twelve out of sixteen PIN photodiodes survived and `pin1`, `pin2`, `pin3`, and `pin13` went defective through thermal stresses in the course of cooling. The overall effective area is estimated conservatively as $A_{\rm eff} \geq 3.71 \times 10^{-4}\,{\rm m}^2$ at 95% confidence level.

We followed the same procedure as in the previous measurement in obtaining energy spectra from raw data. Based on the new ^{57}Fe source data, we used $\sigma_{\rm pin} = 0.378\,{\rm keV}$ as the energy resolution of the PIN photodiodes and $(1-\epsilon_{\rm cut}) = 1.5 \times 10^{-2}$ as the efficiency loss by cutting slow-rise-time pulses in the following analysis. In calculating the expected signal rate, however, we used Eq. (3.43) in place of Eq. (6.66) since the photon absorption by helium is no longer negligible.

Loss of coherence by gravity is still negligibly small. For example, let us estimate the effect at $m_\gamma = 1\,{\rm eV}$ or $N = 6.026 \times 10^2\,{\rm mol/m}^3$. The pressure difference between both ends of the helium column in the container is

$$\delta p = gNML\,|\sin\theta| \leq 26\,{\rm Pa}, \tag{7.2}$$

where $g = 9.8\,{\rm m/s}^2$, $M = 4.0026\,{\rm g/mol}$, and $|\theta| \leq 28^\circ$ is the angle of inclination. From Eq. (6.7), we find that this gradient of pressure corresponds to the first-order nonuniformity index in Fig. 5.38 or in Eq. (5.19) by

$$q_1 L^2 = \frac{4\pi\alpha L}{m_e E k_{\rm B} T}\delta p \lesssim 1.3, \tag{7.3}$$

by which we estimate for the loss of conversion probability as

$$1 - \frac{\max P_{a\to\gamma}}{\max P_{a\to\gamma}|_{\theta=0}} \lesssim 0.01. \tag{7.4}$$

Considering the non-negligible absorption by helium, L is effectively shorter than 2.3 m, hence we would get slightly smaller value for the loss.

The spectra of the first- and second series are combined to search for an expected axion signal for various m_a in them, since the condition of the measurement was basically the same and we applied the same procedure to both raw data set. However, we do not unify the Phase III *plus* data here due to the different condition of the measurement and the different handling of the raw data applied to them. Data from the 34 different gas density settings were combined by using the summed χ^2 as:

$$\chi^2 = \sum_j^{m_\gamma} \sum_i^{\{E_i\}} \frac{(N_{ij}^{\odot}/T_j^{\odot} - N_{ij}^{\rm bg}/T_j^{\rm bg} - S_{ij})^2}{\sigma_{ij}^2}, \tag{7.5}$$

where

$$S_{ij} = \frac{g_{a\gamma}^4 A_{\rm eff}}{\sigma_{\rm pin}\sqrt{2\pi}} \int_{E_i}^{E_{i+1}} dE \int_0^{\infty} dE' e^{-\frac{(E'-E)^2}{2\sigma_{\rm pin}^2}} \times \epsilon(E') \frac{d\hat{\Phi}_a}{dE}(E') \hat{P}_{a\to\gamma}(E', m_\gamma, m_a) \tag{7.6}$$

is the expected signal rate and

$$\sigma_{ij} = \sqrt{\frac{N_{ij}^{\odot}}{(T_j^{\odot})^2} + \frac{N_{ij}^{\rm bg}}{(T_j^{\rm bg})^2}}. \tag{7.7}$$

The energies $4\,\mathrm{keV} < E < 20\,\mathrm{keV}$ were used for the least-squares fitting. As a result, we found no significant excess for any m_a, and thus an upper limit on $g_{a\gamma}$ at 95% confidence level was given following the Bayesian scheme. Figure 7.6 shows the limit plotted as a function of m_a around the new limit. The $g_{a\gamma}$–m_a parameter region predicted by the preferred axion models [30] is also shown in the same figure as a shaded area.

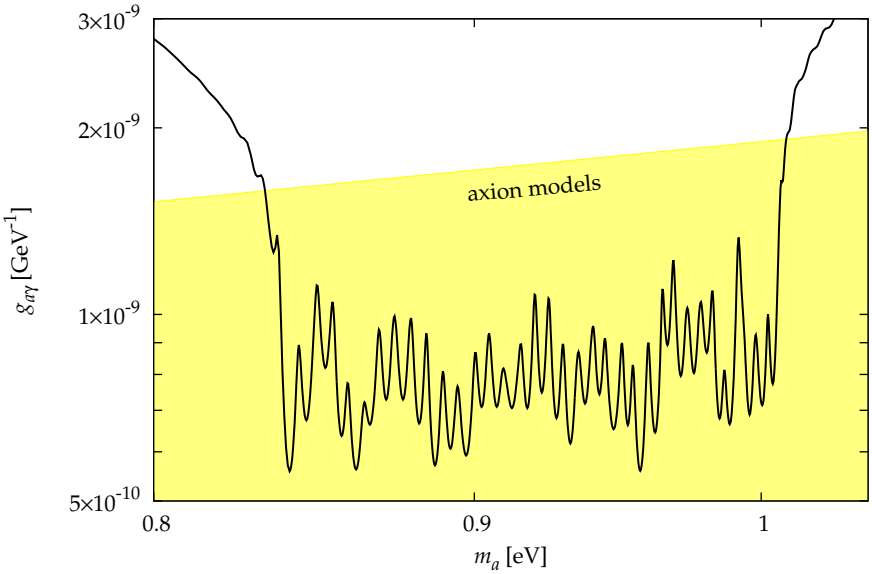

Figure 7.6: The upper limit on $g_{a\gamma}$ as a function of m_a obtained by the analysis where the first and the second series of Phase II are combined (solid curve). The shaded area corresponds to the preferred axion models [30].

Chapter 8

Discussions

8.1 Conclusion

We have developed an axion helioscope and introduced cold helium-4 gas as the dispersion-matching medium in the $4\,\mathrm{T} \times 2.3\,\mathrm{m}$ magnetic field. The axion mass up to 0.27 eV has been scanned in the Phase II measurement. As a result, no evidence for solar axions was observed. We set a new limit on $g_{a\gamma}$ for $0.06\,\mathrm{eV} < m_a < 0.27\,\mathrm{eV}$.

The result is shown as a black solid curve labeled "Phase II" in Fig. 8.1. The previous limit given by the Phase I measurement, and some other limits are plotted in the same figure. Our result is far more stringent than the solar-age limit, $g_{a\gamma} < 2.3 \times 10^{-9}\,\mathrm{GeV}^{-1}$. In deed, this is the first experimental search for solar axions which has enough sensitivity to detect such axions that do not violate the solar model itself in this mass region. Furthermore, the limit is more stringent in most masses than the even tighter helioseismological bound, $g_{a\gamma} < 1 \times 10^{-9}\,\mathrm{GeV}^{-1}$. Watanabe and Shibahashi [105] have argued that the helioseismological bound can be lowered to $g_{a\gamma} < 4.0 \times 10^{-10}\mathrm{GeV}^{-1}$ if the 'seismic solar model' and the observed solar neutrino flux are combined.

In the Phase III measurement, we have scanned the mass region around the lower boundary of the hadronic axion window with an upgraded experimental apparatus. However, no evidence for solar axions was observed. We set a new limit on $g_{a\gamma}$ for $0.84\,\mathrm{eV} < m_a < 1.00\,\mathrm{eV}$, which is also shown as a black solid curve labeled "Phase III" in Fig. 8.1. This is the first result to search for axions using a magnetic helioscope in the $g_{a\gamma}$–m_a parameter region which is predicted by the preferred axion models [30].

The Phase I result [82] and the Phase III *plus* result [104] are plotted as solid blue curves labeled "Phase I" and "Phase III+" in Fig. 8.1, respectively. Some other bounds are also plotted in the same figure.

The exact position of the 'hadronic axion window' or whether it is still open or not are controversial [106, 107]. There is an argument that it has closed by the globular-cluster limit [108]. However, discussions based on mutually independent assumptions are meaningful. It must be essential to test by well-controlled experiments or by direct observations.

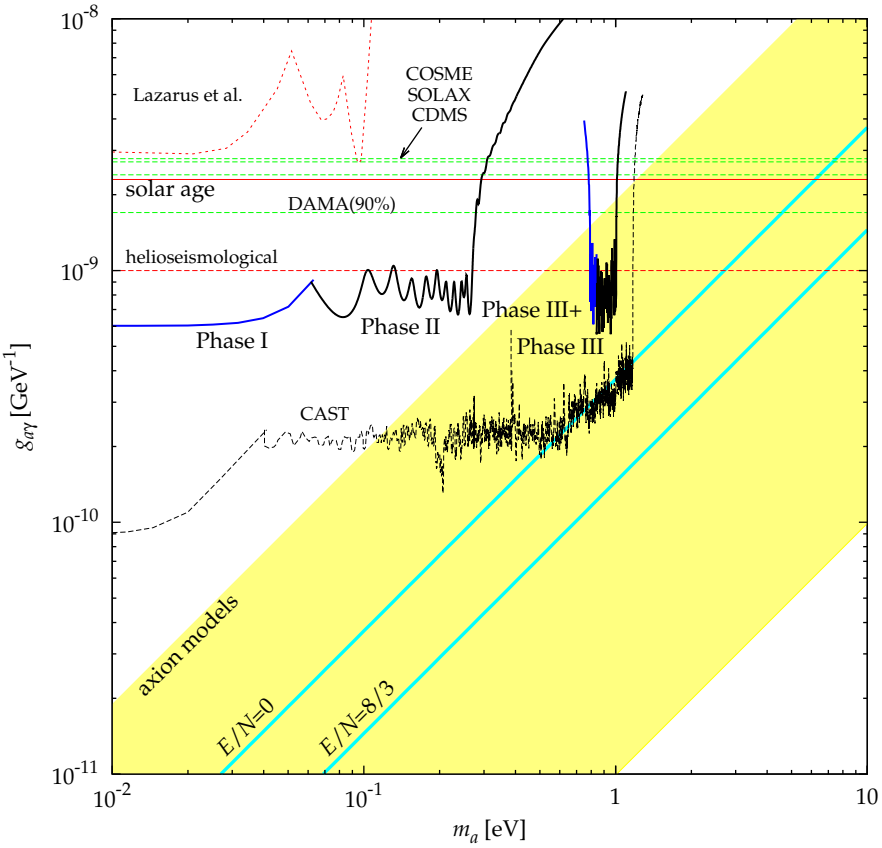

Figure 8.1: Exclusion plot for $g_{a\gamma}$ to m_a. The new limit given by the Phase II- and Phase III measurements is shown by black solid curve, while the limit given by the Phase I measurement [82] and the Phase III *plus* measurement [104] is shown in solid blue curve, the pioneering result by Lazarus *et al.* [67] is shown in dashed red curve, the CAST experiment [70, 71, 72] in dashed black curve, and the limit inferred from the solar age consideration is shown in solid red horizontal line. The horizontal dashed lines are the limits by the SOLAX [75], COSME [77], CDMS [78] and DAMA [76] experiments, and the helioseismological bound. The observational limits except DAMA are at 95% confidence level, while the DAMA limit is at 90% confidence level. The shaded area corresponds to the preferred axion models and two diagonal cyan lines to KSVZ axions and to the case when a GUT is assumed.

8.2 Epilogue

Attempts to introduce helium gas of higher densities to explore higher masses have been unsuccessful due to an emerging thermal nonuniformity in gas.

After the publications of our result [82, 83, 109], The CAST experiment published a new result [72] which covers the regions we have ruled out. It is also plotted in Fig. 8.1 labeled as "CAST" along with their previous results [70, 71]. In the latest measurement, they scanned the mass region between $0.64\,\mathrm{eV} < m_a < 1.17\,\mathrm{eV}$, where they achieved the sensitivity to reach KSVZ axions ($E/N = 0$).

On March 11, 2015, the Tokyo Axion Helioscope, also known as *Sumico*, was dismantled and decommissioned.

Acknowledgements

First of all, I am grateful to Prof. Makoto Minowa who directed the entire experiment. He introduced me into the (low-energy) particle physics, and supported me in many ways. I am thankful to all the members who have been involved in this experiment including Y. Akimoto, H. Hara, T. Horiuchi, T. Horie, A. Ichiki, T. Mizumoto, M. Minowa, S. Mizumaki, S. Moriyama, T. Namba, R. Ohta, F. Shimokoshi, J. Suzuki, Y. Takasu, and A. Yamamoto. Although not all of them are acknowledged in the text, it does not mean that I am regarding their contribution as small, but that the area was so vast that I failed to cover everything. Among others, however, I would like to appreciate Prof. Moriyama. Without his enthusiasm and coercive leadership, it would have been impossible to launch this experiment. I am having great respect for Prof. Yamamoto. He showed us what the professionalism is by giving an example. I am also thankful to S. Otsuka and President Suzuki of Nichirei Seiki Kogyo for many useful advice on the engineering works. The author is thankful to S. Tsuchihashi for sacrificing her name to this experiment. If my memory was correct, the code name was named after her. It remained code name until the end as we failed to get permission from her.

I would like to thank all the people who supported me to finish this work. I would like to thank again Prof. Minowa for allowing me to concentrate on finishing this writing for months. Special thanks to Ryoko for encouraging me, for supporting me, for discussing with me, and for everything else.

This research is supported by the Grant-in-Aid for COE research by the Japanese Ministry of Education, Science, Sports and Culture, and also by the Matsuo Foundation.

Appendix A

Data acquisition software

In the Phase II measurement, acquisition of waveform data from the PIN photodiodes, motion control of the telescope mount, and monitoring of temperatures, gas pressure, etc., everything was performed on a single PC with an Intel Pentium 120 MHz CPU running FreeBSD 2.2.8-RELEASE operating system. The system was later upgraded to a PC with Intel Celeron 1 GHz and, in the Phase III measurement, another PC running Ubuntu Linux was added to use a digital-to-analog converter PCI card which runs only by its proprietary driver.

FreeBSD is a descendant of 4.4BSD, which is the final version of the Berkeley Unix. It was selected since it was one of the most familiar operating system to us. Its network-transparent multiuser oriented feature helped us a lot not only to construct remote alarming system but also to construct network transparent coherent interfaces. To view the temperature–time chart from the office as well as from home, for example, we used to run multiple instances of a program named `simplegraph` which was the identical one running on the console.

The acquisition of waveform data and the motion control of the telescope mount were done via a CAMAC bus, and the environment monitoring was done via a VXIbus. Instead of an all-in-one program which governs everything, we constructed a collection of programs each of which handles individual function. This design helped us to break up individual problems. Furthermore, we were able to revise and to upgrade individual functions without suspending unrelated ones. With this design, however, we needed to arbitrate multiple programs which run concurrently and share some portions of hardware components including the bus adapters.

In order to control hardware in an operating system environment, we need device drivers. We considered some existing data acquisition frameworks before we decided on creating one by ourselves. As for the CAMAC driver, however, all of which we checked out assumed that a single program accessed the bus and seemed to lack mechanisms as the exclusive access control or state management which are needed in multiple access. As for the VXIbus driver, all we were able to find were a system based on expensive Hewlett–Packard workstations or systems based on PC running Microsoft Windows. None of them looked very attractive. Therefore, we constructed a simple cost-effective system based on an IBM PC compatible computer, and created necessary device drivers from scratch as well as the class libraries to use their functions in an object-oriented programming manner.

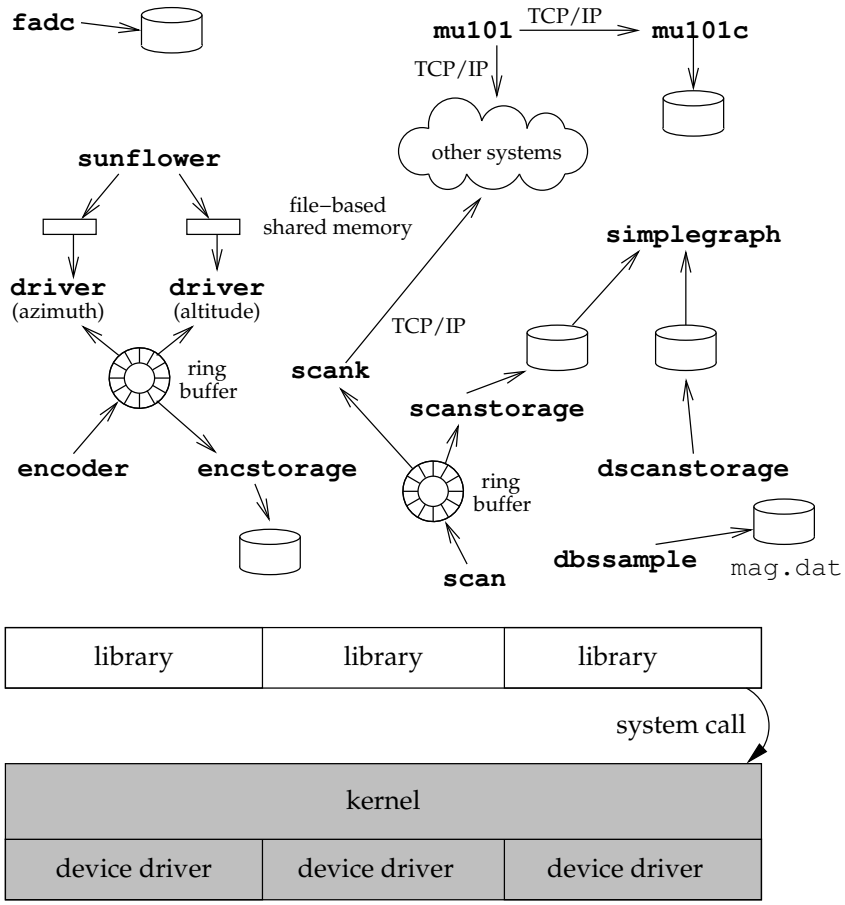

Figure A.1: Data acquisition- and control software architecture.

Figure A.1 illustrates the overview of the data acquisition- and control software of this experiment. At the bottom, the device drivers are interacting with the hardware. Their function is available from the userland through the access libraries which then perform the system call to interact with the device drivers. Application programs are interacting to each other to perform their respective functions.

The `fadc` program collects waveforms from the FADC modules in the CAMAC crate and stores them into a series of files. The `mu101` server regularly monitors the pressure values from the MU101 high precision gauge through an EIA 232 serial line. However, it do not store the values by itself but it lets the information available from other programs via TCP/IP. A separate program `mu101c` connects to the server and stores the retrieved pressure values into a file.

The azimuthal- and altitudinal direction of the helioscope is regularly monitored by the `encoder` process. It retrieves values in two pulse counter modules in the CAMAC crate which accumulate the pulses from each encoders. The estimated direction values are passed via a ring buffer to the `encstorage` process, which stores them into a series of files. The ring buffer is implemented using a file-based shared memory, where old data are available until they are overwritten by a new data. This ring buffer mechanism was incorporated to prevent the `encoder` process from blocking on the chances that accesses to disk drive took a little time.

Two `driver`[1] processes control the motion of two AC-servo motors individually through two pulse generator modules in the CAMAC crate. They obtain the current direction information from the same ring buffer. The target information is provided by the `sunflower` program, which calculates the future solar positions. The target times and directions are passed to each `driver` process via a file-based shared memory.

The `scan` program retrieves the temperature- and Hall-sensor data from the HP E1413 scanning A/D in the VXI crate and pass them via another ring buffer to the `scanstorage` program, which store them into a series of files. The `dbssample` program sets up the VXI digitizer and waits until a quench event occurs. If a quench was detected, it retrieved the transient voltages around the point of the event from the VME memory and recorded them into a file. The `dscanstorage` process peeps into the VME memory regularly and record the immediate voltages successively into a series of files. The stored data were visualized on the screen with the `simplegraph` utility like a multi-input chart recorder. The `scank` server was created to make the temperature information available to other programs via TCP/IP notably to the gas temperature controlling program running in the secondary PC.

Codes of the device drivers and the userland libraries were written by the author. Application programs which run on them were first written by Moriyama and used during the Phase I measurement. In the Phase II measurement and later, however, most of them were rewritten or were revised by the author mainly for the sake of reliability. By reviewing the code, most of the cause of freezing was identified as a problem of exclusive access control to shared resources and some as a problem of timing where new requests were sent to the devices before they got ready. Some components were newly created after the Phase I

[1] The motion control program was named `driver`. Not be confused with the device driver.

measurement by the author.

A.1 Device driver

To control a peripheral device, we need a device driver. The device driver is a computer program which runs as a part of the kernel and enables the operating system to interact with a specific species of devices. The FreeBSD operating system is adopting the monolithic kernel architecture, where a single program called the *kernel* manages the whole system of a computer including the central processing unit (CPU), the main memory, storage devices, and other I/O devices.

Application programs are granted a share of the CPU execution time and a virtual memory where the physical addresses are concealed and access to the protected area of the memory is prohibited by the hardware or simply unavailable. This restricted environment is called the *userland*. From the userland, devices are only accessible through *system calls* to the kernel, where only a limited set of predefined methods are available.

The device drivers, on the other hand, are executed in the privileged mode, since it is part of the kernel program. In the device driver, there are two separate environments called the top half and the bottom half. The top half is initiated by system calls, and runs in the process context where the memory mapping of the caller process is available as is. In addition to it, data objects in the kernel address space are accessible and the stack is switched to a reserved kernel stack. Execution in the top half is a continuation of the user threads. They may give their execution time over to others to wait for an external event by calling the `tsleep` kernel function. The bottom half is initiated by hardware interrupts, and runs in the interrupt context where data objects in the kernel space are accessible, however, those belonging to user processes are unavailable. It uses its own small stack area. In this context, execution is not allowed to be intermitted.

The device drivers for the CAMAC- and VXI buses were implemented with these two contexts in mind. Among others, every data object had to be carefully allocated in the kernel address space using the `malloc` kernel function to communicate between the top- and bottom halves. In addition, care was taken not to call any kernel functions which can cause a wait during in the interrupt context.

We implemented the device drivers as character devices, where devices are accessed from the userland as an operation to device files within the file system using system calls including `open`, `close`, `read`, `write`, and `ioctl`.

A.2 CAMAC

CAMAC stands for Computer Automated Measurement And Control. It defines a simple open-collector bus and modular electronics standard which has been traditionally used for data acquisition in the high energy physics. In the CAMAC bus, its bus space can only be accessed from a fixed bus master device called the crate controller. The bus space is composed of the station numbers of $\mathtt{N} = 1, \ldots, 23$ and the subaddresses of $\mathtt{A} = 0, \ldots, 15$. The crate controller

accesses it through the functions of $\texttt{F} = 0, \ldots, 27$.

We used combination of a KineticSystem Corporation 3922 CAMAC crate controller and a 2927 ISA-bus adaptor card as the PC-side interface. They have an open specification of their status- and control registers, can generate interrupts to the CPU by look-at-me (LAM) signals in the CAMAC bus which can be masked individually with respect to each station, and support bulk data transfer using the system direct memory access (DMA) controller. The register-level information is indispensable in writing device driver. The ability to mask individual LAM signals is crucial in handling individual stations independently. Although the DMA support can be helpful in retrieving the large waveform data, the driver-side interface for it was not implemented before the measurement.

Because of its irregular address space, $(\texttt{N}, \texttt{A}, \texttt{F})$, instead of a flat linear address accessed through read and write, it is difficult to adopt a simple file metaphor of the Unix device files. In our driver, an `ioctl` interface to issue a single $(\texttt{N}, \texttt{A}, \texttt{F})$ operation was made. We also made `ioctl` interfaces to perform crate-wide initialize (`Z`), crate-wide clear (`C`), to assert and deassert crate-wide inhibit (`I`), to test LAM status, and to wait for an event. In the last `ioctl`, the caller process is put to sleep until one of the requested stations asserts LAM, or awoken by timeout or user interrupt (Control-C). The LAM signals are routed properly to each waiting process by the device driver so that the waveform collecting program `fadc` is awoken only by the input/interrupt register which detects event triggers, the encoder reading program `encoder` is awoken only by the pulse counter module, and the motion controlling program `driver` is awoken only by the corresponding AC-servo pulse generator.

The internal of the driver was divided into two layers: one which manages the registers in the ISA card, and another which handles `ioctl` requests from the userland. The latter layer is accessible as the device files named `/dev/camac`N, where $N \in \mathbb{Z}$ and $N \geq 0$, each of which is made available to a single process exclusively.

A.3 VXIbus

VXI stands for VME eXtentions for Instrumentation. The VXIbus is an open standard platform for instrumentation based on the VME (Versa Module Europe) bus. In addition to the 32-bit tri-state TTL bus lines inherited from the VME bus, it defines trigger bus lines for timing, the MODID lines for identifying the slot number (physical address), inter-module analog- and digital connections, and the configuration registers which facilitates plug-and-play. Since it is basically upper-compatible to the VME bus electronically, a VME module can be used in the VXI system with a module adaptor. Any module can become a bus master by an arbitration and can perform read- or write operation in the linear address space.

As the bus adaptor, we used the Hewlett–Packard VXLink system or the combination of HP E1383A VXI module and E1483A ISA-bus adaptor card. This system has an open specification of their registers, and they are considered to have enough function. Although they have the corresponding bit to indicate the bus error (BERR) in their status register, we could not make this system capture bus errors on the VME bus and instead they caused a system hung-up. The only way to circumvent this problem was to code carefully not to develop

bus error. As an alternative, we considered National Instruments MXI system. However, it was unusable since its register-level specification was a blackbox.

We created a device driver which exposed the registers of the VXI modules or the memory in the VME bus space to application programs. Because of their linear address space, application of the file metaphor model was trivial. The VME bus space was made available as a device file where the byte address was directly mapped to the byte offset in the file. Corresponding to the Address Modifiers of the VME bus, 6 device files named `/dev/vxl16d8`, `vxl16d16`, `vxl24d8`, `vxl24d16`, `vxl32d8`, and `vxl32d16` were created. However, the D32 access was not made available because of the hardware limitation. In addition to an interface for the `read` and `write` system calls, we created a kernel interface corresponding to the `mmap` system call. with which the memory window of the VXLink was made directly accessible from application programs. In the access library, the actual access method whether it is through `mmap` or through `read`/`write` is encapsulated by classes which provide users with array-like access into the VME bus.

To perform the Slot-0 module functions, another device file named `/dev/vxlink` was created, with which users can set and get status of the Slot-0 module, can assert SYSRESET, can probe modules in a crate, can wait for IRQ events, etc. Unlike the CAMAC driver, we did not made the VME interrupt event shareable among processes, since the only user of it in this experiment was the digitizer which asserts an interrupt (IRQ1) triggered by the quench detector.

Bibliography

[1] R. D. Peccei and H. R. Quinn, "CP Conservation in the Presence of Pseudoparticles", *Phys. Rev. Lett.* 38 (1977) 1440, "Constraints imposed by CP conservation in the presence of pseudoparticles", *Phys. Rev. D* 16 (1977) 1791.

[2] S. Weinberg, "A New Light Boson?", *Phys. Rev. Lett.* 40 (1978) 223.

[3] F. Wilczek, "Problem of Strong P and T Invariance in the Presence of Instantons", *Phys. Rev. Lett.* 40 (1978) 279.

[4] M. S. Turner, "Windows on the axion", *Phys. Rep.* 198 (1990) 67.

[5] P. Sikivie, "Experimental Tests of the Invisible Axion", *Phys. Rev. Lett.* 51 (1983) 1415, *Phys. Rev. Lett.* 52 (1984) 695(E).

[6] R. Ohta *et al.*, "The Tokyo axion helioscope", *Nucl. Instr. Meth. A* 670 (2012) 73.

[7] G. 't Hooft, "Symmetry Breaking through Bell-Jackiw Anomalies", *Phys. Rev. Lett.* 37 (1976) 8, "Computation of the quantum effects due to a four-dimensional pseudoparticle", *Phys. Rev. D* 14 (1976) 3432.

[8] R. D. Peccei, "The Strong CP Problem", in: *CP violation*, ed. by C. Jarskog, World Scientific, p. 503.

[9] R. D. Peccei, "The Strong CP Problem and Axions", *Lect. Notes Phys.* 741 (2008) 3; eprint: `arXiv:hep-ph/0607268`.

[10] R. Jackiw and C. Rebbi, "Vacuum Periodicity in a Yang-Mills Quantum Theory", *Phys. Rev. Lett.* 37 (1976) 172.

[11] S. Weinberg, "The U(1) problem", *Phys. Rev. D* 11 (1975) 3583.

[12] S. L. Adler, "Axial-Vector Vertex in Spinor Electrodynamics", *Phys. Rev.* 177 (1969) 2426.

[13] J. S. Bell and R. Jackiw, "A PCAC puzzle: $\pi^0 \to \gamma\gamma$ in the σ-Model", *Nuovo Cimento* 60 (1969) 47.

[14] W. A. Bardeen, "Anomalous Ward Identities in Spinor Field Theories", *Phys. Rev.* 184 (1969) 1848.

[15] C. G. Callan Jr., R. F. Dashen, and D. J. Gross, "The structure of the gauge theory vacuum", *Phys. Lett. B* 63 (1976) 334.

[16] W. A. Bardeen, "Anomalous currents in gauge field theories", *Nucl. Phys. B* 75 (1976) 246.

[17] V. Baluni, "CP-nonconserving effects in quantum chromodynamics", *Phys. Rev. D* 19 (1979) 2227.

[18] R. Crewther *et al.*, "Chiral estimate of the electric dipole moment of the neutron in quantum chromodynamics", *Phys. Lett.* 88B (1979) 123, *Phys. Lett.* 91B (1980) 487(E).

[19] C. A. Baker *et al.*, "Improved Experimental Limit on the Electric Dipole Moment of the Neutron", *Phys. Rev. Lett.* 97 (2006) 131801.

[20] A. Nelson, "Naturally Weak CP Violation", *Phys. Lett. B* 136 (1984) 387.

[21] S. M. Barr, "Solving the Strong CP Problem without the Peccei-Quinn Symmetry", *Phys. Rev. Lett* 53 (1984) 329.

[22] D. J. Gross, R. D. Pisarski, and L. G. Yaffe, "QCD and instantons at finite temperature", *Rev. Mod. Phys.* 53 (1981) 43.

[23] C. Vafa and E. Witten, "Parity Conservation in Quantum Chromodynamics", *Phys. Rev. Lett.* 53 (1984) 535.

[24] C. Vafa and E. Witten, "Restrictions on symmetry breaking in vector like gauge theories", *Nucl. Phys. B* 234 (1984) 173.

[25] Y. Asano *et al.*, "Search for a rare decay mode $K^+ \to \nu\bar{\nu}$ and axion", *Phys. Lett.* 107B (1981) 159.

[26] J.-E. Kim, "Weak-Interaction Singlet and Strong CP Invariance", *Phys. Rev. Lett.* 43 (1979) 103.

[27] M. A. Shifman, A. I. Vainshtein, and V. I. Zakharov, "Can confinement ensure natural CP invariance of strong interactions?", *Nucl. Phys. B* 166 (1980) 493.

[28] M. Dine, W. Fischler, and M. Srednicki, "A Simple Solution to the Strong CP Problem with a Harmless Axion", *Phys. Lett. B* 104 (1981) 199.

[29] A. R. Zhitnitskiĭ, "On the possible suppression of axion-hadron interactions", *Sov. J. Nucl. Phys.* 31 (1980) 260.

[30] S. L. Cheng, C. Q. Geng, and W.-T. Ni, "Axion-photon coupings in invisible axion models", *Rhys. Rev. D* 52 (1995) 3132;
eprint: `arXiv:hep-ph/9506295`.

[31] P. C. Bosetti *et al.*, "Observation of prompt neutrinos from 400 Gev proton-nucleus collisions", *Phys. Lett.* 74B (1978) 143.

[32] T. Hansl *et al.*, "Results of a beam dump experiment at the CERN SPS neutrino facility", *Phys. Lett.* 74B (1978) 139.

[33] P. Alibran *et al.*, "Observation of an excess of ν_e, ν_e events in a beam dump experiment at 400 GeV", *Phys. Lett.* 74B (1978) 134.

[34] H. M. Chang *et al.*, "Search for axions from the Kuo-Sheng nuclear power reactor with a high-purity germanium detector", *Phys. Rev. D* 75 (2007) 052004.

[35] A. Zehnder, K. Gabathuler, and J.-L. Vuilleumier, "Search for axions in specific nuclear gamma-transitions at a power reactor", *Phys. Lett.* 110B (1982) 419.

[36] M. Minowa *et al.*, "Invisible Axion Search in ^{139}La $M1$ Transition", *Phys. Rev. Lett.* 71 (1993) 4120.

[37] A. Zehnder, "Axion search in a monochromatic γ-transition: a new lower limit for the axion mass", *Phys. Lett.* 104B (1981) 494.

[38] P. Lehmann *et al.*, "Axion search in the monochromatic $M1$ transition of ^{65}Cu", *Phys. Lett.* 115B (1982) 270.

[39] F. T. Avignon III *et al.*, "Search for axions from the 1115-keV transition of ^{65}Cu", *Phys. Rev. D* 37 (1988) 618.

[40] C. Edwards *et al.*, "Upper Limit for $J/\psi \to \gamma +$ Axion", *Phys. Rev. Lett.* 48 (1982) 903.

[41] D. Antreasyan *et al.*, "Limits on axion and light Higgs boson production in Υ(1S) decays", *Phys. Lett. B* 251 (1990) 204.

[42] K. Ehret *et al.*, "New ALPS results on hidden-sector lightweights", *Phys. Lett. B* 689 (2010) 149.

[43] L. Maiani, R. Petronzio, and E. Zavattini, "Effects of nearly massless, spin-zero particles on light propagation in a magnetic field", *Phys. Lett. B* 175 (1986) 359.

[44] R. Cameron *et al.*, "Search for nearly massless weakly coupled particles by optical techniques", *Phys. Rev. D* 47 (1993) 3707.

[45] W.-T. Ni *et al.*, "Search for an Axionlike Spin Coupling Using a Paramagnetic Salt with a dc SQUID", *Phys. Rev. Lett.* 82 (1999) 2439.

[46] S. J. Asztalos *et al.*, "Improved rf cavity search for halo axions", *Phys. Rev. D* 69 (2004) 011101.

[47] S. J. Asztalos *et al.*, "SQUID-Based Microwave Cavity Search for Dark-Matter Axions", *Phys. Rev. Lett.* 104 (2010) 041301.

[48] M. A. Bershady, M. T. Ressell, and M. S. Turner, "Telescope search for a 3-eV to 8-eV axion", *Phys. Rev. Lett.* 66 (1991) 1398.

[49] M. T. Ressell, "Limits to the radiative decay of the axion", *Phys. Rev. D* 44 (1991) 3001.

[50] D. Grin *et al.*, "Telescope search for decaying relic axions", *Phys. Rev. D* 75 (2007) 105018.

[51] G. G. Raffelt, "Astrophysical Axion Bounds", *Lect. Notes Phys.* 741 (2008) 51; eprint: `arXiv:hep-ph/0611350`.

[52] H. A. Corsico *et al.*, "The potential of the variable DA white dwarf G117-B15A as a tool for fundamental physics", *New Astron.* 6 (2001) 197; eprint: `arXiv:astro-ph/0104103`.

[53] J. Engel, D. Seckel, and A. C. Hayes, "Emission and detectability of hadronic axions from SN 1987A", *Phys. Rev. Lett.* 65 (1990) 960.

[54] J. Preskill, M. B. Wise, and F. Wilczek, "Cosmology of the invisible axion", *Phys. Lett. B* 120 (1983) 127.

[55] L. Abbott and P. Sikivie, "A cosmological bound on the invisible axion", *Phys. Lett. B* 120 (1983) 133.

[56] M. Dine and W. Fischler, "The not-so-harmless axion", *Phys. Lett. B* 120 (1983) 137.

[57] R. Davis, "Cosmic axions from cosmic strings", *Phys. Lett. B* 180 (1986) 255.

[58] P. Sikivie, "Axion Cosmology", *Lect. Notes Phys.* 741 (2008) 19; eprint: arXiv:astro-ph/0610440.

[59] M. Archidiacono *et al.*, "Axion hot dark matter bounds after Planck", *JCAP* 10 (2013) 020; eprint: arXiv:1307.0615.

[60] M. Fukugita, S. Watamura, and M. Yoshimura, "Light Pseudoscalar Particle and Stellar Energy Loss", *Phys. Rev. Lett.* 48 (1982) 1522.

[61] A. G. Sitenko, *Electromagnetic Fluctuations in Plasma*, New York: Academic, 1967.

[62] G. G. Raffelt, "Plasmon decay into low-mass bosons in stars", *Phys. Rev. D* 37 (1988) 1356.

[63] J. N. Barchall *et al.*, "Standard solar models and the uncertainties in predicted capture rates of solar neutrinos", *Rev. Mod. Phys.* 54 (1982) 767.

[64] H. Schlattl, A. Weiss, and G. Raffelt, "Helioseismological constraint on solar axion emission", *Astropart. Phys.* 10 (1999) 353.

[65] G. Raffelt and L. Stodolsky, "Mixing of the photon with low-mass particles", *Phys. Rev. D* 37 (1988) 1237.

[66] K. van Bibber *et al.*, "Design for a practical laboratory detector for solar axions", *Phys. Rev. D* 39 (1989) 2089.

[67] D. M. Lazarus *et al.*, "Search for solar axions", *Phys. Rev. Lett.* 69 (1992) 2333.

[68] K. Zioutas *et al.*, "A decommissioned LHC model magnet as an axion telescope", *Nucl. Instr. Meth. A* 425 (1999) 480.

[69] K. Zioutas *et al.*, "First Results from the CERN Axion Solar Telescope", *Phys. Rev. Lett* 94 (2005) 121301.

[70] S. Andriamonje *et al.*, "An improved limit on the axion-photon coupling from the CAST experiment", *JCAP* 04 (2007) 010.

[71] E. Arik *et al.*, "Probing eV-scale axions with CAST", *JCAP* 02 (2009) 008; eprint: arXiv:0810.4482.

[72] M. Arik *et al.*, "CAST solar axion search with ^{3}He buffer gas: Closing the hot dark matter gap", *Phys. Rev. Lett* 112 (2014) 091302; eprint: arXiv:1307.1985.

[73] J. K. Vogel *et al.*, "IAXO — The International Axion Observatory", in: *Proc. of the 8th Patras Workshop on Axions, WIMPs and WISPs*, Chicago, IL, USA, 2012; eprint: arXiv:1302.3273.

[74] E. A. Paschos and K. Zioutas, "A proposal for solar axion detection via Bragg scattering", *Phys. Lett. B* 323 (1994) 367.

[75] F. T. Avignon *et al.*, "Experimental Search for Solar Axions via Coherent Primakoff Conversion in a Germanium Spectrometer", *Phys. Rev. Lett.* 81 (1998) 5068; eprint: arXiv:astro-ph/9708008.

[76] R. Bernabei *et al.*, "Search for solar axions by Primakoff effect in NaI crystals", *Phys. Lett. B* 515 (2001) 6.

[77] A. Morales *et al.*, "Particle dark matter and solar axion searches with a small germanium detector at the Canfranc Underground Laboratory", *Astropart. Phys.* 16 (2002) 325;
eprint: arXiv:hep-ex/0101037.

[78] Z. Ahmed *et al.*, "Search for Axions with the CDMS Experiment", *Phys. Rev. Lett.* 103 (2009) 141802.

[79] NIST Physical Measurement Laboratory, *XCOM: Photon Cross Section Database*; URL: http://www.nist.gov/pml/data/xcom/.

[80] V. D. Arp and R. D. McCarty, *Thermophysical Properties of Helium-4 from 0.8 to 1500 K with Pressures to 2000 MPa, NIST Technical Note 1334*, U.S. Department of Commerce, National Technical Information Service, 1989.

[81] Y. Inoue *et al.*, "A liquid-helium cooled large-area silicon PIN photodiode x-ray detector", *Nucl. Instr. Meth. A* 368 (1996) 556;
eprint: arXiv:hep-ex/9504010.

[82] S. Moriyama *et al.*, "Direct search for solar axions by using strong magnetic field and X-ray detectors", *Phys. Lett. B* 434 (1998) 147;
eprint: arXiv:hep-ex/980526.

[83] Y. Inoue *et al.*, "Search for sub-electronvolt solar axions using coherent conversion of axions into photons in magnetic field and gas helium", *Phys. Lett. B* 536 (2002) 18; eprint: arXiv:astro-ph/0204388.

[84] T. Namba, "Experimental search for celestial axions utilizing a dipole magnet and X-ray detectors", PhD thesis, The University of Tokyo, 2001.

[85] A. Ichiki, Master's thesis, The University of Tokyo, 2002.

[86] T. Mizumoto *et al.*, "Experimental search for solar hidden photons in the eV energy range using kinetic mixing with photons", *JCAP* 07 (2013) 013; eprint: arXiv:1302.1000.

[87] Y. Sato *et al.*, "Development of a Cryogen-free Superconducting Dipole Magnet", in: *Proc. of the 15th International Conference on Magnet Technology (MT-15)*, ed. by L. Liangzhen, S. Guoliao, and Y. Luguang, Beijing: Science Press, 1998, pp. 262–265, *KEK-Preprint-97-202* (November, 1997).

[88] T. Namba *et al.*, "An X-ray detector using PIN photodiodes for the axion helioscope", *Nucl. Instr. Meth. A* 489 (2002) 224;
eprint: arXiv:astro-ph/010904.

[89] M. Galassi *et al.*, *GNU Scientific Library Reference Manual (3rd Ed.)* ISBN: 0954612078; URL: http://www.gnu.org/software/gsl/.

[90] S. Mizumaki, PhD thesis, The Graduate University for Advanced Studies (Sokendai), 1996.

[91] G. H. Kaplan *et al.*, *Astronomical Journal* 97 (1989) 1197;
URL: http://aa.usno.navy.mil/AA/software/novas/.

[92] The U.S. Naval Observatory, *IERS Rapid Service/Prediction Center for Earth Orientation Parameters*; URL: http://maia.usno.navy.mil/.

[93] D. L. Mills, *Network Time Protocol (Version 3) Specification, Implementation and Analysis, DARPA Network Working Group Report RFC-1305*, 1992.

[94] S. Moriyama, "Direct search for solar axions by using strong magnetic field and X-ray detectors", PhD thesis, The University of Tokyo, 1997.

[95] Y. Akimoto, Y. Inoue, and M. Minowa, "Measurement of the thickness of an insensitive surface layer of a PIN photodiode", *Nucl. Instr. Meth. A* 557 (2006) 684; eprint: `arXiv:physics/0504147`.

[96] V. Radeka, "State of the Art of Low Noise Amplifiers for Semiconductor Radiation Detectors", in: *Proc. Int. Symp. Nucl. Electron.* Vol. 1, Versailles, France, 1968, 46–1.

[97] F. S. Goulding and D. A. Landis, "Signal processing for semiconductor detectors", *IEEE Trans. Nucl. Sci.* NS-29.3 (1982) 1125.

[98] Cryogenic Technologies Group, National Institute of Standards and Technology (NIST), *Material Properties*;
URL: `http://cryogenics.nist.gov/MPropsMAY/materialproperties.htm`.

[99] N. G. Lehtinen *et al.*, "Sensitivity of an underwater acoustic array to ultra-high energy neutrinos", *Astropart. Phys.* 17 (2002) 279.

[100] V. Radeka, "Trapezoidal Filtering of Signals from Large Germanium Detectors at High Rates", *IEEE Trans. Nucl. Sci.* NS-19.1 (1972) 412.

[101] C. M. Lederer and V. S. Shirky, eds., *Table of Isotopes 7th ed.* New York: Wiley-Interscience, 1978.

[102] M. Matsumoto and T. Nishimura, "Mersenne Twister: A 623-dimensionally equidistributed uniform pseudorandom number generator", *ACM Trans. on Modeling and Computer Simulation* 8.1 (January 1998) 3–30;
DOI: `10.1145/272991.272995`.

[103] Y. Akimoto, "Search for solar axions with mass around 1 eV using coherent conversion of axions into photons", PhD thesis, The University of Tokyo, 2007.

[104] R. Ohta, "Search for solar axions with mass below 1 eV using coherent conversion of axions into photons", PhD thesis, The University of Tokyo, 2011.

[105] S. Watanabe and H. Shibahashi, "Constraint on solar axions from seismic solar models" (2001); eprint: `arXiv:hep-ph/0112012`.

[106] P. Astier *et al.*, "Search for eV (pseudo)scalar penetrating particles in the SPS neutrino beam", *Phys. Lett. B* 479 (2000) 371.

[107] J. Hisano, K. Tobe, and T. Yanagida, "Is the $ee\gamma\gamma + \not{E}_T$ event observed by the Collider Detector at Fermilab evidence for a light axino?", *Phys. Rev. D* 55 (1997) 411.

[108] G. G. Raffelt, *Stars as Laboratories for Fundamental Physics*, The University of Chicago Press, 1996.

[109] Y. Inoue *et al.*, "Search for solar axions with mass around 1 eV using coherent conversion of axions into photons", *Phys. Lett. B* 668 (2008) 93; eprint: `arXiv:astro-ph/0806.2230`.